Nanodelivery of novel inhibitors of DNA repair for enhanced cancer therapy

by

Sams Mohammad Anowar Sadat

A thesis submitted in partial fulfillment of the requirements for the degree of

Doctor of Philosophy

in

Pharmaceutical Sciences

Faculty of Pharmacy and Pharmaceutical Sciences

University of Alberta

Abstract

Targeting DNA repair enzymes has attracted much attention in recent year to overcome the therapeutic resistances in cancer therapy. Inhibition of DNA repair enzymes can be used to make cancer cells sensitive to the DNA damaging effect of ionizing radiation or chemotherapy. In addition, the down regulation or mutation of specific DNA repair enzymes and/or tumor suppressor proteins in cancer cells, can make them particularly more sensitive to the inhibition of DNA repair, a process known as "synthetic lethality". Human polynucleotide kinase/phosphatase (PNKP) is a bifunctional DNA repair enzyme which phosphorylates DNA 5′-termini and dephosphorylates DNA 3′-termini that processes the ligation of damaged DNA termini. The inhibition of PNKP can make cancer cells more sensitive to DNA damage by ionizing radiation or Topoisomerase I inhibitors. Through siRNA library screening, a synthetic lethal partnership between loss of PNKP and tumor suppressor Phosphatase and TENsin homolog deleted on chromosome 10 (PTEN). This inspired development of several small molecule inhibitors of PNKP. These newly synthesized PNKP inhibitors are not water-soluble, therefore not injectable.

My research aim was to develop delivery systems at nanometer size range that can target a small molecule inhibitor of PNKP, known as A83B4C63 to the tumor while reducing their access to normal tissues. The nanocarriers were fabricated from self-associating block copolymers based on poly(ethylene oxide) (PEO) and poly(caprolactone) (PEO-PCL) or a-benzyl carboxylate substituted poly(caprolactone), abbreviated as PEO-PBCL. The developed nanocarriers were used for the encapsulation of A83B4C63 alone or with the active metabolite of irinotecan, i.e., SN-38. The developed formulations were characterized for their average diameter, polydispersity, morphology, loading properties, release profiles as well as sensitization of cancer cells to SN38 and/or ionizing radiation both *in vitro* and *in vivo*. To identify the binding affinity between

intracellular PNKP and A83B4C63, a novel biophysical assay known as Cellular Thermal Shift Assay (CETSA) was developed and used. Maximum tolerated dose of A83B4C63 formulated with the aid of Cremophor EL:Ethanol (CE) and nanocarrier formulations was investigated in healthy CD-1 mice. The performed biochemical toxicity and immune histochemical experiments demonstrated that the intravenous (IV) administration of A83B4C63 in nanocarriers or CE form was not toxic up to the maximum examined dose of 50 mg/kg dose, although the nanocarrier injection was tolerated better by mice. The *in vivo* anticancer activity of the above formulations was also determined in colorectal cancer xenografts in mice either in PTEN negative model as monotherapy or in wild type model in combination with radiation therapy using the Small Animal Radiation Research Platform (SARRP). The results provided evidence for the anticancer activity of nanocarrier formulation of A83B4C63 as monotherapy in PTEN deficient HCT116 xenografts in mice. Inhibition of tumor growth was also observed as a result of combination of A83B4C63 nanocarriers with radiation therapy in wild type PTEN+ HCT116 xenografts in mice. This contrasted with the CE formulation of the PNKP inhibitor that did not show any activity, *in vivo*. The superior activity of the nano-formulation of A83B4C63 over CE formulation was attributed to the enhanced distribution of the drug to tumor site by its nanocarrier. A synergistic effect was also observed when nanocarriers of A83B4C63 were combined with SN-38 or its nano-formulation in CRC models, *in vitro*.

The outcomes of this thesis have demonstrated the great feasibility of nano-delivery of a novel inhibitor of DNA repair for CRC therapy either as a single drug in PTEN deficient form or in combination with DNA damaging therapeutics.

Preface

1. Chapter 1 provides a brief introduction about DNA damage and clinical consequences stemming from defective DNA repair, DNA repair and associated therapeutic resistance, PNKP mechanisms and characteristics, DNA double and single strand break repair pathways, synthetic lethality, and targeted drug delivery using polymeric micelles.
2. Chapter 2 of this thesis has been published in the Journal of Controlled Release as Sams M. A. Sadat, Igor M. Paiva, Zahra Shire, Forughalsadat Sanaee, Timothy D. R. Morgan, Marco Paladino, Feridoun Karimi-Busheri, Rajam S. Mani, Gary R. Martin, Frank R. Jirik, Dennis G. Hall, Michael Weinfeld, Afsaneh Lavasanifar. (2021). A synthetically lethal nanomedicine delivering novel inhibitors of polynucleotide kinase 3′-phosphatase (PNKP) for targeted therapy of PTEN-deficient colorectal cancer. This study was a multi-lab investigation. The research group from Dr. Dennis Hall (including Dr. Timothy D R Morgan, Dr. Marco Paladino) contributed to the drug synthesis. Genetic modification of cancer cells and the development of luciferase-positive colorectal cancer cells were carried out in Dr. Frank R Jirik's lab (including Dr. Gary R Martin). I performed and led the main experiments in this study. Dr. Weinfeld and Dr. Lavasanifar were the principal investigators.
3. Chapter 3 of this thesis is In Press in Frontiers in Oncology as Sams M. A. Sadat, Melinda Wuest, Igor M. Paiva, Sirazum Munira, Nasim Sarrami, Forughalsadat Sanaee, Xiaoyan Yang, Marco Paladino, Ziyad Binkhathlan, Feridoun Karimi-Busheri, Gary R. Martin, Frank R. Jirik, Armin M. Gamper, David Murray, Dennis G. Hall, Michael Weinfeld, and Afsaneh Lavasanifar. Nanodelivery of a novel inhibitor of DNA repair enzyme for targeted sensitization of colorectal cancer to ionizing radiation-induced DNA damage. This study was also a multi-lab investigation. The research group from Dr. Dennis Hall (including Dr. Timothy D. R.

Morgan, Dr. Marco Paladino) contributed to the drug synthesis. Genetic modification of cancer cells and the development of luciferase-positive colorectal cancer cells were carried out in Dr. Frank R Jirik's lab (including Gary R Martin). Dr. Melinda Wuest significantly helped in performing the SARRP study and PET imaging and in data analysis. I performed and led the main experiments in this study. Sirazum Munira, Nasim Sarrami, and Dr. Forughalsadat Sanaee helped in performing biodistribution studies. Dr. Feridoun Karimi-Busheri helped in coordinating the projects among multidisciplinary members of our research team. Dr. Armin M. Gamper helped us by providing his IVIS facilities to perform the bioluminescence imaging of tumors-bearing mice. Xiaoyan Yang helped in microscopic identification of DNA damage activities of cancer cells receiving A83B4C63 with or without ionizing radiation, *in vitro*. Dr. Weinfeld and Dr. Lavasanifar were the principal investigators. This is the first preclinical study where we showed the promising *in vivo* tumor growth retardation for the efficacy of PNKP inhibition in combination with radiation therapy.

4. Chapter 4 of this thesis has been published in the Pharmaceutics as Sams M. A. Sadat, Mohammad Reza Vakili, Igor M. Paiva, Michael Weinfeld, Afsaneh Lavasanifar. (2020). Development of self-Associating SN-38-conjugated poly(ethylene oxide)-poly(ester) micelles for colorectal cancer therapy. I performed and led the main experiments in this study and Dr. Mohammad Reza Vakili helped me in the synthesis. Dr. Igor M. Paiva helped in NMR data processing. Dr. Weinfeld and Dr. Lavasanifar were the principal investigators.
5. Chapter 5 of this thesis will be considered for a publication as Sams M. A. Sadat, Mohammad Reza Vakili, Marco Paladino, Dennis G. Hall, Michael Weinfeld, and Afsaneh Lavasanifar. Development of self-associating poly(ethylene oxide)-poly(ester)-based mixed micellar nanoparticle for targeted co-delivery of topoisomerase I toxin (SN-38) and its novel chemo-

sensitizing inhibitor of a DNA repair enzyme, polynucleotide kinase 3′-phosphatase (PNKP) in colorectal cancer. This study was the improvement of the limitations of the published works described in chapter 2 in terms of conjugation of SN-38 with the suitable non-toxic block copolymer. In this study, we have further provided the proof of principle for the validity of this combination therapy using PNKP inhibitor and SN-38 in CRC cell lines, *in vitro*. For this purpose, conjugation of SN-38 to end functional groups on methoxy-poly(ethylene oxide)-block-poly(α-benzyl carboxylate-ε-caprolactone) was pursued. The combination therapeutic approach of this study was expected to enhance the solubilized levels of SN-38 in aqueous media similar to recent other SN-38 solubilizing strategies. I performed and led the main experiments in this study and Dr. Mohammad Reza Vakili helped me in synthesis. Dr. Weinfeld and Dr. Lavasanifar were the principal investigators.

6. Chapter 6 of this thesis will also be considered as part of a manuscript for publication Sams M. A. Sadat, Nasim Sarrami, Sirazum Munira, Forughalsadat Sanaee, Marco Paladino, Jaber Emami, Dennis G. Hall, Michael Weinfeld, and Afsaneh Lavasanifar. Pharmacokinetic and tissue distribution profile of poly(ethylene oxide)-poly(ε-caprolatone)-based micellar NP of an inhibitor of polynucleotide kinase 3′-phosphatase (PNKP), in head and neck xenograft-bearing mice. In this study, the biodistribution profile of A83B4C63-encapsulated poly(ethylene oxide)-poly(ε-caprolactone)-(mPEO-PCL) based micellar NPs in tumor-bearing xenograft mice has been performed in detail. Here, we assessed the biodistribution and pharmacokinetic profile of A83B4C63 delivered by FDA approved block copolymeric NPs in head and neck cancer xenograft-bearing mice. We aimed to determine the level of the PNKP inhibitor in various tissues including xenograft tumors to identify the suitable dose schedule for combination treatment either with ionizing radiation or DNA-damaging chemotherapeutic

agent. The resulting biodistribution profiles of A83B4C63-encapsulated mPEO-b-PCL-based polymeric micelles were also compared with the conventional solubilized formulations of A83B4C63 dissolved in PEG-400.

7. Chapter 7 of this thesis includes the overall conclusion with future directions.

Dedication

To My Parents

Salma Akter & Mohammad Abdus Salam

&

Parents-in-law

Hasna Hena Begum & Md. Sirazul Hoque

Acknowledgements

First and foremost, I would like to thank almighty Allah for giving me the strength and patience to cope with all the difficulties I have faced during this incredible journey.

I would like to express my sincere appreciation to my supervisor Dr. Afsaneh Lavasanifar and my co-supervisor Dr. Michael Weinfeld for their continuous guidance and support. Without their help and assistance, this thesis would not be possible. For their unwavering support, I am grateful forever. Thank you for all the positive vibes that motivated me throughout my studies. The training under Dr. Lavasanifar's supervision has constantly made me headed for distinction. Being at her side and stepwise learning helped me to become an independent researcher and a better person. I am very grateful to be part of your wonderful team. You are humble, patient and great scientists.

I would like to extend my thanks to the extraordinary members of my advisory committee, Dr. Mary Hitt for her helpful suggestions, encouragement, and support.

I would like to thank Dr. Hall and his research group (including Dr. Morgan, Dr. Paladino, and Dr. Akgun) for your continuous support to provide me the synthesized drug. Without your help, my project would not be possible.

I would like to thank Dr. Hasan Uludag, Dr. Raymond Lai, and Dr. Raimar Loebenberg for their fruitful comments and suggestions. I would also like to thank Dr. Raimar Loebenberg for his support, especially in the teaching assistantship.

I sincerely thank Dr. Mohammad Reza Vakili for having introduced me to the chemistry world as well as for his assistance and valuable pieces of advice. I would specifically like to show my gratitude towards my labmates and mentors, Dr. Forugh, Nasim, Munira, Dr. Feridoun Karimi-Busheri, Dr. Rajam Mani, Dr. Aghdass Rasouli-Nia, Dr. Mohammad Reza Vakili, Mr. Mesfin

Fanta and Mrs. Xiaoyan Yang and many others for their helps. Thanks to all of my colleagues for their kind supports whenever needed.

I would like to acknowledge the funding agencies including Canadian Institutes of Health Research (CIHR), Alberta Cancer Foundation (ACF), Faculty of Graduate Studies and Research (FGSR), Nanomedicines Innovation Network (NMIN), and Faculty of Pharmacy and Pharmaceutical Sciences (FOPPS), University of Alberta that have supported my project and me financially during my PhD study.

Finally, I would like to thank my friends and family including my sister Shamim Ara Begum and my brother Sams Shahid who helped contribute to this thesis. I am grateful for your encouragement that I could be successful in the area of graduate studies. I would like to specially thank my beloved wife Sheikh Tasnim Jahan for always standing by my side and helping me throughout my academic career. Last but not the least; I would like to thank my daughter, Alina Zafreen and my son, Afraz Zafeer, for being true inspiration. Thanks for keeping me company on long walks.

Table of contents

List of Tables

List of Figures

List of Abbreviations

5-FU, 5-fluorouracil

ALK, alkaline phosphatase

ALT, alanine aminotransferase

AP, abasic sites

AST, aspartate aminotransferase

ATR, ataxia-telangiectasia mutated and Rad3-related kinase

AUC, area under the curve

BCL, α-benzyl carboxylate-ε-caprolactone

BER, base excision repair

BIL, bilirubin

BSA, bovine serum albumin

BUN, blood urea nitrogen

CBC, complete blood count

$CDCl_3$, deuterated chloroform

CE, cremophor EL: ethanol

CE/A83, A83B4C63-solubilized cremophor EL: ethanol formulation

CETSA, cellular thermal shift assay

C_{max}, peak plasma concentration

CMC, critical micellar concentration

CRC, colorectal cancer

CREA, creatinine

DIC, N, N′-diisopropylcarbodiimide

DLS, dynamic light scattering

DMAP, 4-dimethylaminopyridine

DMEM/F12, dulbecco's modified eagle medium and F12

DMF, dimethylformamide

DMSO, dimethyl sulfoxide

DNA, deoxy ribonucleic acid

DP, degree of polymerization

DSB, double stranded break

EE, encapsulation efficiency

EPR, enhanced permeability and retention effect

FD, free drug

FD/A83, free drug A83B4C63-soubilized with the aid of PEG-400

FDA, food and drug administration

FHA, forkhead-associated domain

GG-NER, global-genome NER

HCT, hematocrit

HGB, hemoglobin

HLB, hydrophilic-lipophilic balance

HNC, head and neck cancer

HR, homologous recombination

HR, homologous recombination

IR, ionizing radiation

IT, intratumoral

IV, intravenous

IVIS, *in vivo* imaging systems

Kcps, kilo counts per second

Kp, tissue to plasma ratio

MAP, maximum a posteriori

MCH, mean corpuscular hemoglobin

MCHC, mean corpuscular hemoglobin concentration

MCV, mean corpuscular volume

MMR, mismatch repair

mPEO, methoxy-polyethylene oxide

mPEO-*b*-PBCL, methoxy-poly(ethylene oxide)-*b*-poly(α-benzyl carboxylate-ε-caprolactone)

mPEO-*b*-PBCL/SN-38, SN-38-incorporated mPEO-*b*-PBCL micelle

mPEO-*b*-PCCL, methoxy-poly(ethylene oxide)-*b*-poly(α-carboxyl-ε-caprolactone)

mPEO-*b*-PCCL/SN-38, SN-38-incorporated mPEO-*b*-PCCL micelle

mPEO-*b*-PCL, methoxy-poly(ethylene oxide)-*b*-poly(ε-caprolactone)

MRT, mean residence time

MS, Median survival

MTD, maximum tolerated dose

MW, molecular weight

NER, nucleotide excision repair

NHEJ, non-homologous end joining

NP, nanoparticle

NP/A83, A83B4C63-encapsulated nanoparticle

PARP, poly (ADP-ribose) polymerase

PCL, poly(ε-caprolactone)

PDI, polydispersity index

PEG-400, polyethylene glycol-400

PEO, polyethylene oxide

PEO-*b*-PBCL, poly(ethylene oxide)-*b*-poly(α-benzyl carboxylate-ε-caprolactone)

PEO-*b*-PCCL, poly(ethylene oxide)-*b*-poly(α-carboxyl-ε-caprolactone)

PET, positron emission tomography

PIP-3, phosphatidylinositol 3, 4, 5-triphosphate

PLT, platelet

PNKP, polynucleotide kinase/phosphatase

PTEN, phosphatase and TENsin homolog deleted on chromosome 10

RBC, red blood cell

RET, reticulocyte

ROI, regions of interest

ROS, reactive oxygen species

SAM, S-adenosyl-L-methionine

SARRP, small animal radiation research platform

SDS, sodium dodecyl sulfate

SN-38, 7-ethyl-10-hydroxy-camptothecin

SSB, single-strand break

SUV, standardized uptake values

TC-NER, transcription-coupled NER

TEM, transmission electron microscopy

THF, tetrahydrofuran

T_{max}, peak plasma concentration time

TOP1, topoisomerase I

TV, tumor volume

UV, ultraviolet

WBC, white blood cell

Z_{crit}, critical value of Z

Z_{obs}, observed Z

ZP, zeta potential

Chapter 1: Introduction

1.1. DNA damages and clinical consequences stemming from defective DNA repairs

All living creatures are encoded by deoxyribonucleic acid (DNA), a key molecule of the living bodies that carry genetic instructions [1]. As an integral part of the cellular and other multiple functional processes in our body, the DNA strands constantly experience millions of lesions by intrinsic and extrinsic damaging agents, such as atmospheric stressors, chemicals, radiation, chemotherapeutics, reactive oxygen species (ROS), and inflammation [2-4]. To correct and repair any mismatches or lesions of the damaged DNA strands, the cells' inherent complex DNA repair systems and their networks constantly exist on demand to continue error-free functioning of the cells [1, 5]. Unless correctly repaired, persistent modifications of the DNA strands are known to serve as mutagenic templates during nucleic acid synthesis as a result of transcription arrest or replication fork collapse due to compromised erroneous DNA polymerization [6]. To prevent the consequences of DNA damage, cells have unique and complex DNA repair mechanisms to restore the genomic complement to its native state [7, 8]. Moreover, in case of persistent DNA damage, cells might have erroneous miscoding lesions to get the damaged strands repaired. Sometimes, bypassing such miscoding damages by the DNA repair systems introduces unwanted mutagenesis in those cells instead of cell death or error-free DNA-repair [6, 9]. Lack of cell death response and unwanted mutagenesis due to erroneous DNA repair can lead to the activation of oncogenes or inactivation of tumor suppressor genes as a part of initiating the cancer-causing process in our body [10, 11].

DNA damage takes place in cells due to the exposure to either intrinsic or extrinsic DNA damaging agents. Interaction with endogenous reactants (e.g. ROS, S-adenosyl-L-methionine or SAM, aldehydes, etc.), replicative stress (e.g. double-stranded breaks or DSBs), replication mistakes (e.g. mismatch, indel), spontaneous hydrolysis (e.g. uracil, apurinic/apyrimidinic or AP

sites) are common intrinsic sources of DNA damages [12]. In most cases, these intrinsic sources have been well-investigated and shown to be involved in cellular mutagenesis and genomic instability for the carcinogenic processes [13-26]. Moreover, ultraviolet (UV) light, ionizing radiation (IR), chemotherapeutics, and atmospheric chemicals are considered as the foremost extrinsic sources of DNA damaging hazards towards genomic instability as well as mutagenesis in exposed cells [27]. For example, melanoma is a common skin cancer threat due to DNA alteration and consecutive polymerase progression (C→T transition mutations) by UV-induced photo lesions [28-30].

Unintended indirect or therapeutically intended direct IR substantially damage DNA upon exposure inside the cells. Mechanistically, IR triggers the radiolysis of intracellular water through ROS production. The oxidative free radicals resulting from intracellular DNA damage-associated ROS are directly involved in damaging bases, and forming abasic (AP) sites and single-strand breaks (SSBs) [26, 31, 32]. Depending on the therapeutic types, doses and dosage regimens, the IR-mediated DNA damages include SSBs, DSBs, and base alterations [33-35]. Ironically, such dose-dependent DNA damages are also directly proportional to the generation of various types of cancers [36], for example, the development of thyroid and brain cancers due to receiving radiation for neck and cranial cancers, respectively.

Clinically used DNA-damaging agents, commonly known as chemotherapeutics, are intended for therapeutic benefit to treat cancer patients. Among them, platinum drugs (e.g. cisplatin, carboplatin, and oxaliplatin), doxorubicin, 5-fluorouracil (5-FU), methotrexate, temozolomide, and etoposide are commonly used, clinically [37]. Like cancer cells, other proliferative cells including hair follicles, nails, mouth, digestive tract, and bone marrow get affected quickly as the chemotherapeutics target the DNA of rapidly multiplying cancer cells.

Collectively, the genomic lesions resulting from the DNA-damaging chemotherapeutics are potential sources of miscoded DNA repair, genomic instability, and irreparable mutation-associated tumorigenesis [36]. Chemotherapy is deemed to be a higher threat compared to radiotherapy in causing this genetic instability because of its systemic exposure [38]. For example, the development of acute myeloid leukemia from the predisposing disease called myelodysplastic syndrome when treated with chemotherapeutic drugs such as alkylating agents, topoisomerase inhibitors, anthracyclines, etc., has been reported [38].

1.2. DNA repair and associated therapeutic resistances

According to the therapeutic needs, DNA is an important target for either radio- or DNA-damaging chemotherapy [39]. The goal of their function is to damage DNA to kill the cancer cells, permanently. However, cells carrying damaged DNA can survive by their inherent DNA repair mechanisms that confer therapeutic resistance to DNA-damaging therapy [40]. Therapeutic resistance can hinder the efficacy of a drug to the respective disease condition and/or help in developing unwanted clinical phenotypes (e.g. cancers, neurological disorders, premature aging, etc.) stemming from either correct or defective DNA repair [5, 41]. Thus, therapeutic resistance has emerged as the key burden in treating several life-threatening disease conditions, particularly in cancers [42]. For example, most of the patients with multiple myeloma have been reported with therapeutic resistance to an initial dose of chemotherapy due to several underlying resistance mechanisms including DNA repair [43-49]. As a result, the drug from the nitrogen mustard alkylating agent family (e.g. melphalan), in respect to combination therapy, has been turned into a gold standard therapy for multiple myeloma in supporting the concept of DNA repair-associated therapeutic resistance [40, 50-53].

There is no definite conclusion on which underlying therapeutic resistance mechanism is predominant in respect to clinical settings. However, many experimental reports have demonstrated enhanced DNA repair as one of the most significant underlying contributors leading to resistance to radio- and chemotherapy [54-60]. With relevance to the therapeutic resistance, some of the DNA repair and tolerance processes are described below:

1.2.1. Base Excision Repair (BER)

The oxidative ROS, ionizing radiation, and alkylating agents damage the bases of intracellular DNA. Base excision repair (BER) is known as one of the main repair pathways in excising and replacing those damaged DNA bases throughout the cell cycle [61, 62]. Ideally, in this repair process, the damaged bases are first recognized and removed by either monofunctional or bifunctional DNA glycosylase. The subsequent generation of single-strand breaks (SSB) requires additional processing for correcting the strand's termini prior to completing downstream elongation and ligation. The end processing and subsequent downstream DNA repair can be achieved by either short-patch (single DNA base) or long-patch (more than two DNA bases) BER pathway. Either of these downstream BER pathways is involved in recruiting several DNA repair proteins or enzymes [63, 64]. The BER system, is considered to be the primary pathway for removing alkylated bases from DNA, and therefore to be involved in repairing the respective DNA lesions from cancer cells leading to therapeutic resistance and further tumorigenesis [65-67].

1.2.2. Nucleotide excision repair (NER)

Active DNA alterations, due to bulky DNA lesions mainly by cyclosporine, UV photoproducts or monoadducts by drugs belonging to the nitrogen mustard family, are primarily repaired by an important DNA repair pathway known as nucleotide excision repair (NER) [68-71]. NER pathway's function is carried out through two sub-pathways commonly known as global-

genome NER (GG-NER) and transcription-coupled NER (TC-NER), which are involved in recognizing the damaged DNA through the action of damage recognition proteins. Subsequently, the sub-pathways take place, with the aid of excision and helicase proteins, in incising the damaged backbone of the DNA. Once the excision of both sides of the oligonucleotide occurs, followed by refilling the nucleotide gap, ligation of the nicks takes place to complete the NER process. Bypassing DNA damages or any repair steps in NER is believed to contribute to genomic instability and cancer predisposition that reflects the therapeutic resistance [72-74]. It is also reported that DNA damage repair by the NER pathway is one of the main reasons for cisplatin resistance [69, 75].

1.2.3. Mismatch repair (MMR)

Mismatch repair (MMR) is a key post-replication repair pathway in fixing DNA polymerase-associated mistakes such as mismatched nucleotides or small indels. Mechanistically, MMR has direct roles in correcting the resulting mismatches and in preventing faulty bypass replication [76, 77]. In an alternative mechanism, MMR is also involved in repair of DNA damage resulting from the oxidative stress-induced DNA methylation [77, 78]. As a result, a defective MMR system could be a potential threat for initiating unwanted cancerous mutations or permanent genetic alterations due to either error-prone replication or unrepaired mismatches. A common example is in endometrial cancer where hypermethylation of DNA is common due to defective MMR systems [77]. It is also evident that therapeutic resistance to DNA-targeting alkylating agents can result from the involvement of direct repair of DNA and incomplete apoptosis following the MMR pathway [78, 79].

1.2.4. Homologous recombination (HR)

Radiation and chemical-induced breaks or modifications in the DNA need to be fixed in a timely manner to avoid unplanned mutations that could be a potential risk for cancer predisposition. Mistimed repair system-induced replication fork collapses and DSBs are the most lethal events that could lead to the loss of essential or nonessential genes towards the development of cancer [80]. Homologous recombination (HR) and Non-Homologous End Joining (NHEJ) are the two chief repair systems to repair DSBs based on the homology structure of the damaged DNA [81, 82]. Many anticancer drugs (e.g. topoisomerase II inhibitors and some crosslinking agents such as melphalan) and radiation cause DSBs and stalled replication forks, which are ideally repaired throughout the cell cycle by HR and NHEJ pathways [83-85]. Cells with a defective or silenced HR or NHEJ repair system are prone to genetic instability and subsequent cancerous diseases. The deficiency or targeted inhibition of such repair pathways was found to sensitize cells to DNA damaging chemotherapeutics or IR. However, emerging data suggest that drug resistance can be due to the involvement of alternative DNA repair sub-pathways for cancer cells which remain unclear to date [86, 87]. A common example is primary-stage HR-defective ovarian cancers. Platinum-based chemotherapy showed significant efficacy in such cancers due to downregulation or mutation of some common HR proteins like BRCA1, BRCA2, XRCC2, and FANCF [88-95]. In the downstream therapeutic timeline, the re-expression or genetic reversion of such proteins appeared to contribute to developing resistance mechanisms to the platinum therapeutics [94-96]. Another example is etoposide therapy in treating small cell lung cancer where overexpression of an HR protein known as RAD51 was prevalent in therapeutic resistance [97, 98].

Since an error-prone NHEJ repair system (similar to HR) safeguards the genome from chromosomal aberrations, its targeted destabilization is involved in sensitizing to DSBs-causing therapies [99-101]. Defective NHEJ-driven DNA-end joining is correlated with genomic instability as well as cancer predisposition [102-105]. To date, defective NHEJ has been identified behind more than 300 chromosomal translocations in developing blood disorders (e.g. lymphoid cells) and multiple solid tumors including prostate cancer and renal cell carcinoma [106-108]. The HR repair pathway is preferentially involved in repairing one-ended DSBs resulting from any replication fork collapse or encountered SSB or cross-link of DNA. However, repairing any of these one-ended DSBs by the NHEJ repair system generates faulty joints. For example, Fanconi anemia syndrome is classified as a cancer predisposition due to chromosomal abnormalities and DNA cross-links associated with faulty repair resulting from defective NHEJ repair [109, 110]. Similarly, chemotherapeutic treatments are also involved in developing resistance due to faulty NHEJ repair systems. A common example is the role of the XRCC4-like factor, known as a key NHEJ repair protein, in developing resistance to cisplatin, oxaliplatin, doxorubicin, and 5-FU in hepatocellular carcinoma [111]. Furthermore, recent studies also showed that 40% of ovarian cancers possess defective NHEJ repair, which is independent of the HR repair system and promotes resistance to systemic therapy with PARP inhibitor alone (Rucaparib®) [112].

The above DNA repair systems highlight the significance of these pathways not only in response to DNA damaging therapies but also their involvement in developing resistance mechanisms.

Table 1.1: Representative predominant sensors, signaling, and effector proteins for major DNA repair pathways.

	Repair pathway						
	DSB repair			SSB repair			
	NHEJ	HR	Alt-NHEJ	SSB	BER	NER	MMR
Source of DNA damage	IR, Radiomimetics, Topo II inhibitor	X-linking agents, Replication inhibitors, Antimetabolites, Topo I inhibitor		IR, ROS, Radiomimetics, Topo I inhibitor, H_2O_2, Alkylating agents	Alkylating agents	Alkylating agents, X-linker, UV	DNA Pol proofreading errors
Damage sensors	Ku70/Ku80	MRN	PARP	PARP	DNA glycosylases, APE1	XPC DDB2 CSA	MSH2, MSH3, MSH6, MLH1, PMS2
Signaling proteins	DNAPK	ATM, ATR, MK2, CtIP, BRCA1, BRCA2, PALB2, RPA				XPA, XPF, RPA	
DNA repair proteins	PNKP, XRCC4, XLF, LIG4, APLF, Artemis, PAXX, WRN	RAD51, MUS81, SLX1/4, RTEL1, BLM, TOPOIII, POLQ, PARI, RECQL5, FANCJ, BLM	PNKP, XRCC1, LIG3, LIG1, CtIP, POLQ	PNKP XRCC1 PNKP POLβ FEN1 TDP1 Aprataxin LIG1 LIG3A	PNKP, XRCC1, POLβ, FEN1, TDP1, Aprataxin, LIG1, LIG3A	XPG, ERCC1, POLE, POLD1, LIG1, LIG3	EXO1, POLD, LIG1

1.3. PNKP: A key end processing DNA repair enzyme:

DNA damage response and subsequent repair of incompatible ends of the damaged DNA is a critical step that involves a complex intracellular protein network [113]. Moreover, the downstream elongation and ligation process of the damaged DNA requires compatible end processing i.e., 5'-phosphate and 3'-hydroxyl termini. The DNA repair followed by any incompatible end processing as well as ligation could be a potential risk for genetic instability and cancer predisposition [114-116]. A number of end processing DNA repair enzymes have been identified and **Table 1.1** shows a list of end processing enzymes involved in the repair of respective damages they correct pathways [63]. In this thesis, both SSB and DSB repair pathways requiring a DNA repair enzyme known as polynucleotide kinase/phosphatase (PNKP) have been emphasized. PNKP plays an important role in correcting DNA termini and further engaging DNA polymerases and ligase for subsequent elongation and ligation of DNA breaks [117].

1.4. Structure and function of PNKP:

PNKP is a bifunctional 57 kDa protein that has both DNA 3'-phosphatase and DNA 5'-kinase activity that dephosphorylates 3′-phosphate termini and phosphorylates 5′-hydroxyl termini, facilitating rejoining of DNA single- and double-strand breaks by DNA polymerases and ligases [118, 119]. The gene of PNKP is located at chromosome 19q13.4 [120] and the mammalian PNKP protein has three distinct domains, as shown in **Fig. 1.1**, including a forkhead-associated (FHA) domain at the N-terminus, kinase domain at the C-terminus, and phosphatase domain in between them [118].

As a phosphothreonine-binding signaling module, the FHA domain is connected with the catalytic domain by a flexible polypeptide linker. In function, the FHA domain is involved in binding to casein kinase 2-mediated phosphorylation sites of the scaffold proteins XRCC1 and

XRCC4, which play a major role in BER and NHEJ DNA repair pathways, respectively [121, 122]. Such recognition-directed PNKP engagement contributes to executing ligation of end-processed termini of broken DNA strands [119, 123].

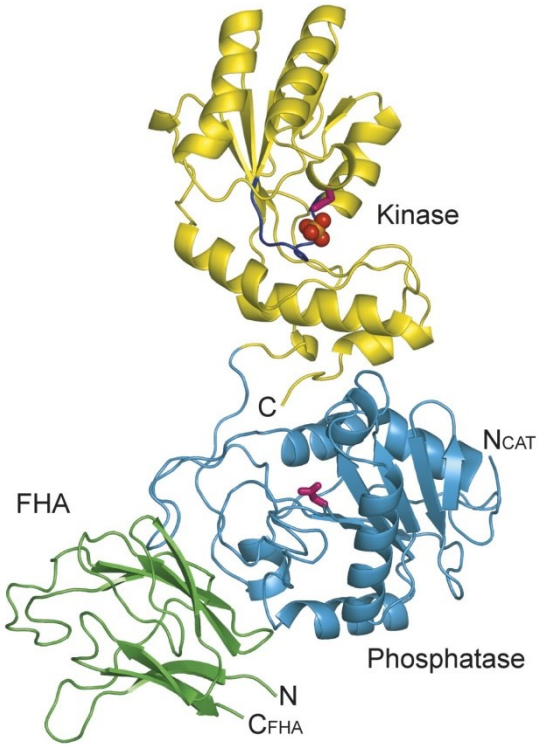

Figure 1.1: Ribbon diagram of mammalian PNKP, with kinase in yellow, phosphatase in blue and FHA domain in green. Catalytic side chains (Asp 170 and Asp 396 in the phosphatase and kinase, respectively) are in pink, the ATP binding P loop is in navy blue, and the sulfate bound at the P loop is in orange and red spheres.

To date, PNKP is believed to be the only DNA repair enzyme that has 5'-kinase activity [124]. Being a member of the adenylate family of kinases, the kinase domain of PNKP selectively binds to the DNA strand 5'-OH terminus without base-pair disruption on the same side as the phosphatase active site [118, 125, 126]. By the virtue of ATP binding sites and the presence of Mg^{2+} ion, the Asp397 residue catalyzes the reaction to phosphorylate the DNA 5'-OH terminus following a nucleophilic substitution (**Fig. 1.2**).

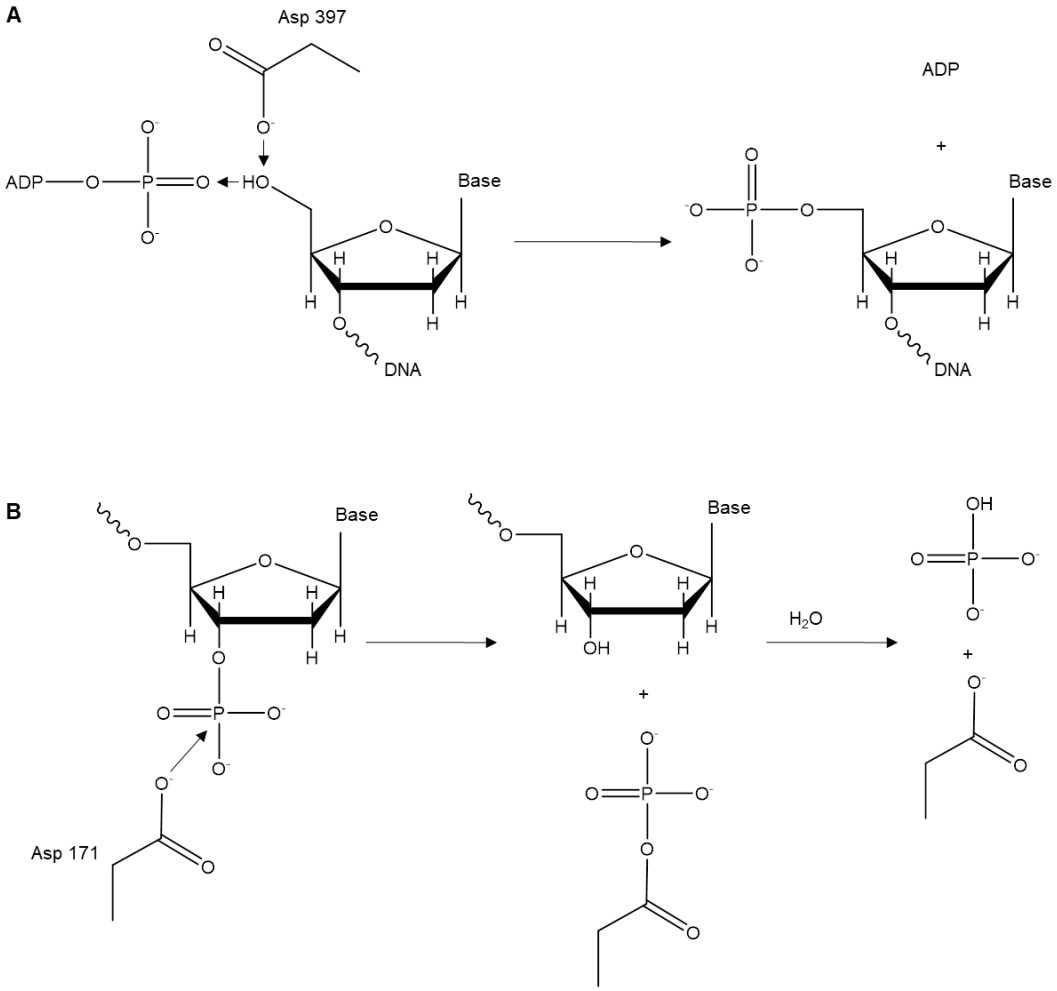

Figure 1.2: Catalytic reactions of the end-processing enzymes. (A) Phosphorylation of 5'-hydroxyl by PNKP catalyzed by Asp397 and dependent on Mg^{2+} ion. ATP is the phosphate donor. (B) 3'-phosphatase activity of PNKP involving nucleophilic arrack by Aspl71 followed by the release of the cleaved phosphate from the aspartate residue.

The phosphatase domain of PNKP belongs to a haloacid dehalogenase superfamily that carries a conserved DxDGT motif [118, 127, 128]. The phosphatase domain catalyzes the removal of 3'-phosphate in the presence of Mg^{2+} ion, which stabilizes the negative charge on the phosphate substrate [125]. At first, nucleophilic attack by Asp171 carboxylate due to negatively charged phosphate substrate generates a covalent phospho-aspartate intermediate as shown in **Fig. 1.2**. Therefore, Asp172-mediated hydrolysis of this covalent bond occurs to generate 3'-OH termini.

The catalytic domain of PNKP is comprised of both kinase and phosphatase activity. However, the kinase and phosphatase domains become nonfunctional when they are not together [127]. Although both catalytic domains function independently by virtue of substrate preferences, the phosphatase activity is believed to take precedence over the kinase activity in both SSB and DSB repair [129]. The presence of both kinase and phosphatase domains of PNKP provides unique flexibility for end processing of the broken DNA termini with either 5′-OH or 3′-phosphate or both [127].

1.5. Synthetic lethality

To date, achieving a targeted anticancer therapy, leaving normal cells unscathed, is a major challenge in clinical oncology and the identification of such new targets is under continuous investigation to overcome the limitation of conventional chemotherapeutics and ionizing radiation that causes unwanted side-effects by damaging DNA in both cancer and normal cells [130-132]. Clinically, such broad-spectrum nonselective therapies lead to major treatment failures [132]. As a result, there is an unmet need to invent novel therapeutic prototypes that could essentially be able to spare the normal cells minimizing side-effects and simultaneously killing the rapidly multiplying cancer cells to maximize the therapeutic benefits. To achieve such targeted anticancer therapy, the concept of synthetic lethality could be one of the promising strategies [130].

Synthetic lethality is described as a compelling occurrence where two non-allelic or non-essential genes are synthetically lethal if simultaneous disruption of both genes leads to cell death but loss of either one alone allows survival of the cells under regular circumstances (**Fig. 1.3**) [130, 133, 134]. Thus in mechanism [135], identifying and targeting a specific gene, that is a synthetic lethal partner of a mutated gene causing cancer, could be a potential cancer cell killing conceptual approach to spare the normal cells. Similarly, synthetic sickness describes another phenomenon

whereby a combination of defective genes causes a non-lethal feebleness condition that could be an effective way to make the cancer cells sensitive to therapeutic stressors [136, 137]. Therefore, both synthetic lethality and sickness have emerged as a targeted therapeutic platform to further develop cancer-specific cytotoxic agents. Due to insufficient methods of identifying synthetic lethal partnerships, it was not fully exploited in the past. However, some advancement has recently been made due to the improved availability of genetic tools for distressing the function of a particular gene in cancer cells [130, 131]. Cancer predisposition occurs due to the mutation of tumor suppressor genes that are the major targets for synthetic lethality [138, 139]. By virtue of advanced chemical and genetic screening technologies, it is not very challenging to identify the cancer cells' genes or proteins that could be possible synthetic lethal partners to mutated tumor suppressor genes in cancer cells [130, 131].

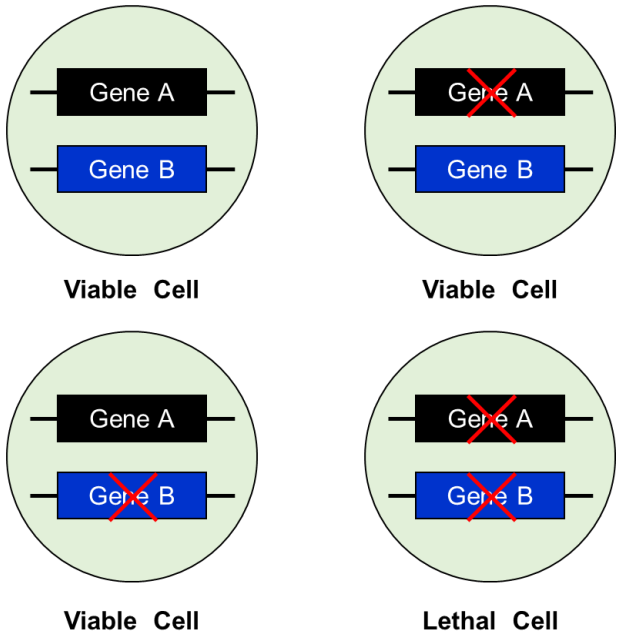

Figure 1.3: The conceptual mechanism of synthetic lethality. Non-essential genes A and B are not lethal to cells if inactivated individually. When both of the genes or their coded proteins are inactivated, cell death occurs.

Recently, DNA repair genes or proteins have gained the most attraction for the synthetic lethal phenomenon, which has been substantiated by the clinical success of the synthetic lethal partnership between the SSB repair protein PARP1 and the breast cancer-associated (BRCA1/2) proteins [140, 141]. Both BRCA1 and BRCA2 are known as tumor suppressor proteins [134, 142]. However, these tumor suppressors have been found to be naturally either lost or mutated in cancer cells of 5-10% of ovarian and breast cancer patients [143]. The inhibition of the DNA repair protein PARP1 in the cancer cells with mutated BRCA1/2 genes appeared to be lethal in those cells. It is well known that PARP inhibition generates DSBs after halting SSB repair [144] and BRCA1/2 proteins are essentially involved in the HR pathway to repair the DSBs of DNA [134, 142]. As a result, the disruption of two main proteins in DNA repair pathways generates the genotoxic DSBs that lead to cell death [142]. **Fig. 4** illustrates a proposed mechanism of synthetic lethality between PARP and BRCA.

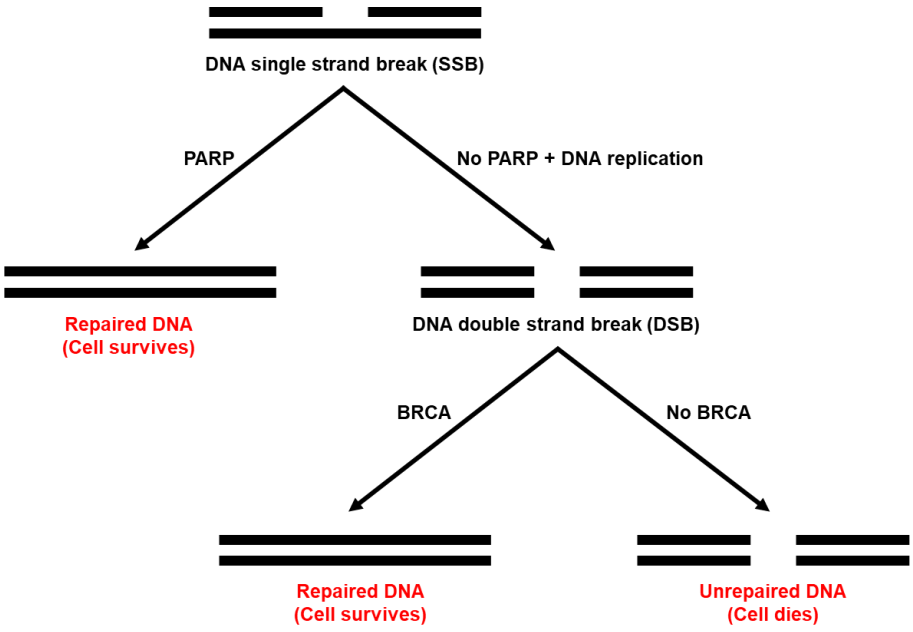

Figure 1.4: Synthetic lethal partnership between PARP and BRCA. PARP participates in SSBR. Inhibiting PARP chemically leads to stalled replication forks creating DSBs. However, cells with inactivated BRCA are sensitive to PARP inhibitors due to the inactivation of both SSBR and HR resulting in cell death.

1.6. Synthetic lethality between PNKP and PTEN

DNA damage and the associated repair mechanisms have starring roles in cancer predisposition as most genetic modifications including mutation or loss of tumor suppressor genes result from defective repair of damaged DNA [145]. Due to endogenous ROS, SSBs are the most common events among all the DNA lesions, and any unrepaired SSBs are out turned with DSBs followed by the collapsed DNA replication forks [146, 147]. As a proof of concept, synthetic lethality was concomitant for inhibiting PARP proteins in BRCA-mutated cancer cells without any endogenous DNA damaging triggers, which could be attributed to the excess production of SSBs per cell cycle followed by DSBs [148, 149]. Following this discovery, it is suggested that inhibition of any SSB repair protein could be synthetically lethal in cancer cells with defective DSB repair proteins.

Phosphatase and TENsin homolog deleted on chromosome 10 (PTEN) is a tumor-suppressor gene with both lipid and protein phosphatase activities [150]. PTEN regulates various cellular processes including cell signaling, survival, metabolism, microenvironment, and proliferation via phosphatidylinositol-3 phosphate kinase (PI3K) pathway [151]. PTEN also plays a key role in maintaining genomic stability [152, 153]. As shown in **Table 1.2**, some recent reports have revealed that PTEN mutation is very common in several cancers including CRCs and head and neck squamous cell carcinomas (HNSCCs) [150-152, 154-157]. The literature provides a strong case for PTEN loss as a valid biomarker in tumorigenesis and prognosis of some deadly cancers [150, 158, 159], emphasizing the potential of therapeutics targeting PTEN deficiency in cancer treatment. Phosphatidylinositol 3, 4, 5-triphosphate (PIP-3) is the main substrate of PTEN; and an increased accumulation of PIP-3 in cancer cells limits the number of apoptotic stimuli, leading to tumor progression [158, 159]. Moreover, PTEN

deficiency is found to be accompanied by the upregulation and/or mutation of other survival/aggression pathways in CRC including the PI3K-AKT pathway, KRAS, BRAF, and PIK3CA mutations. PTEN loss or inactivation has also been shown to be associated with the limited sensitivity or non-responsiveness of tumors to chemo- and/or immunotherapies [160, 161]. It has recently been reported that PTEN loss is also associated with synthetic lethality when PARP is inhibited as observed in BRCA-mutated cancer cells [162]. The mechanism behind this synthetic lethality in PTEN-deficient cancer cells was demonstrated by the defective HR repair pathway [162-165]. In addition, inhibiting another DNA damage response protein known as ataxia-telangiectasia (ATM) also revealed a drastic synthetic lethality in PTEN-deficient cancer cells which could be attributed to the elevation of endogenous ROS levels in PTEN deficient cells [166].

Table 1.2: A list of estimated frequencies for the percentages of PTEN alterations in various cancers.

Cancer Types	PTEN loss (%)	References
Breast	~ 40	[156, 167-172]
Colorectal	40 - 75	[151, 152, 156, 167, 168, 173]
Lung	44 - 56	[156, 167, 174-178]
Prostate (primary)	~ 29	[156, 167, 179, 180]
Prostate (metastatic)	~ 54	[156, 181]
Glioblastoma	~ 65	[156, 168, 182, 183]
Endometrial	20 - 45	[156, 167, 168, 184, 185]
Ovarian (high grade serous)	~ 34	[156]
Ovarian (endometrioid)	~ 44	[156]
Thyroid	~10	[167, 168, 186]
Melanoma	10 - 20	[167, 168, 187-190]
Bladder	~ 53	[167, 191, 192]
Liver	~ 50	[167, 193, 194]
Pancreatic	~ 70	[167, 195-197]
Head and neck (squamous cells)	23 - 30	[198, 199]

A recent genetic screen using a library of 6,961 siRNAs identified PTEN loss to be a synthetic lethal partner of PNKP (15), and this has been confirmed in various cancer cell lines [200, 201]. Our previous studies also revealed a higher background level of DNA double-strand breaks in unirradiated cancer cells with PTEN loss [201]. The concurrent PNKP inhibition led to enhanced apoptosis due to induced endogenous DNA damage by reactive oxygen species in PTEN-deficient cells [200, 201]. Since the discovery of synthetic lethality resulting from PTEN and PNKP co-depletion as shown in **Fig. 1.5**, we have investigated PNKP as a potential therapeutic

target in PTEN$^{-/-}$ cancers [202, 203]. However, the mechanism behind this synthetic lethal partnership has still not been elucidated.

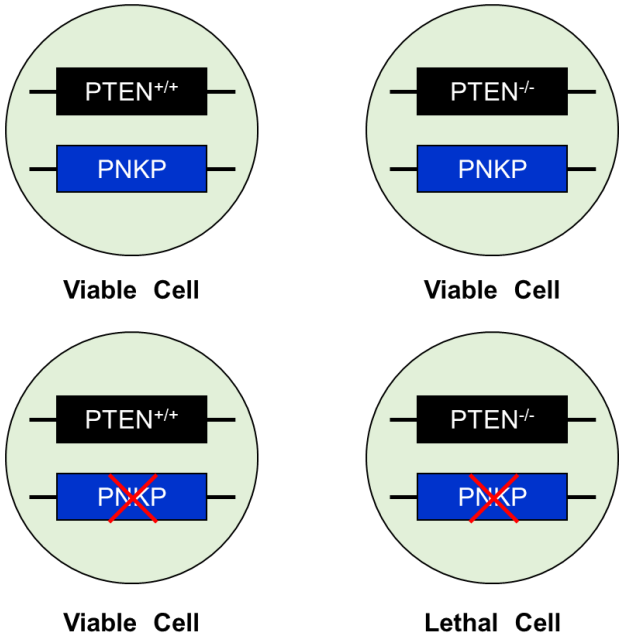

Figure 1.5: The conceptual mechanism of synthetic lethality between PTEN and PNKP. The disruption of either of these genes is not lethal to cells. However, disrupting both of the genes or their coded proteins causes cell death.

1.7. Synthetic sickness to DNA damaging agents: A combination approach for anticancer therapy

Apart from the synthetic lethal partnership between PNKP and PTEN, it is also evident that mutation or loss of PTEN in cancer cells has an up-regulatory role in the PI3K/AKT pathway and cancer progression or metastasis [158, 160, 161, 204-211]. In this thesis, investigations were essentially performed to understand the role of PNKP inhibitors in the induction of synthetic sickness in cancer cells, with or without PTEN knockout (PTEN$^{-/-}$), in combination with DNA damaging IR or chemotherapeutics. PNKP inhibitors are considered to act as chemo- or radio-sensitizer increasing the potency of chemo- or radiotherapy, where lower doses can be used to induce anticancer effects and as a result, side-effects to normal cells can be attenuated.

Combination therapy is currently a common approach in treating different types of cancer. The co-delivery of DNA damaging chemotherapeutic drugs and their chemo-sensitizing DNA repair enzyme inhibitor can be explored to increase the potency and at the same time reduce adverse effects of the combination therapy against various cancers.

After surgery, IR and chemotherapy are the most common anticancer treatments in CRC but these are rarely curative and cause intolerable toxicities in patients. Most importantly, some patients with localized or advanced cancer, who are not ideal candidates for surgery and IR, are mandated for the initiation of chemotherapeutic treatment regimens with a compromised response rate [212]. As a result, the best treatment decisions have been varied and individualized from patient to patient [213-215]. However, resectable surgery is a very common option in CRC and adjunctive chemotherapy or ionizing radiation is often employed before or after surgery [216]. Basically, radiation therapy, often with neoadjuvant chemotherapy, is considered before the surgery to help in shrinking the localized tumors to facilitate the complete resection [217, 218]. In the cases of incomplete resection, to prevent cancer and metastasis, radiation or chemotherapy is considered to kill the cancer cells that may have been left behind in the resection boundary after the surgery [219].

Despite the DNA damaging therapy employed either pre or postoperative surgery, failure of such monotherapy is still associated with suboptimal clinical outcomes. Inherent or thriving cellular resistance mechanisms to the therapeutic modalities can result in predominant reoccurrences in cancer patients [220, 221]. In order to improve the outcomes of pre or postoperative radiotherapy, one important challenge is to discover a nontoxic agent that can act as a radio- or chemo-sensitizer, a process of making cancer cells more sensitive to DNA damaging agents [222]. Following a similar mechanism by which DNA-damaging chemotherapeutic acts, IR

takes advantage of the exposure to high intensity of radiation for cell death. However, cancer cells that survive suboptimal radiation intensity, can develop resistance. As a result, an elevated radiation dose might be required which can harm the nearby normal tissues.

Recently, inhibiting DNA repair has been demonstrated as a promising approach to improve the sensitivity of cancer cells to IR. Different DNA repair enzymes have been validated as therapeutic targets in various cancers for radio-sensitization [63]. In this context, inhibition of PARP has shown promise [223-225]. Other DNA repair enzymes, e.g., ATM, ATR, DNA-PKcs have been extensively investigated to develop new small molecule inhibitors to act as radio- and chemo-sensitizers [226-233]. In these cases, the most challenging part was to develop cancer-specific radio- or chemo-sensitizer because these DNA repair inhibitors could also act non-specifically and pose a potential risk for unwanted mutation and side-effects when used in combination with DNA damaging therapeutics in normal cells. More specific small fusion peptide-based inhibitors of ChK2 kinase activation [234], ATM-NBS1 interaction [235], and DNA-PKcs autophosphorylation [236] have also been developed to act as radio- or chemo-sensitizer. However, these peptide-based targeting strategies suffered from unavoidable stability problems.

1.8. Rationale, hypothesis, and objectives

1.8.1. Rationale

Human polynucleotide kinase-phosphatase (PNKP) was also identified as a key enzyme involved in DNA repair pathways following radiation or treatment with topoisomerase I inhibitors (e.g. Irinotecan) in many types of cancers [237]. The validity of PNKP as a therapeutic target, in sensitizing cancer cells to topoisomerase I inhibitor and IR, has already been shown by our research team and others [118-120, 126, 238]. Being inspired to develop an effective inhibitor of the PNKP enzyme, the research groups of our collaborators, Dr. Dennis Hall and Dr. Michael Weinfeld, have

developed two generations of novel inhibitors of PNKP. A PNKP inhibitor in this library known as A83B4C63 was recently shown to sensitize cancer cells to radiation and irinotecan [202, 203]. A83B4C63 is a second-generation polysubstituted imidopiperidine small molecular drug with a K_D value in the nanomolar range for binding to purified PNKP (**Fig. 1.6)**. The water-solubility of this drug was measured to be < 1 μM with a logD of around 4.16.

To increase the water solubility and at the same time, the specificity and potency of PNKP inhibitors for solid tumors such as CRC or head and neck cancer, encapsulation of A83B4C63 was proposed. This approach was suggested to show anticancer activity as monotherapy in PTEN deficient cancers and in combination with radiation therapy or TOPI inhibitors.

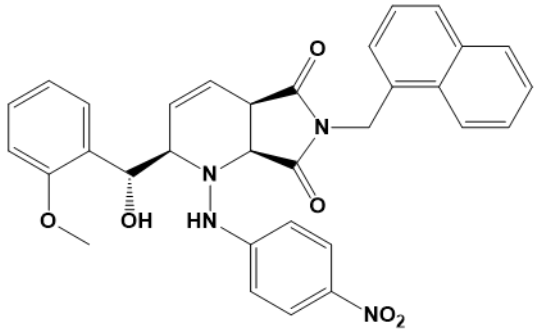

Figure 1.6: The chemical structure of second generation PNKP inhibitor known as A83B4C63.

Broad-spectrum DNA-damaging chemotherapeutics have some limitations including resistance, tumor recurrences, non-specific biodistribution, poor water-solubility, and requirement of high therapeutic doses [239]. Although radiation therapy is classified as localized DNA-damaging therapy, it causes suboptimal therapeutic response to result in therapeutic resistances, recurrences, and genomic instability [240]. Both chemo- and radiation therapy are also considered as palliative therapies in patients with metastatic cancers due to their limited efficacy and there is yet no standard therapeutic recommendation for metastasized cancer management [241-243].

The poor solubility and high dose-dependent side effects of many hydrophobic chemotherapeutic drugs significantly limit the overall clinical outcomes [244, 245]. Polymeric micelles have emerged as a common nanodelivery platform for hydrophobic drugs or hydrophobic drug candidates due to high capacity for the encapsulation of these compounds into the nanocarrier hydrophobic core [239, 246]. One of the main advantages of the polymeric micelles is the core/shell structure that makes modification of their surface possible without any negative effect on the micellar core capacity for drug encapsulation. As a consequence of a hydrophilic shell inducing stealth prperities, polymeric micelles encapsulating hydrophobic drug may bypass the reticuloendothelial system (RES) and improve the biodistribution of the encapsulated drug [247-249]. Long circulating and stealth nano-carriers are known to passively target solid tumors, via enhanced permeability and retention (EPR) effect [250-252]. They can change the distribution of the encapsulated drug the same way, provided to their stability in the systemic circulation and retainment of the encapsulated drug.

Among a wide variety of nanomaterials investigated for passive targeting of hydrophobic drugs, polymeric micelles have attracted much attention due to their smaller size, higher hydrophobic drug encapsulation efficiency, and stealth properties [251, 253-262]. Architecturally, the protective hydrophilic PEG-coating of the biodegradable micelles acts as stealth preventive shield of the core of the micelle carrying hydrophobic payloads in the biological system [256]. One limiting factor, however, is the kinetic stability of the micellar structure and its capacity in retainment of the encapsulated drug in biological media. The poly(ethylene oxide)-poly(a-benzyl carboxylate-e-caprolactone) (PEO-PBCL) micellar structure used here can overcome such limitations. The existence of benzyl core in the polymeric micellar structure has made these nanocarriers particularly much more stable compared to their counterparts. For this reason, we

refer to core/shell structures self-assembled from PEO-PBCL as micellar nanoparticles (NP)s in this thesis.

1.8.2. Hypotheses

1. Nano-delivery of a small molecule PNKP inhibitor can lead to the development of cancer specific monotherapy in PTEN-deficient colorectal cancer.
2. Nano-delivery of a small molecule PNKP inhibitor can lead to the sensitization of wild type colorectal cancer models to IR or Topo I inhibitors.

1.8.3. Objectives

1. To determine the activity of nano-particles of A83B4C63 as monotherapy in PTEN deficient colorectal cancer models making comparisons with the A83B4C63 solubilized by conventional methods
2. To investigating the radio-sensitizing anti-cancer activity of free versus nanoparticles of A83B4C63 in wild type colorectal cancer in vitro and in vivo models.
3. To develop a polymeric micellar nanocarrier formulation of SN-38
4. To investigate the sensitizing activity of free versus nanoparticles of A83B4C63 in combination with free or polymeric micellar Sn-38 formulations in CRC models, *in vitro*.
5. Determining the biodistribution of the A83B4C63 in the form of conventional solubilized formulation and nanoparticle formulation in FaDu xenografts in NIH-III mice.

Chapter 2: A synthetically lethal nanomedicine delivering novel inhibitors of polynucleotide kinase 3′-phosphatase (PNKP) for targeted therapy of PTEN-deficient colorectal cancer

2.1. Introduction

Colorectal cancer (CRC) is the fourth most common cancer. It is responsible for nearly 700,000 deaths per year worldwide [263]. Forty percent of sporadic CRC patients die due to distant metastases highlighting the need for the development of new treatments for this aggressive cancer [264]. The development of CRC carcinogenesis is classified as a multistep process underlying the tumor growth with substantial genetic heterogeneity [158].

Phosphatase and TENsin homolog deleted on chromosome 10 (PTEN) is a tumor-suppressor gene with both lipid and protein phosphatase activities [150]. Recent reports have revealed PTEN mutation in 18 - 30% of cases of sporadic and in 75% of cases of aggressive CRCs [151, 152, 154, 155]. The literature provides a strong case for PTEN loss as a valid biomarker in tumorigenesis and prognosis of CRC [158, 159], emphasizing the potential of therapeutics targeting PTEN deficiency in CRC treatment. Phosphatidylinositol 3, 4, 5-triphosphate (PIP-3) is the main substrate of PTEN; and an increased accumulation of PIP-3 in cancer cells limits a number of apoptotic stimuli, leading to tumor progression [158, 159]. Moreover, PTEN deficiency is found to be accompanied by the upregulation and/or mutation of other survival/aggression pathways in CRC including the PI3K-AKT pathway, KRAS, BRAF, and PIK3CA mutations in CRCs. PTEN loss or inactivation is also shown to be associated with the limited sensitivity or non-responsiveness of CRC tumors to chemo- and/or immunotherapies [160, 161].

Synthetic lethality is an exciting treatment option, because of its potential cancer specificity, that has attracted a lot of attention in recent years [134, 265]. Synthetic lethality refers to the induction of lethality due to a continuous co-disruption of two non-allelic, nonessential genes or their proteins in the same cell [138, 266]. In this context, genetic disorders in cancer versus

normal cells can be exploited to develop synthetically lethal partner treatments functioning only on cancer cells that harbor these genetic abnormalities.

A recent genetic screen using a library of 6,961 siRNAs identified PTEN loss to be a synthetic lethal partner of the DNA repair protein polynucleotide kinase 3′-phosphatase (PNKP) (15), and this has been confirmed in various cancer cell lines including CRC cells [200, 201]. Our previous studies also revealed a higher background level of DNA double-strand breaks in unirradiated CRC cells with PTEN loss [201]. The concurrent PNKP inhibition led to enhanced apoptosis due to induced endogenous DNA damage by reactive oxygen species in PTEN-deficient cells [200, 201]. Since the discovery of synthetic lethality resulting from PTEN and PNKP co-depletion, we have investigated PNKP as a potential therapeutic target in $PTEN^{-/-}$ cancers.

PNKP is a bifunctional end-processing enzyme that phosphorylates DNA 5′-hydroxyl termini and dephosphorylates DNA 3′-phosphate termini, facilitating rejoining of DNA single- and double-strand breaks by DNA polymerases and ligases [118, 119]. We have identified small molecule inhibitors of PNKP, from a library of polysubstituted imidopiperidines, as potential novel synthetically lethal monotherapeutics in PTEN-deficient cancers [202, 267]. To overcome the problem of low aqueous solubility, enhance cancer specificity, increase accessibility, and potentiate the activity of lead inhibitors within this library towards tumor-associated PNKP, we proposed the development of polymeric micellar NP formulations [267]. In this context, polymeric micellar formulations based on poly(ethylene oxide)-*b*-poly(α-benzyl carboxylate-ε-caprolactone) (PEO-*b*-PBCL) and poly(ethylene oxide)-*b*-poly(α-carboxyl-ε-caprolactone) (PEO-*b*-PCCL) of two lead PNKP inhibitors, namely A83B4C63 and A12B4C50, respectively, were developed and examined for their functional properties and PNKP-inhibitory effects, *in vitro* [267]. A83B4C63 is a second generation polysubstituted imidopiperidines synthesized by our research group with an

IC_{50} and K_D value in low μM and nM range in binding to purified PNKP, respectively. It is a poorly water-soluble drug (water solubility < 1 μM) with a log D > 4.16. The current manuscript, reports on the preclinical assessment of activity and safety of PEO-*b*-PBCL NP formulations of A83B4C63 (**Fig. 2.1**) as a new cancer nanomedicine functioning through efficient inhibition of tumor-associated PNKP in $PTEN^{-/-}$ colorectal tumors. Comparisons are made with a conventional water solubilized formulation of this lead compound using Cremophor EL: Ethanol (CE), which is FDA approved and routinely used to formulate poorly water-soluble drugs, for example for paclitaxel injection (Taxol®) of cancer patients. Administration of CE, however, is associated with poorly tolerated acute and chronic toxic side-effects, such as anaphylaxis, nephro- and neurotoxicity in patients [268, 269]. CE is also known to interfere with the pharmacokinetics of several drugs [270-276], thus it is not considered an ideal carrier for drug administration in patients. In case of A83B4C63, CE was used since other inert solubilizing agents, such as low molecular weight PEGs, were not able to achieve high enough soluble drug concentrations required for intravenous (IV) administered doses of A83B4C63 in mice.

Polymeric micelles are well-known NPs mainly used for the solubilization and tumor-targeted delivery of poorly water-soluble drugs [259-262]. Current literature on the use of nanodelivery systems, including polymeric micelles, pertains mainly to their application in enhancing the therapeutic index, mostly through a reduction in drug toxicity and side-effects on normal tissues [277, 278]. The research presented here explored the preclinical development of a new drug in the form of nanomedicine in cancer treatment. The results highlight the potential benefit of nanomedicines as means for expediting the clinical development of lead pharmacological entities with suboptimal properties (such as poor water-solubility and/or suboptimal potency) in the drug development process.

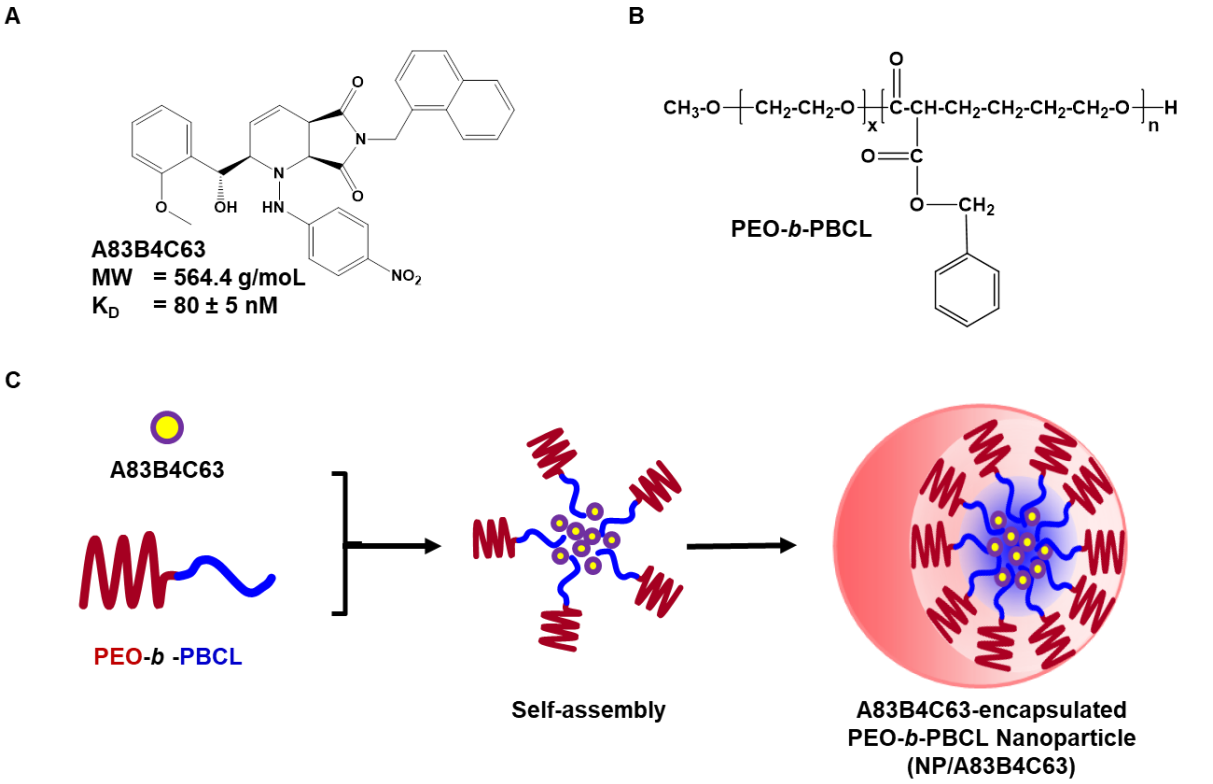

D

Micellar Formulation	Size (nm)	PDI [a]	Loading [b] (%)	Loading Efficiency [c] (%)
NP/A83B4C63	48.9±0.25	0.22±0.07	22.57±0.40	69.12±11.23

[a] PDI: Polydispersity index

[b] Loading (%) = $\frac{The\ amount\ of\ encapsulated\ A83B4C63}{The\ total\ amount\ of\ PEO-b-PBCL\ polymer} X\ 100$

[c] Loading efficiency (%) = $\frac{The\ amount\ of\ encapsulated\ A83B4C63}{The\ initial\ amount\ of\ A83B4C63\ added} X\ 100$

E

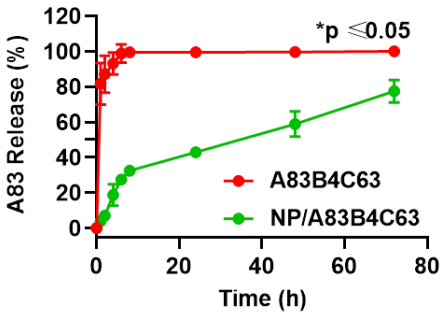

Figure 2.1: Chemical structure of (A) 2-[hydroxy(2-methoxyphenyl)methyl]-6-(naphthalene-1-ylmethyl)-1-[(4-nitrophenyl)amino]-2H, 4aH, 7aH-pyrrolo[3,4-b]pyridine-5,7-dione or A83B4C63 and (B) methoxy poly(ethylene oxide)-b-poly(α-benzyl carboxylate-ε-caprolactone or PEO-*b*-PBCL. (C) Illustration of the encapsulation process for A83B4C63, into PEO-*b*-PBCL micellar NPs. (D) Physicochemical characterization of A83B4C63-encapsulated PEO-*b*-PBCL NPs (NP/A83B4C63) (n = 10). (E) The A83B4C63 release profile of NP/A83B4C63 micelles compared to free A83B4C63 from dialysis tubing (MWCO = 3.5 kDa) in aqueous solution (4% albumin in ultrapure water) at 37ºC. Data are represented as mean ± SD (n = 3). Significances of the differences were considered if *p ≤0.05 following one-way ANOVA followed by Tukey's method. Data are expressed as mean ± SD (n = 3).

2.2. Materials and methods

2.2.1. Materials

Methoxy-polyethylene oxide (PEO) (average molecular weight of 5000 g/mol) and all research grade organic solvents were purchased from Sigma (St. Louis, MO, USA). α-Benzyl carboxylate-ε-caprolactone monomer was synthesized by Alberta Research Chemicals Inc. (Edmonton, AB, Canada). Stannous octoate was purchased from MP Biomedicals Inc. (Tuttlingen, Germany). In-house-made PNKP-detecting primary antibodies [279], and β-actin (Santa Cruz, CA, USA) were used.

2.2.2. Synthesis of A83B4C63 and PEO-*b*-PBCL copolymer

The polysubstituted imidopiperidine compound, A83B4C63, was synthesized using a three-component aza[4+2]/allylboration reaction and purified to homogeneity via HPLC as previously described [280]. The structure of the compound was confirmed by NMR, IR, and LC-MS as previously reported [267].

The affinity (K_D) of A83B4C63 to purified recombinant PNKP protein was determined by fluorescence quenching as previously described (20). The distribution coefficient (log D at pH 7.4) and aqueous solubility (Kinetic) were determined by WuXi AppTec (Shanghai) Co (https://www.wuxiapptec.com/) using standard protocols. The IC_{50} of A83B4C63 was determined using a 70-µL reaction mixture containing 7 µL of 10X reaction buffer (500 mM Tris (pH 8), 100 mM $MgCl_2$, 1 mM EDTA, 1 mM spermidine and 10 mM dithiothreitol), 3.5 µL A83B4C63 dissolved in DMSO (final concentration in reaction mixture from 0 to 100 µM), 3.5 µL of 10 ng/µL PNKP and 49 µL of distilled water were mixed and incubated for 5 min at 37°C and 7 µL of 0.5 mM 3'-phosphorylated 20-mer oligonucleotide (sequence: 5'-ATTACGAATGCCCACACCGC-3'-Phos; Integrated DNA Technology, Coralville, IA) was added. The reaction was incubated for

10 more minutes and then 3 × 20 µL aliquots were transferred to a 384-well plate (Corning, Kennebunk, ME). PiColorLock Gold reagent (Abcam, Cambridge, MA) was prepared shortly before use by adding 1/100th volume of accelerator to PiColorLock Gold reagent. 5 µL of this preparation was then added to each 20-µl aliquot of the reaction samples and incubated for 10 min at room temperature before measuring absorbance at 620 nm using a FLUOstar Omega plate reader (Mandel Scientific Company Inc., Canada). The same protocol was used to determine if the PEO-*b*-PBCL polymer (dissolved in water) inhibits PNKP phosphatase activity.

The block copolymer, PEO-*b*-PBCL with 26 degree of polymerization for the PBCL block was synthesized by ring-opening polymerization of α-benzyl carboxylate-ε-caprolactone using methoxy-PEO (MW: 5000 g/mol) as an initiator and stannous octoate as catalyst according to the method described previously (40-42). The synthesized copolymers were characterized for their average molecular weights by ^{1}H NMR (600 MHz Avance III - Bruker, East Milton, ON, Canada) using deuterated chloroform ($CDCl_3$) as solvent and tetramethylsilane as an internal reference standard.

2.2.3. Formulation, characterization, and *in vitro* release study of A83B4C63 loaded PEO-*b*-PBCL NPs

A83B4C63-loaded PEO-*b*-PBCL NPs (NP/A83B4C63) were prepared as previously described [267]. In brief, 10 mg A83B4C63 and 30 mg PEO-*b*-PBCL polymer were completely dissolved in acetone. Then, the organic phase was transferred dropwise to 10 mL aqueous phase and left overnight with continuous stirring with a magnetic bar under vacuum to completely evaporate the organic solvent. The un-encapsulated A83B4C63 was removed by centrifugation at 11600 × g for 5 min to obtain NP/A83B4C63. The NP/A83B4C63 solution was then transferred into Amicon Ultra-15 centrifugal filter tubes (molecular weight cut-off, 100 kDa; Millipore, ON,

Canada) and centrifuged at 11600 × g for 20 min at 4ºC. The average size and polydispersity index (PDI) of the NPs were measured by dynamic light scattering (DLS) using a Malvern Zetasizer 3000 (Malvern Instruments Ltd, Malvern, UK). A83B4C63 loading and loading efficiency were measured and analyzed using a Varian Prostar 210 HPLC system. Reversed phase chromatography was carried out with a Microsorb-MV 5 μm C18-100 Å column (4.6 mm × 250 mm) with 20 μL of sample injected and eluted under isocratic conditions with a solution of 0.1% trifluroacetic acid / acetonitrile (1:1 v/v) at a flow rate of 0.7 mL/min at room temperature. Detection was performed at 280 nm wavelength for A83B4C63 using a Varian 335 Photodiode Array HPLC detector (Varian Inc., Palo Alto, CA, USA). In this study, A83B4C63 control was solubilized with DMSO for all *in vitro* experiments, while for *in vivo* experiments, A83B4C63 was dissolved with the aid of CE.

In vitro release of A83B4C63 was investigated using dialysis technique. Each dialysis bag (Spectrapor dialysis tubing, MWCO = 3.5 kDa, Spectrum Laboratories, Rancho Dominguez, CA, U.S.A.) containing 3 mL of the PEO-*b*-PBCL micellar or free A83B4C63 (dissolved with the aid of DMSO) was immersed into 300 mL release medium (4% albumin in ultrapure water) maintained at 37ºC in a shaking water bath with 65 rpm (Julabo SW 22, Seelbach, Germany). At selected time intervals (0, 1, 2, 4, 6, 8, 24, 48, and 72 h), 300 μL aliquots from inside of the dialysis bag were withdrawn and replaced with an equal volume of fresh water. The concentrations of A83B4C63 in collected samples were measured and analyzed using a Varian Prostar 210 HPLC system. All experiments were carried out in triplicate. Detection was performed at a wavelength of 280 nm.

2.2.4. Cell lines

HCT116 or HCT116/PTEN$^{+/+}$, a human wild-type CRC parental cell line and its PTEN knock out (HCT116/PTEN$^{-/-}$) variant [281] were kindly provided by Dr. Todd Waldman (Georgetown University School of Medicine, Lombardi Comprehensive Cancer Center, Washington, DC, USA). Both cell lines were cultured at 37ºC in 5% CO_2 in a humidified incubator in a 1:1 mixture of Dulbecco's modified Eagle medium and F12 (DMEM/F12) supplemented with 10% FBS, 50 U/mL penicillin, 50 mg/mL streptomycin, 2 mmol/L L-glutamine, 0.1 mmol/L nonessential amino acids, and 1 mmol/L sodium pyruvate. All culture supplements were purchased from Invitrogen (Burlington, ON, CA). All cell lines were routinely tested for mycoplasma in the lab.

2.2.5. *In vitro* cytotoxicity evaluations

The CellTiter 96® AQueous One Solution Cell Proliferation Assay (MTS) kit was purchased from Promega, USA and used to assess the cytotoxicity of A83B4C63 as free drug and NP formulation in both HCT116/PTEN$^{+/+}$ and HCT116/PTEN$^{-/-}$ cell lines according to the manufacturer's protocol. Initially, 2000 cells were plated in each well of 96-well flat-bottomed plates 24 h prior to the treatments. Then, cells were treated with A83B4C63 as free drug and NP form with a concentration range of 0.5 to 10 μM. Control cells received only 0.1% DMSO. After experimental incubation time points, 20 μL of MTS reagent was added in each well and further incubated for 2 h at 37ºC before measuring the absorbance at a wavelength of 490 nm using a BioTEK (Winooski, VT, USA) microplate reader. In addition, the Caspase-Glo 3/7 assay reagent (Promega, Madison, WI, USA) was used according to the manufacturer's protocol to detect the *in vitro* caspase activity in HCT116/PTEN$^{+/+}$ and HCT116/PTEN$^{-/-}$ cells following similar treatment

conditions as mentioned above in the MTS assay. The relative luminescence was measured and analyzed compared to the control. Each experiment was performed in triplicate.

2.2.6. *In vitro* and *in vivo* cellular thermal shift assay (CETSA)

Initially, the CETSA procedure was performed in both HCT116/PTEN$^{+/+}$ and HCT116/PTEN$^{-/-}$ cell lines, *in vitro*. The ability of A83B4C63 to interact with intracellular PNKP and the consequent stabilization of PNKP in the intact cells was analyzed by CETSA [282] using a modified protocol developed for PNKP binding. In brief, cells were cultured in 75-cm^2 tissue culture flasks until the cell confluence reached 85 - 90%. After 4 h of cell treatment with A83B4C63 (as free or NP formulation) and 0.1% DMSO in media (as control) at 37ºC, cells were trypsinized, harvested, washed twice with ice-cold PBS before re-suspending in PBS containing protease inhibitors. The re-suspended cells were aliquoted into five PCR tubes and heated for 3 min to 45ºC, 46ºC, 47ºC, 48ºC, and 49ºC. Afterwards, cells were lysed using liquid nitrogen following four repeated cycles of freeze-thaw and centrifuged at 17000 × g for 20 min to extract the soluble fraction of cellular proteins in the supernatant. Three independent replicates were performed. Equal amounts of proteins were loaded onto 10% SDS-PAGE gels for western blot analysis. After the wet transfer, the nitrocellulose membranes were analyzed for PNKP using an in-house anti-PNKP antibody with a dilution ratio of 1:500. Thereafter, PNKP protein levels were quantified by densitometry analysis using ImageJ software.

The CETSA procedure was also performed *in vivo,* following extraction of tumor cells from the tumor xenografts in animals treated with A83B4C63 formulation intratumorally [283]. In brief, only human colorectal HCT116/PTEN$^{-/-}$ cells were inoculated and grown as subcutaneous (SC) tumor xenografts in the right flank of NIH-III female nude mice of 4 - 6 weeks of age. When the tumor volume reached 150 to 200 mm^3, mice were randomly assigned and grouped into three

test groups (two mice per group). Mice received three intratumoral (IT) injections of A83B4C63 in the free (solubilized with CE) and PEO-*b*-PBCL NP forms at a dose of 1 mg/kg, two days apart. The mice in the placebo group received IT injections of 5% dextrose with the same schedule. Twenty-four hours after the last injection, the mice were euthanized and the excised tumors were collected in the supplemented media and mechanically dispersed using sterile frosted slides for cell suspension. Then, the dissociated cell suspensions were filtered twice using 70-mm cell strainers, counted, and transferred into PCR tubes for CETSA following the above-mentioned protocol.

2.2.7. Western blot analysis

Western blotting was performed to assess the *in vitro* levels of caspase, PARP, and PNKP proteins following cell treatment with A83B4C63 as free drug and NP form in both HCT116/PTEN$^{+/+}$ and HCT116/PTEN$^{-/-}$ cell lines. In brief, 1×10^6 cells were plated in each well of 6-well plates 24 h prior to the treatments. Then, cells were treated with A83B4C63 as free drug and NP form at a concentration of 10 μM. Control cells received only 0.1% DMSO. After experimental incubation time points, protein extracts for western blot analysis were prepared using commercial RIPA lysis buffer (ThermoFisher Scientific, Canada) supplemented with a cocktail of protease inhibitors (Millipore Sigma, Canada). Protein concentrations were measured using the BCA assay kit (Pierce/ThermoFisher Scientific, Canada) according to the manufacturer's protocol. Equal concentrations of protein were separated by SDS-PAGE and transferred to nitrocellulose membranes. After blocking with 5% skimmed milk in TBST (50 mM Tris-HCl, pH 7.4, 150 mM NaCl, and 0.1% Tween 20), the blots were incubated with the respective primary antibodies (caspase-3 catalog# 9662S, cleaved caspase-3 cat# 9661S, caspase-7 cat# 9492S, cleaved caspase-7 cat# 9491S, PARP cat# 9542S) and secondary antibody (HRP-linked anti-rabbit IgG cat# 7074S)

purchased from Cell Signaling Technology (Whitby, ON, Canada). The protein bands were detected using an enhanced chemiluminescence (ECL) based system (Pierce/ThermoFisher Scientific, Canada). The band intensities for the PNKP protein were quantified by performing optical density analysis using ImageJ software.

2.2.8. Maximum tolerated dose (MTD) determination in CD-1 mice

Randomly assigned and grouped healthy CD-1 female mice (4 - 6 weeks of age; 4 mice per group) were injected three times two days apart intravenously with 2.5, 5, 10, 15, 20, or 50 mg/kg doses of A83B4C63 in the free drug and NP forms. Mice in the placebo group received IV injections of 5% dextrose with the same schedule. The weights of the mice were measured up to two weeks following the first injections. After two weeks, the groups receiving the treatments at the doses of 10, 20, and 50 mg/kg were euthanized to collect different organs including brain, heart, lung, liver, kidney, and spleen. Tissue samples were fixed with 10% formalin buffer (pH 7.4) until they were embedded in paraffin, sectioned at 5-micron thickness and stained with Hematoxylin and Eosin (HE). Tissue samples were then evaluated by a pathologist (Dr. P. N. Nation, Animal Pathology Services Ltd., Edmonton, Canada) who was blind to the treatment groups.

2.2.9. Hematology and blood biochemistry

Blood samples from the above animals were collected by cardiac punch 24 h after the last injection, processed, and analyzed for animals that received the doses of 10, 20, and 50 mg/kg of A83B4C63 as free and NP formulations (Prairie Diagnostic Services, Saskatoon, Canada). The levels of hemoglobin (HGB), hematocrit (HCT), mean corpuscular volume (MCV), mean corpuscular hemoglobin (MCH), mean corpuscular hemoglobin concentration (MCHC) as well as counts for red blood cells (RBC), reticulocytes (RET), white blood cells (WBC) or leukocytes,

differential count (neutrophils, lymphocytes, monocytes, eosinophils, basophils), platelets (PLT) and complete blood count (CBC) were measured. In addition, the levels of blood urea nitrogen (BUN), creatinine (CREA), bilirubin (BIL), alkaline phosphatase (ALK), alanine aminotransferase (ALT), aspartate aminotransferase (AST) were measured in plasma.

2.2.10. Xenograft models

All mice were purchased from Charles River Laboratories. All animal studies were conducted in accordance with the guidelines of the Canadian Council on Animal Care with approval from the Animal Care and Use Committee of the University of Alberta, Edmonton, AB, Canada. The HCT116/PTEN$^{+/+}$, HCT116/PTEN$^{-/-}$, and Luc^{+}/HCT116/PTEN$^{-/-}$ xenograft tumor mouse models were generated by subcutaneous injection of 0.5×10^6 cells in a 100 µL mixture of culture media and matrigel matrix (Corning, MA, USA) (1:1 v/v) in the right flank of 4 - 6 week-old female NIH-III nude mice. The CRC cell implanted mice were routinely monitored every day for tumor growth and signs of sickness. Animals reaching early endpoints as set in our animal protocol were euthanized.

2.2.11. *In vivo* anticancer activity of A83B4C63 as CE or NP formulations after IT and IV administration

This study was performed only on HCT116/PTEN$^{-/-}$ xenografts developed as described above. We waited until all tumors became palpable. At the time of first injection, the tumor volume was 80 to 220 mm^3 in this study. Mice were randomly assigned into test groups receiving CE-solubilized and NP formulations of A83B5C63 or control group receiving 5% dextrose, intratumorally (n = 5). The A83B4C63 dose was 1 mg/kg, which was injected three times two days apart.

Both HCT116/PTEN$^{-/-}$ and HCT116/PTEN$^{+/+}$ subcutaneous xenografts in mice were developed as described above. When the tumor volume reached 30 to 100 mm^3, tumor-bearing mice for each model were randomly assigned to test and control groups. In the first experiment, three control groups were intravenously injected with 5% dextrose, drug-free CE vehicle, and empty PEO-*b*-PBCL NPs (n = 5). Two test groups received A83B4C63 in CE formulation diluted with dextrose or A83B4C63 in PEO-*b*-PBCL NPs (NP/A83B4C63). The injection schedule for both control and test groups was set at three times one day apart at a dose of 25 mg/kg of A83B4C63. Excipient dose in control groups was selected equivalent to their amounts in the test groups. The length (L) and width (W) of the tumor were measured 2 - 3 times per week and the tumor volume (TV) was calculated using the formula $TV = (L \times W^2)/2$. The measurements continued until the early end points for animal euthanasia, as defined in our animal protocol, were reached. Tumor growth and time to reach early end points for animals in test and control groups were then followed up as described above.

In the second experiment, subcutaneous Luc^{+}/HCT116/PTEN$^{-/-}$ tumor-bearing mice were developed as described above and used to investigate the anticancer activity of A83B4C63 as CE or NP formulations using a different dosing schedule (n = 8). Three groups of animals were intravenously injected 6 times with either 5% dextrose, free A83B4C63 (solubilized with the aid of CE) and NP/A83B4C63 one day apart at a dose of 25 mg/kg. Mice were given one week of rest after the first three IV injections. Mice were monitored daily for tumor growth and signs of sickness according to our approved animal protocol [284]. Tumor growth was followed by digital caliper measurement as described above as well as IVIS imaging. For the optical imaging, mice were subcutaneously injected with the XenoLight D-Luciferin - K+ salt bioluminescent substrate (PerkinElmer, UK) at a dose of 10 µL/g of body weight before the luciferase detection. Mice were

anesthetized and placed in the dark chamber of a Xenogen IVIS machine for whole-body animal imaging and the emitted photons were quantified and analyzed using Living Image Software (Xenogen). Imaging of live animals was performed twice a week.

2.2.12. Assessment of plasma and tissue accumulation of A83B4C63 in CE and NP forms in HCT116 tumor-bearing mice

For assessing the distribution profile of A83B4C63 in CE and NP forms HCT116/PTEN$^{-/-}$ tumor-bearing NIH-III mice were developed as described above. When the tumor volume reached 1200 to 1500 mm^3, mice were randomly assigned and grouped into 3 test groups (3 mice per group). The test groups received A83B4C63 as free drug (CE formulation) or its NP form three times, one day apart at an IV dose of 25 mg/kg. The control mice received 5% dextrose. 24 and 48 h after the last injection, all mice were euthanized, and blood and major tissues were collected to define drug levels using an LC-MS method of quantification. All snap-frozen dissected tissues were weighed and homogenized with an ice-cooled solution of acetonitrile/water (50:50 v/v) using an electric hand homogenizer. The collected whole blood samples of the mice were centrifuged at 2000 × g for 5 min at 4ºC to separate the plasma. Tissue homogenate samples were centrifuged at 2000 × g for 15 min at 4ºC. Then 100 µL of tissue homogenate or plasma was transferred into an LC-MS glass vial and completely dried out by speed vacuum using liquid nitrogen. Propranolol dissolved in the solution of acetonitrile/water with 50:50 v/v ratios was used as an internal standard. The dried residues in sample vials were reconstituted with 100 µL of internal standard solution with vigorous vortexing before placing into the auto-sampler of the LC-MS (Waters Quattro Micro ± ES MS Triple Quadrupole, Milford, MA, USA) fitted with an Agilent Technology: Poroshell 120 SB-C18 2.1x50 mm, 2.7 micron column. The mobile phase consisted of 50:50 v/v ratios of water with 0.1% formic acid and acetonitrile with 0.1% formic acid.

2.2.13. Immunostaining and microscopy

Following the method described above, both HCT116/PTEN$^{-/-}$ and HCT116/PTEN$^{+/+}$ subcutaneous xenografts mice were developed. The test groups of mice received A83B4C63 either in CE or NP formulation, three times one day apart at a dose of 25 mg/kg and the two control groups received IV injection of dextrose 5% and A83B4C63-free empty NP formulation (n = 3). Twenty four hours after the last injection; all mice were euthanized to collect the tumors. To evaluate the *in vivo* anti-proliferative activity of A83B4C63 in CRC tumor-bearing mice, biomarker Ki-67 antigen staining was conducted following a previously described method [285]. In brief, solid tumors were excised, fixed in formalin buffer (pH 7.4), and paraffin embedded. The deparaffinized tissue sections (5 micron) of each tumor on glass slides were rehydrated, incubated with 0.3% hydrogen peroxide, and processed for antigen retrieval using a heat-induced procedure. After blocking, the samples were processed for Ki-67 antibody staining. A Vectastain ABC horseradish peroxidase kit and DAB substrate (Vector Laboratories, Burlingame, CA) were used for the development and detection. The sections were counterstained with hematoxylin, dehydrated, and mounted to be visualized using an Olympus BX41 microscope (Olympus, Japan). The sections were washed with PBS between each of the incubations.

2.2.14. Statistical analysis

GraphPad Prism6 software (La Jolla, CA, USA) was used for statistical analysis. Significance of differences between groups were assessed using one-way and two-way ANOVA followed by Tukey's post-hoc test, where appropriate. If a significant difference was found among the groups, median ranks between pairs of groups were compared using the Mann-Whitney U test. A value of $p \leq 0.05$ was considered as statistically significant in all experiments.

2.3. Results

2.3.1. Physicochemical characterization and *in vitro* release profile of NP/A83B4C63

A simple one-step self-assembly method was employed to encapsulate A83B4C63 (**Fig. 2.1A**) in NPs made from PEO-*b*-PBCL copolymers (**Fig. 2.1B**). The NPs were prepared at a 1:3 w/w A83B4C63/PEO-*b*-PBCL ratio that yielded 22.57 ± 0.40% loading and 69.12 ± 11.23% encapsulation efficiency of A83B4C63 into PEO-*b*-PBCL NPs (**Fig. 2.1C** and **2.1D**). The NP/A83B4C63 were ~50 nm in diameter on average and showed a low polydispersity index (PDI), i.e., ~0.25.

Fig. 2.1E shows the comparative *in vitro* release profiles of A83B4C63 from the NP/A83B4C63 compared to free A83B4C63. Within 6 h, 98.72 ± 1.09% free A83B4C63 was released from the dialysis bag pointing to the suitability of experimental condition [71]. In contrast, only 29.34 ± 1.57% A83B4C63 was released over 6 h from NP/A83B4C63 micelles. After 72 h, the release of A83B4C63 from NP/A83B4C63 reached ~70%, indicating control by the micellar carrier over the release of encapsulated A83B4C63 against media containing physiological concentration of BSA.

2.3.2. Binding of A83B4C63 to purified and intracellular PNKP

A K_D value for the binding of A83B4C63 of 80 ± 5 nM was obtained by monitoring the quenching of intrinsic (tryptophan) fluorescence as a function of inhibitor concentration (**Supplementary Fig. 2.1A**). The log D and solubility of A83B4C63 were determined to be > 4.16 and < 1 μM, respectively. The IC_{50} for the inhibition of the phosphatase activity, determined using an assay to measure the release of inorganic phosphate from an oligonucleotide (**Supplementary Fig. 2.1B**), was found to be 2.04 μM (equivalent to 1.15 μg/mL). In comparison, the IC_{50} for inhibition by PEO-*b*-PBCL was determined to be 79.9 μg/mL (**Supplementary Fig. 2.1B**).

A CETSA protocol was developed and used to assess the direct intracellular binding capability of A83B4C63 to PNKP in live HCT116/PTEN$^{-/-}$ and HCT116/PTEN$^{+/+}$ CRC cells. The applied *in vivo* results from CETSA are illustrated in **Fig. 2.2**. The PNKP-A83B4C63 binding was considered positive if there was a significantly higher PNKP protein level in A83B4C63-treated cells than DMSO-treated cells at temperatures above the threshold for PNKP denaturation making its band less detectable in immunoblots. A significant stabilization of PNKP at 46 - 48ºC validated the intracellular binding of A83B4C63 at a concentration of 10 µM in both CRC cell types compared to media (0.1% DMSO)-treated cells (**Supplementary Fig. 2.2A** and **2.2B**).

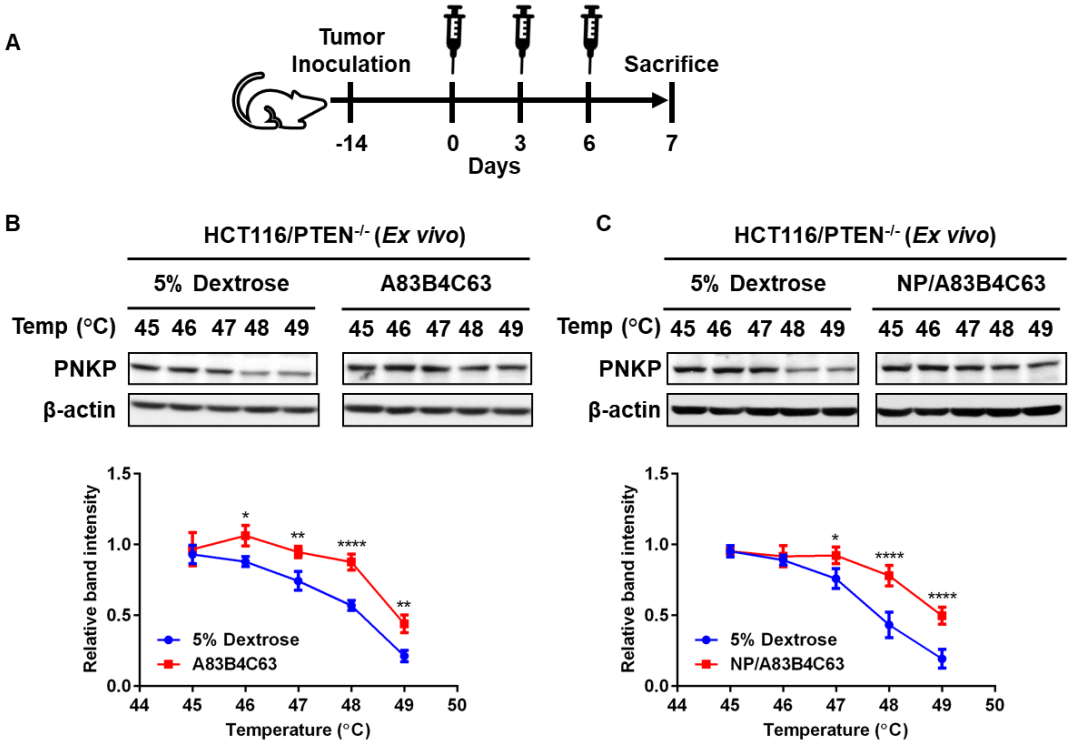

Figure 2.2: (A) A representative experimental design for *in vivo* CETSA to measure the intracellular PNKP binding ability of A83B4C63 injected as free drug (solubilized with CE) or its NP form intratumorally injected to HCT116/PTEN$^{-/-}$ subcutaneous xenograft tumors in NIH-III female nude mice. Subcutaneous HCT116/PTEN$^{-/-}$ tumors in NIH-III nude mice received three IT injections of A83B4C63 in the free drug (solubilized with CE) and PEO-*b*-PBCL NP form at a dose of 1 mg/kg two days apart. The control mice received 5% dextrose IT. 24 h after the last injections, the tumors were excised, and isolated cells from the tumors were used for CETSA sample preparation. Representative in vivo intracellular binding affinity of (B) A83B4C63 and (C) NP/A83B4C63 in HCT116/PTEN$^{-/-}$ CRC xenograft tumors. PNKP protein levels were quantified by densitometric analysis using ImageJ software. Data are presented as mean ± SD (n = 3). Compared to the control cells, differences were considered significant if $*p \leq 0.05$, $**p \leq 0.01$, $***p \leq 0.001$, and $****p \leq 0.0001$; Student's t test.

There have been very few CETSA results reported to measure the intracellular drug-target protein binding *in vivo.* We developed and optimized the CETSA method to evaluate the *in vivo* PNKP-A83B4C63 binding. The results for A83B4C63 binding following IT injection of CE or NP formulations of the drug in HCT116/PTEN$^{-/-}$ CRC xenografts in female NIH-III nude mice is shown **Fig. 2.2B** and **2.2C**. A significant increase in PNKP stabilization is observed at 46 - 49ºC and 47 - 49ºC in A83B4C63- and NP/A83B4C63-treated xenografts, respectively. The overall *in vivo* CETSA results demonstrates that nano-encapsulation using PEO-*b*-PBCL polymeric formulation well-preserved the binding potency of A83B4C63.

2.3.3. *In vitro* toxicity of A83B4C63 and NP/A83B4C63 in CRC cells

The results of the MTS assay on HCT116/PTEN$^{-/-}$ and HCT116/PTEN$^{+/+}$ cells following treatment with 5 and 10 μM A83B4C63 and NP/A83B4C63 for 72 h is shown in **Fig. 2.3A**. A dose response was observed following 72 h treatment only in HCT116/PTEN$^{-/-}$ cells treated with free or NP forms of A83B4C63. After 72 h incubation, nearly 25 - 30% cell viability was observed in A83B4C63-treated HCT116/PTEN$^{-/-}$ cells. This level reached 40 - 45% for NP/A83B4C63-treated HCT116/PTEN$^{-/-}$ cells.

Because the MTS assay is primarily an assay of metabolic activity, to confirm the cytotoxicity of the PNKP inhibitor after a 72 h incubation, live images of the identically treated cells with the PTEN$^{-/-}$ and PTEN$^{+/+}$ phenotypes were taken and evaluated (**Fig. 2.3B**). Changes in

cellular morphology were observed in A83B4C63-treated HCT116/PTEN$^{-/-}$ cells compared to control cells. Moreover, non-viable floating cells (round dark blackish in color) were noticeable in both A83B4C63- and NP/A83B4C63-treated HCT116/PTEN$^{-/-}$ cells. Although very few floating dead cells were imaged in A83B4C63-treated HCT116/PTEN$^{+/+}$ cells, no distinct number of dead cells were detectable in NP/A83B4C63 treatment even after 72 h incubation. The microscopic observations (**Fig. 2.3B**) are in accordance with the *in vitro* cytotoxicity data assessed by the MTS assay (**Fig. 2.3A**). These results validate the synthetic lethality as a result of PNKP inhibition in PTEN-deficient CRC cells [267].

To evaluate the role of caspases in A83B4C63-mediated cell death, caspase activity was assessed using the Caspase-Glo 3/7 assay after treating both HCT116/PTEN$^{-/-}$ and HCT116/PTEN$^{+/+}$ cells following similar treatment conditions as the cytotoxicity assay (**Fig. 2.3C**). Both A83B4C63 and NP/A83B4C63 exhibited significantly higher levels of caspase-3/7 activity in the PTEN-deficient cells than the wild-type counterpart. This level was higher for A83B4C63 compared to NP/A83B4C63 after 24 and 48 h treatments. However, the caspase-3/7 activity for A83B4C63 treatments was significantly reduced after 72 h, while in NP/A83B4C63-treated PTEN-deficient cells, the activity was found to persist. Relatively lower caspase-3/7 activity was observed for A83B4C63 treatments in HCT116/PTEN$^{+/+}$ cells at 24 and 48 h incubation times and not at the 72 h incubation time point compared to that for HCT116/PTEN$^{-/-}$ cells. The caspase-3/7 activity was negligible for NP/A83B4C63 treatment in wild-type CRC cells within the 24-72 h incubation time points.

Western blot analysis was then performed to assess the level of respective caspase and other apoptosis related proteins in the treated whole cell-lysates. As shown in **Fig. 2.3D** and **Supplementary Fig. 2.3G**, total caspase-3, cleaved caspase-3, total caspase-7, cleaved caspase-7,

PARP, and cleaved PARP were detected and compared with the positive control of etoposide. There were no detectable cleaved caspase-3 and PARP proteins (even after longer film exposure) following A83B4C63 treatment regardless of the CRC cell type. However, an increase in cleaved caspase-7 was detected in HCT116/PTEN$^{-/-}$ cells when treated with A83B4C63 and NP/A83B4C63. Taken together, these results indicate that A83B4C63 triggers the enzymatic caspase-7 activation pathway, possibly promoting cellular apoptosis in PTEN-deficient CRC cells resulting in synthetic lethality.

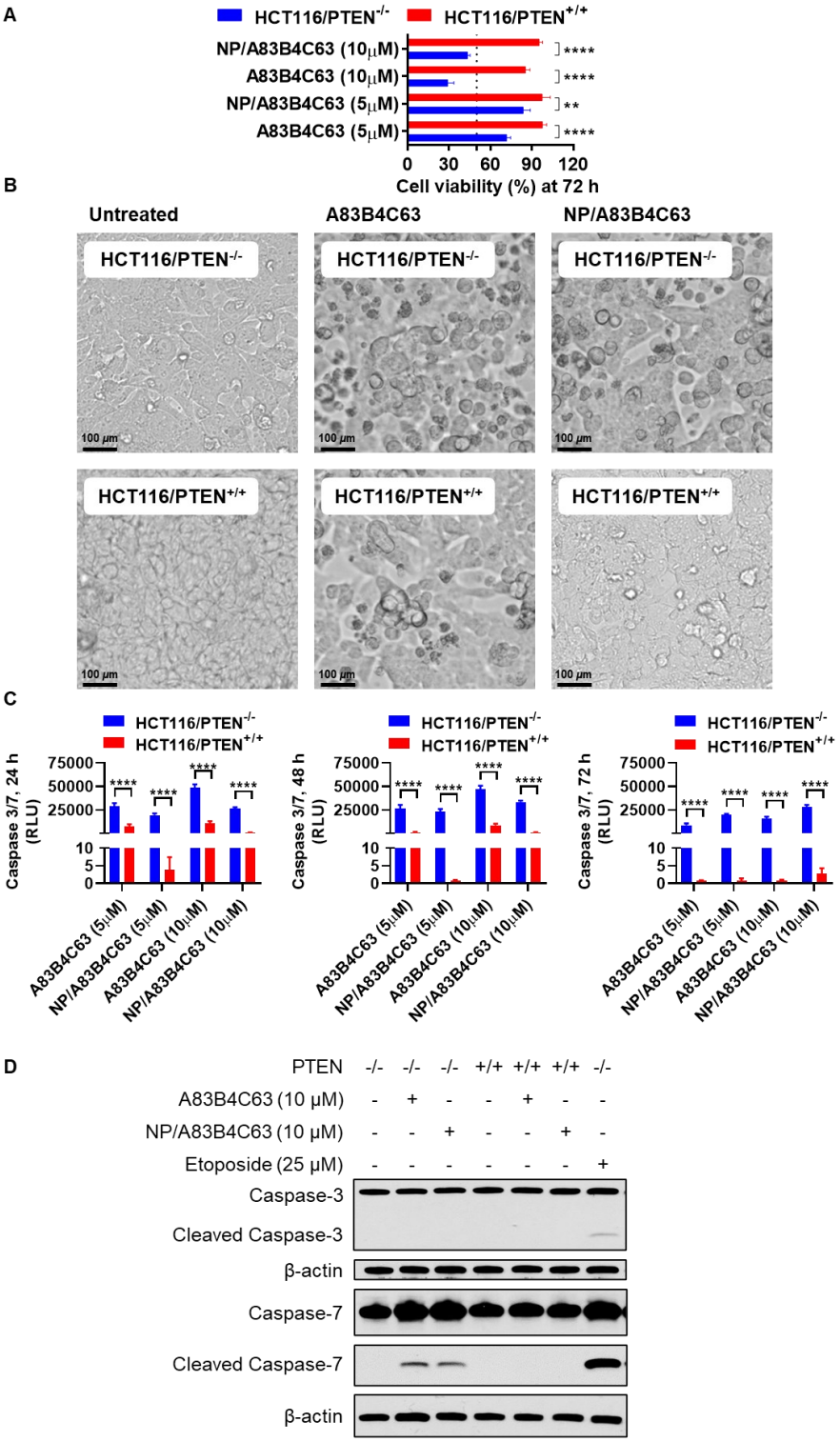
A
HCT116/PTEN-/-
HCT116/PTEN+/+
NP/A83B4C63 (10μM)
A83B4C63 (10μM)
NP/A83B4C63 (5μM)
A83B4C63 (5μM)
****
****
**
****
0 30 60 90 120
Cell viability (%) at 72 h
B
Untreated
A83B4C63
NP/A83B4C63
HCT116/PTEN-/-
HCT116/PTEN+/+
100 μm
C
Caspase 3/7, 24 h (RLU)
Caspase 3/7, 48 h (RLU)
Caspase 3/7, 72 h (RLU)
75000
50000
25000
10
5
0
A83B4C63 (5μM)
NP/A83B4C63 (5μM)
A83B4C63 (10μM)
NP/A83B4C63 (10μM)
D
PTEN -/- -/- -/- +/+ +/+ +/+ -/-
A83B4C63 (10 μM) - + - - + - -
NP/A83B4C63 (10 μM) - - + - - + -
Etoposide (25 μM) - - - - - - +
Caspase-3
Cleaved Caspase-3
β-actin
Caspase-7
Cleaved Caspase-7
β-actin

Figure 2.3: (A) *In vitro* cytotoxicity of A83B4C63 and NP/A83B4C63 in HCT116/PTEN$^{+/+}$ and HCT116/PTEN$^{-/-}$ cells after 72 h incubation at 37ºC as determined by MTS assay. The cells were treated with free drug and its NP form with a range of concentration from 0.5 μM to 10 μM. A83B4C63 was solubilized with 0.1% DMSO and the control cells received only 0.1% DMSO. Each point represents mean ± SD (n = 4). Compared to the control cells, significant differences were considered if *$p \leq 0.05$, **$p \leq 0.01$, ***$p \leq 0.001$, and ****$p \leq 0.0001$. (B) Microscopic observation of HCT116/PTEN$^{+/+}$ and HCT116/PTEN$^{-/-}$ cells after 72 h treatment with free A83B4C63 and NP/A83B4C63. Cells treated with 0.1% DMSO are shown as untreated control. (C) Measurement of time-dependent caspase-3/7 activity by Caspase-Glo 3/7 assay kit in HCT116/PTEN$^{+/+}$ and HCT116/PTEN$^{-/-}$ cells after 24, 48, and 72 h incubation. Data are expressed as mean ± SD (n = 4). Compared to the control cells, differences were considered significant if *$p \leq 0.05$, **$p \leq 0.01$, ***$p \leq 0.001$, and ****$p \leq 0.0001$ following two-way ANOVA followed by Tukey's test. (D) Western blot detection of caspase-3, cleaved caspase-3, caspase-7, and cleaved caspase-7 in both cell lines after 48 h exposure to A83B4C63 and NP/A83B4C63 at 37ºC in 5% CO_2 (n = 3). 25 μM Etoposide-treated cells (24 h incubation) were used as positive control. β-actin was used as a loading control. The conditions for all sample preparations and western blots were the same.

2.3.4. *In vivo* safety and maximum tolerated dose (MTD) determination of A83B4C63 formulations

Healthy CD-1 female mice were used to determine the preclinical MTD and safety profile of A83B4C63 formulations with an escalating IV dose ranging from 2.5 to 50 mg/kg. Any abnormal loss in total body weight of the mice (> 15%) and distress symptoms such as reduced motor activity, failure to eat or walk or groom normally, piloerection, discharge, and allodynia were considered as signs of toxicity of the systemic treatments triggering animal euthanasia based on our approved animal protocols. The weight variation of the mice for each treatment group was below 10% of the mean weight before the mice were randomly assigned and grouped. After three IV injections of either formulation of A83B5C63, the mean body weight of the mice for each treatment group was not statistically different from control mice treated with 5% dextrose vehicle (**Fig. 2.4B** and **Supplementary Fig. 2.4A**). The results of this study demonstrate both A83B4C63 and NP/A83B4C63 to be safe systemic monotherapeutic candidates with an MTD ≥ 50 mg/kg.

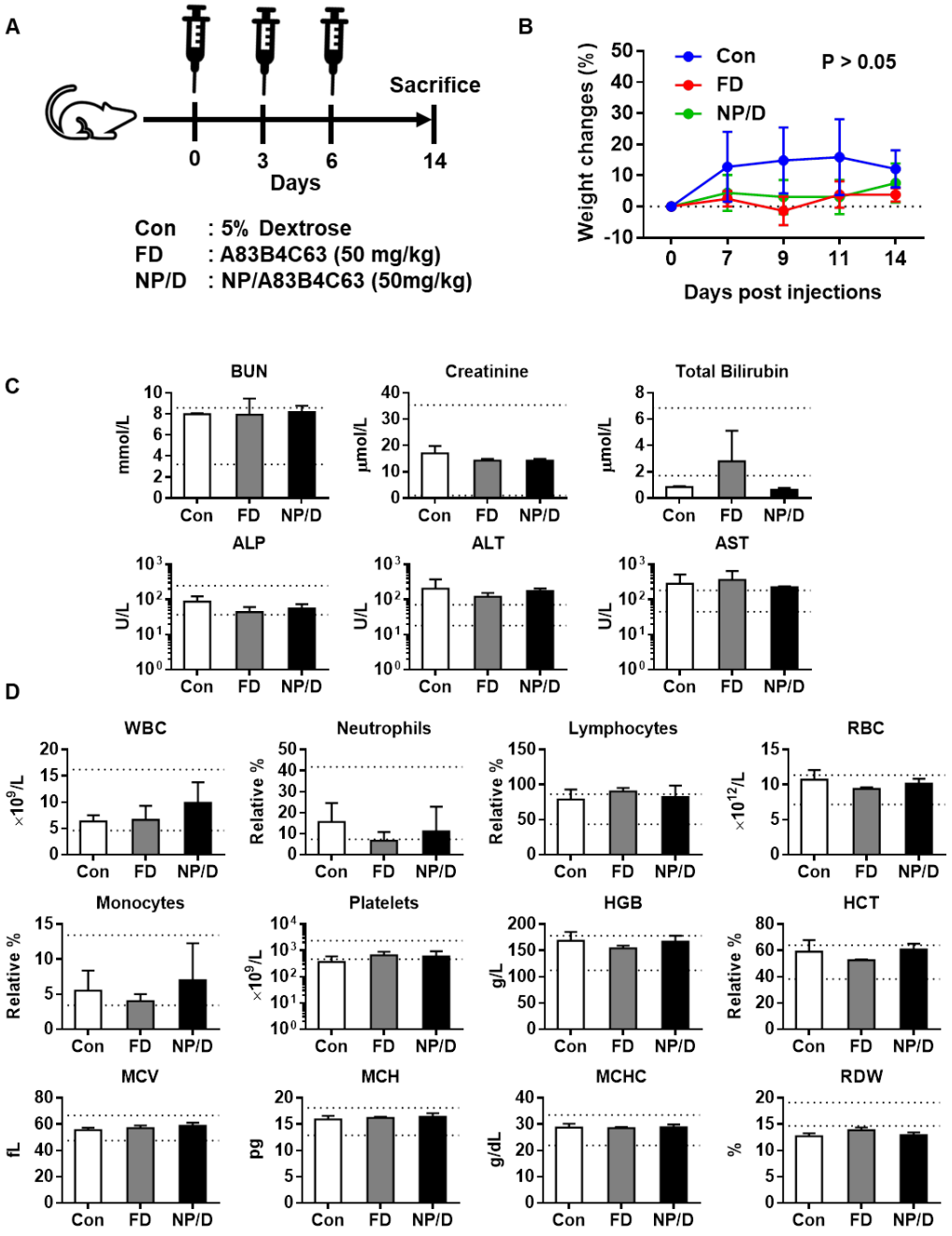

Figure 2.4: (A) Representative experimental design for MTD determination of A83B4C63 and NP/A83B4C63 in healthy CD-1 female mice (n = 4). Randomly assigned and grouped mice were intravenously injected three times with a two day interval between injections with different doses ranging from 2.5-50 mg/kg of A83B4C63 in either CE or NP formulation. The control mice received 5% dextrose. (B) Percent weight changes of mice for each treatment group up to two weeks following the first injections. (C) Biochemical changes in blood (BUN – blood urea nitrogen, ALP – alkaline phosphatase, ALT – alanine aminotransferase, AST – aspartate aminotransferase). (D) Hematological changes in mouse blood. The normal range of each biomarker of drug toxicity is shown by dotted lines. Each point represents mean ± SD (n = 4) and significant if $*p \leq 0.05$. Con = 5% dextrose, FD = A83B4C63 solubilized with CE, and NP/D = NP/A83B4C63.

To further evaluate the *in vivo* side-effects or toxicity of systemic A83B4C63 and NP/A83B4C63 compared to mice receiving 5% dextrose, biochemical tests of collected blood samples, 24 h after the third injection, were performed including BUN, CREA, BIL, ALK, ALT, and AST parameters. As shown in **Fig. 2.4C** and **Supplementary Fig. 2.4B**, all the assessed biochemical factors were within the normal range for all treatment groups. In addition to biochemical tests, the hematological analysis of the same blood samples was also conducted and the levels of RBC, HGB, HCT, MCV, MCH, MCHC, RET, WBC or leukocyte count, differential count (neutrophils, lymphocytes, monocytes, eosinophils, basophils), PLT and CBC were measured before the mice were euthanized. We found no noticeable changes in these parameters from the healthy CD-1 mice treated with 5% dextrose, A83B4C63, and NP/A83B4C63 (**Fig. 2.4D** and **Supplementary Fig. 2.4C**).

The histopathological evaluation of various organs of the treated CD-1 female mice including brain, heart, lung, liver, kidney, and spleen was also performed to identify the potential tissue toxicity of A83B4C63 and NP/A83B4C63 at the highest dose of 50 mg/kg. We observed no histopathological differences in the tissue sections from various organs between the treatment groups and control, further confirming the safe and non-toxic systemic administration of both A83B4C63 and NP/A83B4C63 formulations at the maximum tested dose of 50 mg/kg (**Fig. 2.5**).

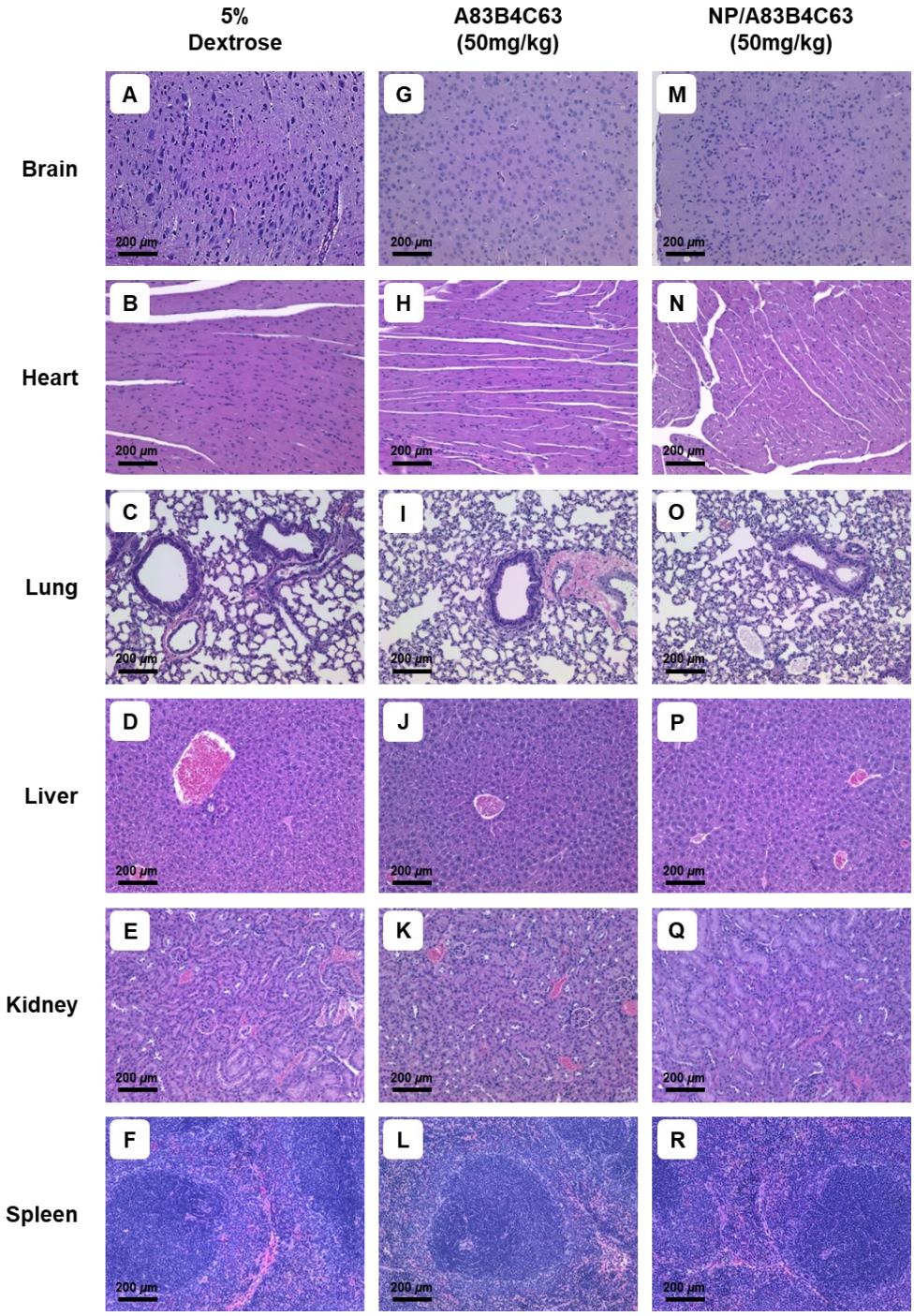

Figure 2.5: Histopathological evaluation of CD-1 murine organs including brain (A, G, M), heart (B, H, N), lung (C, I, O), liver (D, J, P), kidney (E, K, Q), and spleen (F, L, R) following intravenous injection of A83B4C63 in CE formulation or NP/A83B4C63. Randomly assigned and grouped mice were injected IV with 5% dextrose (Column-1), 50 mg/kg A83B4C63 in CE formulation (Column-2), or 50 mg/kg NP/A83B4C63 (Column-3) three times with a two day interval between injections. After two weeks, all mice were euthanized and collected organs were fixed, embedded in paraffin, sectioned, and stained with Hematoxylin and Eosin (H&E). All images were taken with an objective magnification of 20X.

2.3.5. *In vivo* therapeutic activity of A83B4C63 (CE) and NP/A83B4C63 intratumorally in HCT116 CRC xenograft models

To assess the *in vivo* therapeutic activity of A83B4C63 in HCT116 CRC xenograft models, in the first experiment, IT injection of the drug was carried out based on a design shown in **Supplementary Fig. 2.5A**. As shown in **Supplementary Fig. 2.5C**, at an IT dose of 1 mg/kg (calculated based on the obtained *in vitro* IC_{50} value in the cytotoxicity assay, approximate volume of the tumor and weight of the mouse), both free and encapsulated A83B4C63 treated mice exhibited relatively longer survival (time to reach humane end points) and growth retardation of HCT116/PTEN$^{-/-}$ tumors compared to tumor-bearing control mice that received dextrose 5%. While mice receiving 5% dextrose showed survival between 25 - 39 days, animals-treated with A83B4C63 IT in CE or NP form survived between 30 - 60 and 29 - 50 days, respectively (**Supplementary Fig. 2.5D**). However, no significant difference was observed for average tumor volume growth curves among the treatment groups and the tumor growth of individual mice for each treatment group is shown in **Supplementary Fig. 2.5B.** Moreover, the mean body weights of the mice receiving IT treatments were within 20% weight variation and not statistically different (**Supplementary Fig. 2.5E**). The IT administration of A83B4C63 was performed here to provide relatively similar concentrations of the CE versus NP formulation of the drug directly in the tumor. Under these conditions, an equal trend was observed which did not reach statistically significant inhibition of tumor growth for both CE and NP formulation of the A83B4C63 in PTEN deficient HCT116 xerographs. At the time of injection, the tumors were relatively large in this study and that could be the reason for low drug activity in the IT route of administration.

2.3.6. *In vivo* therapeutic activity for IV administration of A83B4C63 (CE) and NP/A83B4C63 in HCT116 CRC xenograft models

To explore the therapeutic activity of systemic A83B4C63 and NP/A83B4C63 a dose of 25 mg/kg three times a week was injected intravenously in both HCT116/PTEN$^{-/-}$ and HCT116/PTEN$^{+/+}$ xenograft models. All mice were inoculated with the respective cell types 14 days before the first injection. According to the study design (**Fig. 2.6A**), the tumor-bearing control mice received IV 5% dextrose. The mice receiving systemic CE and empty PEO-*b*-PBCL were also considered as controls for A83B4C63 and NP/A83B4C63 formulations, respectively. As shown in **Fig. 2.6B**, mice receiving 5% dextrose, CE, empty PEO-*b*-PBCL NPs, and A83B4C63 in CE formulation exhibited rapid tumor progress, while NP/A83B4C63-treated mice displayed significant growth retardation of HCT116/PTEN$^{-/-}$ tumors. The tumor growth of individual mice for each treatment group is shown in **Supplementary Fig. 2.6**. The survival data showed prolongation of life span for up to a maximum day-82 post treatment in mice treated with NP/A83B4C63, which was significantly ($p = 0.0204$) longer than all other control treatments of HCT116/PTEN$^{-/-}$ tumors (maximum time to humane end points of 32 - 57 and 32 - 52 and 39 - 53 days for dextrose 5%, CE control and empty NPs, respectively) and that of A83B4C63 in CE formulation (maximum life span of 39 - 60 days) (**Fig. 2.6D**). The wild-type HCT116/PTEN$^{+/+}$ xenograft, on the other hand, did not show any tumor growth retardation for any of the treatment or control groups (**Fig. 2.6C**). As such, all mice reached the early humane endpoint between 24 and 52 days following treatment (**Fig. 2.6E**). The overall results, implicated the *in vivo* synthetic lethal partnership between PTEN loss and PNKP inhibition as the PNKP inhibitor in its NP formulation was only effective in reducing the growth of PTEN$^{-/-}$ CRC xenografts. The measured mean body weight variation of the mice receiving systemic treatments were also within 20%

margin (**Fig. 2.6F** and **2.6G**) and did not show any statistical difference irrespective of the animal model.

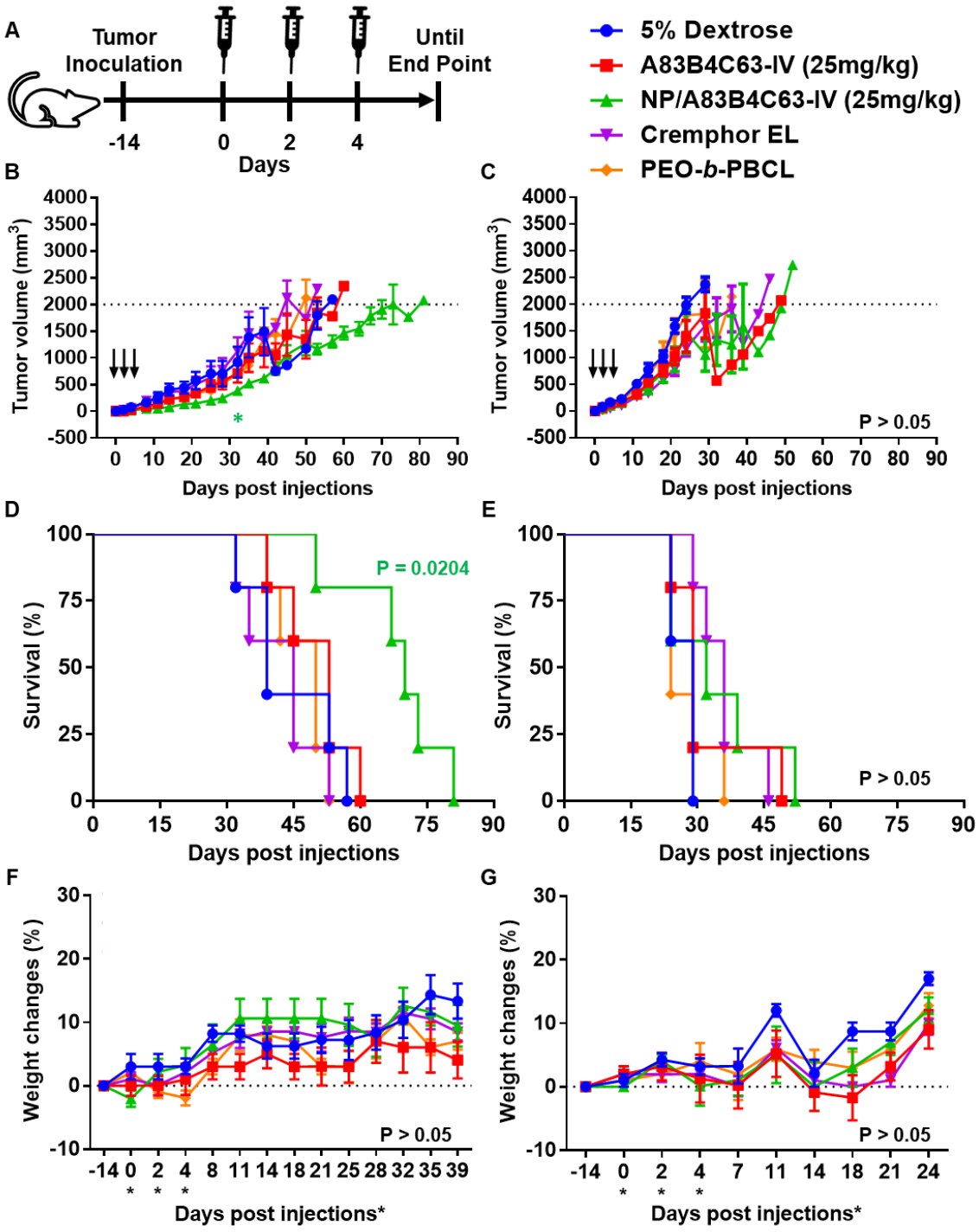

Figure 2.6: (A) Schematic study design for evaluating the anticancer activity of A83B4C63 and NP/A83B4C63 in NIH-III female nude mice following IV administration (n = 5). Colorectal HCT116/PTEN$^{-/-}$ and HCT116/PTEN$^{+/+}$ cells were inoculated and grown as SC tumor xenografts in the right flank of the mice. When tumors became palpable, for each xenograft type the mice were divided into 5 groups (25 mice in total), which were intravenously injected with (i) 5% dextrose, (ii) free CE, (iii) empty PEO-*b*-PBCL NPs, (iv) A83B4C63 formulated with the aid of CE, or (v) PEO-*b*-PBCL NP (NP/A83B4C63) formulation three times with a one day interval at a dose of 25 mg/kg. Average tumor volume growth curves for mice in each treatment group for both (B) HCT116/PTEN$^{-/-}$, and (C) HCT116/PTEN$^{+/+}$ xenografts. Using digital calipers, the length (L) and width (W) of the tumor mass were measured 2 - 3 times per week and the tumor volume (TV) was calculated according to the following formula, $TV = (L \times W^2)/2$. (D and E) Kaplan-Meier survival curves of mice bearing HCT116/PTEN$^{-/-}$ and HCT116/PTEN$^{+/+}$ xenografts, respectively. Both survival curves include overall median survival (MS) days for each of the treatment groups. (F and G) The average percentage for the body weights of mice bearing HCT116/PTEN$^{-/-}$ and HCT116/PTEN$^{+/+}$ xenografts, respectively. Each point represents the mean ± SD (n = 5). Differences were considered significant if $*p \leq 0.05$.

2.3.7. Biodistribution profile of A83B4C63 formulations

The results of biodistribution study as presented in **Fig. 2.7** show A83B4C63 as CE formulation was eliminated from plasma quickly. A83B4C63 concentration in CE formulation reached 400 ng/mL and below quantifiable levels within 24 and 48 h, respectively. In contrast, for NP formulation, A83B4C63 concentration stayed at around 700 and 600 ng/mL, at 24 and 48 h respectively. For CE formulation, A83B4C63 level in tumor was decreased from < 25 ng/g to undetectable limits, from 24 to 48 h. We observed a similar trend in all other normal tissues for this formulation. Drug levels at 24 h time point followed this order for CE formulation of A83B4C63: Plasma > liver > lung > kidney ≥ heart > tumor > spleen ≥ brain. In contrast, A83B4C63 in NPs showed an increase in its tumor levels from 24 to 48 h, but a decrease in concentration from 24 to 48 h in all normal tissues and plasma. As a result, at 48 h following the last injection of NP formulation, while drug concentration in tumor was at its highest level, its concentration in most tissues was below the quantifiable limit, except for plasma and liver. Drug levels at 24 h time point followed this order for NP formulations of A83B4C63: Plasma > liver > lung > kidney ≥ heart > tumor > spleen ≥ brain, which was like that obtained for the CE formulation of the drug. At 48 h, this order was changed to the following: plasma > tumor > liver > heart.

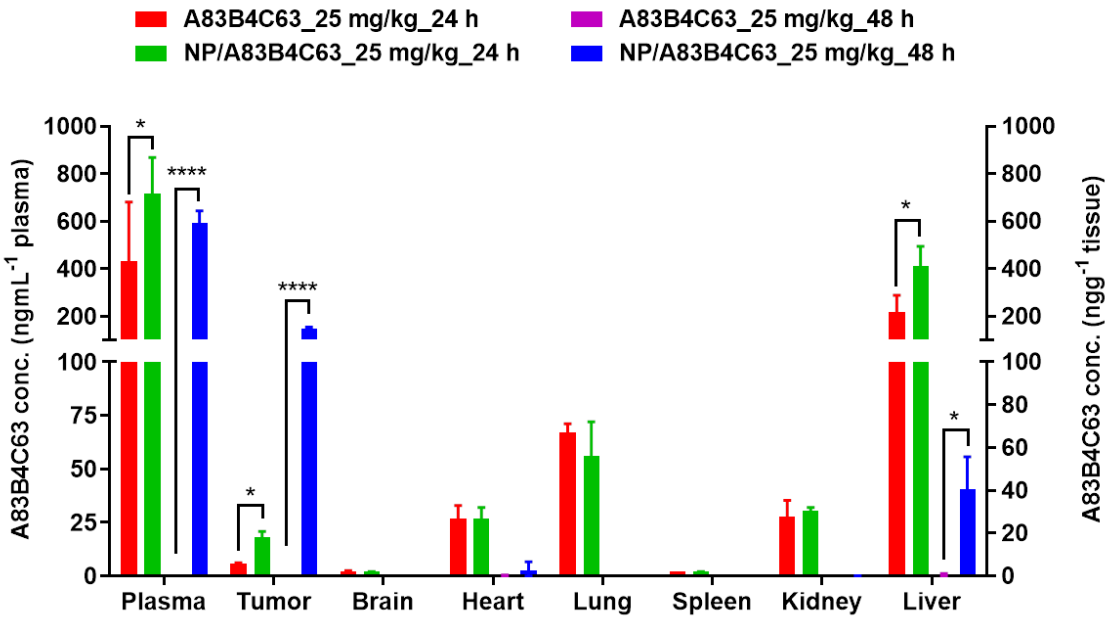

Figure 2.7: Assessing the biodistribution of A83B4C63 in HCT116/PTEN-/- xenograft bearing NIH-III female nude mice (n = 3) after 24 h and 48 h systemic exposure of A83B4C63 in free drug (CE) and NP forms via tail vein. Mice were inoculated with HCT116/PTEN-/- CRC cells. 21 days following tumor cell inoculation, the mice received free A83B4C63 in CE formulation and NP/A83B4C63 intravenously at a dose of 25 mg/kg three times with a one day interval. The control mice received 5% dextrose. 24 and 48 h after the last IV injection, all mice were euthanized to collect tumors. Drug concentration was quantified using LC-MS (mean ± SD). Differences were considered significant if *$p \leq 0.05$, **$p \leq 0.01$, ***$p \leq 0.001$, and ****$p \leq 0.0001$ following two-way ANOVA followed by Tukey's test.

2.3.8. *In vivo* live imaging to assess the therapeutic activity after IV administration of A83B4C63 (CE) and NP/A83B4C63 in Luc^{+}/HCT116/PTEN$^{-/-}$ CRC xenograft models following an extended dosing schedule.

To further evaluate the *in vivo* monotherapeutic activity of NP/A83B4C63, luciferase-positive Luc^{+}/HCT116/PTEN$^{-/-}$ cells were subcutaneously injected into the right flank of female athymic NIH-III nude mice. Tumor growth in mice was detected by bioluminescence live imaging following six injection dose schedules as shown in **Fig. 2.8A**. Based on the average radiance for bioluminescence of Luc^{+}/HCT116/PTEN$^{-/-}$ cells in mice (**Fig. 2.8B**), NP/A83B4C63 treatment was found to repress tumor growth significantly when compared to the 5% dextrose- and A83B4C63 (CE formulation)-treated groups (**Fig. 2.8E**). At day-22 (**Fig. 2.8F**), the quantitative

analysis exhibited a significant difference in average radiance in the NP/A83B4C63-treated group in comparison to the 5% dextrose-treated group (P = 0.0015), as well as the A83B4C63 in CE formulation-treated group (P = 0.0213). The tumor growth in the mice was also measured using digital slide calipers. The tumor volume of Luc^{+}/HCT116/$PTEN^{-/-}$ cells in the respective treatment groups of mice followed a similar trend in tumor growth to that observed by radiance detection (**Fig. 2.8C**). In addition, the quantitative analysis based on the tumor volume using calipers at day-22 post tumor implantation demonstrated a significant difference in the NP/A83B4C63-treated group compared to the 5% dextrose-treated group (P = 0.0063) and to the A83B4C63-treated group (P = 0.0465) (**Fig. 2.8D**). The average tumor volumes rapidly increased to 1178 ± 574 mm^3 and 990 ± 515 mm^3 in the mice treated with 5% dextrose and A83B4C63, respectively, whereas the tumor volumes remained as low as 386 ± 180 mm^3 in mice treated with IV NP/A83B4C63 at day-22 post tumor implantation. The tumor growth of individual mice for each treatment group is shown in **Supplementary Fig. 2.7**. In summary, these results validate the activity of systemic NP/A83B4C63 administration in the $PTEN^{-/-}$ CRC xenograft model. Moreover, the NP/A83B4C63 treatment, similar to the control groups, generated no significant change in total body weight of tumor-bearing mice (**Fig. 2.8H**), validating the safety profile of this systemic monotherapeutic system as similarly observed in CD-1 healthy mice.

Systemic NP/A83B4C63 administration also improved the survival of Luc^{+}/HCT116/$PTEN^{-/-}$ tumor-bearing mice significantly (P = 0.0078) compared to control mice receiving 5% dextrose or A83B4C63 in CE formulation. The survival rates were 37.5% in the 5% dextrose-treated group, 62.5% in the free A83B4C63-treated group, and 100% in NP/A83B4C63-treated group at day-26 post tumor inoculation. The tumor volumes reached the endpoints for the mice receiving 5% dextrose- and free A83B4C63-treated mice by day-36 post tumor inoculation.

However, in NP/A83B4C63-treated group, the survival curve was significantly extended for two mice up to day-75 post tumor inoculation. The results indicated that the monotherapeutic activity of this formulation prevented the rapid growth of PTEN-deficient CRC cells, *in vivo*.

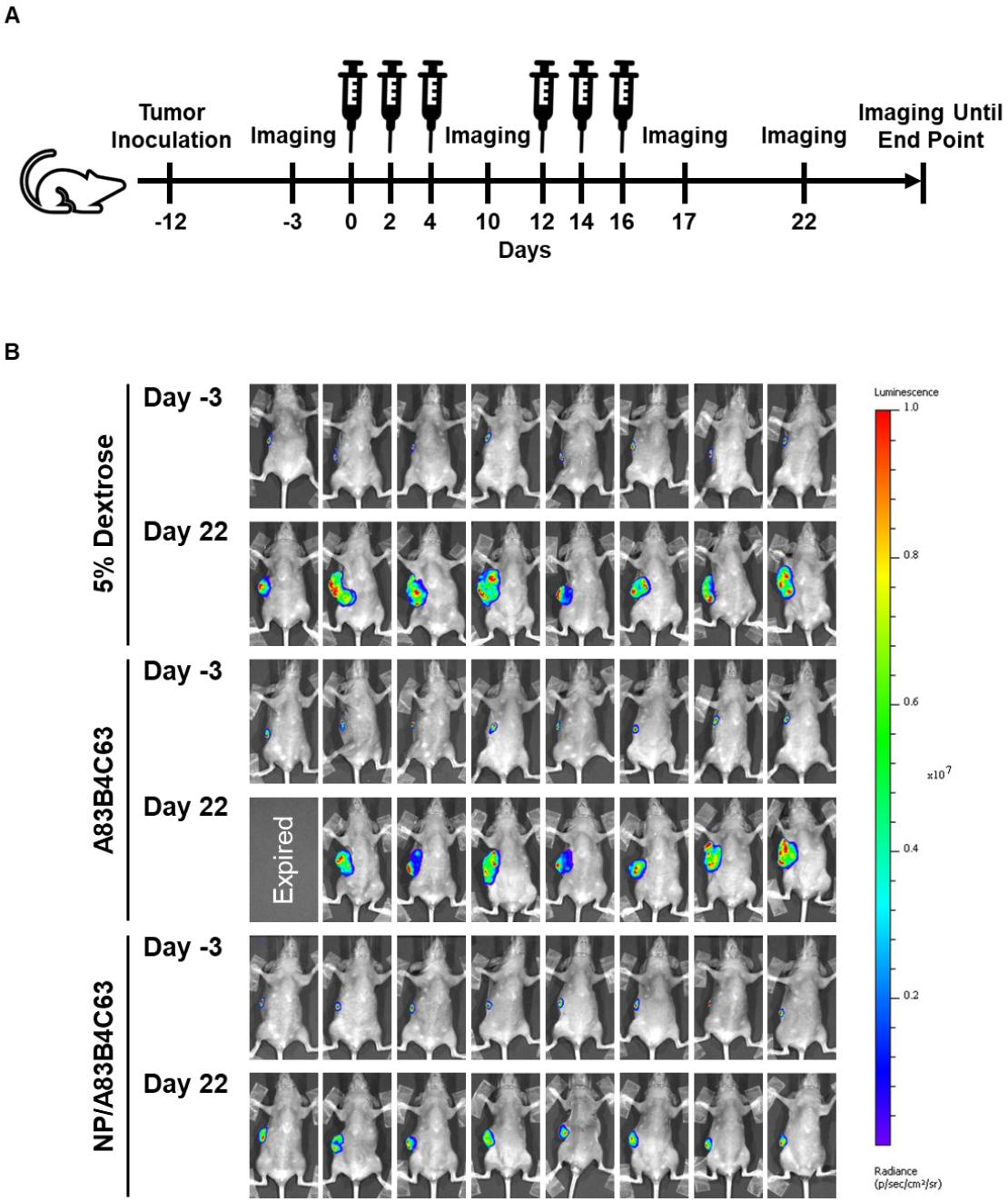

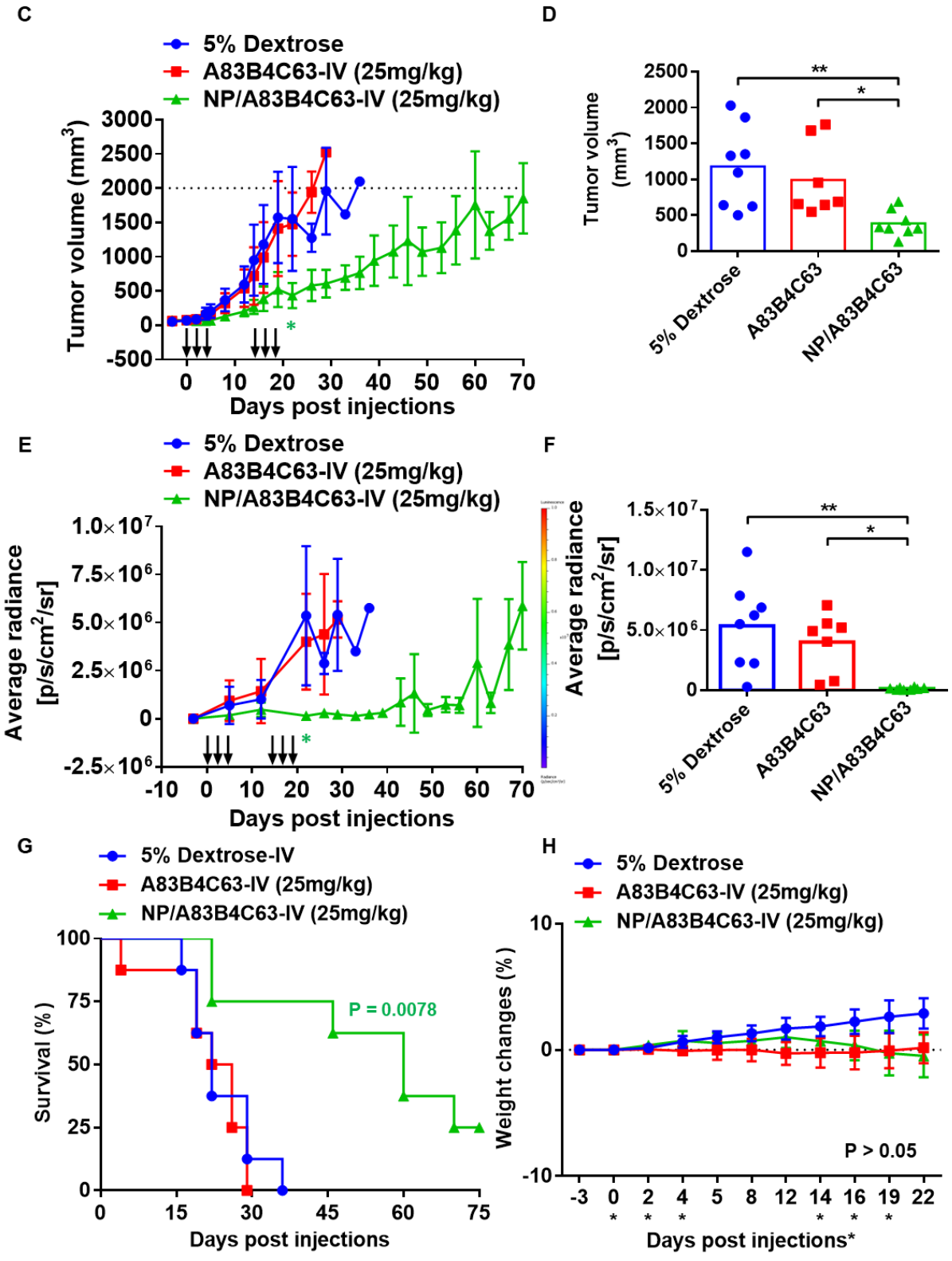
C
5% Dextrose
A83B4C63-IV (25mg/kg)
NP/A83B4C63-IV (25mg/kg)
Tumor volume (mm3)
Days post injections
D
Tumor volume (mm3)
5% Dextrose
A83B4C63
NP/A83B4C63
E
5% Dextrose
A83B4C63-IV (25mg/kg)
NP/A83B4C63-IV (25mg/kg)
Average radiance [p/s/cm2/sr]
Days post injections
F
Average radiance [p/s/cm2/sr]
5% Dextrose
A83B4C63
NP/A83B4C63
G
5% Dextrose-IV
A83B4C63-IV (25mg/kg)
NP/A83B4C63-IV (25mg/kg)
Survival (%)
P = 0.0078
Days post injections
H
5% Dextrose
A83B4C63-IV (25mg/kg)
NP/A83B4C63-IV (25mg/kg)
Weight changes (%)
P > 0.05
Days post injections*

Figure 2.8: (A) The experimental scheme for *in vivo* therapeutic evaluation of A83B4C63 as CE and NP formulation in $PTEN^{-/-}$ CRC tumor-bearing mice (n = 8). The female athymic NIH-III nude mice were implanted with 0.5×10^6 Luc^+/HCT116/$PTEN^{-/-}$ cells on their right flank. The mice were imaged for luciferase intensity 3 days before the treatment started. To evaluate the anti-tumor activity of A83B4C63 and NP/A83B4C63, the mice were intravenously injected with either (i) 5% dextrose, (ii) A83B4C63 in CE formulation, or (iii) NP/A83B4C63 6 times with a dose of 25 mg/kg. (B) Representative bioluminescence images from the tumor-bearing mice on days-3 and -22. (C) Average tumor volumes for the treated mice. Using digital calipers, the length (L) and width (W) of the tumor mass were measured 2 - 3 times per week and the tumor volume (TV) was calculated according to the following formula, $TV = (L \times W^2)/2$. (D) Average tumor volumes of treated groups on day-22 post injection measured using digital slide calipers. (E) Quantitative analysis for the average bioluminescence signal for the three groups of mice. (F) Average radiance (photons per s per cm^2 per square) obtained from the treated groups on day-22 post injection. (G) Kaplan-Meier survival curves and overall median survival (MS) days of treated mice bearing Luc^+/HCT116/$PTEN^{-/-}$ xenografts. The represented survival curve was calculated based on the tumor volumes of the treated mice reached to terminal end point as of 2000 mm^3. (H) Analysis of individual animal body weights plotted as mean change (%) in body weight.

2.3.9. *In vivo* anti-proliferative activity of NP/A83B4C63

Immunostaining for Ki-67, a common exclusively nuclear protein associated with cell proliferation in tumors, is considered to be an important prognostic evaluation for anticancer therapy [286-288]. An enhanced Ki-67 expression is associated with accelerated intracellular mitotic function. We, therefore, have investigated Ki-67 expression levels in the xenograft tumors obtained from 5% dextrose-, A83B4C63-, NP/A83B4C63-, and A83B4C63-free empty NP-treated mice. In line with our tumor growth data, only tumors generated by HCT116/$PTEN^{-/-}$ cells showed decreased Ki-67-positive cells in NP/A83B4C63-treated mice (**Fig. 2.9**). In contrast, NP/A83B4C63 treatment did not show any anti-proliferative efficacy in wild-type xenograft tumors. The Ki67 tumor staining for mice treated with A83B4C63 in CE formulation was not different from that of the control groups, irrespective of the tumor phenotype.

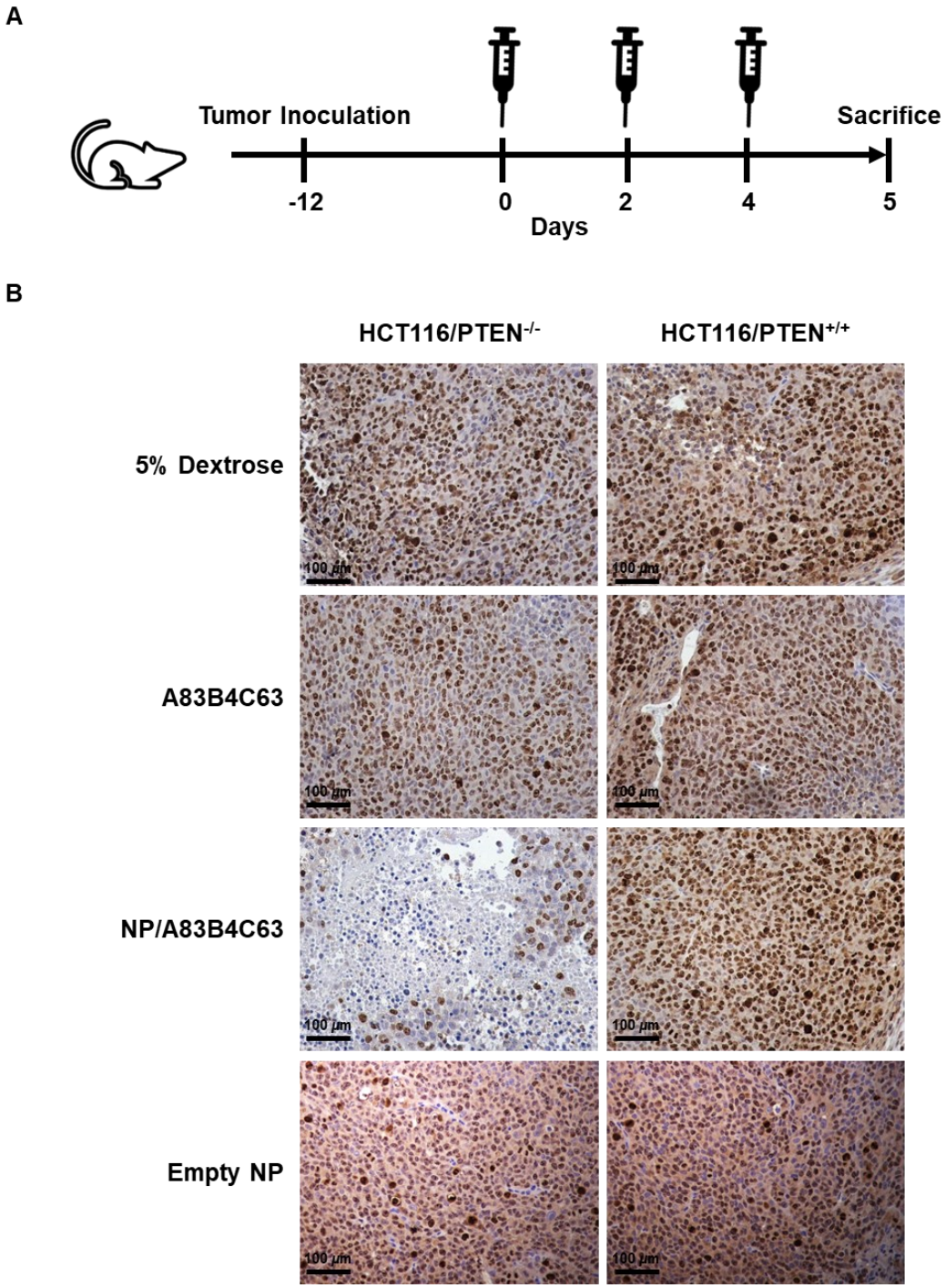

Figure 2.9: (A) Study design for assessing anti-proliferative activity of A83B4C63 formulations by immunohistochemistry in PTEN$^{-/-}$ and wild-type HCT116 xenografts. Twenty four hours after the last injection, all mice were euthanized to collect the tumors. (B) Representative images of Ki-67 expression in the excised tumors obtained with paraffin-stained 5 micron tissue sections from HCT116/PTEN$^{-/-}$ and HCT116/PTEN$^{+/+}$ xenografts of mice treated with three IV tail vein injections of 5% dextrose, free A83B4C63, NP/A83B4C63, and A83B4C63-free empty NP at dose of a 25 mg/kg with one day interval (n = 4). Images were taken using an Olympus BX41 microscope at 20X magnification.

2.4. Discussion

Mutation or loss of tumor suppressor genes plays a key role in tumor development and therapeutic resistance in cancer patients [289]. Although, the retrieval or restoration of the mutated or missing tumor suppressor genes has generated considerable research interest, to date, the successes in clinical translation of such approaches has been scarce [290, 291]. In an alternative therapeutic approach, the loss of tumor suppressor genes in cancer cells can be exploited to achieve targeted cancer therapeutics through synthetic lethality partnerships, where simultaneous loss of expression or function of two proteins leads to cancer cell death, while the expression or functionality of either one in normal cells leads to cell survival. In principle, synthetic lethality only targets the lethal partner of the mutant or depleted tumor suppressor gene or protein in the tumor cells, thereby leaving the normal cells unaffected. This has been substantiated by the clinical success for the synthetic lethal partnership between PARP1 and BRCA1/2 [140, 141].

Our research team has previously identified two tumor suppressor genes, i.e., SHP-1 and PTEN, as synthetic lethal partners of PNKP [200]. We have also shown the potential of small molecule inhibitors of PNKP to induce a synthetic lethal response in PTEN-depleted cancer cells when delivered as free or encapsulated compounds [201, 267]. The main objective of this study was to validate the anticancer activity and mechanism of action of a nano-encapsulated lead PNKP inhibitor, i.e., A83B4C63, in CRC xenograft models as synthetic lethal partner of PTEN loss. For this purpose, we have used very stable micellar NPs based on PEO-*b*-PBCL that have previously been shown to encapsulate A83B4C63 effectively and slow down its release rate, *in vitro* [267]; two main properties required for potential in passive tumor targeted drug delivery, *in vivo*. Two cancer targeting approaches are used in this strategy to ensure preferential action of the DNA repair inhibitor in cancer over normal cells, (a) development of NPs for targeted tumor delivery of PNKP

inhibitor and (b) targeting of PTEN deficiency in cancer for the induction of synthetic lethality by the encapsulated PNKP inhibitor. This strategy is expected to provide an optimal level of cancer selectivity for the PNKP inhibitors minimizing the drug's side-effects on normal cells. Preferential drug delivery to solid tumors by NPs can also potentiate the encapsulated drug by providing higher drug levels at the tumor site *in vivo* [259-262].

Free A83B4C63 is a poorly water-soluble compound. The results of our study have shown the encapsulation of A83B4C63 into PEO-*b*-PBCL NPs overcame this limitation, improving the solubilized drug levels to > 6 mg/mL, which made this compound suitable for systemic administration by IV injection to mice [292]. The slow *in vitro* release of A83B4C63, shown in our previous study, low critical micellar concentration (CMC) of PEO-*b*-PBCL (0.20 μM), and its high kinetic stability imposed by π- π stacking of the benzyl carboxylate group in the NP core, were all expected to lead to preferential accumulation of encapsulated A83B4C63 by the NPs to solid tumors as a result of the EPR effect [293, 294]. The progressive time dependent accumulation of PEO-*b*-PBCL micelles in subcutaneous wild-type HCT116 subcutaneous tumor models in mice has recently been shown by our research group using positron emission tomography (PET) [295]. Similar observations have been made by our group in orthotopic breast tumor models, using near infrared imaging [278]. This has, in fact, been shown in our studies where NP formulations of A83B4C63 showed higher plasma and tumor drug levels 48 h following administration of three IV doses in mice compared to its formulation using conventional solubilizing agents (**Fig. 2.7**). This may indicate higher biological stability of NP-encapsulated A83B4C63, compared to its CE formulation.

The encapsulated A83B4C63 was shown to be active as a monotherapeutic in PTEN-deficient HCT116 cells. *In vitro*, it caused 40 - 45% loss of cell viability at 10 μM concentration

in PTEN$^{-/-}$ CRC cells (**Fig. 2.3A**) [267]. In contrast, PTEN$^{+/+}$ cells were shown to be ≥ 90% viable when treated with A83B4C63 irrespective of its formulation. Cytotoxic behavior of A83B4C63 was only observed in PTEN$^{-/-}$ cells **(Fig. 2.3),** despite similar binding of this lead inhibitor to the intracellular PNKP in both PTEN$^{+/+}$ and PTEN$^{-/-}$ CRC cell lines, *in vitro* (**Supplementary Fig. 2.2A** and **2.2B**). In line with the above observation, higher levels of caspase 3/7 expression were observed in PTEN$^{-/-}$ cell treated with free A83B4C63 as well its NP formulation at 5 and 10 μM drug concentration (**Fig. 2.3**). Unlike MTS assay results, in PTEN$^{-/-}$ cells, we did not observe a clear dose response for caspase 3/7 expression particularly for the free drug, which may imply involvement of other non-caspase related mechanisms of cell death and/or limitated sensitivity of the assay method beyond a threshold. Following IT administration at a dose of 1 mg/Kg, A83B4C63 either in NP or CE formulation showed a trend in the reduction of tumor size and better survival of the mice in PTEN$^{-/-}$ xenografts (**Supplementary Fig. 2.5C** and **2.5D**). This activity coincided with binding of A83B4C63 either in CE or NP formulations with tumoral PNKP following IT administration of the drug (**Fig. 2.2B** and **2.2C**).

In the next step of preclinical evaluation of our lead PNKP inhibitor, and prior to systemic IV administration of A83B4C63, its MTD as well as potential biochemical, and histopathological effects following IV administration were determined in healthy CD-1 mice. An injection schedule similar to that for the anticancer activity study was chosen for this dose escalating study [296]. Our results showed A83B4C63 either as CE or NP formulation were well-tolerated up to the tested dose of 50 mg/kg. Furthermore, the biochemical and histopathological examination of the major organs of the treated mice did not reveal any toxicity. Despite no observable change in biochemical and histopathological markers of toxicity by CE or NP formulations of A83B4C63, we visually observed a few behavioral changes, including hyperactivity, restlessness, aggressive attitude,

anxiety, and higher physical sensitivity while touching skin in the course of experimentation, in mice injected with the CE formulation.

In further *in vivo* studies, while NP/A83B4C63 at a repeated dose of 25 mg/kg was able to impede the growth of $PTEN^{-/-}$ and $Luc^{+}/PTEN^{-/-}$ HCT116 xenografts significantly (**Fig. 2.6B** and **2.8C**), free A83B4C63 failed to show any substantial effect. The superior activity of the NP formulations of A83B4C63 compared to its CE formulation can, at least partly, be attributed to enhanced delivery of the encapsulated drug to the tumor by its NP carriers **(Fig. 2.7)**. In addition to the results of biodistribution study on the encapsulated and free A83B4C63, two other pieces of evidence confirm this explanation. First, any potential effect on the inhibition of tumor growth or *in vivo* cancer cell proliferation (evidenced by Ki67 staining of tumor xenografts) by the NP alone (empty NPs) was ruled out (**Supplementary Fig. 2.5** and **Fig. 2.9**, respectively). Besides, upon IT administration, an equal trend in inhibition of tumor growth was observed for both CE and NP formulations of the A83B4C63 in PTEN deficient HCT116 xerographs. The latter indicate the equal activity of A83B4C63 in CE versus NP formulation when delivered locally and at the same dose to the tumor, *in vivo*.

The applied dose of A83B4C63 for IV injection is in line with the injected dose for conventional chemotherapeutic drugs like irinotecan, and other inhibitors of DNA repair proteins, such as PARP inhibitors like Olaparib, and inhibitors of ataxia-telangiectasia mutated and Rad3-related (ATR) inhibitor like Ceralasertib in animal models [297-299]. A similar level of distributed A83B4C63 in $PTEN^{-/-}$ versus $PTEN^{+/+}$ tumors rules out the potential role of drug levels in tumor site in observed activity of NP/A83B4C63 in $PTEN^{-/-}$ tumors and provides further evidence for the synthetic lethality as the main reason behind effectiveness of this formulation in PTEN-negative tumors as monotherapy. The anti-proliferative activity evidenced by Ki-67 staining only in $PTEN^{-}$

$^{/-}$ tumors of mice treated only with NP/A83B4C63 (**Fig. 2.9**) provided further evidence for the anticancer activity of A83B4C63/NPs as a synthetically lethal nanomedicine in cancer cells harboring PTEN deficiency.

Altogether, the above observations further confirmed a synthetic lethal partnership between PTEN loss and PNKP inhibition and validated the potential of A83B4C63/NPs as a lead PNKP inhibitor for monotherapy in PTEN-deficient CRCs. The biochemical mechanism(s) underlying the synthetic lethality resulting from PTEN loss and PNKP inhibition are still not fully elucidated, although we have previously found a high proportion of the cell death mediated by apoptosis in PTEN/PNKP-deficient cells [200-202, 267]. Here, we observed an upregulation of cleaved caspase-7 following treatment of PTEN-deficient CRC cells with both free and encapsulated A83B4C63 (**Fig. 2.3D**). It is known that caspase-7 plays an important role in the execution phase of cellular apoptosis [300]. It has also been reported that PARP is cleaved by caspase-7 along with caspase-3 [301, 302]. Being cleaved, PARP facilitates the apoptosis. However, the activation of both caspase-3 and PARP was not identified in PTEN-deficient CRC cells when treated with PNKP inhibitor (**Fig. 2.3D** and **Supplementary Fig. 2.3G**), even after longer film exposure. The underlying mechanism behind these observations remains poorly understood and needs further investigations.

The results also showed better activity of A83B4C63, as free drug *in vitro*, compared to its NP formulation in PTEN-deficient HCT116 cells. This was expected due to slow release of drug from the NPs. In contrast, upon IV administration, the NP formulation of A83B4C63 was found to be the only active form of the drug in PTEN-deficient HCT116 xenografts, most likely because of higher drug levels in the tumors following NP delivery.

The current study focused on the use of A83B4C63 as a lead PNKP inhibitor formulated in PEO-*b*-PBCL NPs as synthetically lethal monotherapeutic in PTEN-negative CRC models. Micellar NPs of this lead PNKP inhibitor can also enhance the effect of DNA damaging chemotherapeutics (particularly topoisomerase I inhibitors) or ionizing radiation particularly in $PTEN^{-/-}$ tumors, as shown in our previous *in vitro* studies [267]. Preclinical evaluation of such effects in tumor-bearing animals will be the subject of future studies.

2.5. Conclusion

In summary, our preclinical data have demonstrated that NPs of a PNKP phosphatase inhibitor exhibit *in vivo* synthetic lethality in a PTEN-deficient CRC xenograft model. The presented data provides a strong case for potential benefit of nanotechnology in the formulation of lead compounds for clinical development during the drug development process.

2.6. Acknowledgments

We thank Dr. Mary Hitt, Dr. Raymond Lai, Dr. Gregory Tyrrell, and Moinul Haque in Faculty of Medicine and Dentistry (University of Alberta) for their advice and technical assistance. We also thank Mesfin Fanta and Xiaoyan Yang (Cross Cancer Institute, Edmonton, Canada) for their support. We also thank Hao Fu and Dr. Burcin Akgun for support in the HPLC analysis and purification of compound A83B4C63. This work was supported by grants funded by the Canadian Institutes of Health Research (MOP 15385) to M.W. and (MOP 159757) to A.L., the Alberta Cancer Foundation Transformative Program Project (26603) and Nanomedicine Innovation Network (NMIN) grant (2019-T1-06) to D.H., F.J., A.L., and M.W., and both Alberta Innovates and CIHR Fellowships to Sams M. A. Sadat.

2.7. Declaration

The authors declare the following competing financial interest(s): Material in this manuscript has been included in recent US patent applications. Dr. Lavasanifar is Vice-President of Meros Polymers which has the license to PEO-PBCL polymer used in this manuscript.

Supporting information

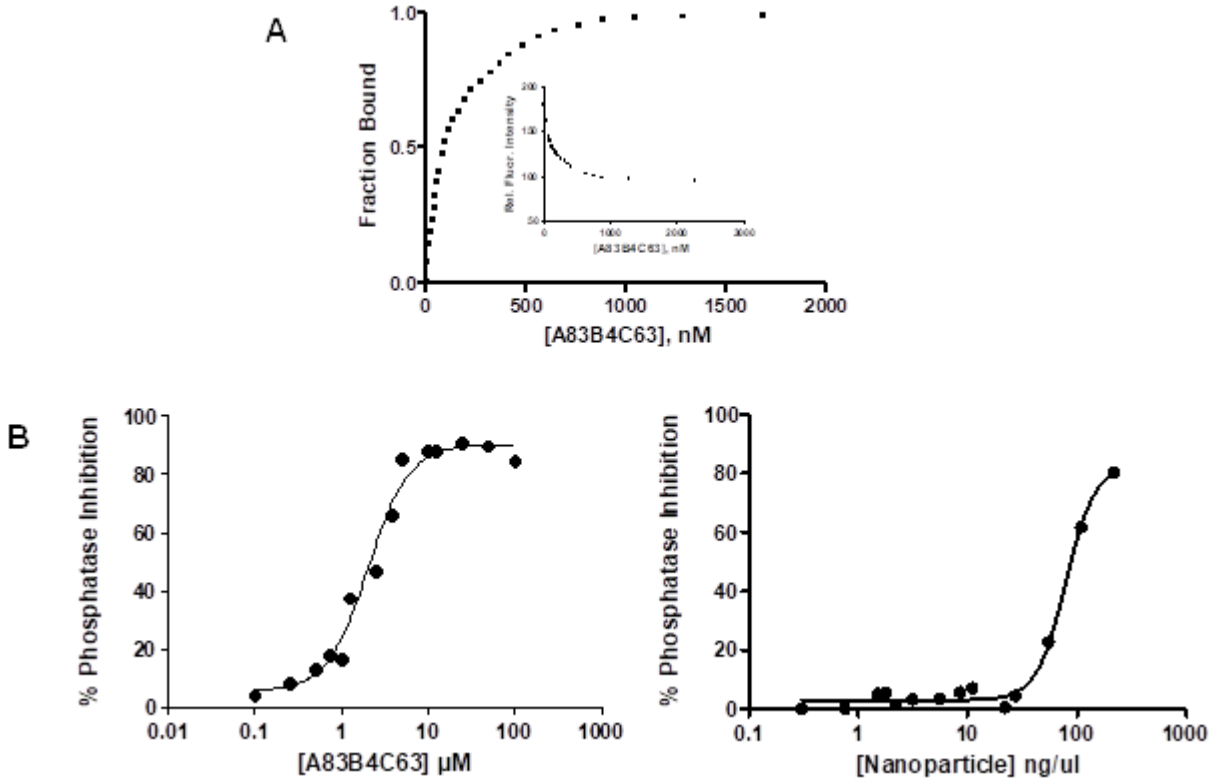

Supplementary Figure 2.1: (A) Determination of the affinity (KD) between A83B4C63 with PNKP. Unimodal binding pattern and the binding affinity of A83B4C63 with PNKP (80 ± 5 nM). The protein was excited at 295 nm, and fluorescence intensity was monitored at 330 nm (see inset). The fraction bound (i.e., relative fluorescence intensity) versus ligand concentration is plotted. (B) Inhibition of PNKP phosphatase activity (IC50) determinations for A83B4C63 (2.04 µM equivalent to 1.15 µg/mL) and empty PEO-*b*-PBCL (79.9 µg/mL). The IC_{50} plots show the mean of 3 independent determinations.

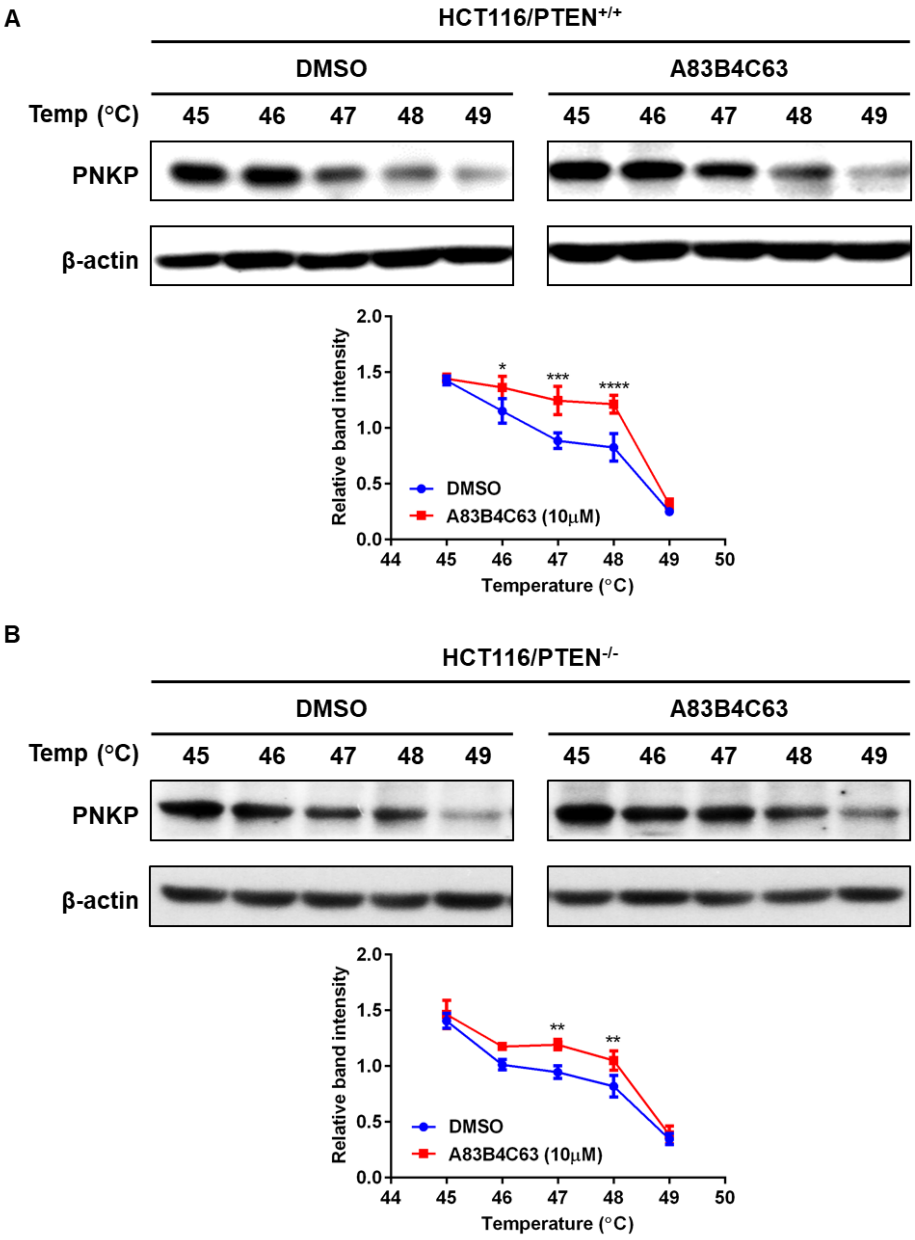

Supplementary Figure 2.2: Representative CETSA for A83B4C63-induced stabilization of PNKP in (B) HCT116/PTEN$^{+/+}$ and (C) HCT116/PTEN$^{-/-}$ cells. PNKP protein levels were quantified by densitometric analysis using ImageJ software. Data are presented as mean ± SD (n = 3). Compared to the control cells, differences were considered significant if *$p \leq 0.05$, **$p \leq 0.01$, ***$p \leq 0.001$, and ****$p \leq 0.0001$; Student's t test.

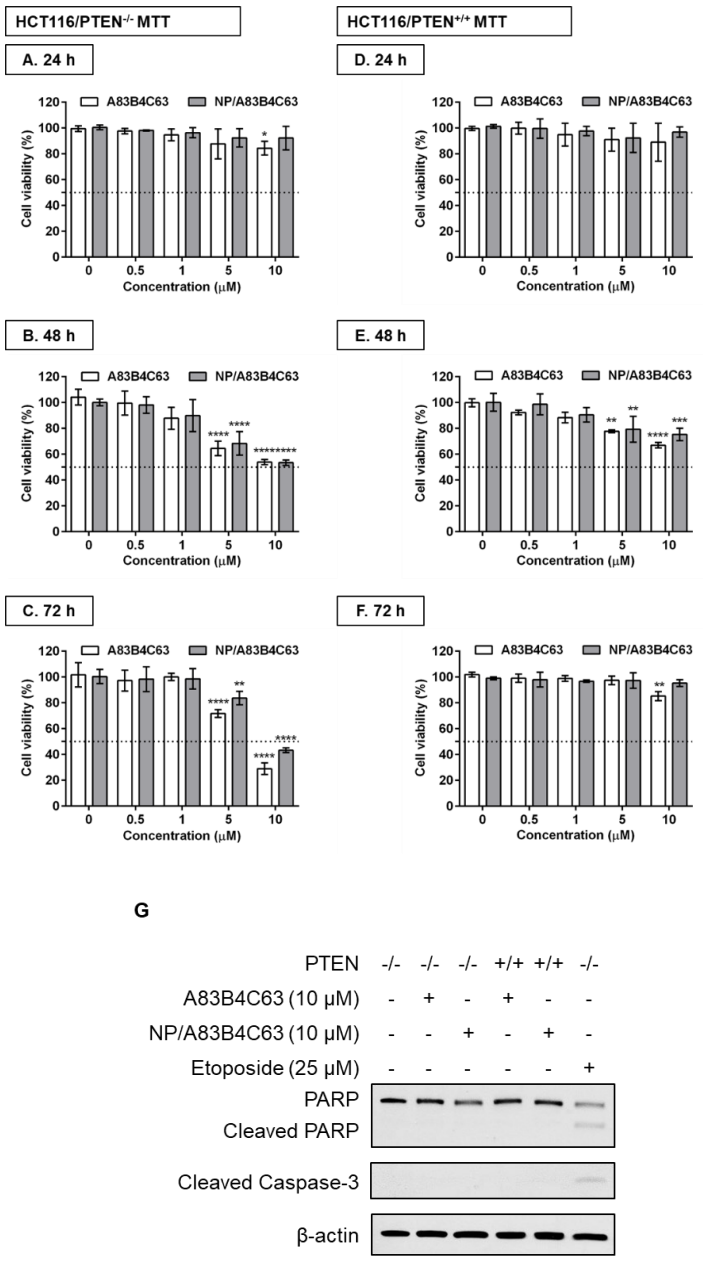

Supplementary Figure 2.3: (A-F) In vitro cytotoxicity of A83B4C63 and NP/A83B4C63 in HCT116/PTEN$^{+/+}$ and HCT116/PTEN$^{-/-}$ cell lines after 24, 48 h, and 72 h incubation as measured by MTS assay. The cells were treated with free drug and its NP formulation at a concentration range of 0.5 to 10 μM. A83B4C63 was solubilized with the aid of 0.1% DMSO and the control cells received only 0.1% DMSO. Each point represents mean ± SD (n = 4). Compared to the control cells, differences were considered significant if *$p \leq 0.05$, **$p \leq 0.01$, ***$p \leq 0.001$, and ****$p \leq 0.0001$. (G) Western blot detection of PARP, cleaved PARP, and cleaved caspase-3 in both cell lines after 48 h exposure to A83B4C63 and NP/A83B4C63 (n = 3). Etoposide-treated cells (25 □M, 24 h incubation) were used as positive control. β-actin was used as a loading control. The conditions for all sample preparation and western blot were the same.

A

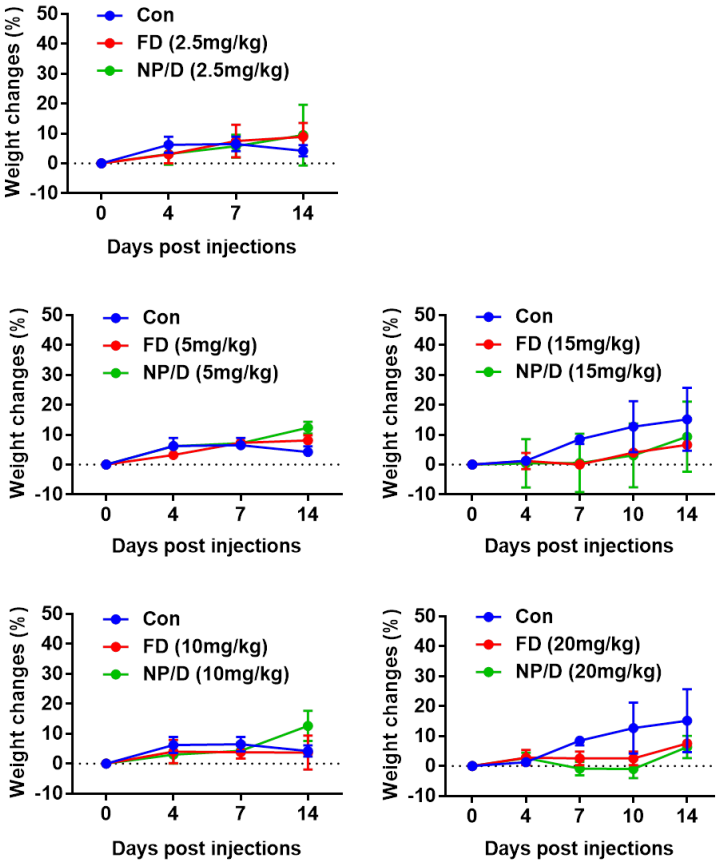
Con
FD (2.5mg/kg)
NP/D (2.5mg/kg)
Weight changes (%)
Days post injections
Con
FD (5mg/kg)
NP/D (5mg/kg)
Con
FD (15mg/kg)
NP/D (15mg/kg)
Con
FD (10mg/kg)
NP/D (10mg/kg)
Con
FD (20mg/kg)
NP/D (20mg/kg)

B

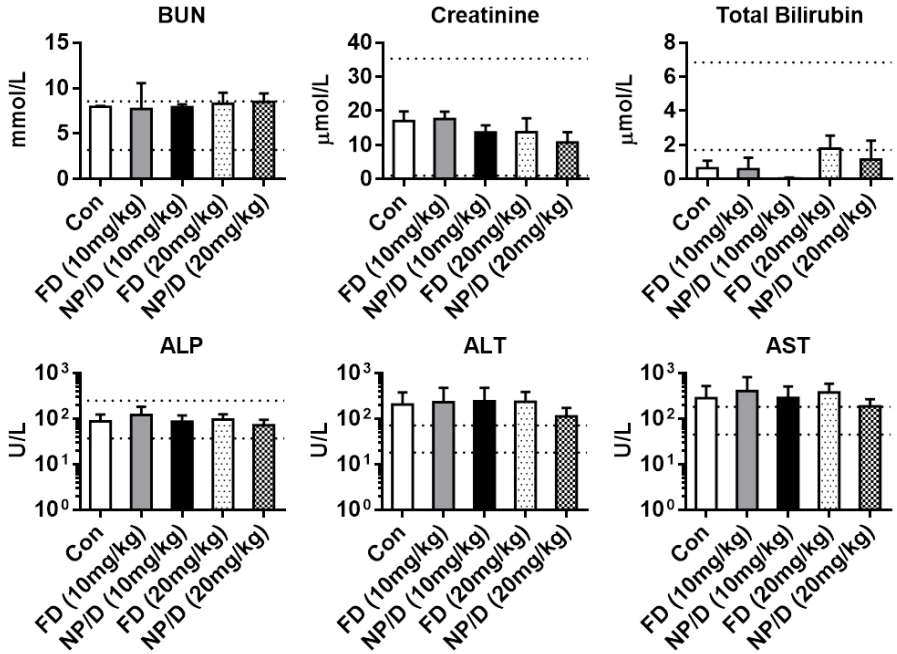
BUN
mmol/L
Creatinine
μmol/L
Total Bilirubin
μmol/L
ALP
U/L
ALT
U/L
AST
U/L
Con
FD (10mg/kg)
NP/D (10mg/kg)
FD (20mg/kg)
NP/D (20mg/kg)

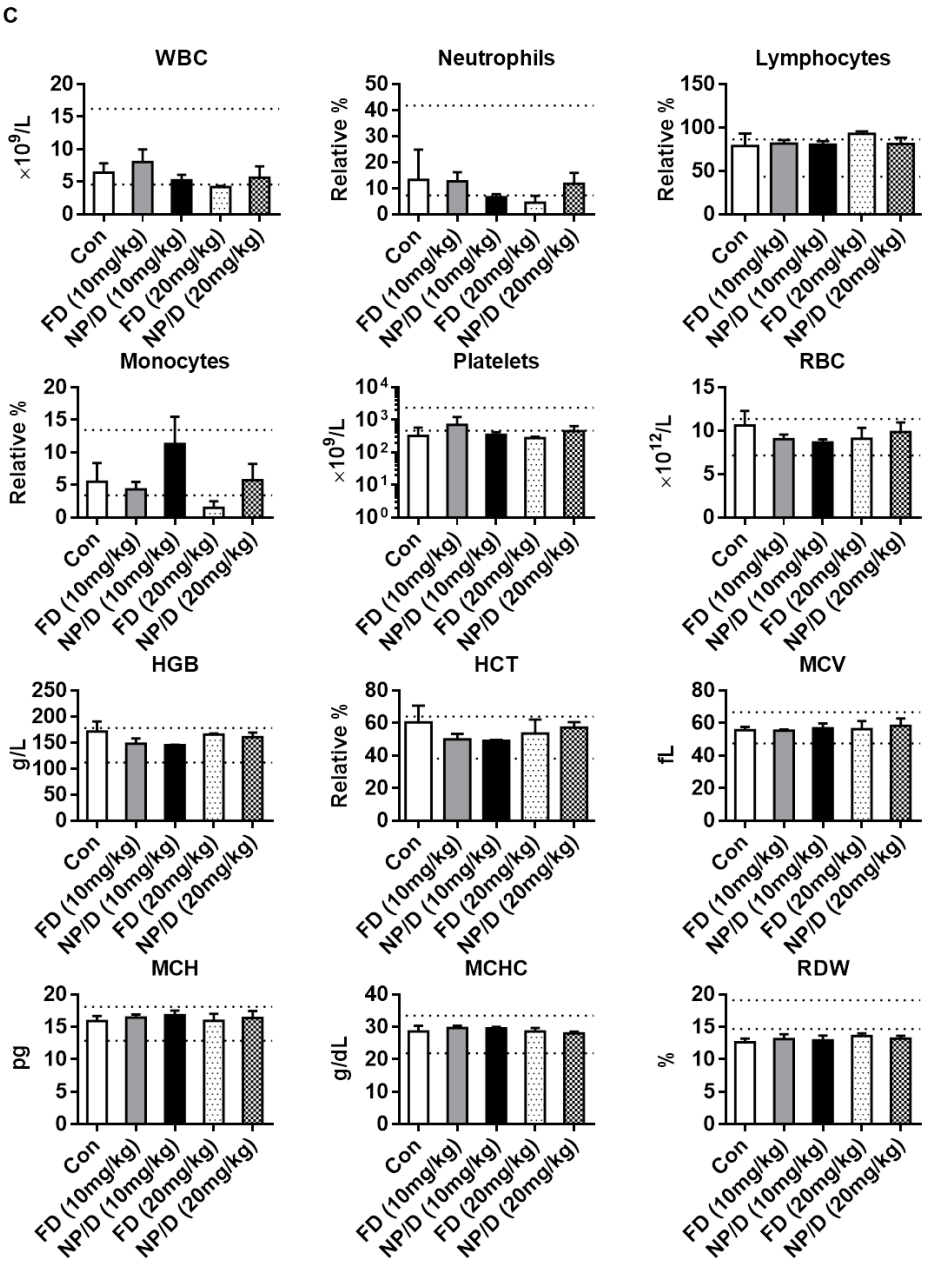

Supplementary Figure 2.4: (A) Representative percentage in weight change for female CD-1 healthy mice following IV injection of 2.5, 5, 10, 15, and 20 mg/kg doses of free A83B4C63 (solubilized with the aid of CE) and NP/A83B4C63 administered three times with a two day interval between injections. The control mice (con) received IV 5% dextrose. The average percentage (%) for the body weights of the mice were measured up to two weeks following the first injections. (B) Biochemical; and (C) hematological changes in blood samples collected from the mice receiving either 10 or 20 mg/kg doses. The normal range of each biomarker of drug toxicity is shown by dotted lines. Each point represents mean ± SD (n = 4).

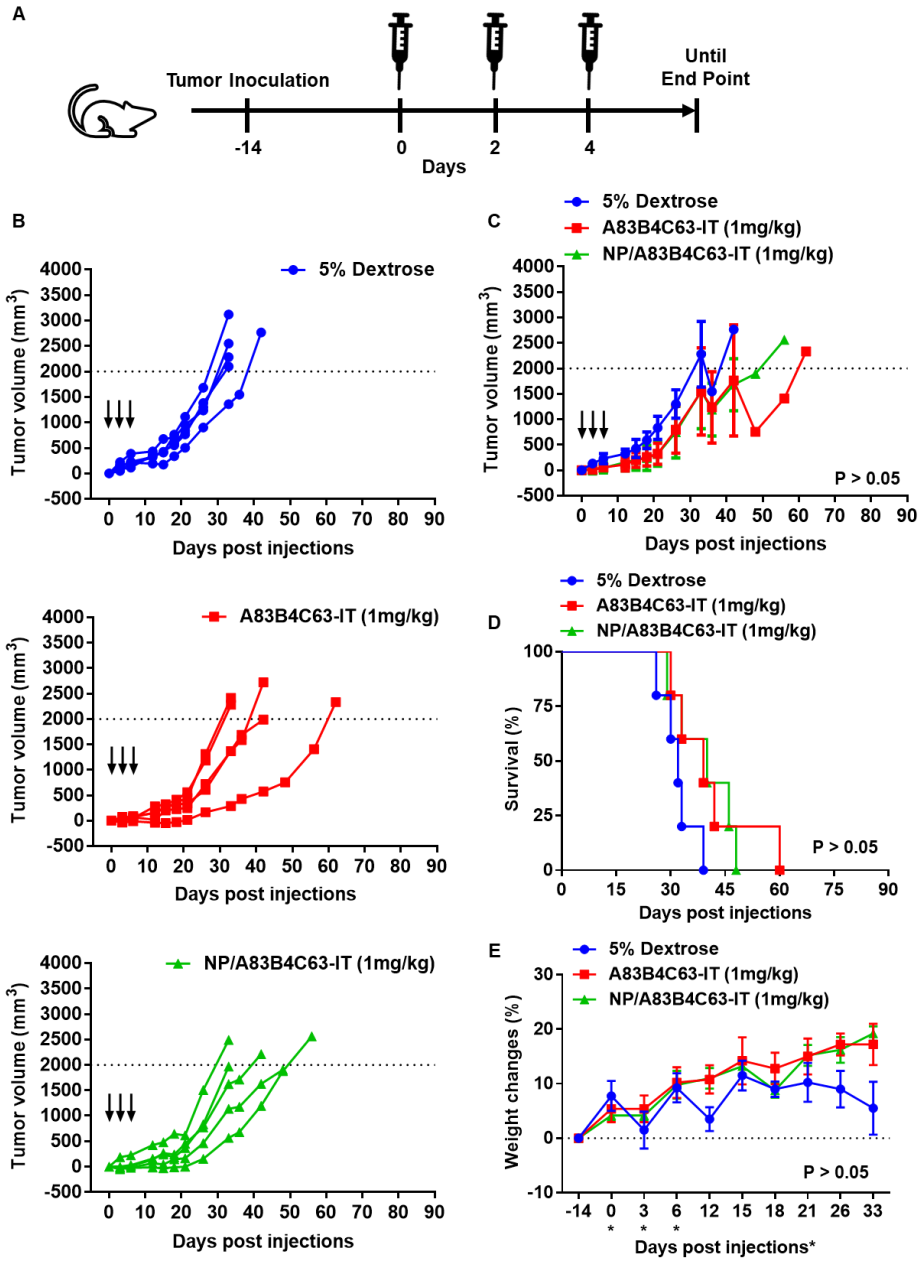

Supplementary Figure 2.5: (A) Study design for evaluating the anticancer activity of intratumoral (IT) injection of A83B4C63 as CE formulation or NP/A83B4C63 in NIH-III female nude mice (n = 5). HCT116/PTEN$^{-/-}$ cells were inoculated and grown as SC tumor xenografts in the right flank of the mice. 14 days following tumor inoculation, mice were intratumorally injected with either 5% dextrose, 1 mg/kg A83B4C63 solubilized with the aid of CE, or NP/A83B4C63 formulation (1 mg/kg of A83B4C63) three times with a two day interval between injections. Using digital calipers, the length (L) and width (W) of the tumor mass were measured 2-3 times per week and the tumor volume (TV) was calculated according to the following formula, TV = (L × W2)/2. (B) Representative tumor volume growth curves for each individual mouse in each treatment group. (C) Average tumor volume growth curves for mice in each treatment group. (D) Kaplan-Meier survival curves including overall median survival (MS) days and (E) the average percentage (%) for the body weights of treated HCT116/PTEN$^{-/-}$ xenograft mice. Each point represents the mean ± SD (n = 5).

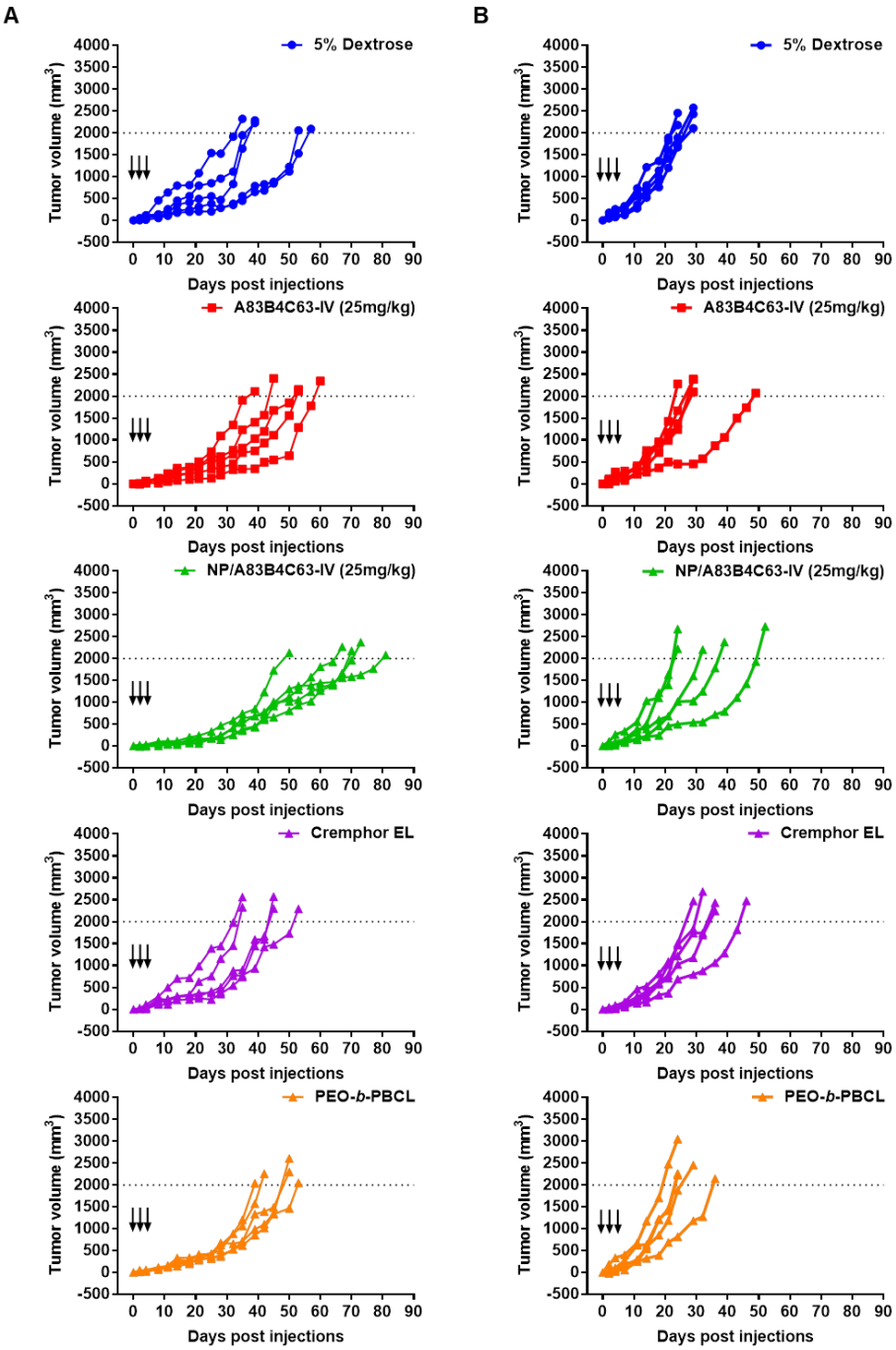

Supplementary Figure 2.6: Tumor volume growth curves for individual mice in each treatment group for both (A) HCT116/PTEN$^{-/-}$, and (B) HCT116/PTEN$^{+/+}$ xenografts mice (n = 5). Colorectal HCT116/PTEN$^{-/-}$ and HCT116/PTEN$^{+/+}$ cells were inoculated and grown as SC tumor xenografts in the right flank of the mice. When tumors became palpable, for each xenograft type the mice were divided into 5 groups (25 mice in total), which were intravenously injected with (i) 5% dextrose, (ii) free CE, (iii) empty PEO-b-PBCL NPs, (iv) A83B4C63 formulated with the aid of CE, or (v) PEO-*b*-PBCL NP (NP/A83B4C63) formulation three times with a one day interval at a dose of 25 mg/kg.

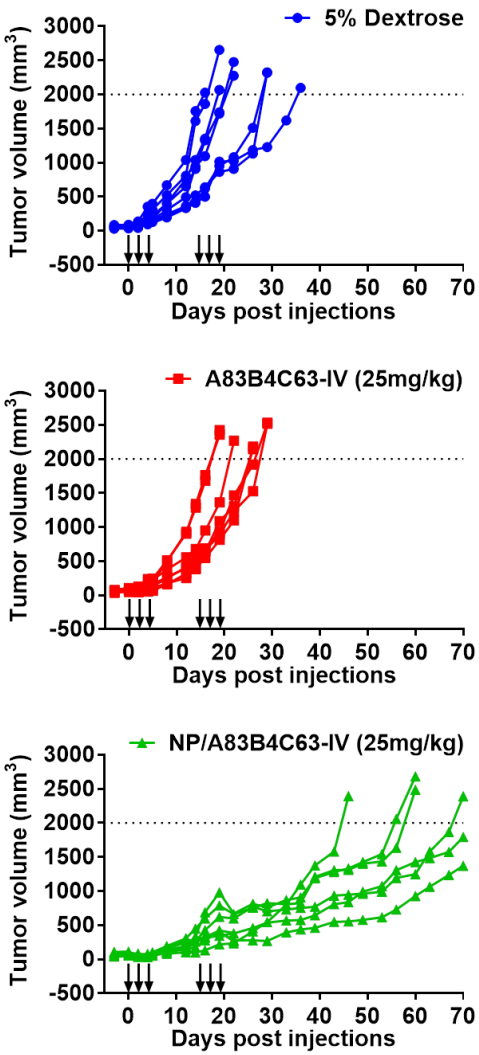

Supplementary Figure 2.7: Luc^{+}/HCT116/$PTEN^{-/-}$ tumor volume growth curves for individual mice in each treatment group after six IV injections with 5% dextrose, A83B4C63, and NP/A83B4C63 at a dose of 25 mg/kg with one day intervals between injections (n = 8). After the first three IV injections, all mice were given a rest for one week.

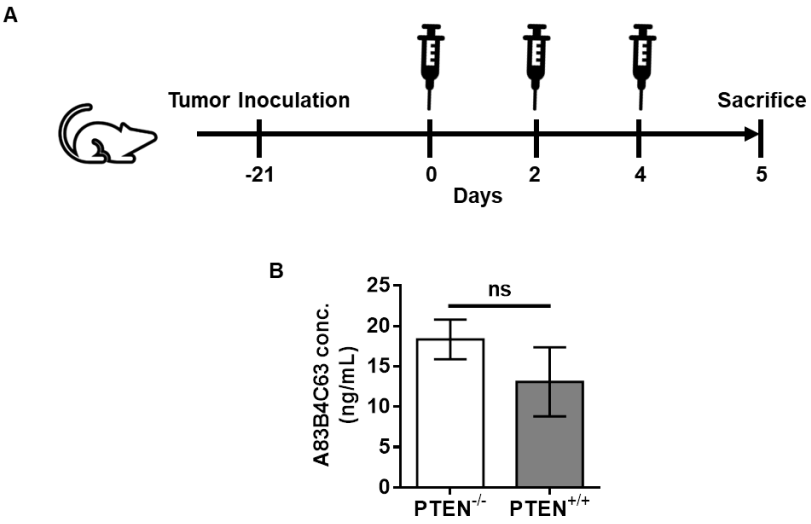

Supplementary Figure 2.8: (A) Schematic study design for assessing the tumoral concentration of A83B4C63 in both HCT116/PTEN$^{-/-}$ and HCT116/PTEN$^{+/+}$-bearing NIH-III female nude mice (n = 3) after 24 h systemic exposure of NP/A83B4C63 via tail vein. Mice were inoculated with HCT116/PTEN$^{-/-}$ and HCT116/PTEN+/+ CRC cells. 21 days following tumor cell inoculation, the mice received NP/A83B4C63 intravenously at a dose of 25 mg/kg three times with a one day interval. The control mice received 5% dextrose. 24 h after the last IV injection, all mice were euthanized to collect tumors. (B) Average concentration of A83B4C63 in HCT116/PTEN$^{-/-}$ and HCT116/PTEN$^{+/+}$ xenograft tumor tissues. The A83B4C63 concentration in the tumor tissues was quantified using LC-MS (mean ± SD). Differences were considered significant if $p \leq 0.05$.

Chapter 3: Nanodelivery of a novel inhibitor of polynucleotide kinase/phosphatase (PNKP) for targeted sensitization of colorectal cancer to radiation-induced DNA damage

3.1. Introduction

Colorectal cancer (CRC) is the second most common cause of cancer death, globally [303] and its incidence is expected to increase by 33% by 2028 [304]. Clinical outcomes from the conventional treatment options in CRC seem to depend on the location as well as molecular features of individual tumors [305]. Thus, the best treatment decisions must be individualized for patients [213-215]. Surgery is a very common option for most CRC patients [216]. Adjunctive chemotherapy or ionizing radiation (IR) is often accompanied before or after surgery. Although, IR is not preferred option to treat colon cancer but it is fairly common in rectal cancer [216]. Radiation therapy, often with adjuvant chemotherapy, is considered to help in shrinking the localized CRC tumors before the surgery [217, 218]. Radiation therapy may also be used to remove the cancer cells that may have been left behind the resection boundary after the surgery [219].

Inherent or acquired cellular resistance mechanisms in CRC cells can undermine the effect of IR, eventually leading to cancer reoccurrences in CRC patients [220, 221]. IR generates DNA strand breaks. However, the intracellular capacity in the repair of damaged DNA is one of the major causes of resistances to IR [221, 222]. Inhibition of DNA repair is considered as a promising approach to improve the sensitivity cancer cells to IR, thus, different DNA repair enzymes have been validated as the therapeutic targets for radio-sensitization in various cancers [63, 223, 224, 306-310].

Human polynucleotide kinase-phosphatase (PNKP) is identified as a key enzyme involved in DNA repair following damage by IR or topoisomerase I inhibitors (e.g. Irinotecan) in many types of cancers including CRC [118, 127, 237, 267]. PNKP phosphorylates DNA 5′’-termini and dephosphorylates DNA 3′’-termini that allow DNA ligases to rejoin the damaged strands of the DNA. The validity of PNKP as a therapeutic target, in sensitizing cancer cells to topoisomerase I inhibitor and IR, has been previously shown by our research team and others [118-120, 126, 238]. Through the RNAi screens, we have made an exciting discovery that the deficiency of a tumor

suppressor protein, i.e., phosphatase and TENsin homolog (PTEN), makes the cancer cells even more sensitive to the PNKP inhibition [202, 203]. This has inspired the development of the small molecule inhibitors of PNKP by our research team.

A83B4C63 is a second generation polysubstituted imidopiperidines small molecular inhibitor of PNKP with IC_{50} and K_D values in low micromolar and nano molar range, respectively. The water-solubility of A83B4C63 is <1 mM and its log D is ~4.16, which makes this compound a non-ideal candidate for the drug development process. To overcome the limitation of poor water-solubility and at the same time, reduce the access and radio/chemo-sensitizing effects of A83B4C63 in normal tissues, we have developed NP formulations of this compound, which were based on methoxy poly(ethylene oxide)-poly(a-benzyl carboxylate-e-caprolactone) (mPEO-*b*-PBCL). Passive targeting of solid tumors by NPs, is attributed to the presence of leaky vasculature as well as impaired drainage of the lymphatic system at the tumor site [251, 255-262]. The nanocarriers of appropriate size and surface properties can extravasate from the leaky vasculature at the tumor sites, while the impaired lymphatic drainage prevents their rapid removal out of the tumor microenvironment [311, 312]. This phenomenon, which is known as enhanced permeation and retention (EPR) effect, is believed to play a key role in preferential distribution of nanocarriers in solid tumors compared to many normal tissues [313-316].

In our previous studies, the nano-formulation of A83B4C63 were shown to effectively reduce the viability of PTEN-deficient CRC, as monotherapy [317]. The mPEO-*b*-PBCL based NPs of A83B4C63, were also shown to sensitize CRC cells to IR and irinotecan, *in vitro* [267]. *In vivo*, the NPs of A83B4C63 were tolerated better than conventional formulations of this compound and showed significantly enhanced delivery and activity of incorporated A83B4C63 in PTEN-deficient HCT116 xenografts in mice. The objective of current study was to assess the effect of the conventional versus mPEO-*b*-PBCL nano-formulation of A83B4C63 in sensitization of wild type CRC models to IR, both *in vitro* and *in vivo*.

3.2. Materials and methods

3.2.1. Materials

Methoxy polyethylene oxide (mPEO) (average molecular weight of 5000 g/mol), Cremophor EL: Ethanol (CE), and all research grade organic solvents were purchased from Sigma (St. Louis, MO, USA). α-Benzyl carboxylate-ε-caprolactone monomer was synthesized by Alberta Research Chemicals Inc. (Edmonton, AB, Canada). Stannous octoate was purchased from MP Biomedicals Inc. (Tuttlingen, Germany).

3.2.2. Synthesis of A83B4C63 and PEO-*b*-PBCL copolymer

The polysubstituted imidopiperidine compound, A83B4C63, was synthesized using a three-component aza[4+2]/allylboration reaction and purified to homogeneity via HPLC as previously described [280]. The structure of the compound was confirmed by NMR, IR, and LC-MS as previously reported [267].

The mPEO-*b*-PBCL block copolymer with 26 degree of polymerization for the PBCL block was synthesized by ring-opening polymerization of α-benzyl carboxylate-ε-caprolactone using mPEO (MW: 5000 g/mol) as an initiator and stannous octoate as catalyst according to the method described previously [267, 318] (**Fig. 3.1**). The synthesized copolymers were characterized for their average molecular weights by ^{1}H NMR (600 MHz Avance III - Bruker, East Milton, ON, Canada) using deuterated chloroform ($CDCl_3$) as solvent and tetramethylsilane as an internal reference standard.

3.2.3. Formulation and characterization of A83B4C63-encapsulated mPEO-*b*-PBCL NPs

A83B4C63-encapsulated mPEO-*b*-PBCL NPs (NP/A83) were prepared as previously described [267]. In brief, 10 mg A83B4C63 and 30 mg mPEO-*b*-PBCL polymer were completely dissolved in 1 mL of acetone. Then, the organic phase was transferred dropwise to 10 mL aqueous

phase and left overnight with continuous stirring with a magnetic bar under the fume hood to completely evaporate the organic solvent. The un-encapsulated A83B4C63 was removed by centrifugation at 11600 × g for 5 min to obtain NP/A83. The NP/A83 solution was then transferred into Amicon Ultra-15 centrifugal filter tubes (molecular weight cut-off, 100 kDa; Millipore, ON, Canada) and centrifuged at 11600 × g for 20 min at 4ºC in order to concentrate as required. The average size and polydispersity index (PDI) of the NPs were measured by dynamic light scattering (DLS) using a Malvern Zetasizer 3000 (Malvern Instruments Ltd, Malvern, UK). A83B4C63 loading and loading efficiency were measured and analyzed using a Varian Prostar 210 HPLC system. Reversed phase chromatography was carried out with a Microsorb-MV 5 µm C18-100 Å column (4.6 mm × 250 mm) with 20 µL of sample injected and eluted under isocratic conditions with a solution of 0.1% trifluroacetic acid / acetonitrile (1:1 v/v) at a flow rate of 0.7 mL/min at room temperature. Detection was performed at 280 nm wavelength for A83B4C63 using a Varian 335 Photodiode Array HPLC detector (Varian Inc., Palo Alto, CA, USA). In this study, A83B4C63 control was solubilized with DMSO for all *in vitro* experiments, while for *in vivo* experiments, A83B4C63 was dissolved with the aid of CE (CE/A83). Finally, the A83B4C63 loading and loading efficiency were calculated according to the following equations:

$$\text{A83B4C63 loading (\%)} = \frac{\text{The amount of encapsulated A83B4C63}}{\text{The total amount of mPEO}-b-\text{PBCL polymer}} \times 100$$

$$\text{A83B4C63 encapsulation efficiency (\%)} = \frac{\text{The amount of encapsulated A83B4C63}}{\text{The initial amount of A83B4C63 added}} \times 100$$

3.2.4. Transmission electron microscopy (TEM)

The morphology of self-assembled structures under study was investigated by TEM using a Morgagni TEM (Field Emission Inc., Hillsboro, OR) with Gatan digital camera (Gatan, Pleasanton, CA). In brief, 20 µL of micellar solution with a polymer concentration of 0.25 mg/mL was placed on a copper-coated grid. The grid was held horizontally for 1-2 min to allow the

colloidal particles to settle down. The excess fluid was removed by filter paper. The copper-coated grids holding the aqueous samples were then negatively stained by 2% phosphotungstic acid. After 2 min, the excess fluid was removed by filter paper and the grid was loaded into the TEM for image analysis.

3.2.5. Cell lines

Wild type HCT116 and luciferase positive Luc^{+}/HCT116 cell lines were routinely cultured at 37ºC in 5% CO_2 in a humidified incubator in a 1:1 mixture of Dulbecco's modified Eagle medium and F12 (DMEM/F12) supplemented with 10% FBS, 50 U/mL penicillin, 50 mg/mL streptomycin, 2 mmol/L L-glutamine, 0.1 mmol/L nonessential amino acids, and 1 mmol/L sodium pyruvate. All culture supplements were purchased from Invitrogen (Burlington, ON, CA). All cell lines were routinely tested for mycoplasma in the lab.

3.2.6. Microscopic study for γ-H2AX evaluations

1×10^5 wild type HCT116 cells were seeded onto each glass coverslip in a 35-mm Petri dish and incubated overnight to attach. The cells were then pretreated with the nano-formulations for 24 h prior to 3 Gy γ-irradiation. After the γ-irradiation, the cells were incubated for two time points up to 6 h. After the incubation, the cells were fixed with 4% of paraformaldehyde in PBS for 20 min, then permeabilized, and blocked with 1% BSA in 1 x PBS/0.1% Tween 20 for 20 min. After 3 washes with 1 x PBST, anti-phospho-histone H2A.X (Ser139) antibody (catalog# 05-636, Millipore, Temecula, CA) at 1:4000 dilution was applied to the cells and incubated for 1 h at room temperature. The cells were washed three times with 1 x PBST and then incubated with Alexa Fluor 488 goat anti-mouse secondary antibody (catalog# A11059, Life Technologies, Carlsbad, CA) at a 1:200 dilution in 0.1 % BSA/1 x PBST for 1 h in the dark. After washing the cells, the coverslips were mounted on the slides with DAPI-containing mounting media [319] (Molecular

Probes, Eugene, Oregon) at 1 μg/mL concentration. Images were taken with the Axio Imager Z2 microscope (Carl Zeiss, Jena, Germany) using MetaMorph 7 and MetaXpress 6 software (Molecular Devices, San Jose, CA) to image and quantify foci.

3.2.7. *In vitro* apoptotic activity evaluations by western blot

Western blot was used to assess the DNA damage (γ-H2AX expression levels) and apoptosis (level of cleaved caspase 3/7 and PARP) of A83B4C63 as free drug (CE/A83) and NP (NP/A83) formulation in HCT116 cell line with or without radiation. Initially, 1.5 million cells were plated in each of 100 mm dishes 24 h prior to the treatments. Then, cells were treated with CE/A83 and NP/A83, or vehicles alone, at an A83 concentration of 10 μM, or equivalent drug free vehicles i.e, CE and NP. After 24 h incubation with A83 formulations or vehicle controls, cells were exposed to a fixed dose of radiation (4 Gy) using ^{60}Co Gamma irradiation platform (AECL, Chalk River, ON, Canada) facility at Cross Cancer Institute, Edmonton, Canada. The cells were harvested either after 1 or 4 h of exposure to IR. Each experiment was performed in triplicate.

The protein levels, followed by western blotting, were quantified by densitometry analysis using ImageJ software to assess the *in vitro* levels of caspase, PARP, and γ-H2AX proteins following the treatment with A83B4C63 as free drug and NP form in HCT116 cell line with or without IR at a fixed dose of 4 Gy. After experimental incubation time points, protein extracts for western blot analysis were prepared using commercial RIPA lysis buffer (ThermoFisher Scientific, Canada) supplemented with a cocktail of protease inhibitors (Millipore Sigma, Canada). Protein concentrations were measured using the BCA assay kit (Pierce/ThermoFisher Scientific, Canada) according to the manufacturer's protocol. Equal concentrations of protein were separated by SDS-PAGE and transferred to nitrocellulose membranes. After blocking with 5% skimmed milk in TBST (50 mM Tris-HCl, pH 7.4, 150 mM NaCl, and 0.1% Tween 20), the blots were incubated

with the respective primary antibodies (caspase-3 catalog# 9662S, caspase-7 catalog# 9492S, PARP catalog# 9542S, phospho-histone H2A.X (Ser139) (20E3) catalog# 9718S) and secondary antibody (HRP-linked anti-rabbit IgG cat# 7074S) purchased from Cell Signaling Technology (Whitby, ON, Canada). The protein bands were detected using an enhanced chemiluminescence (ECL) based system (Pierce/ThermoFisher Scientific, Canada).

3.2.8. Xenograft models

All mice were purchased from Charles River Laboratories. All animal studies were conducted in accordance with the guidelines of the Canadian Council on Animal Care with approval from the Animal Care and Use Committee of Cross Cancer Institute at the University of Alberta, Edmonton, AB, Canada. The HCT116 and Luc^+/HCT116 xenograft tumor mouse models were generated by subcutaneous injection of 0.5×10^6 cells in a 100 µL mixture of culture media and matrigel matrix (Corning, MA, USA) (1:1 v/v) in the right flank of 4 - 6 week-old female NIH-III nude mice. The CRC cell implanted mice were routinely monitored for tumor growth and signs of sickness. Animals reaching early endpoints as set in our animal protocol were euthanized. All animals were euthanized at day-22 following the tumor inoculation.

3.2.9. *In vivo* anticancer activity of combination therapies

This study was performed on Luc^+/HCT116 xenografts developed as described above. When the tumor volume reached 80 to 150 mm^3, mice were randomly assigned into test groups receiving empty NP without IR (n = 6), or empty NP (n = 6), CE/A83 (n = 6), and NP/A83 (n = 7) formulations of A83B5C63 with a fixed radiation dose of 3 x 5 Gy. The treatments (empty NPs, PNKP inhibitor A83B4C63 alone or CE/A83, A83B3C63-encapsulated NPs or NP/A83) were started on day 0. On day -2, tumor sizes were measured through the digital slide caliper and *in vivo*

imaging system (IVIS) imaging. All drugs were given via intravenous (IV) injection via tail vein and administered on days 0, 2, and 4. The IV A83B4C63 dose was 25 mg/kg, which was injected three times one day apart. Mice received three radiation doses every alternative day. The excipient dose, i.e., empty NP in control groups was selected equivalent to their amounts in the NP/A83 test group. The length (L) and width (W) of the tumor were measured using digital slide calipers two times per week and the tumor volume (TV) was calculated using the formula $TV = (L \times W^2)/2$. The measurements continued until day 22 (since the day of tumor inoculation) when all mice were euthanized.

The fractionated radiation therapy using a daily dose of 5 Gy was started on day 1 and given 3x including days 3 and 4. Radiation therapy was administered using the image-guided small-animal radiation research platform (SARRP; Xstrahl Inc. Suwanee, GA, U.S.A.) with 220 kVp X-rays and 13 mA using 2 beams and a 10 x 10 mm square-shaped collimator with isocenter positioned in the center of the tumor. Radiation doses were calculated using cone beam computed tomography images measured with the SARRP and the integrated Muriplan/Murislice software (Xstrahl Medical & Life Sciences, Camberley, UK) after contouring the tumor shape and defining the isocenter. Mice were anesthetized with isoflurane (100% O_2) for each radiation therapy session. After finishing the combination therapy on day 4, the mice were analyzed with bioluminescence or PET imaging for tumor growth on days 10-12 before they were euthanized.

3.2.10. *In vivo* imaging systems (IVIS) for evaluating anticancer activity of CE/A83 and NP/A83 with or without radiation

The animals inoculated with Luc^+/HCT116 and treated as described above were also imaged for the expression of luciferase to follow their tumor growth. For the optical imaging, mice were subcutaneously injected with the XenoLight D-Luciferin - K+ salt bioluminescent substrate

(PerkinElmer, UK) at a dose of 10 µL/g of body weight before the luciferase detection. Mice were anesthetized and placed in the dark chamber of a Xenogen IVIS machine for whole-body animal imaging and the emitted photons were quantified and analyzed using Living Image Software (Xenogen). Imaging of live animals was performed twice a week.

3.2.11. PET imaging

Luc^+/HCT116 tumor-bearing female NIH-III nude mice from the radiation therapy study (as described above) were analyzed on days 10-12 after last treatment for tumor proliferation using positron emission tomography (PET). Mice were anesthetized by isoflurane (100% O_2). A needle catheter was placed into the tail vein of these mice and 3 - 6 MBq of [^{18}F]FLT in 100 to 150 mL saline were injected. [^{18}F]FLT was synthesized at the cyclotron research facility of the Cross Cancer Institute (Edmonton, AB, Canada) according to the previously described procedure [320] using 5-O-(4,4-dimethoxytrityl)-2,3-anhydrothymidine (ABX GmbH, Radeberg, Germany) as a precursor. Radioactivity in the injection solution in a 0.5 mL insulin syringe was determined using a dose calibrator (AtomlabTM 300, Biodex Medical Systems, Shirley, NY, USA). After radiotracer injection, mice were allowed to regain consciousness for about 40 to 45 min before anesthetizing them again. They were immobilized in prone position into the center field of view of a preclinical INVEON® PET scanner (Siemens Preclinical Solutions, Knoxville, TN, U.S.A.). Acquisition data was collected in three-dimensional list mode for 10 min, reaching ~60 min post injection. Static PET images were reconstructed using maximum a posteriori (MAP) algorithm. Image files were further processed using the ROVER v2.0.51 software (ABX GmbH, Radeberg, Germany). Masks defining three-dimensional regions of interest (ROI) over tumor tissue were defined and ROI's were analyzed with 50% threshold of radioactivity uptake. Mean standardized

uptake values [SUV_{mean} = (measured radioactivity in the ROI/mL tumor tissue)/(total injected radioactivity/mouse body weight)] were calculated for each ROI.

3.2.12. Biodistribution of CE/A83 and NP/A83 formulations in HCT116 tumor-bearing mice

The biodistribution profile of A83B4C63 in CE and NP forms were assessed in wild type HCT116 tumor-bearing NIH-III mice. Tumor bearing mice were developed as described above, except for the use of HCT116 cells instead of Luc^+/HCT116. When the tumor volume reached 1200 to 1500 mm^3, mice were randomly assigned and grouped into three test groups (n = 3). The test groups received CE/A83 or its NP form three times, one day apart at an IV dose of 25 mg/kg. The control mice received empty NPs. 4, 24, and 48 h after the last injection, all mice were euthanized, and blood, excised tumors and other organs including brain, heart, lung, liver, kidney, spleen were collected to define drug levels using an LC/MS/MS method of quantification as previously described method [317]. In brief, all snap-frozen dissected tumor tissues were weighed and homogenized with an ice-cooled solution of acetonitrile/water (50:50 v/v) using an electric hand homogenizer. The collected whole blood samples of the mice were centrifuged at 2000 × g for 5 min at 4ºC to separate the plasma. Tissue homogenate samples were centrifuged at 2000 × g for 15 min at 4ºC. To 250 µL of plasma/homogenized tissues 1000 µL cold acetonitrile was added. The mixture was vortexed for 5 min and then the samples were centrifuged at 2000 × g for 20 min. The solutions were separated and transferred to clean tubes and evaporated to dryness.

An Agilent 1100 HPLC system coupled to a Waters Quattro Micro triple quadrupole mass spectrometer (Waters, Milford, MA) and attached to an Agilent Poroshell 120 SB- C18 2.7-micron LC column with dimensions of 2.1 mm x 50 mm was used. The column was heated to 35°C. The mobile phase consisted of water with 0.1% formic acid (A) and acetonitrile with 0.1% formic acid (B). A gradient elution was programmed to commence with 20% B for post-injection followed by

gradual increase in 3 min of B to 95%. The composition was maintained for 3 min when it was gradually decreased back to 20% of B in 0.1 min. The flow rate was 0.3 mL/min and 2 µL of sample was injected. Standard curves were linear over the range of 1 - 1000 ng/mL ($r^2 > 0.99$; coefficient of variation < 20%). The lowest limit of quantification was set at 1 ng/mL. The mass spectrometer was operated in positive mode with capillary voltage at 3.2 kV, source temperature at 120°C, desolvation temperature at 275°C, and desolvation gas flow at 800 L/Hr. Instrumental control and data analysis were performed using MassLynx software (Waters, Milford, MA).

Propranolol dissolved in the solution of acetonitrile/water with 50:50 v/v ratios was used as an internal standard. The dried residues in sample vials were reconstituted with 100 µL of internal standard solution with vigorous vortexing before placing into the auto-sampler of the LC/MS/MS (Waters Quattro Micro ± ES MS Triple Quadrupole, Milford, MA, USA) fitted with an Agilent Technology: Poroshell 120 SB-C18 2.1x50 mm, 2.7-micron column. The mobile phase consisted of 50:50 v/v ratios of water with 0.1% formic acid and acetonitrile with 0.1% formic acid.

The terminal elimination rate constant was estimated from the log-linear portion of the plasma concentration - time curves. Because of destructive sampling procedure used for the collection of blood and tissues from different animals at each time point, the area under the plasma /tissue curve (AUC) was estimated using the trapezoidal rule from the average plasma concentrations at different time points and the variance of AUC was estimated using Bailer's method based on the standard error of mean (SEM). Ratio of tissue concentration at each time point to that of plasma (Kp) was also calculated and reported.

3.2.13. Statistical analysis

GraphPad Prism 9 software (La Jolla, CA, USA) was used for statistical analysis. Significance of differences between groups was assessed using one-way and two-way ANOVA followed by Tukey's post-hoc test, where appropriate. If a significant difference was found among the groups, median ranks between pairs of groups were compared using the Mann-Whitney U test. A value of $p \leq 0.05$ was considered as statistically significant in all experiments. For biodistribution experiment, the pairwise comparisons of AUCs were carried out at α level of 0.05. The critical values of Z (Zcrit) for the two-sided test using the Bonferroni-adjusted was 2.24. The observed Z (Zobs) was calculated based on Bailer's method. Zobs values greater than Zcrit were considered as a significant difference between the AUCs.

3.3. Results

3.3.1. Physicochemical characterization

The ^{1}H NMR spectra and peak assignments of mPEO-*b*-PBCL (**Fig. 3.1A**) and A83B4C63 (**Fig. 3.1B**) were previously reported [254, 267, 294, 321, 322]. According to the calculations based on the ^{1}H NMR spectra, the DP was 26 for PBCL block in mPEO-*b*-PBCL copolymers. A83B4C63 encapsulation into the mPEO-*b*-PBCL micellar NPs was performed following a simple one-step self-assembly nanoprecipitation method (**Fig. 3.1B**). 21.97 ± 0.65% loading and 70.28 ± 3.47% encapsulation efficiency were measured when A83B4C63-encapsulated mPEO-*b*-PBCL NPs (NP/A83) were prepared at a 1:3 w/w A83B4C63/mPEO-*b*-PBCL ratio. The NP/A83 were ~60 nm in diameter on average and showed a low polydispersity index (PDI), i.e., < 0.25 (**Fig. 3.1C**). After A83B4C63-solubilization by CE formulation, the average size of CE/A83 micelles was < 35 nm in diameter, which was significantly lower (****$p \leq 0.0001$) than that of NP/A83. However, no significant difference was measured for the PDI values obtained from CE/A83 and

NP/A83. The diameter of the empty carriers from both formulation types e.g., NP, CE, were significantly lower (*$p \leq 0.05$) than their drug-encapsulated counterparts. As shown in **Fig. 3.1D**, the TEM image, confirmed the formation of spherical NP/A83 micelles with uniform size. In TEM image, a similar distribution pattern in the micellar population having a clear boundary was observed that also indicated the lower aggregation tendency among the formed micelles.

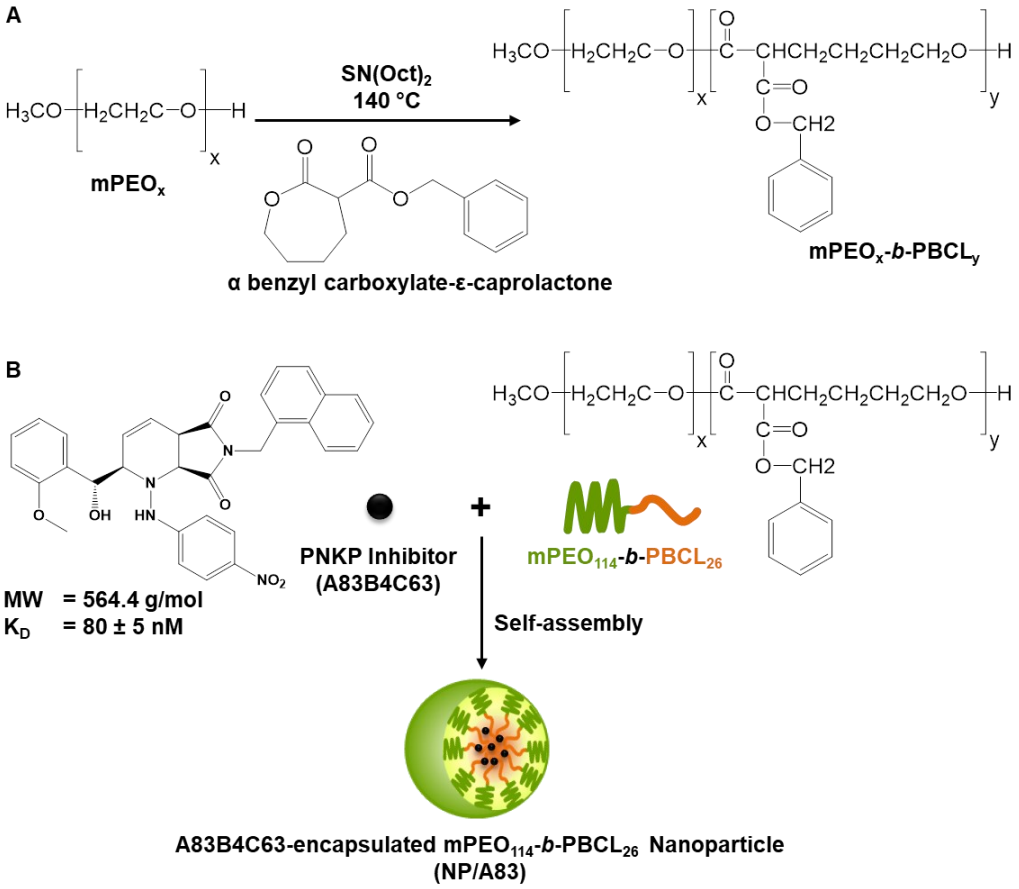

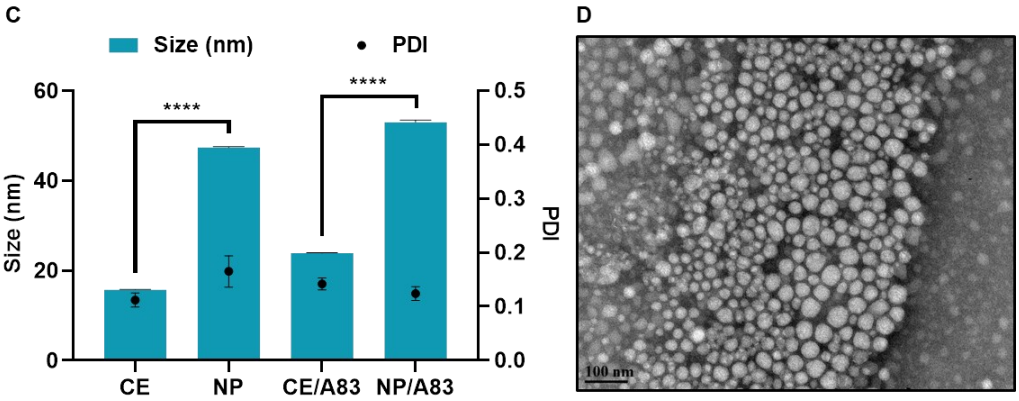

Figure 3.1: Chemical structure of (A) methoxy poly(ethylene oxide)-b-poly(α-benzyl carboxylate-ε-caprolactone or mPEO-*b*-PBCL and (B) illustration of encapsulation process of 2-[hydroxy(2-methoxyphenyl)methyl]-6-(naphthalene-1-ylmethyl)-1-[(4-nitrophenyl)amino]-2H, 4aH, 7aH-pyrrolo[3,4-b]pyridine-5,7-dione or A83B4C63. (C) Physicochemical characterization of water-soluble CE, empty NP, A83B4C63-solubilized (CE/A83), and A83B4C63-encapsulated mPEO-b-PBCL (NP/A83) formulations (n = 10). Hydrodynamic diameter and polydispersity index (PDI) of NP/A83 micelles in aqueous medium were obtained using dynamic light scattering (DLS) technique. (D) TEM image of A83B4C63-encapsulated micellar formulation (NP/A83) in aqueous medium. The TEM image was obtained at a magnification of 110,000X at 75 kV. The bar in the bottom left corner of each image indicates a scale of 100 nm.

3.3.2. Microscopic DNA damage activity evaluation

Upright microscopic evaluations were performed to assess the DNA damage activity of PNKP inhibition in conjugation with a fixed dose of IR (3 Gy). **Fig. 3.2A** shows the wide-field fluorescence images of the γ-H2AX expression-positive cells that treated with CE/A83 and NP/A83. Here, we studied the temporal and spatial distribution of the foci of the phosphorylated form of the histone protein H2AX (γ-H2AX) that is known to be activated, upon γ-irradiation, by the introduction of double-strand breaks of intracellular DNA. Qualitative analysis based on the microscopic images for the distribution of foci in each cell fairly indicated the higher cluster of DNA damage in cells when they were treated with A83B4C63 delivered by either CE or NP formulations. Quantitative analysis was also performed using the MetaXpress 6 software to quantify the number of foci in each cell. In this experiment, significantly higher number of γ-H2AX expressed-positive foci was observed 40 min after the γ-irradiation in NP/A83-treated cells than that of CE/A83 and untreated (radiation alone) treatment groups. However, the number of positive foci went down at 6 h post γ-irradiation for both A83B4C63 formulations. Significantly higher foci numbers at 40 min and 6 h post γ-irradiation time points in cells pretreated with either CE/A83 or NP/A83 or than the cells treated with γ-irradiation alone demonstrated the proof of concept for anticipated radio-sensitizing activity of our PNKP inhibitor, i.e., A83B4C63.

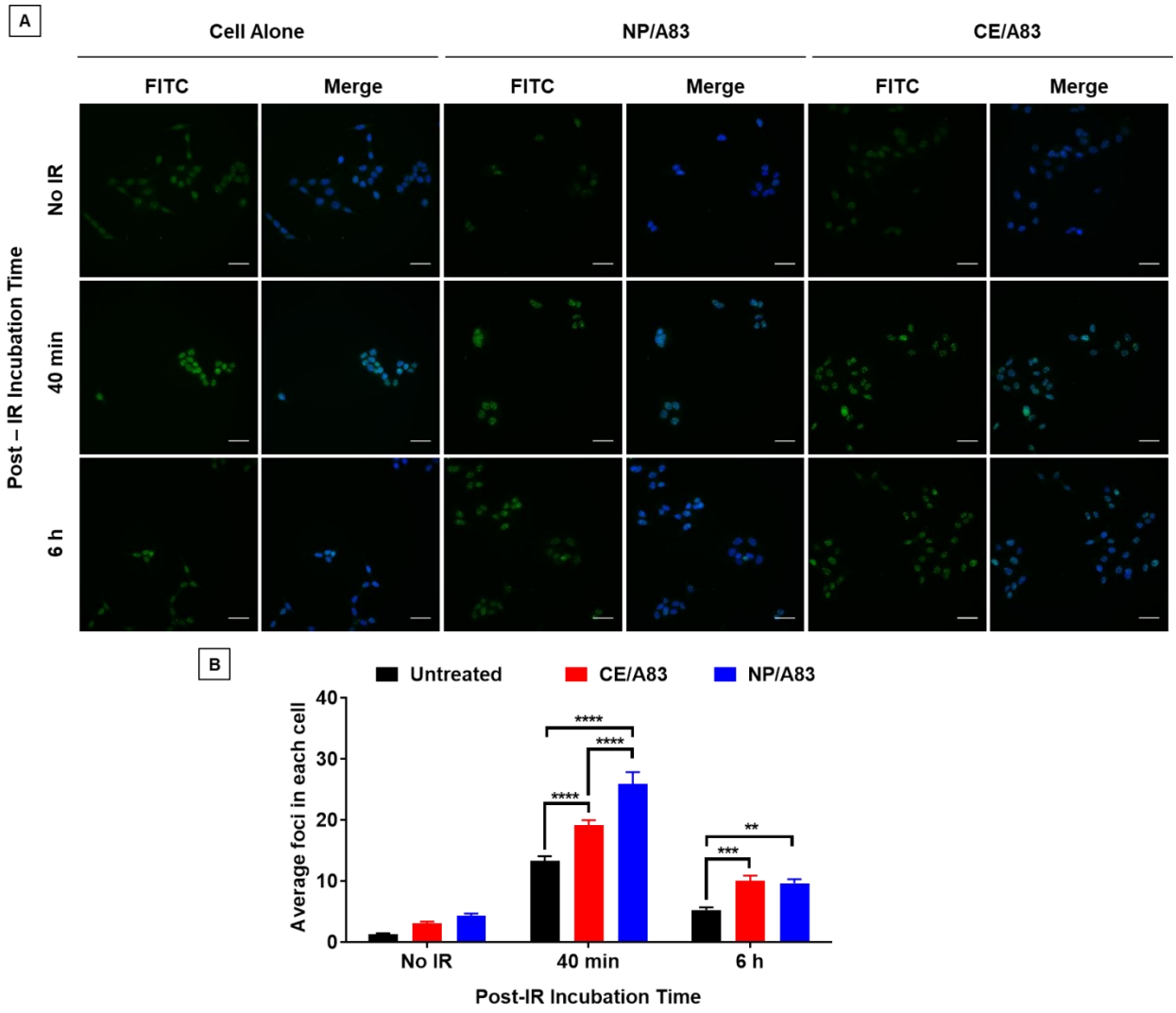

Figure 3.2: Formation and repair of double strand breaks of DNA analyzed by γ-H2AX foci formation (H2A.X Ser139) in HCT116 cells. (A) Representative images of γ-H2AX (green) foci and nuclei (blue) were counterstained with DAPI. (B) Quantitative analysis for the number of foci in each treated cell. 24 h prior to 3 Gy γ-irradiation, cells onto the coverslips were treated with 10 μM CE/A83 and NP/A83. After 40 min and 6 h γ-irradiation, cells were fixed, permeabilized, and stained for foci to be visualized under the microscope. MetaXpress 6 software was used to take images and to quantify the number of foci in each cell. Data from three independent experiments were compared by two ways ANOVA multiple comparison test following Tukey's method. Differences were considered significant if $*p \leq 0.05$, $**p \leq 0.01$, $***p \leq 0.001$, and $****p \leq 0.0001$. Micrographs displayed are representative of at least three independent experiments; scale bar = 40 μm.

3.3.3. Apoptotic activity evaluation

Fig. 3.3 represents the comprehensive apoptotic activity of A83B4C63 with or without γ-irradiation in HCT116 cells. We observed the potential radio-sensitizing activity of the PNKP

inhibitor (either CE/A83 or NP/A83 formulation) with a fixed γ-irradiation dose of 4 Gy, which induced apoptosis in HCT116 CRC cells as confirmed by increase in the levels of cleaved PARP, γ-H2AX, cleaved caspase-7, and cleaved caspase-3 expressions. As shown in **Fig. 3.3A** and **Fig. 3.3B**, both CE/A83 and NP/A83 formulations induced similar expression level of cleaved PARP after 1 h post γ-irradiation. At 4 h post γ-irradiation, the cleaved PARP's expression level was significantly reduced in HCT116 cells that were treated with CE/A83 (****$p \leq 0.0001$). NP/A83-treated cells at 4 h post γ-irradiation showed a reduced expression of cleaved PARP at **$p \leq 0.01$ compared to 1 h time point. At 4 h post γ-irradiation, the expression level of cleaved PARP was significantly higher in cells pretreated with NP/A83 than that of CE/A83. To verify the cleaved PARP induction activity and microscopic observation in the above section, immunoblotting was also performed to investigate the γ-H2AX expression levels in the whole cell lysate after the combination treatments (**Fig. 3.3A** and **Fig. 3.3C**). Similar to what observed for the cleaved PARP levels in cells treated with CE/A83 plus IR, a decreasing trend for γ-H2AX expression was observed over time. In contrast, an increasing trend for γ-H2AX expression was observed in NP/A83-treated HCT116 cells plus γ-irradiation over time. At 4 h post γ-irradiation, the expression of level of γ-H2AX was significantly higher in cells treated with NP/A83 plus IR than that of CE/A83 plus IR and IR alone.

Fig. 3.3D, and **Fig. 3.3E** represent the elevated levels of two major proteins involved in apoptosis, i.e., cleaved caspase-7 and cleaved caspase-3 in the A83B4C63-pretreated HCT116 cells plus γ-irradiation. CE/A83 formulation combined with γ-irradiation at 40 min interval demonstrated significantly higher expression of both cleaved caspase-7 and cleaved caspase-3. This was not the case at longer time intervals between CE/A83 incubation and IR exposure. On the contrary, significantly higher induction levels of cleaved caspase-7 and cleaved caspase-3 were

observed for the 4 h interval between γ-irradiation of HCT116 cells and NP/A83 treatment. Carriers alone without A83B4C63, did not induce radio-sensitization. Notably, neither CE/A83 nor NP/A83 alone (without IR combination) showed any apoptotic activity by means of elevated expression levels of cleaved PARP, γ-H2AX, cleaved caspase-7, and cleaved caspase-3 proteins. No apoptotic activity due to either empty nanocarriers or A83B4C63 nanocarriers without γ-irradiation was observed, confirming the lack of off-target activity by A83B4C63 formulations under experimental conditions.

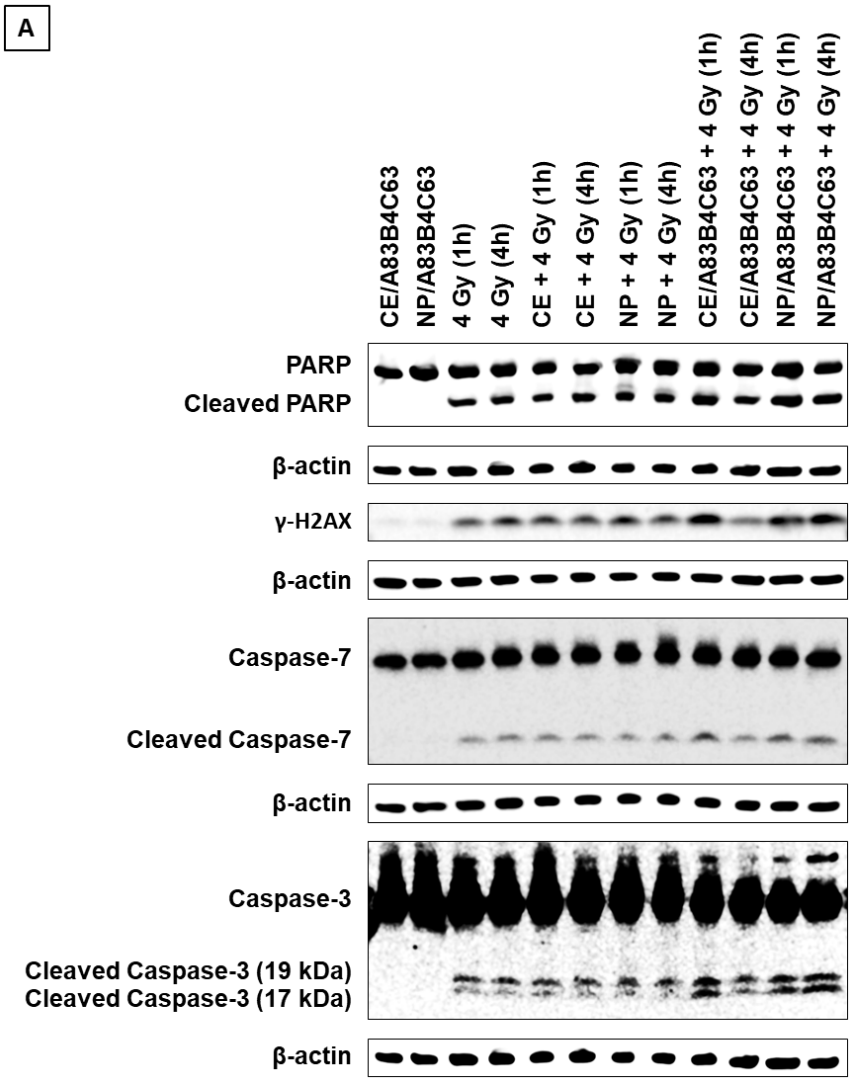

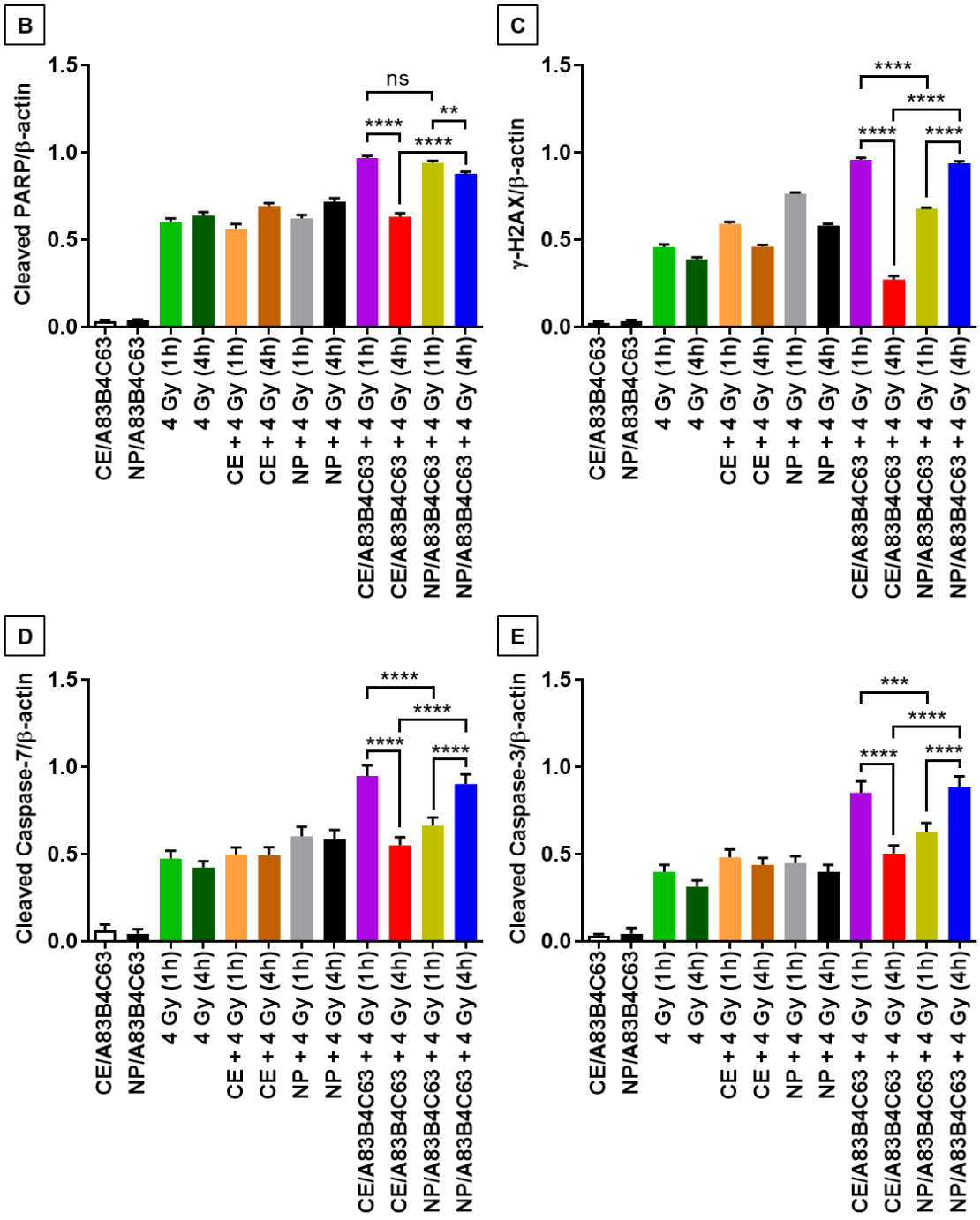

Figure 3.3: (A) Representative western blot detection of cleaved PARP, γ-H2AX, cleaved caspase-7, and cleaved caspase-3 in time-dependent radio-sensitizing HCT116 CRC cell line pretreated with or without PNKP inhibitor (either CE/A83 or NP/A83 formulation). β-actin was used as a loading control. The conditions for all sample preparations and western blots were the same. The statistical analysis for the protein expression levels of (B) cleaved PARP, (C) γ-H2AX, (D) cleaved caspase-7, and (E) cleaved caspase-3 was performed after normalized to β-actin. Differences were considered significant if $*p \leq 0.05$, $**p \leq 0.01$, $***p \leq 0.001$, and $****p \leq 0.0001$ following two-way ANOVA followed by Tukey's method. Data are expressed as mean ± SD (n = 3).

3.3.4. *In vivo* radio-sensitizing activity of CE/A83 and NP/A83 in wild type HCT116 xenografted mice

To explore the radio-sensitizing anticancer activity of intravenously administered CE/A83 and NP/A83 at a dose of 25 mg/kg three times a week in Luc^{+}/HCT116 xenografts mice, all mice were inoculated with the 0.5 million cells 10 days (day -10) before the treatment schedule as shown in **Fig. 3.4A**. According to the experimental design (**Fig. 3.4A**), the tumor-bearing control mice received empty NPs in isotonic 5% dextrose. Mice receiving systemic empty NPs plus IR were also used as control group. To investigate the anticancer activity for this combination treatment approaches, we conducted both digital slide calipers measurement and bioluminescence live imaging to monitor the growth of xenograft tumors in mice.

As shown in **Fig. 3.4B**, the mice receiving empty NP with no IR exhibited rapid CRC tumor growth according to the slide caliper measurement compared to other treatment groups that received IR. Following the similar trend, empty NP plus IR and CE/A83 plus IR receiving mice also showed moderate tumor progress. However, NP/A83 plus IR demonstrated slowest tumor growth compared to other treatment groups. **Fig. 3.4C** represents the average tumor volumes obtained from the treated groups on day 12 since post first IV injection where a significant retardation of growth in the xenografted tumor was observed, only for the NP/A83 plus IR-receiving mice compared to the control.

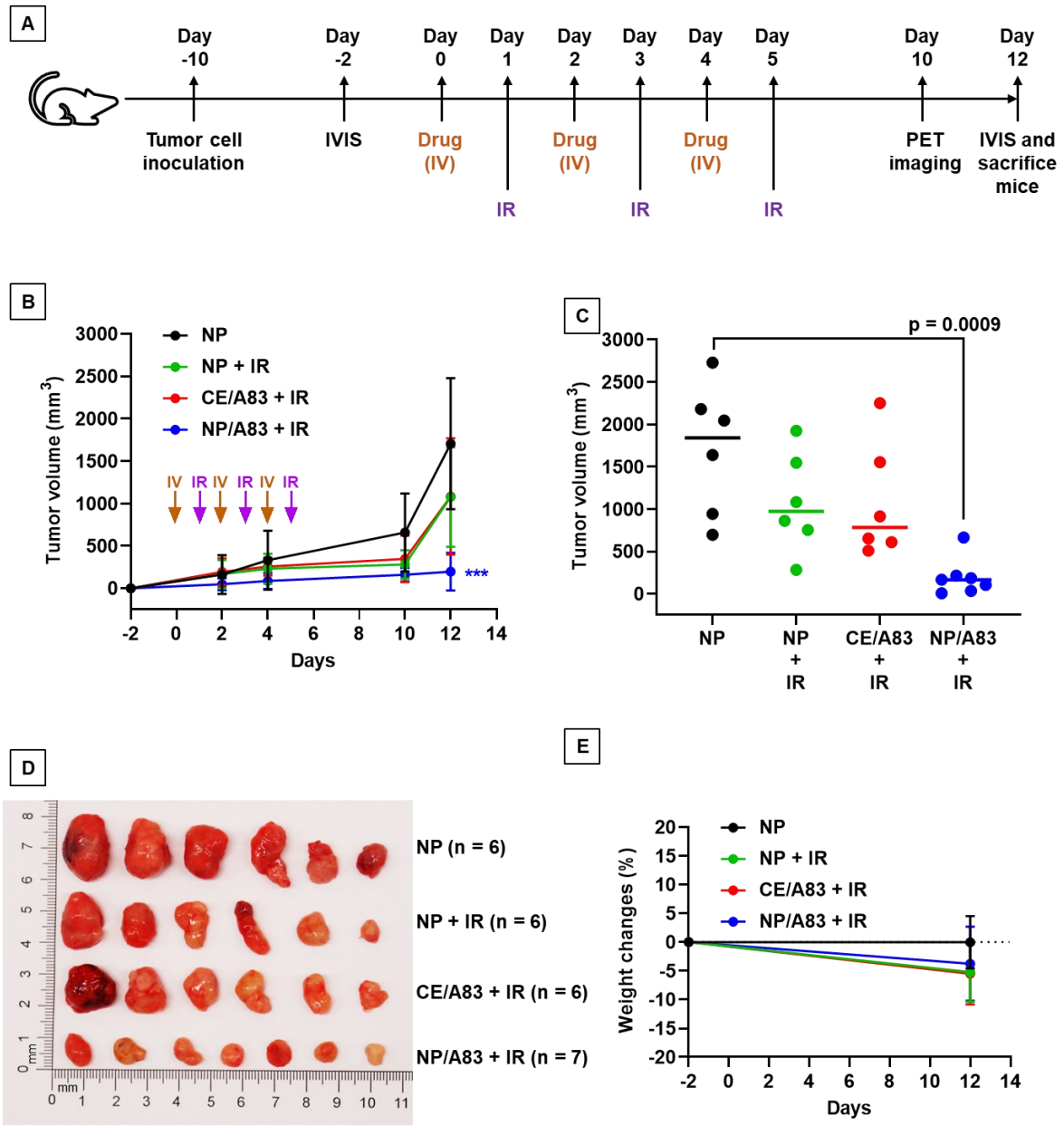

Figure 3.4: (A) Schematic experimental design for evaluating the anticancer activity of A83B4C63 as CE and NP formulations in female NIH-III nude mice following IV administration (n = 6 or 7). Colorectal Luc$^+$/HCT116 cells were inoculated and grown as SC tumor xenografts in the right flank of the mice. When tumors became palpable, total of 25 mice were divided into 4 groups (6 + 6 + 6 + 7), which were intravenously injected with (i) control empty NPs, (ii) control empty NP plus 3 x 5 Gy IR, (iii) CE/A83 (A83B4C63 formulated with the aid of CE) plus 3 x 5 Gy IR, and (iv) NP/A83 (A83B4C63-encapsulated mPEO$_{114}$-*b*-PBCL$_{26}$ micelles) plus 3 x 5 Gy IR three times with a one day interval at a dose of 25 mg/kg. (B) Average tumor volume growth curves for mice in each treatment group for Luc$^+$/HCT116 CRC xenograft. (C) The average tumor volumes obtained from the treated groups on day-12 post injection. Using digital calipers, the length (L) and width (W) of the tumor mass were measured 2 times per week and the tumor volume (TV) was calculated according to the following formula, TV = (L × W2)/2. (D) Images for the representative tumors from (B). (E) The average percentage for the body weights of mice bearing Luc$^+$/HCT116 xenografts. Differences were considered significant if *$p \leq 0.05$.

As shown in **Fig. 3.4D**, the trend of decrease in the average size of the excised tumors from NP/A83-treated mice matched the average tumor volumes obtained from either slide calipers or bioluminescence measurements. At the day of termination (day 12), the average tumor volumes reached 1706.02 ± 773.80, 1076.45 ± 586.78, and 1082.72 ± 685.81 mm^3 (n = 6), in the mice treated with empty NP, empty NP plus IR, and CE/A83 plus IR, respectively, whereas the tumor volumes remained as low as 196.56 ± 221.01 mm^3 (n = 7) in mice treated with IV NP/A83 plus IR. The overall results clearly showed the *in vivo* radio-sensitizing activity of A83B4C63 in its NP formulation in wild type Luc^+/HCT116 CRC xenografts in mice, which was in contrast to no activity for CE formulation of this PNKP inhibitor compared to control groups receiving empty NPs with or without IR ($p > 0.05$). **Fig. 3.4D** also shows the images of the excised tumors from the xenograft mice of all treatment groups at the termination day. These data verified the results of tumor growth measurement by the digital slide calipers and IVIS imaging. The measured mean body weight variation of the mice receiving systemic treatments were within 20% margin (**Fig. 3.4E**) and did not show any statistical difference irrespective of the treatment groups.

To further evaluate the *in vivo* radio-sensitizing anticancer activity of A83B4C63, tumor growth in mice was also detected by bioluminescence live IVIS imaging in animals. Based on the average radiance for bioluminescence of Luc^+/HCT116 cells in mice (**Fig. 3.5A**), NP/A83 pretreatment with fractionated IR dose of 3 x 5 Gy was found to retard the tumor growth significantly when compared to the other treatment groups. At day 12 (**Fig. 3.5B**), the quantitative analysis exhibited a significant difference in average radiance in the NP/A83-pretreated group (*$p \leq 0.05$, two-way ANOVA) in comparison to that of other pretreatment groups including the empty NP, empty NP plus IR, and CE/A83 plus IR. Therefore, the radiance for bioluminescence of Luc^+/HCT116 xenografts in the respective treatment groups of mice showed a similar pattern in

tumor growth to that observed by slide calipers measurements. When comparison was made between the day -2 (2 days prior to starting treatments) and day 12 (termination day), significant differences indicating tumor growth was determined for all treatment groups except NP/A83-treated mice that did not show any difference in the luminescence of xenografts from day -2 to day 12. The data validated the anti-tumoral activity of systemic NP/A83 administration in the HCT116 CRC xenograft model as a novel radio-sensitizing nanomedicine.

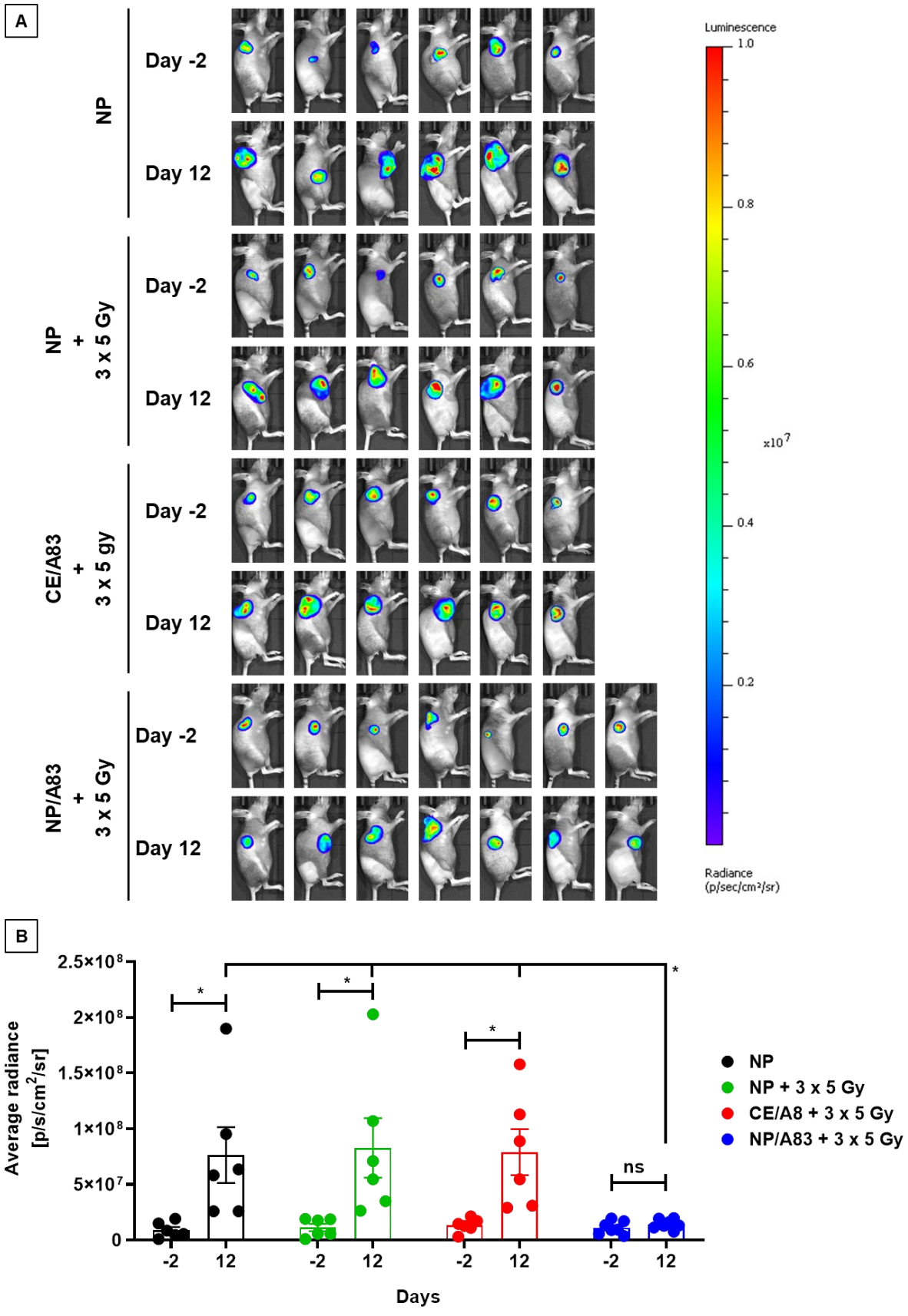
A
NP
Day -2
Day 12
NP
+
3 x 5 Gy
Day -2
Day 12
CE/A83
+
3 x 5 gy
Day -2
Day 12
NP/A83
+
3 x 5 Gy
Day -2
Day 12
Luminescence
1.0
0.8
0.6
x10^7
0.4
0.2
Radiance
(p/sec/cm²/sr)
B
Average radiance
[p/s/cm²/sr]
2.5×10^8
2×10^8
1.5×10^8
1×10^8
5×10^7
0
*
*
*
*
ns
-2
12
-2
12
-2
12
-2
12
Days
NP
NP + 3 x 5 Gy
CE/A8 + 3 x 5 Gy
NP/A83 + 3 x 5 Gy

Figure 3.5: (A) Representative bioluminescence images from the tumor-bearing mice on days-2 and -12 for evaluating the radio-sensitizing anticancer activity of A83B4C63 as CE and NP formulations in female NIH-III nude mice following IV administration (n = 6 or 7). 0.5×10^6 colorectal Luc^+/HCT116 cells were inoculated and grown as SC tumor xenografts in the right flank of the female athymic NIH-III nude mice. When tumors became palpable, total of 25 mice were randomly assigned into 4 groups (6 + 6 + 6 + 7), which were intravenously injected with (i) control empty NPs, (ii) control empty NP plus 3 x 5 Gy IR, (iii) CE/A83 (A83B4C63 formulated with the aid of CE) plus 3 x 5 Gy IR, and (iv) NP/A83 (A83B4C63-encapsulated $mPEO_{114}$-*b*-$PBCL_{26}$ micelles) plus 3 x 5 Gy IR three times with a one day interval at a dose of 25 mg/kg. The mice were imaged for luciferase intensity 2 days before the treatment started. Radiation therapy was given using image-guided SARRP platform. (B) Quantitative analysis for the average radiance (photons per s per cm^2 per square) bioluminescence signal for the four treatment groups of mice on day -2 (2 days prior to start treatment) and day 12 (termination day). Differences were considered significant if $*p \leq 0.05$.

3.3.5. [^{18}F]FLT tracer uptake in HCT116 CRC xenograft mice

Fig. 3.6A shows the non-invasive PET imaging of [^{18}F]FLT-uptake as a surrogate proliferation or *in vivo* pharmacodynamic biomarker in highly multiplying cancer cells in HCT116 xenograft mice to determine the radio-sensitizing activity of A83B4C63 formulations in the xenograft tumors. In line with the results of caliper and bioluminescence measurements, administration of NP/A83 at 25 mg/kg dose plus IR, led to a significant reduction of thymidine uptake in HCT116 xenografts in mice. This contrasted with CE/A83 plus IR that did not show any significant reduction of thymidine uptake when compared to the control receiving empty NPs plus IR. The [^{18}F]FLT-PET imaging, 7 days after last treatment, showed standardized uptake (SUV_{mean}) values of 1.35 ± 0.12, 1.18 ± 0.18, 1.03 ± 0.17, and 0.62 ± 0.09, for empty NP, empty NP plus IR, CE/A83 plus IR , and NP/A83 plus IR , respectively. When compared for significant differences as shown in **Fig. 3.6B**, NP/A83 plus 3 x 5 Gy IR-treated mice group resulted in significantly lower SUV_{mean} value than that of empty NP without IR at α level of 0.001. The difference in SUV_{mean} value for mice that received NP/A83 plus IR was significantly lower than the mice that received empty NPs or CE/A83 plus IR ($*p < 0.05$). However, no significant differences were observed between the NP/A83 plus IR and CE/A83 plus IR treatment groups.

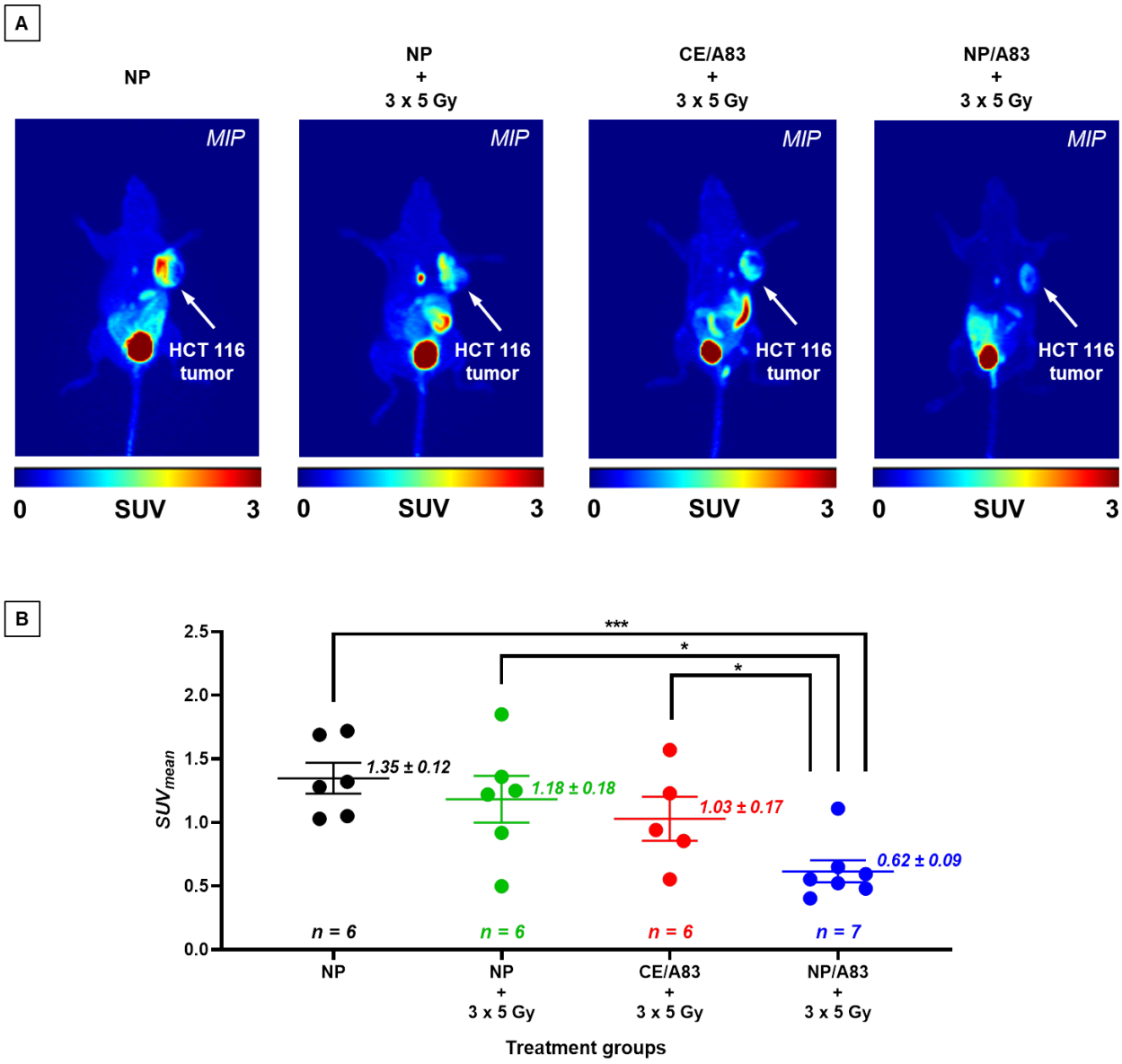

Figure 3.6: (A) Typical [^{18}F]FLT-PET images of female athymic NIH-III nude mice (one representative image of mouse from each treatment group) post treatment with empty NP, CE/A83, and NP/A83 with a fractionated 3 x 5 Gy dose of radiation under isoflurane anesthesia. The control mice received empty NP without radiation. The white arrows indicate the xenograft CRC tumors and color scale represents the SUV_{mean} value. (B) The quantitative analysis for the obtained SUV_{mean} values to determine the [18F]FLT uptake of corresponding CRC tumor xenografts in mice post treatments. Differences were considered significant if $*p \leq 0.05$, $**p \leq 0.01$, and $***p \leq 0.001$ following two-way ANOVA followed by Tukey's method. Data are shown as mean ± SD from n experiments.

3.3.6. Biodistribution profile of CE and NP formulations of A83B4C63

Fig. 3.7 and **Table 3.1** represent the plasma or tissue concentration versus times profile, as well as tissue to plasma ratio of A83B4C63 formulations and their AUC following IV administration of the above formulations at a dose of 25 mg/kg three times in wild type HCT116 bearing mice (**Fig. 3.7A**). As shown in **Fig. 3.7B**, the concentration of A83B4C63 administered by CE/A83 formulation fell below the limit of quantification after 24 h while NP/A83 formulation yielded significantly higher plasma drug concentrations (****$p \leq 0.0001$) between the boundary of quantification levels up to 48 h. The concentration of A83B4C63 administered by NP/A83 formulation was significantly higher at 24 h (*$p \leq 0.05$) and 48 h (****$p \leq 0.0001$) when compared with that of CE/A83. This resulted in a significantly higher plasma AUC level for the mice that received NP/A83 (34246.64 ± 3710.36) treatment to those that received CE/A83 (21078.86 ± 1534.31) (*$p \leq 0.05$, student's t-test).

Biodistribution data (**Table 3.1)** showed significantly higher AUC values for NP/A83 than the CE/A83 in tumor (*$p \leq 0.5$, student's t-test). However, no significant differences were observed between these treatment groups in respect to the organs including lung, heart, and spleen.

A83B4C63 concentrations in excised tumors from the mice were also measured and the results are shown in **Fig. 3.7C**. The results showed tumor accumulation of A83B4C63 delivered by NP/A83 formulation at 48 h post injection. Whereas the detected concentrations of A83B4C63 in CE/A83-treated xenografts were below the limit of detection at this time point. Calculation of tumor to plasma concentration ratio for the two formulations showed a significant increase for at 48 h for the NP formulation, as well.

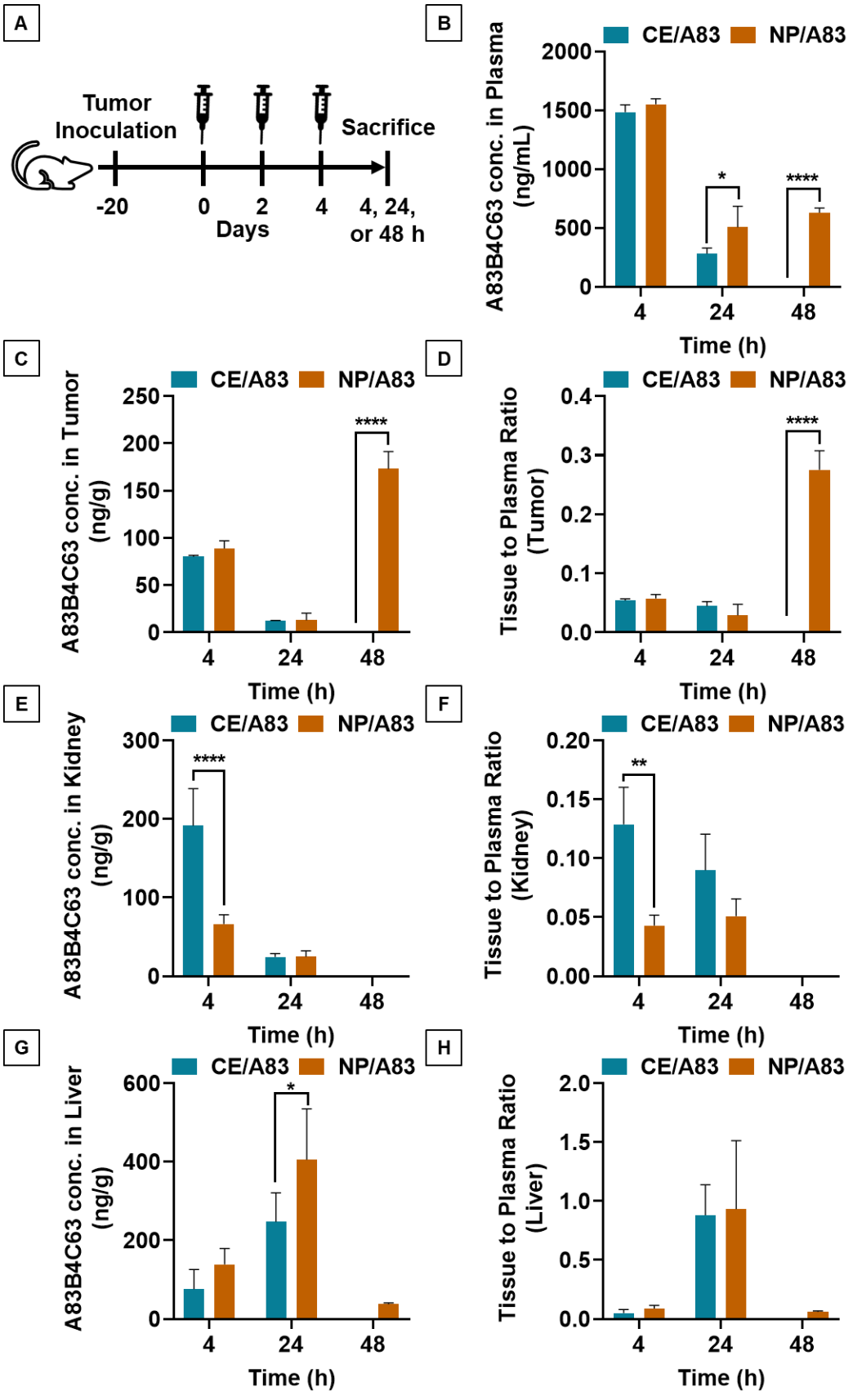
A
Tumor Inoculation
Sacrifice
-20
0
2
4
4, 24, or 48 h
Days
B
CE/A83
NP/A83
A83B4C63 conc. in Plasma (ng/mL)
2000
1500
1000
500
0
*
****
4
24
48
Time (h)
C
A83B4C63 conc. in Tumor (ng/g)
250
200
150
100
50
0
****
D
Tissue to Plasma Ratio (Tumor)
0.4
0.3
0.2
0.1
0.0
E
A83B4C63 conc. in Kidney (ng/g)
300
200
100
F
Tissue to Plasma Ratio (Kidney)
0.20
0.15
0.10
0.05
0.00
**
G
A83B4C63 conc. in Liver (ng/g)
600
400
200
H
Tissue to Plasma Ratio (Liver)
2.0
1.5
1.0
0.5

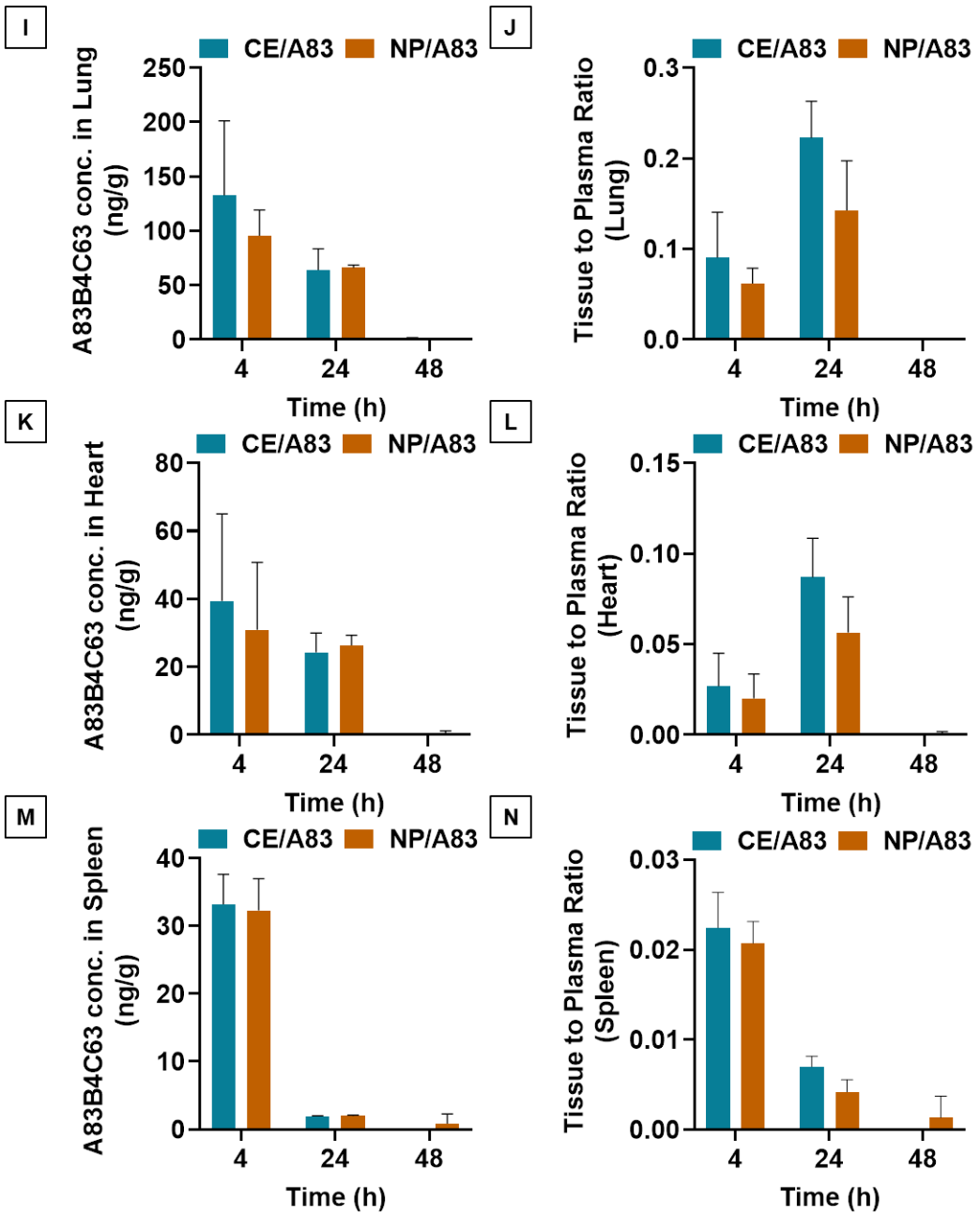
I
A83B4C63 conc. in Lung (ng/g)
CE/A83
NP/A83
250
200
150
100
50
0
4
24
48
Time (h)
J
Tissue to Plasma Ratio (Lung)
CE/A83
NP/A83
0.3
0.2
0.1
0.0
4
24
48
Time (h)
K
A83B4C63 conc. in Heart (ng/g)
CE/A83
NP/A83
80
60
40
20
0
4
24
48
Time (h)
L
Tissue to Plasma Ratio (Heart)
CE/A83
NP/A83
0.15
0.10
0.05
0.00
4
24
48
Time (h)
M
A83B4C63 conc. in Spleen (ng/g)
CE/A83
NP/A83
40
30
20
10
0
4
24
48
Time (h)
N
Tissue to Plasma Ratio (Spleen)
CE/A83
NP/A83
0.03
0.02
0.01
0.00
4
24
48
Time (h)

Figure 3.7: (A) The experimental schedule for determining bio-fate of A83B4C63 intravenously delivered via CE and NP formulations in CRC tumor-bearing mice. (B-N) The biodistribution profile of A83B4C63 in wild-type HCT116 CRC xenograft bearing NIH-III female nude mice (n = 3) 4, 24, and 48 h after tail vein administration of CE/A83 and NP/A83 formulations. Mice were inoculated with HCT116 CRC cells. 21 days following tumor cell inoculation, the mice received CE/A83 and NP/A83 formulations intravenously at a dose of 25 mg/kg three times with one day interval. The control mice received empty NPs, equivalent to the amounts used in the test groups. 4, 24, and 48 h after the last IV injection, all mice were euthanized to collect blood plasma by cardiac puncture. Then, tumors and other organs including kidney, liver, lung, hear, spleen were collected, snap frozen in liquid nitrogen, and stored in -80°C freezer for later use. Drug concentration was quantified using LC/MS/MS (mean ± SD). (B) A83B4C63 plasma concentration versus time curves of CE/A83 and NP/A83 formulations in HCT116 xenograft tumor-bearing mice. (C, E, G, I, K, and M) represent A83B4C63 concentrations obtained from the excised tumor, kidney, liver, lung, hear, and spleen, respectively, after administration of CE/A8 and NP/A83 in xenograft mice. (D, F, H, J, L, and N) represents the ratio of tissues (tumor, kidney, liver, lung, hear, and spleen, respectively) to plasma concentration of CE/A83 and NP/A83-treated xenograft mice. Differences were considered significant if $*p \leq 0.05$, $**p \leq 0.01$, $***p \leq 0.001$, and $****p \leq 0.0001$ following two-way ANOVA followed by Tukey's test. However, the significance of differences was only illustrated between the treatment groups at each time point.

Notably, CE/A83 formulation resulted in significantly higher accumulation of A83B4C63 in kidney at 4 h post dose time point compared to that of NP/A83 ($****p \leq 0.0001$) (**Fig. 3.7E**). Similarly, the kidney to plasma ratio (Kp value) yielded a significantly higher ratios for A83B4C63 in the kidney of mice treated with CE/A83 ($**p \leq 0.01$) compared to that of NP/A83-treated mice. In contrast, the obtained A83B4C63 concentration was significantly higher in the liver samples of NP/A83-treated mice than that of CE/A83-treated mice at 24 h ($*p \leq 0.05$) post dose, only. However, no significant difference was observed in liver to plasma ratio between CE/A83 and NP/A83 treatment groups.

Table 3.1: Calculated area under the curve (AUC) for plasma concentrations of CE/A83 and NP/A83 formulations in HCT116 tumor-bearing mice until 48 h time point post drug administration. Significant differences between CE/A83 and NP/A83 were distinguished at p value of 0.05 (n = 3) according to student's t-test.

Specimens	**Formulations**	**AUC ± SEM (ng.h/mL or g)**
Plasma	CE/A83	21078.86 ± 1534.31
	NP/A83	34246.64 ± 3710.36*
Tumor	CE/A83	1071.11 ± 21.00
	NP/A83	3254.89 ± 259.94*
Kidney	CE/A83	2455.59 ± 374.71*
	NP/A83	1211.89 ± 177.67
Liver	CE/A83	6198.00 ± 2032.99
	NP/A83	10773.38 ± 3161.52*
Lung	CE/A83	2740.85 ± 695.96
	NP/A83	2409.93 ± 249.46
Heart	CE/A83	931.07 ± 188.99
	NP/A83	894.02 ± 161.52
Spleen	CE/A83	374.87 ± 45.43
	NP/A83	376.25 ± 49.65

3.4. Discussion

Human PNKP phosphorylates DNA 5′-termini and dephosphorylates DNA 3′-termini, therefore allowing DNA ligases to rejoin the strands and plays a key role in both single- and double-strand breaks repair [119]. PNKP has been identified as a potential therapeutic target in different types of cancer, as depletion of PNKP in cancer cells or tumor xenografts has shown a synthetic lethal partnership with the loss of a tumor suppressor protein, i.e., PTEN [267, 317]. Moreover, the downregulation of PNKP by siRNA or its inhibition by small molecule inhibitors have shown to make cancer cells sensitive to IR and topoisomerase I inhibitors [118, 127, 202, 203, 267].

We have identified new small molecule inhibitors of PNKP. Initial attention was on the DNA 3′-phosphatase activity of PNKP, with a polysubstituted imidopiperidine, A12B4C3, identified as the first hit [202, 203]. At a non-cytotoxic dose, A12B4C3, effectively sensitized human lung cancer A549 cells to IR and camptothecin. However, it failed to further sensitize the cancer cells that were already depleted of PNKP by shRNA, providing strong evidence for PNKP as the druggable target of A12B4C3 [127]. The Reilly group showed that A12B4C3 sensitizes human myeloid leukemia cells to radio-immunotherapy providing more evidence for the promise of PNKP inhibitors as radio-sensitizers [323].

PNKP inhibitors render tumors more susceptible to DNA damage by IR or topoisomerase I inhibitors but may act similarly on normal cells leading to intolerable toxicities in patients. To overcome the problem of non-specificity for cancer and at the same time, to enhance the solubility of PNKP inhibitors for *in vivo* administration, we have developed NP formulations of a second generation polysubstituted imidopiperidine, named as A83B4C63. Nanocarriers can significantly improve therapeutic index of anticancer agents [311, 312]. Nanocarriers are small enough to enter

leaky blood vessels in solid tumors, but not normal blood vessels [324]. Lymphatic function in tumors is impaired, thus nanocarriers are not drained effectively and accumulate in the tumor [325-327]. They have capacity to deliver higher quantities of drugs to targets and can be actively targeted to tumor cells [316]. Nanocarriers of conventional anticancer agents (e.g., doxorubicin, paclitaxel, and irinotecan) have already found their way into clinic [328, 329].

At a concentration range of 1-10 μM, both free and encapsulated A83B4C63 in PEO-*b*-PBCL NPs were effective in reducing the viability of $PTEN^{-/-}$ HCT116 cells but did not affect the wild-type (WT) or HCT116/ $PTEN^{+/+}$ cell viabilities [267, 317]. Our previous study has also shown the success of PEO-*b*-PBCL NP formulations of A83B4C63 as monotherapeutic in the inhibition of tumor growth only in PTEN-deficient HCT116 tumor xenografts, due to synthetic lethality in this cancer model [317]. This contrasted with the CE formulations of this drug candidate that did not show any anticancer activity, in HCT116/$PTEN^{-/-}$ tumor xenografts, when compared to control mice receiving 5% dextrose. The current study, focused on *in vitro* and *in vivo* evaluation of NP versus CE formulations of A83B4C63 in sensitization of HCT116/ $PTEN^{+/+}$ tumors to IR. Radiation therapy is commonly used to treat rectal cancer [216, 330]. In colon cancer, radiation therapy, is mostly used as a neoadjuvant therapy before surgery or as an adjuvant therapy after or during surgery to make sure all cancerous cells are removed [217-219]. Radiation therapy is also used in metastatic CRC, where cancer is spread to liver, or lung [310].

The NP/A83 formulation was successfully reproduced and showed an average particle size of < 60 nm with low PDI, which was consistent with our previous reports [267, 331]. The NP/A83 formulation enhanced the solubilized levels of A83B4C63 in water to a level over 6.5 mg/mL, enabling administration of the compound to mice at desired therapeutic doses [292]. Comparisons were made with a conventional CE-based solubilizing formulation of A83B4C63. CE is well-

known water-soluble nanocarrier for cyclosporin A, paclitaxel [332-334]. However, CE is associated with acute or chronic side-effects (e.g. anaphylaxis, nephro- and neurotoxicity) [268, 269] and is also known to interfere with the pharmacokinetics of several drugs [270-276].

In vitro studies on HCT116 cells revealed the activity of A83B4C63 either as CE or NP formulation in enhancing DNA damage by IR. This was evidenced through the measurement of γ-H2AX foci formation, which showed an increase in foci numbers upon co-treatment of cells with IR plus both A83B4C63 formulations compared to the IR treatment alone (**Fig. 3.2**). The A83B4C63 formulations on their own, without IR, did not show any significant rise to the level of γ-H2AX foci at the dose applied here, reflecting the lack of DNA damage by the A83B4C63 alone. The NP formulation showed a significant increase in the level of induced γ-H2AX foci formation only at 40 min after the radiation and not at the longer time points, when compared to the CE formulation. The reason for this observation is not clear but may reflect better access of NP-encapsulated A83B4C63 to intracellular PNKP at early incubation times in the cells compared to the one solubilized with the aid of CE.

Similar to the microscopy results, assessment of γ-H2AX expression by western blot did not show any effect on DNA damage for the A83B4C63 formulations on their own (**Fig. 3.3B**). When A83B4C63 formulations were combined with IR, DNA breaks as reflected by the expression of γ-H2AX significantly enhanced compared to the IR therapy alone. Analysis of the blots on the expression of cleaved PARP, cleaved Caspase 3 and 7, followed a similar trend to what observed on the γ-H2AX expression, confirming the activation of apoptotic mediators following enhanced DNA damage by co-treatment of A83B4C63 formulation with IR, compared to IR alone. While the effect of CE formulation decreased overtime, the effect of NP formulation was enhanced overtime. This led to a significant increase in radio-sensitizing activity of NP/A83

over CE/A83 at 4 h time point. Like the γ-H2AX expression, use of NP/A83 over CE/A83 led to an increase in the expression of cleaved PARP, cleaved Caspase 3 and 7 at the longer time points followed by the IR exposure.

For the *in vivo* studies, a relatively low fractionated dose (3 x 5 Gy) of IR was used to avoid potential side-effects on normal tissues surrounding the irradiated site [335]. The treatment groups were shown to be safe and well-tolerated as there was no evident for any toxicity symptoms and weight reduction in mice during and after the treatments. The wild type HCT116 xenografts showed significant retardation of tumor growth only when NP/A83 treatment was combined with the fractionated dose of IR using SARRP facility (**Fig. 3.4**). This observation was like our findings on the anticancer effect of A83B4C63 as synthetic lethal monotherapeutics in PTEN-deficient HCT116 xenografts, in which only NP/A83 and not CE/A83 was shown to be effective anticancer agent. The activity of NP/A83 as radio-sensitizer was confirmed through the measurement of tumor proliferation in three separate ways: tumor volume measurements using slide caliper (**Fig. 3.4**), IVIS imaging of LUC^+ tumors (**Fig. 3.5**) and PET imaging using [^{18}F]FLT (**Fig. 3.6**) as the anti-proliferative marker in live animals. It is reported that FLT-PET is predominant over FDG-PET in predicting early response to anti-cancer treatment efficacy [336]. Collectively, these data validated the intravenously administered NP/A83 as more effective radio-sensitizer than CE/A83 in CRC xenografts in mice. The data showed the failure of CE/A83 formulation in radio-sensitizing activity, *in vivo*, despite the effectiveness of this formulation in enhancing γ-H2AX as well as cleaved PARP, cleaved Caspase 3 and 7 expressions, *in vitro*.

To shed some light on the reason behind the superior activity of NP/A83 over CE/A83 i*n vivo*, we investigated the biodistribution profile of A83B4C63 in wild type HCT116 CRC tumor bearing mice following a similar administration schedule as used in the anticancer activity study.

A83B4C63 is a new investigational drug and the effect of CE on its pharmacokinetic profile is not known. Our data on the biodistribution of NP/A83 versus CE/A83 formulations at 4, 24, and 48 h post last injection, revealed an interesting pattern (**Fig. 3.7**). In plasma, the following administration of CE formulation, A83B4C63 was eliminated rapidly, and no detectable drug levels were identified at 48 h time point. The NP/A83, on the other hand, enhanced the resident time of A83B4C63 in plasma. This profile coincided with a delayed accumulation of A83B4C63 in tumor 48 h following the last dose. Accordingly, a significant enhancement in the AUC, C_{max}, and MRT of A83B4C63 in tumor for the NP over CE formulation was achieved. This pattern contrasted with the distribution profile of NP versus CE formulations of A83B4C63 in normal tissues, where a decline in drug levels for both formulations were seen from 24 to 48 h. Among the normal tissues, liver was the only organ that showed significantly higher AUC for the NP formulation of A83B4C63. Interestingly the MRT of A83B4C63 was not affected by its formulation in this organ. On the other hand, the AUC of NP formulations of A83B4C63 showed reduction in kidneys compared to the CE formulation. The reason for delayed accumulation of A83B4C63 by its NP formulation in wild type HCT116 xenografts is not clear and needs further investigation. Nevertheless, a sustained inhibition of PNKP resulted from higher accumulation of its nano-formulation in tumor xenografts along with continuous release of the drug in the tumor site might have attributed to the higher activity of NP/A83 over CE/A83, *in vivo*. The delayed distribution of NP/A83 in tumor may provide opportunities for the optimization of intervals between chemo or radiation co-treatments with NP/A83, which will be explored in future.

3.5. Conclusion

In summary, our data demonstrated that the PEO-PBCL nanocarriers of a A83B4C63 to be effective radio-sensitizing agents in CRC models, both *in vitro* and *in vivo*. The presented data provides a strong case for potential benefit of nanotechnology in the formulation of drug candidates for clinical development during the drug development process.

3.8. Acknowledgments

We thank Dr. Mary Hitt in Faculty of Medicine and Dentistry (University of Alberta) for their advice and technical assistance. We also thank Hao Fu for support in the HPLC analysis and purification of compound A83B4C63. This work was supported by grants funded by the Canadian Institutes of Health Research (MOP 15385) to M.W. and (MOP 159757) to A.L., the Alberta Cancer Foundation Transformative Program Project (26603) to D.H., F.J., A.L., and M.W. Funding from Nanomedicine Innovation Network (NMIN) grant (2019-T1-06) to D.H., M.W. and A.L. is also acknowledged. Sams M.A. Sadat acknowledges funding from Alberta Innovates and CIHR Fellowships.

3.9. Declaration

The authors declare the following competing financial interest(s): Material in this manuscript has been included in recent US patent applications. Dr. Lavasanifar is Vice-President of Meros Polymers which has the license to mPEO-*b*-PBCL polymer used in this manuscript.

Chapter 4: Development of self-associating SN-38-conjugated poly(ethylene oxide)-poly(ester) micelles for colorectal cancer therapy

4.1. Introduction

Cancer-related mortality has increased by ~40% over the past 40 years and is anticipated to show a further 60% increase by 2030 [337]. Among all cancerous diseases, colorectal cancer (CRC) is the second most fatal cancer worldwide. Approximately, 1.8 million new CRC cases occurred and 881,000 deaths were reported in 2018 [338]. For CRC patients with localized disease, surgery is a curative option. However, despite improved screening practices, CRC is commonly diagnosed at advanced stages where metastasis to nearby or distant organs is seen. In CRC patients with metastatic disease, the curative benefit of first-line surgical interventions is limited. Patients with *de novo* metastatic disease or those showing relapse and advancement to metastatic stage after the first round of therapy, make up over 60% of CRC patients [339]. Chemotherapy and radiotherapy are the leading treatment strategies in these patients and are usually used either to control unresectable tumor growth and its further spread; or reduce the size of locally metastasized cancer making the patient a candidate for surgery and tumor removal at the metastatic site [340].

Irinotecan is a water soluble prodrug of SN-38 and a DNA topoisomerase I (Topo-I) inhibitor approved by the FDA for treating CRC [341]. After enzymatic activation in liver and cancer cells, <10% of irinotecan is converted to its biologically active metabolite; i.e., 7-ethyl-10-hydroxy-camptothecin (SN-38), which is 100-1000 times more potent than irinotecan [342]. To achieve the therapeutic effect, a much higher dose of irinotecan is required. Moreover, the conversion of irinotecan to SN-38 depends on the genetic polymorphism or inter-individual variability of carboxylesterase activity [343, 344]. The administration of high irinotecan doses in CRC patients is also associated with observavtion of severe side effects such as diarrhea, myelosuppression, acute cholinergic-like syndrome and neutropenia [345].

The direct clinical use of SN-38 exhibits an appealing alternative to avoid the dose-limiting side-effects of irinotecan and overcome its less than optimal potency. However, the clinical use of SN-38 is limited by its inherent poor water-solubility and biological inactivation through the glucuronidation pathway [346]. To solve these problems, a number of approaches have been explored, among which, the nanoparticle-based delivery of SN-38 has gained the most attention due to the additional advantage in passive targeting of solid tumors by NPs [251, 255-258]. Among different NPs tried for delivery of SN-38, supramolecular polymeric micellar structures stand out [347]. This is due to the potential of polymeric micellar structures to solubilize SN-38 and protect it within their hydrophobic core from the destabilizing effect of the biological milieu leading to its enhanced biological stability while preserving SN-38 toxicity against cancer cells [256].

The main objective of the present work was to develop a polymeric micellar formulation of SN-38 in biodegradable nanocarriers based on poly(ethylene oxide)-poly(ester) block copolymers. For this purpose, conjugation of SN-38 to pendant carboxyl functional groups on methoxy-poly(ethylene oxide)-block-poly(α-carboxyl-ε-caprolactone) (mPEO-*b*-PCCL) or end functional groups on methoxy-poly(ethylene oxide)-block-poly(α-benzyl carboxylate-ε-caprolactone) (mPEO-*b*-PBCL) was pursued (**Fig. 4.1**). This strategy was expected to enhance the solubilized levels of SN-38 in aqueous media. The results of comparative studies on physicochemical properties, kinetic and thermodynamic stability as well as *in vitro* cytotoxicity and hemolytic activity of the two generated polymeric micellar formulations, i.e., mPEO-*b*-PCCL/SN-38 and mPEO-*b*-PBCL/SN-38, are presented here.

Similar strategies have been reported before by the conjugation of SN-38 through its free hydroxyl group to other carriers [348-351]. An SN-38 conjugated to micelle-forming PEO-poly(glutamic acid) formulation, known as NK012, has completed phase II clinical trials in triple-

negative breast cancer and relapsed small cell lung cancer [352, 353]. The SN-38 polymeric micellar drug conjugates that are the subject of current study, may prove to be beneficial compared to NK012, due to the more hydrophobic nature of their core-forming block compared to poly(glutamic acid), leading to improved stability. The proved biodegradability of the poly(ester) core, may be considered as an additional potential advantage over poly(amino acid) structures.

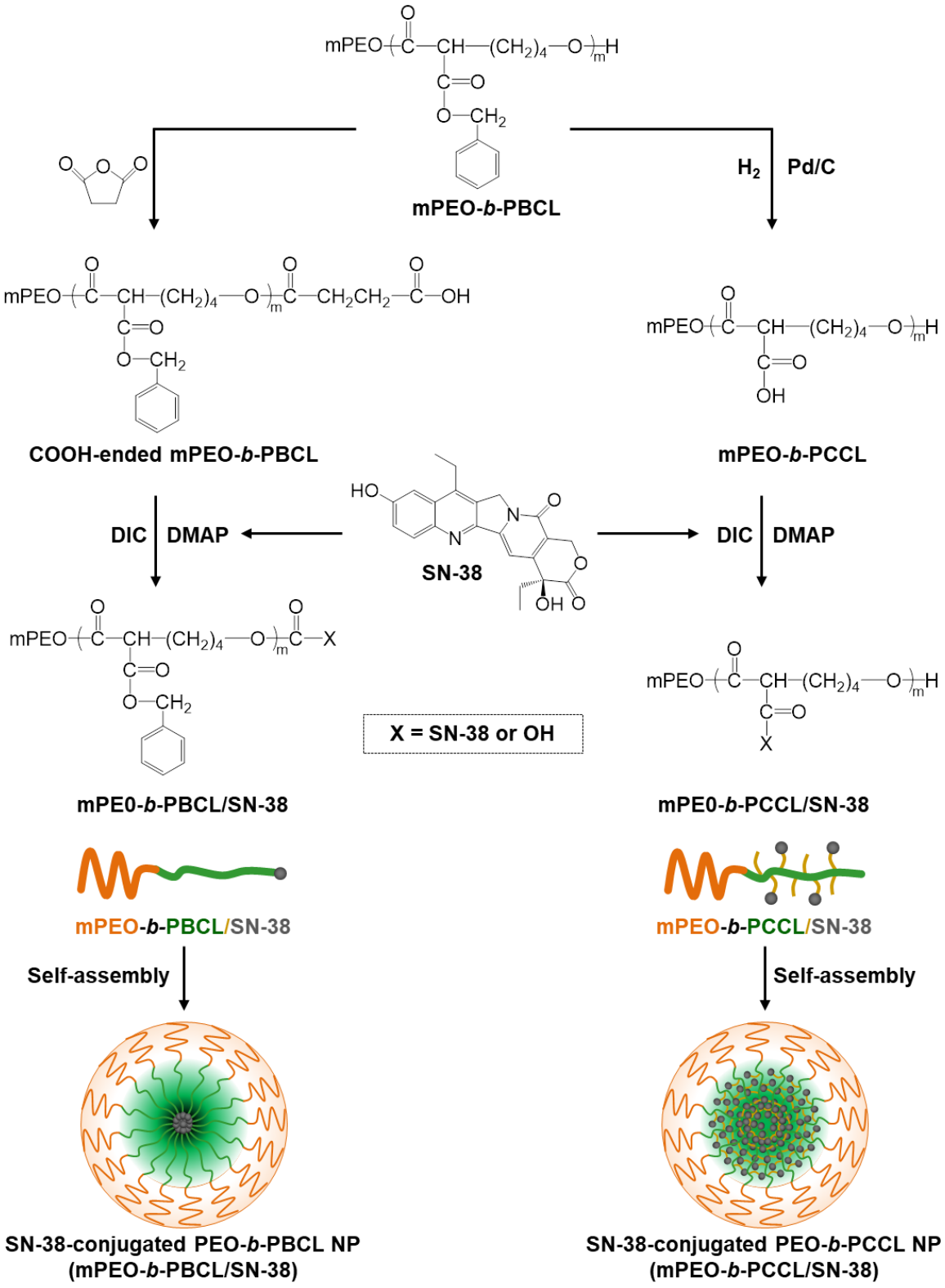

Figure 4.1: Chemical structures of SN-38, mPEO-*b*-PBCL, mPEO-*b*-PCCL, and schematic procedures to synthesize mPEO-*b*-PBCL/SN-38 and mPEO-*b*-PCCL/SN-38 forming self-assembled micelles.

4.2. Materials and methods

4.2.1. Materials

Methoxy-polyethylene oxide (mPEO) (average molecular weight of 5000 $gmol^{-1}$), sodium dodecyl sulfate (SDS), palladium on charcoal, and bovine serum albumin (BSA) and all research grade organic solvents were purchased from Sigma (St. Louis, MO, USA). α-Benzyl carboxylate-ε-caprolactone monomer was synthesized by Alberta Research Chemicals Inc. (Edmonton, AB, Canada). Stannous octoate was purchased from Sigma-Aldrich, purified and dehydrated by toluene azeotropic distillation followed by vacuum distillation. (S)-4, 11-Diethyl-4, 9-di-OH-1, 12-dihydro-4H-2-oxa-6,12a-diaza-dibenzo[b, h]fluorene-3,13-dione (SN-38) (purity > 97%) was purchased from abcr GmbH (Karlsruhe, Germany). All other chemicals and reagents used were of analytical grade.

4.2.2. Synthesis of block copolymers

The copolymers of mPEO-*b*-PBCL with two different degrees of polymerization (DP = 12 and DP = 20) were synthesized by ring-opening polymerization of α-benzyl carboxylate-ε-caprolactone using mPEO (MW: 5000 $gmol^{-1}$) as an initiator and stannous octoate as catalyst according to a previously described method [354]. In the first step, 2 g and 0.5 g of mPEO were added to 1.19 g and 0.6 g of α-benzyl carboxylate-ε-caprolactone (BCL) monomer to prepare two products with DPs of 12 and 20, respectively. Stannous octoate (0.1% w/w of the polymer) was then added to an ampoule and sealed under vacuum. The sealed ampoule was kept in an oven for 4 h at 140ºC. After 4 h polymerization reaction, the ampoule was cooled down to room temperature to stop the polymerization reaction. In the second step, block copolymers were dissolved in dichloromethane and subsequently precipitated in hexane and centrifuged at 3000 rpm to discard

the supernatant. The final product was washed twice with hexane and completely dried in a vacuum oven overnight at room temperature.

mPEO-*b*-PCCL copolymer was synthesized by catalytic debenzylation of mPEO-*b*-PBCL in the presence of H_2 according to a method described previously [294]. Briefly, a solution of mPEO-*b*-PBCL (1 g) in 50 mL anhydrous tetrahydrofuran (THF) was prepared and placed into a cylindrical flask where palladium on charcoal (300 mg) was dispersed. The mixture was vigorously stirred with a magnetic stirrer under continuous H_2 gas flow at 0.2 $Lmin^{-1}$ for 8 h at room temperature. Afterwards, the mixture was centrifuged at 3000 rpm to remove the catalyst. The collected supernatant was evaporated to precipitate the product. mPEO-*b*-PCCL was washed with diethyl ether repeatedly to remove impurities. The final product was dried under vacuum for 48 h at room temperature.

4.2.3. Synthesis of carboxyl-terminated mPEO-*b*-PBCL block copolymers

mPEO-*b*-PBCL copolymer was chemically modified by a reaction with succinic anhydride to generate mPEO-*b*-PBCL copolymer, the end-capped carboxylic acid functional group (mPEO-*b*-PBCL-COOH). First, 1 g of mPEO-*b*-PBCL and 1.5 times molar excess of succinic anhydride were mixed and placed in a previously flame-dried ampoule. The ampoule was sealed and kept in an oven for 4 h reaction at 140ºC. Thereafter, COOH-terminated block copolymers were dissolved in dichloromethane and subsequently, precipitated in hexane and centrifuged at 3000 rpm to discard the supernatant [355]. The final product was washed twice with hexane and completely dried in a vacuum oven overnight at room temperature.

4.2.4. Conjugation of SN-38 to mPEO-*b*-PBCL-COOH copolymers

Conjugation of SN-38 to mPEO-*b*-PBCL was conducted by activation of the carboxylic acid terminal group on PBCL block using N, N′-diisopropylcarbodiimide (DIC) and 4-

dimethylaminopyridine (DMAP). At first, 21 mg of SN-38 and 13 mg of DMAP were dissolved together in 2 mL of anhydrous dimethylformamide (DMF). Separately, 0.2 g (0.026 mmoles) of mPEO-*b*-PBCL-COOH copolymer (DP = 12 for PBCL block) was dissolved in 2 mL of DMF. The vial containing the polymer solution was placed in an ice-water bath and stirred under Ar gas. DIC (100 uL) was added to the solution at 0°C and kept for 20 min. The solution of SN-38 and DMAP was then added to the reaction solution. The reaction solution was stirred under Ar gas for 48 h at room temperature. The reaction mixture was then diluted with 6 mL dimethyl sulfoxide (DMSO) and dialyzed against DMSO for 48 h and deionized water overnight to remove unreacted SN-38 and other impurities and by-products. The solution was freeze-dried to obtain a dry product.

4.2.5. Conjugation of SN-38 to mPEO-*b*-PCCL copolymers

Conjugation of SN-38 to mPEO-*b*-PCCL was conducted by activation of carboxylic acid pendant groups on PCCL block using N, N′-diisopropylcarbodiimide (DIC) and 4-dimethylaminopyridine (DMAP). At first, 50 mg of SN-38 and 39 mg of DMAP were dissolved together in 4 mL of DMF. Separately, 0.25 g (0.031 mmoles) of mPEO-*b*-PCCL copolymer (DP = 20, for the second bock) was dissolved in 3 mL of DMF. The vial containing the polymer solution was placed in an ice-water bath. The solution was then stirred under Ar gas. DIC (110 uL) was added at 0°C to the polymer solution under Ar gas. The reaction container was kept for 20 min. The SN-38 and DMAP solution was then added to the reaction solution and were stirred under Ar gas for 48 h at room temperature. The reaction mixture was then diluted with 3mL DMSO and dialyzed against DMSO for 48 h and then deionized water overnight to remove unreacted SN-38 and other impurities and by-products. The final aqueous solution was freeze-dried to obtain the dry product.

4.2.6. Characterization of block copolymers and drug-copolymer conjugates

The synthesized block copolymers and SN-38-copolymer conjugates were characterized for their number average molecular weights by ^{1}H NMR (600 MHz Avance III - Bruker, East Milton, ON, Canada) using deuterated chloroform ($CDCl_3$) as a solvent. The DP of the PBCL and PCCL blocks was calculated from the ^{1}H NMR based on the ratio of the peak intensity of protons from the ethylene (-CH_2CH_2O-) moiety of PEO (δ = 3.65 ppm) to the peak intensity of the protons from the (-$COOCH_2$-) methylene of caprolactone (δ = 4.05 ppm), considering a molecular weight of 5000 $gmol^{-1}$ for the PEO block. The level of debenzylation of mPEO-*b*-PCCL polymer was also measured based on ^{1}H NMR. The yield of the hydrogenation reaction was determined taking into account the signal of methylenes from the benzyl group at ~7.4 ppm (-CH_2-Ph) and the signal of methylene protons from the caprolactone backbone at 4.05 ppm (-O-CH_2-C=O). The ratio of their integration was then multiplied by 100 in order to obtain the molar percentage of the remaining benzyl groups.

SN-38 conjugation level was measured using a Synergy-H1 BioTEK microplate reader (Winooski, VT, USA) at a wavelength of 383 nm. The level of SN-38 conjugation was expressed in loading percentage (% w/w) with respect to the carboxylic acid-terminated residue of mPEO-*b*-PBCL and α-carboxylic-ε-caprolactone residue of mPEO-*b*-PCCL.

4.2.7. Self-assembly of block copolymers and physicochemical characterization of self-assembled structures

The mPEO-*b*-PBCL, mPEO-*b*-PBCL/SN-38, mPEO-*b*-PCCL, and mPEO-*b*-PCCL/SN-38 micelles were prepared as previously described [267]. In brief, 10 mg copolymers or drug-copolymer conjugates were completely dissolved in 1 mL acetone. Then, the organic phase was transferred dropwise to 3 mL aqueous phase and left overnight under continuous stirring with a

magnetic bar inside the fume hood to completely evaporate the organic solvent. The size (Z-average diameter), polydispersity index (PDI), zeta potential (ZP), and critical micellar concentration (CMC) of the micelles were measured by dynamic light scattering (DLS) using a Malvern Zetasizer 3000 (Malvern Instruments Ltd, Malvern, UK).

Table 4.1: Physicochemical characteristics of the self-assembled block copolymers and SN-38-conjugated block copolymer micelles (n = 4).

Micellar Formulations [a]	**Size** [b] **± SD (nm)**	**PDI** [c] **± SD**	**Zeta Potential** [d] **± SD (mV)**	**CMC** [e] **± SD (μgmL^{-1})**	**SN-38 Loading** [f] **(% w/w)**
$mPEO_{114}$-*b*-$PBCL_{12}$	46.25±0.11	0.12±0.01	0.09±0.03	4.43±0.21	-
$mPEO_{114}$-*b*-$PBCL_{12}$/SN-38	43.60±0.14 [g]	0.13±0.01	-1.14±0.23 [g]	3.88±0.11 [g]	11.47±0.10
$mPEO_{114}$-*b*-$PCCL_{20}$	56.76±0.41	0.17±0.01	0.04± 0.01	69.92±0.82	-
$mPEO_{114}$-*b*-$PCCL_{20}$/SN-38	38.47±0.34 [g]	0.11±0.02	-1.69±0.18 [g]	54.57±0.12 [g]	12.03±0.17

[a] The number shown in the subscript indicates the degree of polymerization of each block as determined by ^{1}H NMR spectroscopy.
[b] Hydrodynamic diameter (Z average) determined by DLS.
[c] Average PDI of micellar size distribution.
[d] Average surface charge (zeta potential) of the micelles.
[e] Average CMC measured by DLS.
[f] SN-38 loading $(w/w\,\%) = \frac{\text{Amount of conjugated SN}-38}{\text{Total amount of polymer}} \times 100$; measured using UV-Vis spectrophotoscopy.
[g] Differences were considered significant if $^*p \leq 0.05$, $^{**}p \leq 0.01$, $^{***}p \leq 0.001$, or $^{****}p \leq 0.0001$ following unpaired student's t test when compared to their counterpart polymeric micelles without SN-38.

In order to investigate micellar stability, CMC of the formulations was also determined by a DLS technique following a previously published method [294]. In brief, a series of micellar solutions of mPEO-*b*-PBCL, mPEO-*b*-PBCL/SN-38, mPEO-*b*-PCCL, and mPEO-*b*-PCCL/SN-38 with a concentration range of 1000 to 0.24 μgmL^{-1} were prepared in glass vials. The intensity of the scattered light for prepared samples was detected at an angle of 173º under single attenuator index. Measurements were carried out in polystyrene cells at 25ºC. The count rate (Kcps) as a function of the intensity of the scattered light was plotted against the concentration of copolymers and SN-38-copolymer conjugates.

To determine the stability of micelles against dissociation, kinetic stability was also measured by a DLS method as previously described [356]. In brief, micelles were prepared using individual copolymers having a concentration of 3 $mgmL^{-1}$ and incubated with an aqueous solution of a destabilizing agent, sodium dodecyl sulfate (SDS) (20 $mgmL^{-1}$) at a ratio of 2:1 (v/v). The intensity of scattered light and PDI were measured at different incubation time intervals (0, 1, 2, 4, 8, and 24 h).

4.2.8. Transmission electron microscopy (TEM)

The morphology of self-assembled structures under study was investigated by TEM using a Morgagni TEM (Field Emission Inc., Hillsboro, OR) with Gatan digital camera (Gatan, Pleasanton, CA). In brief, 20 μL of micellar solution with a polymer concentration of 1 $mgmL^{-1}$ was placed on a copper-coated grid. The grid was held horizontally for 1 min to allow the colloidal particles to settle down. The excess fluid was removed by filter paper. The copper-coated grids holding the aqueous samples were then negatively stained by 2% phosphotungstic acid. After 2 min, the excess fluid was removed by filter paper and the grid was loaded into the TEM for image analysis.

4.2.9. *In Vitro* drug release

In vitro release of SN-38 from the self-assembled structures was investigated using dialysis-bag diffusion technique. Each dialysis bag (Spectrapor dialysis tubing, MWCO = 3.5 kDa, Spectrum Laboratories, Rancho Dominguez, CA, U.S.A.), containing 3 mL of the micellar formulation in water or free SN-38 dissolved in DMSO, was immersed into 300 mL release medium (4% albumin in ultrapure water) maintained at 37ºC in a shaking water bath at 65 rpm (Julabo SW 22, Seelbach, Germany). At selected time intervals (0, 1, 2, 4, 6, 8, and 24 h), 300 µL aliquots from inside of the dialysis bag were withdrawn and replaced with an equal volume of fresh release media (water). The concentrations of SN-38 in collected samples were determined by UV-Vis spectrophotometer (BioTEK, Winooski, VT, USA). Detection was performed at a wavelength of 383 nm. All experiments were carried out in triplicate. Finally, the release profiles of the formulations were compared using the similarity factor, f_2, and the profiles were considered significantly different if $f_1 \leq 15$ and $f_2 \leq 50$ according to the following equations:

$$\text{Difference factor } (f_1) = \left(\frac{\sum_n^{j=1}|Rj - Tj|}{\sum_n^{j=1} Rj}\right) \times 100$$

$$\text{Similarity factor } (f_2) = 50 \log\left(\left[1 + \left(\frac{1}{n}\right)\sum_n^{j=1}|Rj - Tj|^2\right]^{-0.5} \times 100\right)$$

where, n is the number of time points; Rj is % released of the reference at time point j and Tj is % released of test formulations at time point j.

4.2.10. Cell lines

Three CRC cell lines, i.e., HCT116, HT-29, and SW620 C were purchased from ATCC (Manassas, VA). The cells were cultured at 37ºC in 5% CO_2 in a humidified incubator in a 1:1 mixture of Dulbecco's modified Eagle medium and F12 (DMEM/F12) supplemented with 10% FBS, 50 UmL^{-1} penicillin, 50 $mgmL^{-1}$ streptomycin, 2 $mmolL^{-1}$ L-glutamine, 0.1 $mmolL^{-1}$

nonessential amino acids, and 1 $mmolL^{-1}$ sodium pyruvate. All culture supplements were purchased from GIBCO Life Technologies Inc. (Burlington, ON). All cell lines were routinely tested for mycoplasma in the lab.

4.2.11. *In vitro* cytotoxicity assay

The CellTiter 96® AQueous One Solution Cell Proliferation Assay (MTS) kit was purchased from Promega, USA and used to assay the cytotoxicity of SN-38, irinotecan, mPEO-*b*-PBCL, mPEO-*b*-PCCL, mPEO-*b*-PBCL/SN-38, and mPEO-*b*-PCCL /SN-38 against HCT116, HT-29, and SW620 cells according to the manufacturer's protocol. In brief, 2×10^3 cells were plated in each well of 96-well flat-bottomed plates 24 h prior to the treatments. Then, cells were treated with the formulations at the concentration ranges of 0.001 to 100 μM for SN-38 and 0.00334 to 334 μgmL^{-1} for polymeric micellar SN-38 or empty polymeric micellar formulations. Control cells received only 0.1% DMSO. After different experimental incubation time points, 20 μL of MTS reagent was added in each well and further incubated for 1 h at 37ºC before measuring the absorbance at 490 nm using a BioTEK microplate reader. The cell viability percentages were calculated using the following formula:

$$\text{Cell viability (\%)} = \frac{\text{Absorbance of treated cells} - \text{Absorbance of blank well}}{\text{Absorbance of untreated cells} - \text{Absorbance of blank well}} \times 100$$

4.2.12. Caspase 3/7 activity measurements

The caspase-glo 3/7 assay reagent was purchased from Promega (Madison, WI, USA) and used according to the manufacturer's protocol to detect and quantify the *in vitro* caspase activity of free SN-38, irinotecan, mPEO-*b*-PBCL, mPEO-*b*-PCCL, mPEO-*b*-PBCL/SN-38, and mPEO-*b*-PCCL /SN-38 in HCT116, HT-29, and SW620 cell lines. In brief, the cells were first seeded onto 96-well plates at a density of 2×10^3 cells per well and incubated for 24 h. Cells were then treated with the media containing various formulations at a final concentration equivalent to the

respective IC_{50} concentrations of free SN-38, irinotecan, mPEO-*b*-PBCL/SN-38, and mPEO-*b*-PCCL/SN-38 for 6 h. The concentrations of mPEO-*b*-PBCL and mPEO-*b*-PCCL in each well were equivalent to the concentrations of these polymers in mPEO-*b*-PBCL/SN-38 and mPEO-*b*-PCCL /SN-38 treatments, respectively. Control cells received only 0.1% DMSO. After 6 h incubation, the caspase-glo 3/7 assay reagent was added in each well and kept at room temperature for 45 min. The relative luminescence was measured and analyzed compared to the control. Each experiment was carried out in triplicate.

4.2.13. Hemolytic activity assessment

Whole blood was collected from 22 weeks old Sprague-Dawley rats (~300g) in heparinized tubes (BD Vacutainer, Toronto, ON) by cardiac puncture under anesthesia. Erythrocytes were separated from the heparinized blood by centrifugation at 2000×g for 10 min and then washed twice with isotonic PBS (pH 7.4). Separated erythrocytes were re-suspended and diluted in PBS to a final cell count of 2×10^7 cells per mL. The aliquots of 200 µL cell suspension were treated with various concentrations of mPEO-*b*-PBCL, mPEO-*b*-PCCL, mPEO-*b*-PBCL/SN-38 and mPEO-*b*-PCCL/SN-38 and incubated at 37ºC with gentle mixing for 30 min. After the incubation, the tubes were centrifuged at 2000×g for 15 min to remove the unlysed erythrocytes and the supernatants containing released hemoglobin were transferred into 96-well plates. The absorbance of hemoglobin was measured at a wavelength of 540 nm using a microplate reader. Isotonic PBS was used as a negative control and full hemolysis (positive control) was achieved by mixing the erythrocyte suspension with pure water. Finally, hemolytic activity was assayed as the % of hemolysis caused by various concentrations of the treatment groups compared to hemolysis in pure water. The percentage of hemolysed erythrocytes was calculated using the equation:

$$\%\ \text{Hemolysis} = \frac{(\text{Absorbance of sample} - \text{Absorbance of negative control}) \times 100}{\text{Absorbance of positive control} - \text{Absorbance of negative control}}$$

4.2.14. Statistical analysis

Data are shown as mean ± standard error of at least three experiments. GraphPad Prism6 software (La Jolla, CA, USA) was used for statistical analysis. Significance of difference between groups was assessed using one-way ANOVA followed by Tukey's post-hoc analysis. If a significant difference was found among the groups, median ranks between pairs of groups were compared using the Mann-Whitney U test. Differences in physicochemical characterization of micellar formulations were also tested using the unpaired student's t-test. A value of $p \leq 0.05$ was considered as statistically significant in all experiments.

4.3. Results

4.3.1. Physicochemical characterization

The ^{1}H NMR spectra for mPEO-*b*-PBCL/SN-38 and mPEO-*b*-PCCL/SN-38 and peak assignments are shown in **Fig. 4.2**, while the ^{1}H NMR spectra for free SN-38, mPEO-*b*-PBCL, mPEO-*b*-PCCL are shown in **Supplementary Fig. 4.1-4.3** [294, 321, 322]. According to calculations based on the ^{1}H NMR spectra, the DP was 12 and 20 for PBCL and PCCL blocks in MPEO-*b*-PBCL and mPEO-*b*-PCCL, respectively. The 100% catalytic hydrogenolysis conversion of mPEO-*b*-PBCL to mPEO-*b*-PCCL was also confirmed by ^{1}H NMR in mPEO-*b*-PCCL. The conjugated content (% w/w) of SN-38 to mPEO-*b*-PBCL and mPEO-*b*-PCCL were 11.47 ± 0.10 and 12.03 ± 0.17, respectively, as measured by UV spectroscopy.

The physicochemical characteristics of the self-assembled mPEO-*b*-PBCL, mPEO-*b*-PCCL, mPEO-*b*-PBCL/SN-38, and mPEO-*b*-PCCL/SN-38 micelles including size, surface charge, PDI, and CMC are summarized in **Table 4.1**. The average diameters of micelles formed from mPEO-*b*-PBCL, mPEO-*b*-PCCL, mPEO-*b*-PBCL/SN-38 and mPEO-*b*-PCCL/SN-38 were

below 100 nm and showed a relatively narrow polydispersity range below 0.2. As a result of the chemical conjugation of SN-38 to both copolymers, the average hydrodynamic diameters of mPEO-*b*-PBCL/SN-38 and mPEO-*b*-PCCL/SN-38 were significantly reduced (****$p < 0.0001$) when compared to that of the SN-38-free block copolymers. The mean zeta potential of the micelles formed from mPEO-*b*-PBCL and mPEO-*b*-PCCL were neutral at a range from 0.04 – 0.09 mV. However, the mean zeta potential shifted towards negative when SN-38 was conjugated to mPEO-*b*-PBCL and mPEO-*b*-PCCL copolymers. Statistically, the presence of conjugated SN-38 in both block copolymer micelles resulted in significant changes in zeta potentials (mPEO-*b*-PBCL/SN-38; $p = 0.01$ and mPEO-*b*-PCCL/SN-38; $p = 0.004$ compared to the micelles prepared using their respective SN-38-free block copolymers).

All self-assembled micelles showed CMC in the μgmL^{-1} range as shown in **Table 4.1**. The measured CMCs of mPEO-*b*-PBCL, mPEO-*b*-PCCL, mPEO-*b*-PBCL/SN-38 and mPEO-*b*-PCCL/SN-38 were 4.43 ± 0.21, 3.88 ± 0.11, 69.92 ± 0.82, and 54.57 ± 0.12 μgmL^{-1}, respectively. After statistical analysis, the CMCs of mPEO-*b*-PCCL and mPEO-*b*-PCCL/SN-38 were significantly higher than that of the micelles prepared from mPEO-*b*-PBCL and mPEO-*b*-PBCL/SN-38. Notably, the CMC appeared to become lower upon conjugation of SN-38 irrespective of the polymer structure (mPEO-*b*-PBCL/SN-38; $p = 0.03$ and mPEO-*b*-PCCL/SN-38; $p = 0.0008$ when compared with their respective SN-38-free copolymeric micelles).

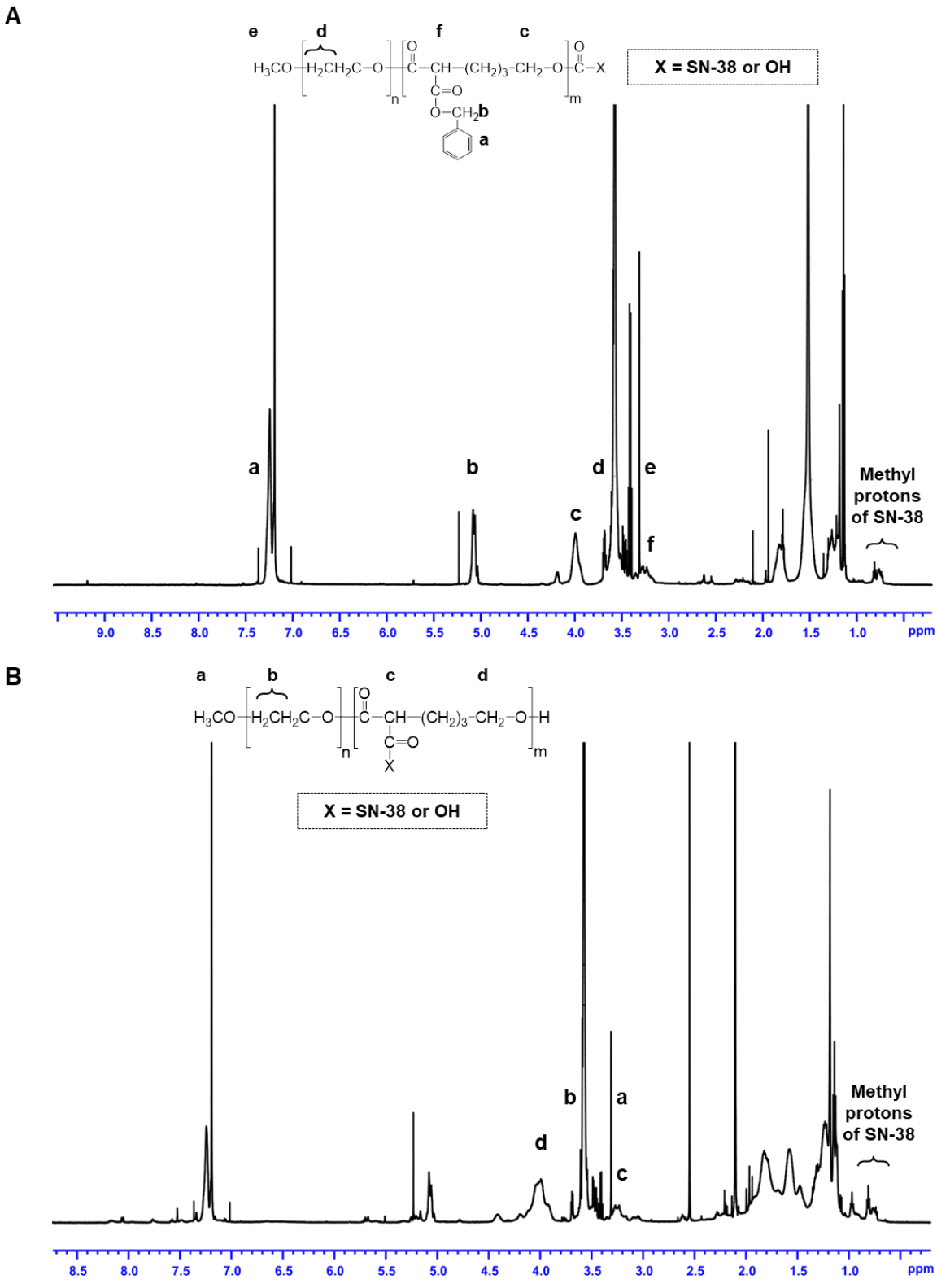

Figure 4.2: [1]H NMR spectra and corresponding peak assignments for (A) mPEO-*b*-PBCL/SN-38, (B) mPEO-*b*-PCCL/SN-38.

4.3.2. Transmission electron microscopy (TEM)

The morphology of the self-assembled structures was investigated by TEM images, confirming the formation of spherical-shaped mPEO-*b*-PBCL, mPEO-*b*-PCCL, mPEO-*b*-PBCL/SN-38, and mPEO-*b*-PCCL/SN-38 micelles with uniform size (**Fig. 4.3)**. The size of the micelles was also measured from TEM images using ImageJ software. The average diameters of self-assembled mPEO-*b*-PBCL (47.8 ± 1.29 nm), mPEO-*b*-PCCL (55.82 ± 2.72 nm), mPEO-*b*-PBCL/SN-38 (44.98 ± 4.84 nm), and mPEO-*b*-PCCL/SN-38 (42.66 ± 3.58 nm) micelles obtained by DLS appeared to be similar. Moreover, a similar distribution pattern in micellar population having a clear boundary was observed in TEM images of all micelles, indicating the lower aggregation tendency of micelles.

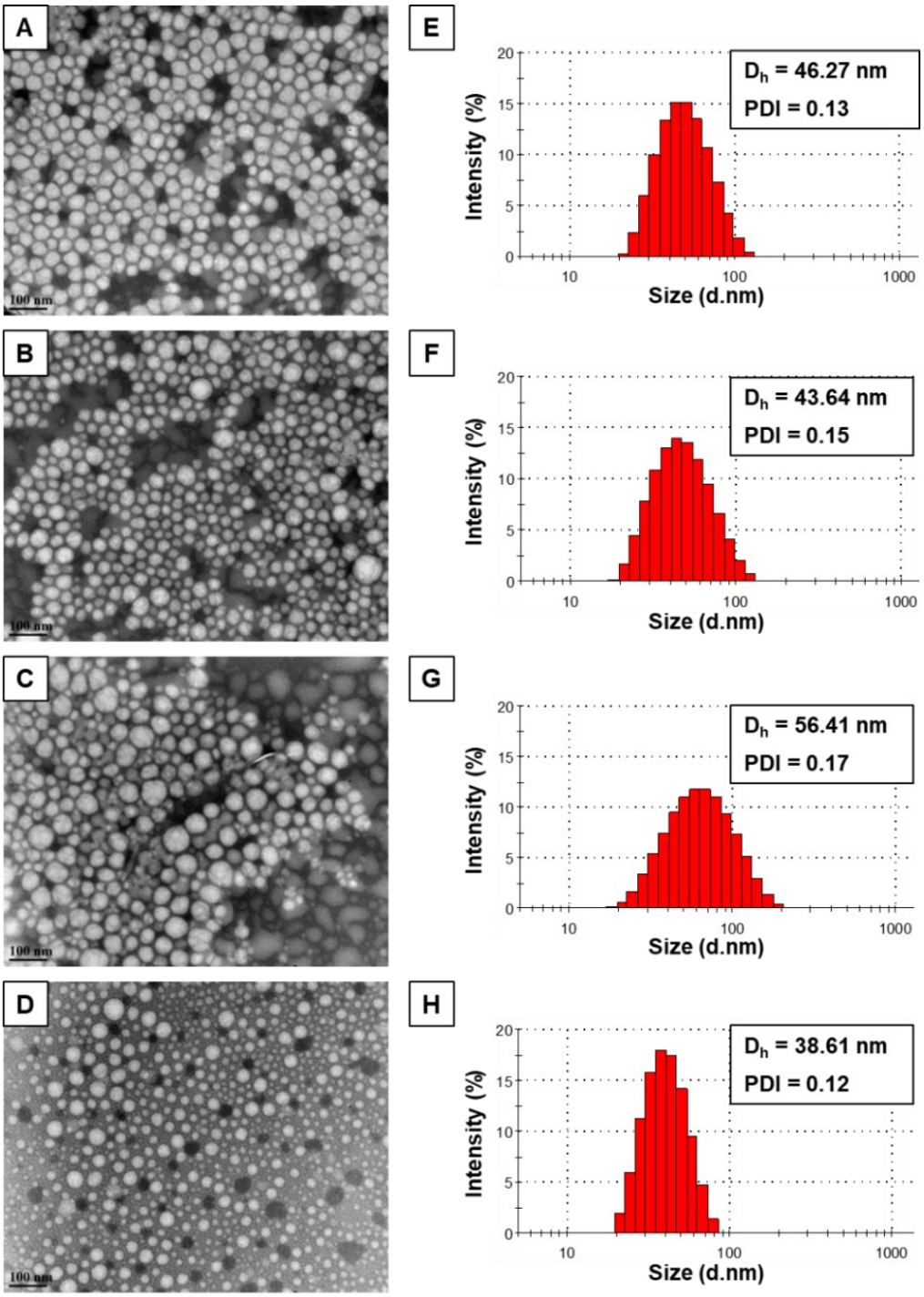

Figure 4.3: TEM images of the polymeric and SN-38-conjugated micelles formed from (A) mPEO-*b*-PBCL, (B) mPEO-*b*-PBCL/SN-38, (C) mPEO-*b*-PCCL, and (D) mPEO-*b*-PCCL/SN-38. Images were obtained at a magnification of 110,000X at 75 kV. The bar in the bottom left corner of each image indicates a scale of 100 nm. Hydrodynamic diameter (D_h), PDI, and size distribution of (E) mPEO-*b*-PBCL, (F) mPEO-*b*-PBCL/SN-38, (G) mPEO-*b*-PCCL, and (H) mPEO-*b*-PCCL/SN-38 micelles in aqueous medium were obtained using dynamic light scattering (DLS).

4.3.3. Kinetic stability of block copolymeric micelles

Using DLS, the kinetic stability of block copolymeric micelles was investigated in the presence of a destabilizing surfactant, i.e., SDS, over 24 h. **Fig. 4.4A** and **4.4B** represent the % intensity of the micellar peak and PDI, respectively, for mPEO-*b*-PBCL, mPEO-*b*-PCCL, mPEO-*b*-PBCL/SN-38, and mPEO-*b*-PCCL/SN-38 micelles over time (1, 2, 4, 8, and 24 h) in the presence of SDS. Notably, mPEO-*b*-PBCL and mPEO-*b*-PBCL/SN-38 micelles exhibited complete resistance against the destabilizing agent and remained intact throughout the incubation period up to 24 h. In contrast, mPEO-*b*-PCCL micelles were completely dissociated right after mixing with SDS and the detected intensity of the micellar peak was below 1%. Due to complete dissociation, no PDI data were detectable by DLS at this time point as shown in **Fig. 4.4B**. In the case of mPEO-*b*-PCCL/SN-38, a dramatic drop in the % intensity of the micellar peak was observed immediately after SDS incorporation and 82% dissociation was recorded within 8 h. After 24 h, 0% intensity of micellar peak was recorded due to 100% dissociation of mPEO-*b*-PBCL/SN-38 micelles in the presence of SDS.

As shown in **Fig. 4.4B**, both mPEO-*b*-PBCL and mPEO-*b*-PBCL/SN-38 micelles showed no change in PDI values obtained by DLS throughout the entire incubation period with SDS. In the case of mPEO-*b*-PCCL/SN-38 micelles, PDI values gradually increased above 0.8 within 8 h and reached to 1 after 24, implying complete micellar dissociation in the presence of the destabilizing agent. Overall, the data suggest that mPEO-*b*-PBCL-based micellar formulation is kinetically more stable than their PEO-*b*-PCCL counterparts.

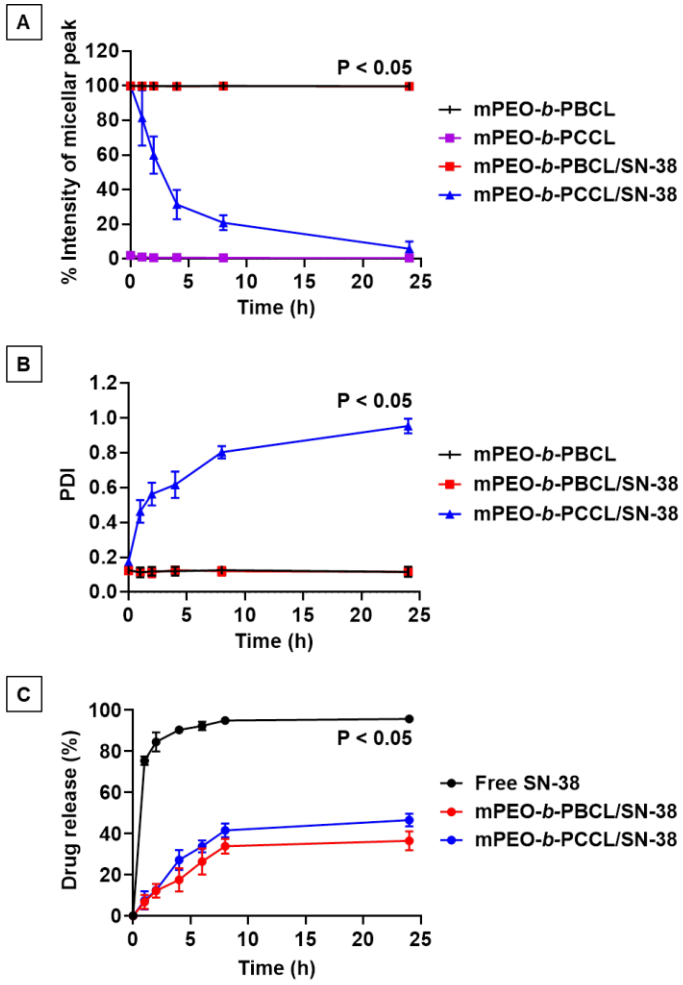

Figure 4.4: Average (A) percentage of intensity and (B) PDI of mPEO-*b*-PBCL, mPEO-*b*-PBCL/SN-38, mPEO-*b*-PCCL (no PDI data), and mPEO-*b*-PCCL/SN-38 micellar peak (3 $mgmL^{-1}$) in the presence of SDS (20 $mgmL^{-1}$) at a ratio of 2:1 (v/v) as a function of time up to 24 h. Each point represents mean ± SD (n = 3). (C) The drug release profile of mPEO-*b*-PBCL/SN-38 and mPEO-*b*-PCCL /SN-38 micelles compared to free SN-38 from dialysis tubing (MWCO = 3.5 kDa) in aqueous solution (4% albumin in ultrapure water) at 37ºC. Data are represented as mean ± SD (n = 3). The results of statistical analysis using following one-way ANOVA followed by Tukey's method showed a significant difference between PEO-*b*-PBCL and mPEO-*b*-PCCL; between mPEO-*b*-PBCL/SN-38 and mPEO-*b*-PCCL/SN-38 in Fig. 4.4A, between mPEO-*b*-PCCL/SN-38 and PEO-*b*-PBCL; between mPEO-*b*-PCCL/SN-38 and mPEO-*b*-PBCL/SN-38 in Fig. 4.4B, and between free SN-38 and mPEO-*b*-PBCL/SN-38; between free SN-38 and mPEO-*b*-PCCL/SN-38 in Fig. 4.4C. Significances of the differences were considered if *p ≤ 0.05. Data are expressed as mean ± SD (n = 3).

4.3.4. *In vitro* drug release

Fig. 4.4C shows a comparative *in vitro* release profile of SN-38 from mPEO-*b*-PBCL/SN-38 and mPEO-*b*-PCCL/SN-38 micelles versus free SN-38. Within 6 h, 92.3% drug was rapidly released from the dialysis bag containing free SN-38 solubilized using DMSO. Such apparent burst

release indicates a condition where diffusion controls the release of drug [357]. In contrast, only 26.8% and 33.8% of SN-38 were released over 6 h from mPEO-*b*-PBCL/SN-38 and mPEO-*b*-PCCL/SN-38 micelles, respectively. In addition, the release of SN-38 from mPEO-*b*-PBCL/SN-38 micelles over 24 h was 36.5%, which was significantly lower than that of mPEO-*b*-PCCL/SN-38 micelles (47%) (Unpaired Student's t-test, $*p < 0.05$). After 24 h, the release of free SN-38 was 96%. As shown in **Table 4.2**, the release profiles between free SN-38, mPEO-*b*-PBCL/SN-38, and mPEO-*b*-PCCL/SN-38 micelles were also analyzed by measuring the difference (f_1) and similarity (f_2) factors. As a result, calculated f_1 and f_2 values were found above 15 and below 50, respectively, when the percent release of free SN-38 was compared with that of both micellar SN-38 formulations. However, the calculated f_2 values were found above 50 when the release profiles between mPEO-*b*-PBCL/SN-38 and mPEO-*b*-PCCL/SN-38 micelles were compared, suggesting similar release kinetics. The overall *in vitro* release study supports the efficiency of micellar formulations for sustained release of SN-38.

Table 4.2: Calculated difference factor (f1) and similarity factor (f2) for SN-38 release profiles from mPEO-b-PBCL/SN-38 and mPEO-b-PCCL/SN-38 micellar formulations. The profiles were considered similar if $f1 \leq 15$ and $f2 \geq 50$.

Formulations	**Difference factor (f_1)**	**Similarity factor (f_2)**
Free SN-38 and $mPEO_{114}$-*b*-$PBCL_{12}$	75.01	8.73
Free SN-38 and $mPEO_{114}$-*b*-$PCCL_{20}$/SN-38	68.27	10.65
$mPEO_{114}$-*b*-$PBCL_{12}$/SN-38 and $mPEO_{114}$-*b*-$PCCL_{20}$/SN-38	26.95	56.97

4.3.5. *In vitro* cytotoxicity

The MTS assay was performed up to 72 h to determine the anticancer activity of micellar mPEO-*b*-PBCL/SN-38 and mPEO-*b*-PCCL/SN-38 formulations against CRC cell lines (HCT116, HT-29, SW620) in comparison to empty polymeric micelles, free SN-38, and irinotecan. **Fig. 4.5** shows the average percentages of cell survival over 24, 48, and 72 h treatment with the formulations. The ranges for IC_{50}s for each of the treatments at different incubation time points are summarized in **Table 4.3**. As shown in **Fig. 4.5**, free SN-38, irinotecan, mPEO-*b*-PBCL/SN-38, and mPEO-*b*-PCCL/SN-38 showed time and dose dependent cytotoxicity against all cell lines under study. However, no toxicity was observed for drug free mPEO-*b*-PBCL and mPEO-*b*-PCCL. SN-38 solubilized with DMSO exhibited the highest toxicity against all cell lines. The HCT116 CRC cell line showed the least sensitivity to free SN-38 (IC_{50}: 0.01 ± 0.002 μM) over 72 h incubation compared to that of HT-29 (IC_{50}: 0.002 ± 0.001 μM) and SW620 (IC_{50}: 0.002 ± 0.001 μM) cell lines. Both mPEO-*b*-PBCL/SN-38 and mPEO-*b*-PCCL/SN-38 treatments exhibited a significant reduction in the viability of CRC cell lines under study over 72 h when compared to irinotecan. The calculated IC_{50} values for irinotecan were 6.94 ± 2.51, 11.35 ± 4.04, and 6.63 ± 3.64 μM after 72 h incubation with HCT116, HT-29, and SW620 cell lines, respectively. The obtained IC_{50} values for mPEO-*b*-PBCL/SN-38 micellar treatments were 0.11 ± 0.04 μM (HCT116), 0.39 ± 0.16 μM (HT-29), and 0.10 ± 0.04 μM (SW620) for 72 h treatment. For mPEO-*b*-PCCL/SN-38 after similar treatment period, the calculated IC_{50}s were 0.04 ± 0.02 μM (HCT116), 0.08 ± 0.04 μM (HT-29), and 0.02 ± 0.01 μM (SW620). Overall, the CRC cells under study were on average 70- to 330-fold more sensitive to the polymeric micellar conjugates of SN-38 developed here than irinotecan. There was no significant difference between the IC_{50} of mPEO-*b*-PCCL/SN-38 and mPEO-*b*-PBCL/SN-38 micelles over 72 h in all three CRC cell lines. The

similar trend in cell viability reduction observed for the SN-38-conjugated micellar formulations suggest that both mPEO-*b*-PBCL/SN-38 and mPEO-*b*-PCCL/SN-38 micelles effectively preserved and delivered the active structure of SN-38 to the CRC cell lines.

Table 4.3: IC_{50} range of free SN-38, irinotecan, mPEO-*b*-PBCL/SN-38, and mPEO-*b*-PCCL/SN-38 against HCT116, HT-29, and SW620 cell lines after 24, 48, and 72 h of incubation (n = 4).

Cells	**Time (h)**	**SN-38 (μM)**	**Irinotecan (μM)**	**mPEO-*b*-PBCL/SN-38 (μM)**	**mPEO-*b*-PCCL/SN-38 (μM)**
HCT116	24	0.092 - 0.145	4.135 - 12.550	0.696 - 1.262	0.189 - 0.425
	48	0.039 - 0.065	3.367 - 6.409	0.711 - 1.308	0.032 - 0.067
	72	0.007 - 0.009	5.387 - 8.941	0.084 - 0.148	0.027 - 0.059
HT-29	24	0.296 - 0.496	8.622 - 31.060	0.742 - 2.069	0.601 - 0.963
	48	0.038 - 0.056	14.120 - 27.760	0.337 - 0.662	0.0986 - 0.195
	72	0.001 - 0.003	8.847 - 14.560	0.294 - 0.526	0.062 - 0.115
SW620	24	0.016 - 0.028	10.470 - 52.080	1.039 - 4.041	0.920 - 1.300
	48	0.012 - 0.018	8.532 - 18.220	0.171 - 0.303	0.038 - 0.059
	72	0.002 - 0.003	4.537 - 9.680	0.0792 - 0.136	0.018 - 0.028

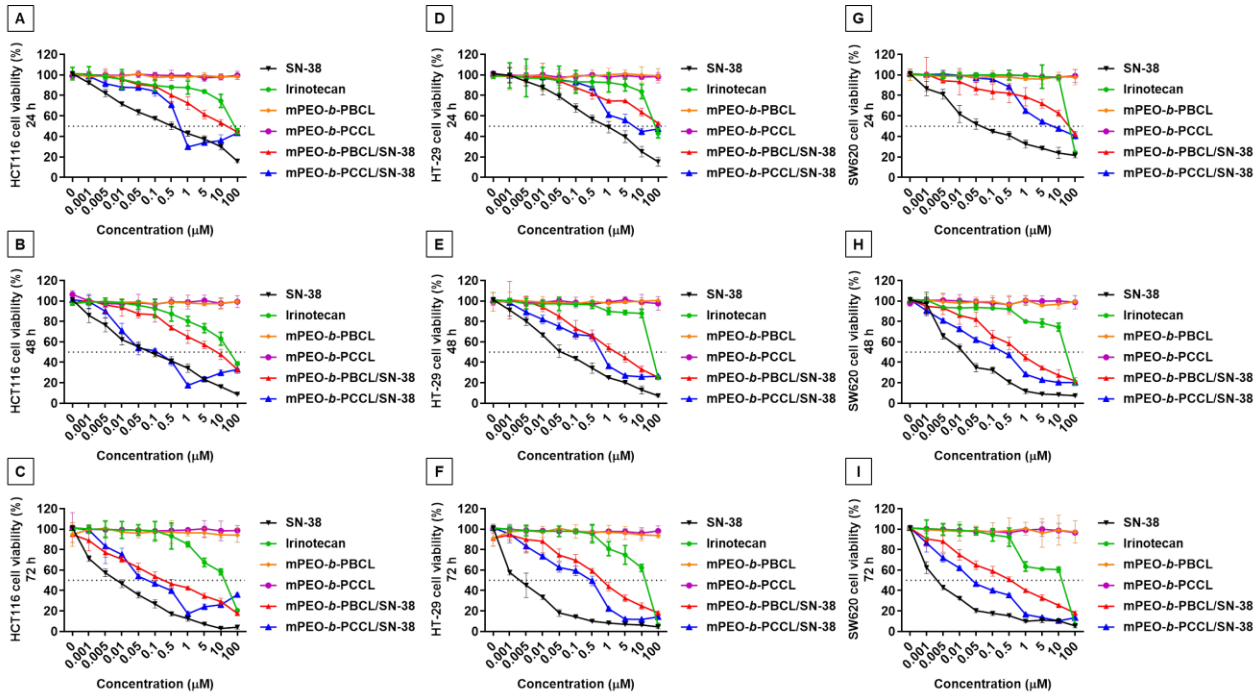

Figure 4.5: *In vitro* cytotoxicity assay for free SN-38 (black), irinotecan (green), mPEO-*b*-PBCL (orange), mPEO-*b*-PCCL (purple), mPEO-*b*-PBCL/SN-38 (red), and mPEO-*b*-PCCL/SN-38 (blue) in (A-C) HCT116, (D-F) HT-29, and (G-I) SW620 cell lines after 24 h, 48 h, and 72 h incubation at 37ºC in 5% CO_2. The cells were treated with the free drugs and polymeric micelles with a range of concentration from 0.001 μM to 100 μM. SN-38 was solubilized with DMSO and the untreated cells received only 0.1% DMSO. Each point represents mean ± SD (n = 4).

4.3.6. Caspase 3/7 activity

As shown in **Fig. 4.6**, significantly higher caspase-3/7 activation was observed with free SN-38, irinotecan, mPEO-*b*-PBCL/SN-38, and mPEO-*b*-PCCL /SN-38 treatments, at their respective IC_{50}s (24 h), compared to untreated or drug free mPEO-*b*-PBCL and mPEO-*b*-PCCL treated cells. At their respective IC_{50}s, mPEO-*b*-PBCL/SN-38 and mPEO-*b*-PCCL /SN-38 micellar treatments resulted in s ≈ 2-fold higher activation of caspase-3/7 compared to irinotecan. Notably, no statistically significant difference was observed between caspase 3/7 activation by free SN-38 and mPEO-*b*-PCCL /SN-38 in HT-29 and SW620 celll lines. The mPEO-*b*-PBCL/SN-38 formulation however showed less activity in this regard compared to free SN38 in all cell lines under study. A small, but significant, difference between the caspase 3/7 activation of the two

micellar SN-38 formulations was observed in the HCT116 and SW620 cell lines but the difference in the HT-29 cell line did not reach significance. Overall results strongly demonstrate that unlike irinotecan, the free SN38, mPEO-*b*-PBCL/SN-38 and mPEO-*b*-PCCL/SN-38 micelles trigger the enzymatic caspase-3/7 activation pathway that promotes the cellular apoptosis in CRC cell lines.

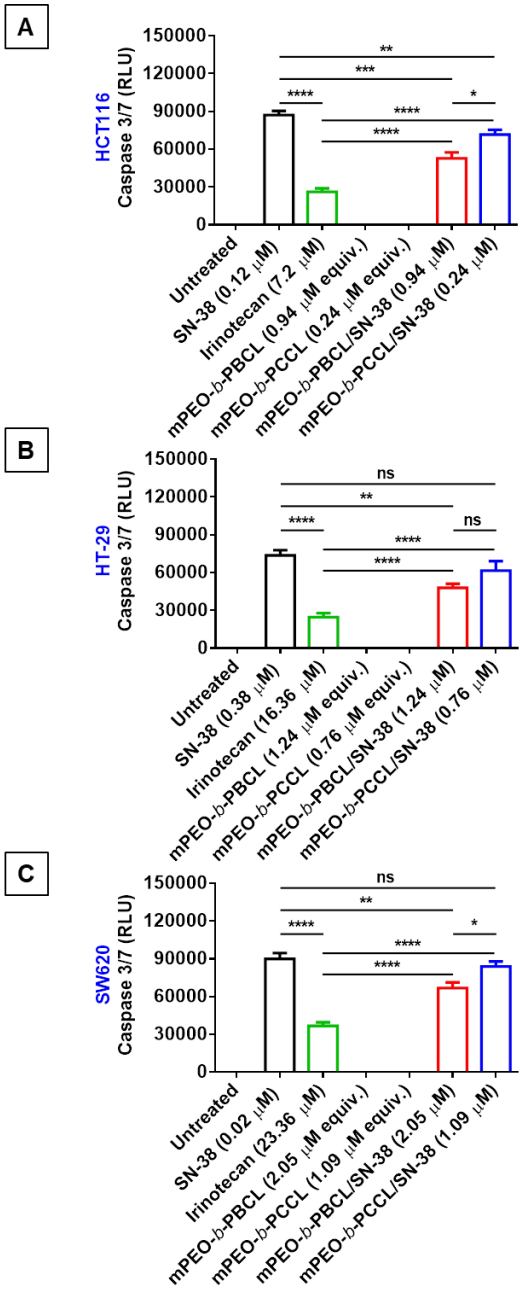

Figure 4.6: Caspase activity assay for free SN-38, irinotecan, mPEO-*b*-PBCL, mPEO-*b*-PCCL, mPEO-*b*-PBCL/SN-38, and mPEO-*b*-PCCL/SN-38 in (A) HCT116, (B) HT-29, and (C) SW620 cell lines. The cells were treated with the media containing the respective IC_{50} (24 h) concentrations of free SN-38, irinotecan, mPEO-*b*-PBCL/SN-38, and mPEO-*b*-PCCL/SN-38 for 6 h. Treated amounts of mPEO-*b*-PBCL and mPEO-*b*-PCCL were equivalent to the amounts of mPEO-*b*-PBCL/SN-38 and mPEO-*b*-PCCL/SN-38, respectively. The untreated (control) cells received only 0.1% DMSO. The significances of the differences are indicated as *p ≤0.05, **p ≤ 0.01, ***p ≤ 0.001, and ****p ≤ 0.0001 following two-way ANOVA multiple comparison test followed by Tukey's method. Data are expressed as mean ± SD (n = 6).

4.3.7. Hemolytic activity assessment

As shown in **Fig. 4.7A**, 30 min exposure to mPEO-*b*-PBCL did not exhibit any hemolytic activity at a polymer concentration as high as 16.67 μgmL^{-1}, which was the polymer concentration equivalent to the highest concentration of SN-38 (5 times higher than its IC_{50}). Similarly in **Fig. 4.7B**, mPEO-*b*-PBCL/SN-38 showed no hemolytic activity at a concentration of 5 μM that was 5 times higher than its IC_{50} (1 μM after 24 h treatment). However, mPEO-*b*-PCCL showed 15.32 ± 0.18%, 19.42 ± 0.34%, and 25.63 ± 0.13% hemolysis at 0.67 μmL^{-1}, 3.34 μgmL^{-1}, and 16.67 μgmL^{-1} concentrations, respectively which was significantly ($P \leq 0.0001$) higher than the hemolytic activities caused by mPEO-*b*-PBCL at similar levels (**Fig. 4.7A**). The measured percentages of hemolytic activity of mPEO-*b*-PCCL/SN-38 micelles were 10.19 ± 0.15, 13.45 ± 0.14, and 14.46 ± 0.15 at polymer concentrations of 0.67 μgmL^{-1}, 3.34 μgmL^{-1}, and 16.67 μgmL^{-1}, respectively, which was significantly ($P \leq 0.05$) reduced compared to that of mPEO-*b*-PCCL micelles following SN-38 conjugation (**Fig. 4.7B**). The overall results suggest that mPEO-*b*-PBCL and its SN-38 conjugated form are unlikely to affect red blood cells, [358]. In contrast, mPEO-*b*-PCCL and its SN-38 conjugated form can cause hemolysis, despite a reduction in the hemolytic activity of the polymer upon SN-38 conjugation.

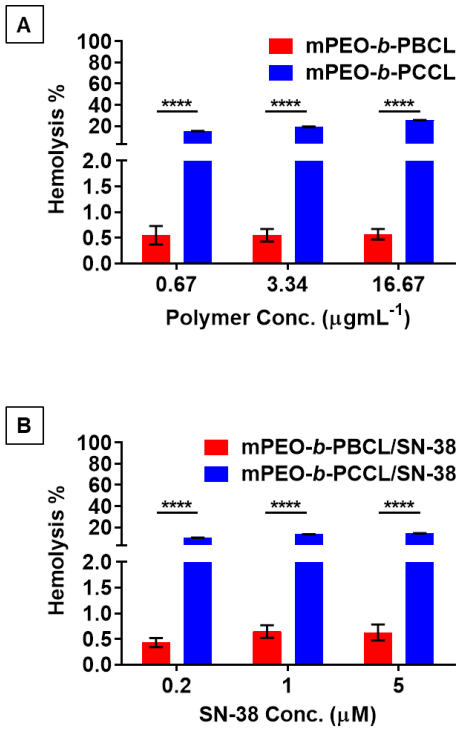

Figure 4.7: Hemolytic activity of (A) mPEO-*b*-PBCL and mPEO-*b*-PCCL; (B) mPEO-*b*-PBCL/SN-38 and mPEO-*b*-PCCL/SN-38 micellar formulations against rat RBCs. Each error bar represents the mean ± SD (n = 3). The concentrations of the polymers in the micellar formulations (0.67, 3.34, and 16.67 μgmL^{-1}) were equivalent to their respective concentration in the SN-38-conjugated formulations. SN-38 concentration of 0.2 (5 times less than IC_{50}), 1 (≈ IC_{50}), and 5 μM (5 times higher than IC_{50}) and their equivalent polymer concentrations were chosen for the study. Isotonic PBS and full hemolysis by pure water were used as negative and positive controls, respectively. All marked points were compared and were statistically significant if *p ≤ 0.05, **p ≤ 0.01, ***p ≤ 0.001, and ****p ≤ 0.0001.

4.4. Discussion

Irinotecan is a clinically used chemotherapeutic agent in CRC patients causing dose-dependent unwanted toxicities. The adverse side-effects of irinotecan are partly due to high required doses of the drug necessitated by irinotecan's inefficient (< 10%) conversion to its active form (SN-38) in liver and cancer cells. The main objective of this study was to develop a micellar delivery system for the active metabolite of irinotecan, SN-38, so that its solubility in water can be improved and its delivery to cancerous cells can be enhanced. To this end, SN-38 was chemically conjugated to the poly(ester) core of two different micellar formulations, i.e., mPEO-

b-PBCL and mPEO-*b*-PCCL (**Fig. 4.1**). The effect of the chemistry of the poly(ester) core in these SN-38 polymeric micellar-drug conjugates on the physicochemical and functional characteristics of these nanodelivery systems of SN-38 was then investigated, *in vitro*, in order to select an optimum formulation for future *in vivo* studies.

Our studies showed that, as a result of SN-38 chemical conjugation to mPEO-*b*-PBCL and mPEO-*b*-PCCL copolymers, the solubilized levels of SN-38 in water improved to > 10 $mgmL^{-1}$, which meets the criteria for systemic therapy [292]. This was through the formation of associated colloidal delivery systems of SN-38 with sufficient thermodynamic and kinetic stability in an aqueous media. Moreover, chemical conjugation or physical encapsulation of SN-38 into various delivery systems is challenging due to the inherent poor solubility of SN-38 in organic solvents that are mostly used for chemical reaction and solubilization depending on the types of delivery formulation [359-362]. This limitation was shown to impede high loading and loading efficiency of SN-38 into the delivery systems. Notably, only 20% (w/w) SN-38 loading was observed in NK012 formulation, which is the only SN-38-conjugated PEG-poly(glutamic acid) micellar NPs under clinical trial phase-II investigation [352, 363]. The conjugation level of SN-38 in mPEO-*b*-PBCL/SN-38 and mPEO-*b*-PCCL/SN-38 under this study were < 15% (w/w); pointing to the necessity for further optimization to increase the loading despite the high potency of SN-38. Higher drug conjugation levels were expected for PEO-*b*-PCCL compared to the PEO-*b*-PBCL due to the existance of higher pendent functional COOH groups in PCCL-based polymer compared to that for the PBCL polymer, which only holds one COOH group at the end of polymer chain. In practice, we observed a slightly higher SN-38 loading in PCCL-based polymer than PBCL-based polymer; however, no significant difference was observed after statistical analysis.

In previous studies, a proportional correlation was identified between the hydrophobicity of block copolymers and the kinetic stability of polymeric micelles [293, 364]. An increase in the hydrophobicity of the copolymers, either by core-forming block elongation (higher degree of polymerization) or by introducing more hydrophobic pendant or end groups, was shown to reduce the CMC, aggregation, dissociation rate, and hydrolytic degradation of formed micelles as a result of improved thermodynamic and kinetic stability. In line with previous observations, conjugation of hydrophobic SN-38 to the core of both polymeric micellar formulations under study here led to improved thermodynamic and kinetic stability of micelles. However, mPEO-b-PBCL/SN-38 micelles showed significantly lower CMC and superior kinetic stability than that of mPEO-b-PCCL/SN-38. This could be due to the presence of aromatic and more hydrophobic benzyl pendant groups in the mPEO-*b*-PBCL and intra-micellar benzyl π-π stacking interactions compared to the pendant carboxyl group in the mPEO-b-PCCL/SN-38 structure [293, 294]. In agreement with the above observation, the presence of the benzyl structure in the micellar core also contributed to the prevention of micellar dissociation by destabilizing agents perhaps by making the core more rigid. In contrast, more rapid dissociation and PDI elevation of mPEO-*b*-PCCL/SN-38 micelles have been observed owing to the presence of hydrophilic carboxyl pendent groups in the core structure. In addition, the COOH groups of the PCCL backbone, being partially ionized at neutral pH, could be responsible for micellar swelling and dissociation due to the generation of repulsive forces between similarly charged -COOH groups [365, 366].

In our study, the release of SN-38 from mPEO-*b*-PBCL/SN-38 and mPEO-*b*-PCCL/SN-38 micelles was significantly slower than free SN-38 from dialysis bags, validating the slow cleavage of the linkage between SN-38 and the polymeric backbone and/or cleavage of SN-38-caprolactone derivatives from the micellar core. Over 90% burst release of free SN-38 from the

dialysis bag within 6 h demonstrated that the release of the drug from the dialysis bag to the release medium was not a rate-limiting factor. We used a 3500 Da MW cut off for the dialysis membrane that does not allow passage of SN-38 conjugated polymer or micelles to the recipient media, but cleaved SN-38 and/or SN-38-attached to caprolactone oligomers and/or derivatives resulting from the degradation of the polymeric backbone, can easily pass through the dialysis membrane. Despite lower hydrophobicity of the PCCL compared to the PBCL core, the release profiles of SN-38 from both micellar structures were similar. This may reflect a similar kinetics of SN-38-polymer link cleavage within the micellar core, since the release study was performed above the CMC of each polymeric-drug conjugate.

We then investigated the cytotoxicity of polymer-SN-38 micellar conjugates to assess whether the released SN-38 species from the formulations and/or the polymer-drug conjugates in intact form, are bioactive and have equal potency to that of free SN-38. The cytotoxicity resulting from SN-38-incorporated micelles followed a similar trend as observed in the release study. Both SN-38-conjugated micellar formulations resulted in similar viability reduction in human CRC cell lines (**Fig. 4.5**). The free SN-38 was more cytotoxic than micellar SN-38. This was expected due to the sustained release of SN-38 from mPEO-*b*-PBCL/SN-38 and mPEO-*b*-PCCL/SN-38 micelles. Furthermore, both micellar SN-38 formulations were shown to be more cytotoxic than irinotecan in human CRC cell lines perhaps due to more efficient release of active SN-38.

To confirm the *in vitro* mechanism of cytotoxic action for micellar SN-38 formulations, their ability to induce caspase 3/7 was tested in comparison to free SN-38 or irinotecan. The study was conducted at respective IC_{50} concentrations (24 h) of these drugs, so that a comparison on the mode of cytotoxic drug action rather than drug potency could be made. It is evident that caspases, a family of conserved proteases, play an important role in programmed cell death [367]. Polymeric

micellar SN-38 significantly enhanced the caspase-3/7 activation levels compared to irinotecan in all the CRC cell lines at their respective IC_{50}s. Higher caspase-3/7 activation level for mPEO-*b*-PCCL/SN-38 over mPEO-*b*-PBCL/SN-38 treatment in some CRC cells could be a reflection of higher micellar kinetic stability of mPEO-*b*-PBCL/SN-38, which may eventually lead to lower drug release/core cleavage, extra- or intracellulalry, compared to that for the PCCL/SN-38 based formulation [368]. The difference in cytotoxicity and caspease-3/7 activation of the two formulations may also be due to differences in the intracellular trafficiking of the polymer/SN-38 conjugates or SN-38 released species from the two formulations. Further studies are required to elucidate this point.

In general, drug delivery systems in systemic circulation are expected to be in contact with RBCs, which is the most abundant cellular constituent of the blood [369, 370]. From a safety viewpoint, it is indispensable to investigate the effects of delivery systems on cells encountered throughout the pathway to reach the site of therapeutic targets prior to preclinical and clinical studies. Therefore, SN-38 micellar formulations were tested for hemolytic activity. In our study, mPEO-*b*-PBCL/SN-38 micelles showed no hemolytic activity On the other hand, mPEO-*b*-PCCL/SN-38 micelles resulted in relatively higher percentages of hemolysis at various concentrations under study. As previously investigated, the hemolytic activity (< 15% at IC_{50} concentration) of mPEO-*b*-PCCL/SN-38 could be attributed to the presence of ionized pendent -COOH groups [371]. This was evident as the hemolytic activity of drug-free mPEO-*b*-PCCL micelles reached > 25% supporting the role of –COOH functional group-associated hemolytic activity [372].

4.5. Conclusion

In summary, in this study, the chemical conjugation of SN-38 to the hydrophobic core of self-associating PEO-poly(ester) micelles through two different strategies was successfully performed. This led to aqueous solubilized levels of SN-38 that are suitable for systemic administration in the form of PEO-poly(ester) based nanocarriers in *in vivo* animal models of CRC. Between the two polymeric micellar formulations, those with pendent SN-38/and free COOH groups, i.e., mPEO-*b*-PCCL/SN-38 were found to be less kinetically and thermodynamically stable and hemolytic. Both micellar NPs maintain the cytotoxic activity and mechanism of action of SN-38 in CRC cells, *in vitro*. The overall findings point to superiority of mPEO-*b*-PBCL/SN-38 micellar formulation as a potential delivery system for SN-38 against CRC.

4.6. Acknowledgments

This study was supported by the Canadian Institutes of Health Research to Afsaneh Lavasanifar (FRN159757) and the Alberta Cancer Foundation Transformative Program Project (26603) to Michael Weinfeld. Sams Sadat was supported by Alberta Innovates and CIHR Fellowship. The authors thank Mr. Vishwanatha Somayaji, Faculty of Pharmacy and Pharmaceutical Sciences, University of Alberta for assistance with ^{1}H NMR analysis and the Advanced Microscopy Facility (AMF), Department of Biological Sciences, University of Alberta for assistance with TEM analysis.

4.7. Declaration

The authors declare the following competing financial interest(s): Material in this manuscript has been included in recent US patent applications. Dr. Lavasanifar is Vice-President of Meros Polymers which has the license to PEO-PBCL polymer used in this manuscript.

Supporting information

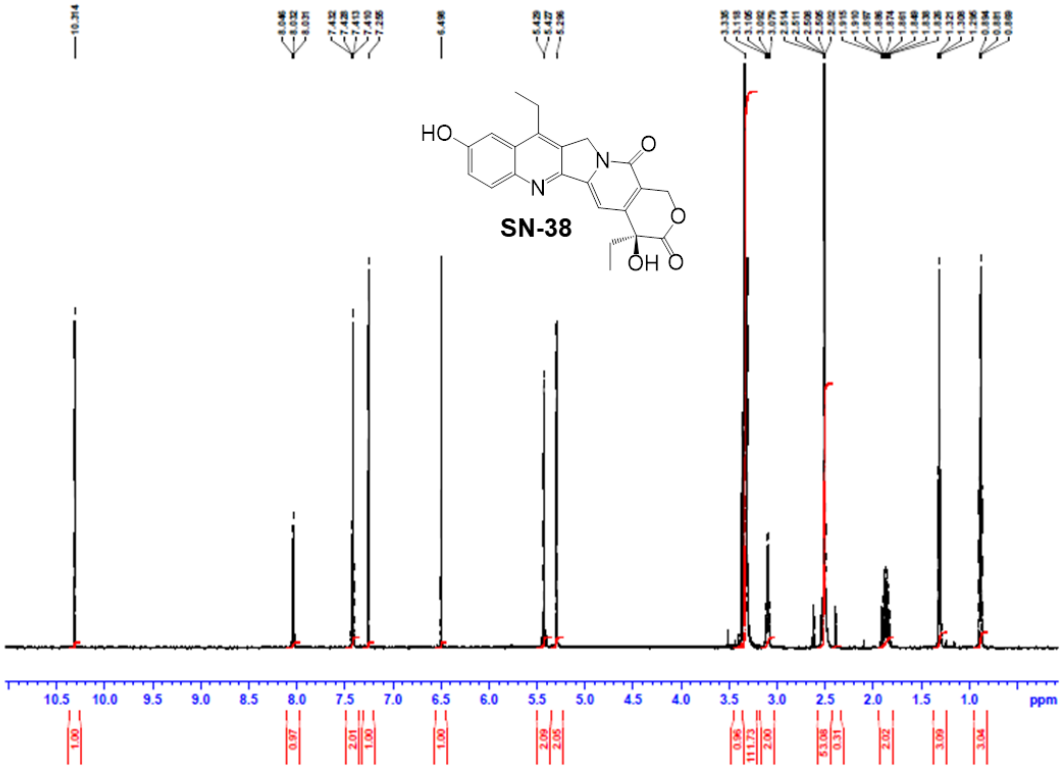

Supplementary Figure 4.1: ^{1}H NMR spectra of SN-38.

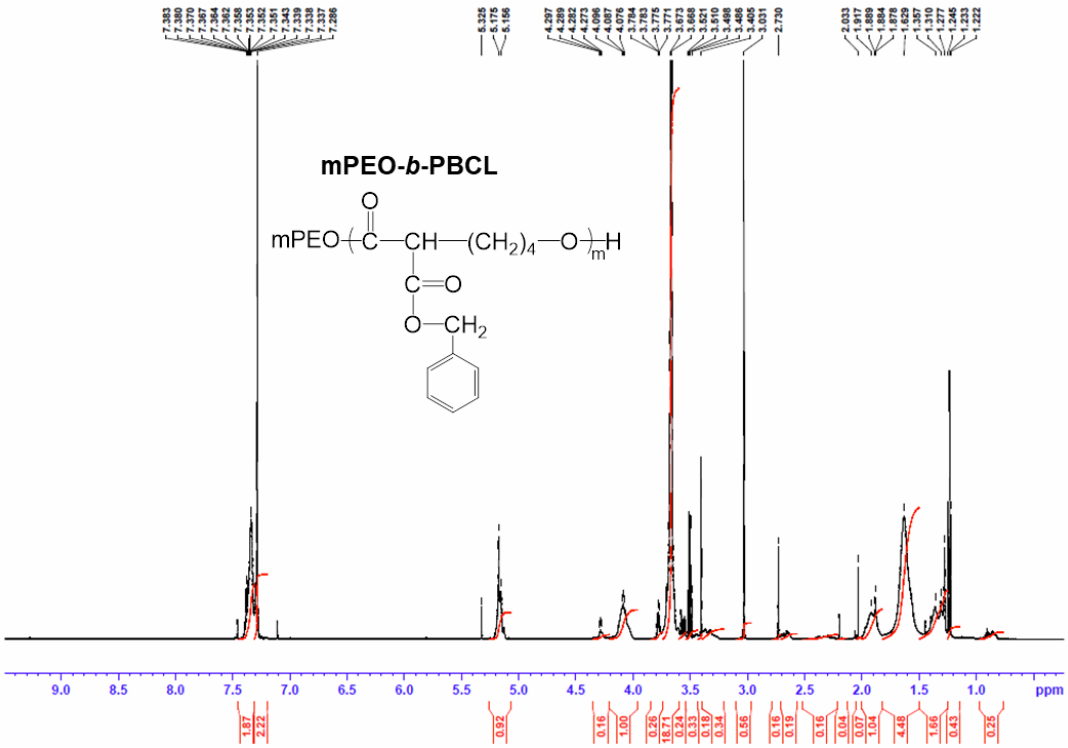

Supplementary Figure 4.2: ^{1}H NMR spectra of mPEO-*b*-PBCL.

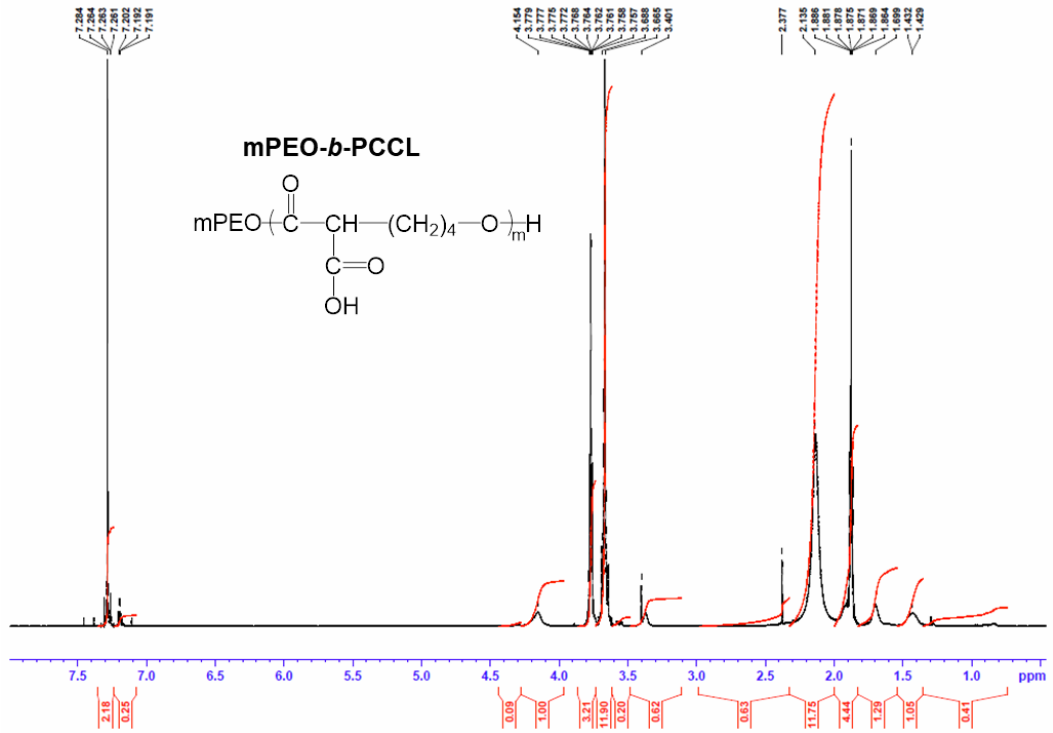

Supplementary Figure 4.3: ^{1}H NMR spectra of mPEO-*b*-PCCL.

Chapter 5: Synergistic nanomedicine delivering topoisomerase I toxin (SN-38) and inhibitors of polynucleotide kinase 3′-phosphatase (PNKP) for enhanced treatment of colorectal cancer

5.1. Introduction

Combination therapy is a common approach in treating different types of cancer. Drug combinations may be used to provide additive effects on heterogenous tumor populations leading to better control of tumor growth. Alternatively, drug combinations may be used to sensitize cancer cells to the effect of common chemotherapeutics and show synergistic anticancer effects. Application of nanomedicine for the precise and controlled spatial and temporal delivery of synergistic drug combinations to tumor tissue and cells and/or synergistic dose ratios can enhance the effect of common chemotherapeutics to a greater extent. An example nanomedicine developed for this purpose is the U.S. Food and Drug Administration (FDA) approved liposomal formulation of daunorubicin and cytarabine (VYXEOS, Jazz Pharmaceuticals, Inc.) for treating acute myeloid leukemia [373].

Our research group has previously reported on the development of novel inhibitors of a DNA repair enzyme, polynucleotide kinase 3′-phosphatase (PNKP), that were able to sensitize colorectal cancer (CRC) cells to the DNA damaging effect of topoisomerase I (TOP1) inhibitor, irinotecan, as well as ionizing radiation (IR), *in vitro* [202, 267]. A polymeric micelle (PM) formulation of a small molecule inhibitor of PNKP, known as A83B4C63, was shown to redirect the encapsulated A83B4C63 away from normal tissue to HCT116 tumor xenograft. As a result, the PM formulation of A83B4C63, which was made from self-assembly of methoxy poly(ethylene oxide)-*b*-poly(α-benzyl carboxylate-e-caprolatcone) (mPEO-*b*-PBCL) was effective in increasing the inhibitory effect of IR on the growth of HCT116 xenografts, a CRC tumor, *in vivo*.

Irinotecan, also known as CPT-11, Camptosar, 7-ethyl-10-[4-(1-piperidino)-1-piperidino] carbonyloxycamptothecin, is a semi-synthetic camptothecin derivative, approved by the FDA for primary CRC treatment [374]. Irinotecan, is the water-soluble prodrug of SN-38, and is

metabolized by endogenous carboxylesterase into its biologically active metabolite; 7-ethyl-10-hydroxycamptothecin or SN-38. The active metabolite of irinotecan is 1,000 times more potent than its prodrug [375]. Besides, the conversion from irinotecan to SN-38 is very limited and slow (< 10%) and cell dependent. [345, 376]. Nanodelivery of SN-38 and its combination with inhibitors of PNKP was hypothesized to overcome the problem of poor-solubility for SN-38 and at the same time enhance the potency of anti-TOP1 treatment in CRC. In this context, PMs co-encapsulating both drugs were expected to be particularly more effective owing to delivery of the synergistic combination to the same population of cells at the same time. This combinational nanomedicine was also expected to reduce the side-effect of the therapy, by alleviating the need for application of high doses of TOP1 inhibitor and reducing delivery of the synergistic combination to normal tissues [346, 375].

In the current manuscript, we described development of PMs based on mPEO-β-PBCL for co-delivery of A83B4C63 and SN-38, a potent TOPI inhibitor, at synergistic ratios (**Fig. 5.1**) and characterized the physicochemical properties of this formulation making comparison with PMs for individual A83B4C63 or PMs for SN-38 alone. The effect of mixing the PMs of A83B4C63 as a separate entity to that of TOPI inhibitor as free or PM formulation or upon co-encapsulation in the same PM, on their anticancer activity in two compounds in CRC cells have been explored.

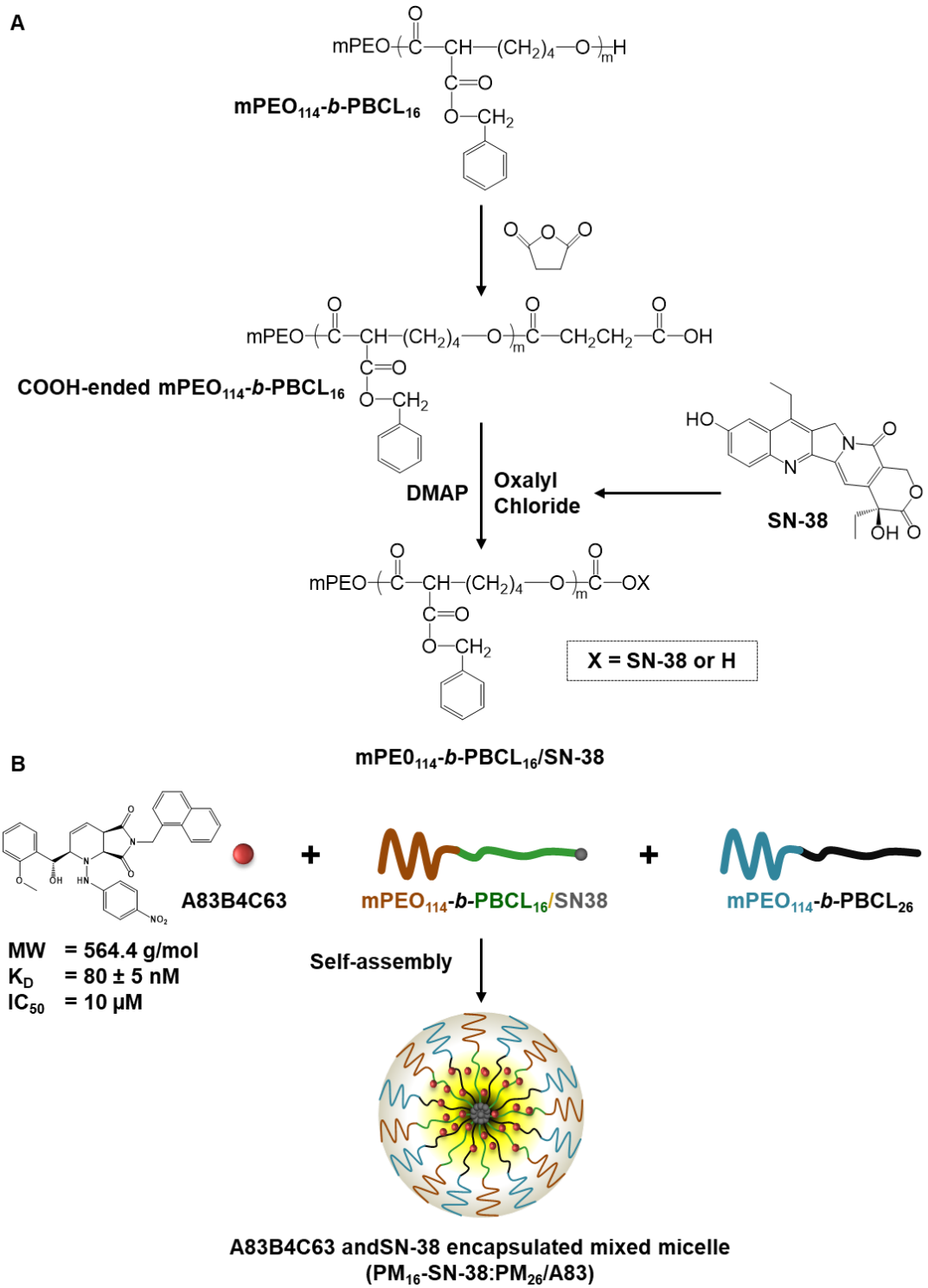

Figure 5.1: Scheme for (A) the synthesis of mPEO$_{114}$-*b*-PBCL$_{16}$/SN-38; (B) Self-assembly to mixed micelles composed of mPEO$_{114}$-*b*-PBCL$_{16}$/SN-38 and mPEO$_{114}$-*b*-PBCL$_{26}$ co-encapsulating A83B4C63. PM$_{16}$-SN-38 is the abbreviation used for mPEO$_{114}$-*b*-PBCL$_{16}$/SN-38, while PM26/A83 is the abbreviation used for mPEO$_{114}$-PBCL$_{26}$ micelles physically encapsulating A83B4C63. A mixture of the two polymer co-encapsulating SN-38 and A83B4C63 is abbreviated as PM$_{16}$-SN-38: PM$_{26}$/A83.

5.2. Materials and methods

5.2.1. Materials

Methoxy-polyethylene oxide (mPEO) (average molecular weight of 5000 $gmol^{-1}$), sodium dodecyl sulfate (SDS), and bovine serum albumin (BSA) and all research grade organic solvents were purchased from Sigma (St. Louis, MO, USA). α-benzyl carboxylate-ε-caprolactone monomer was synthesized by Alberta Research Chemicals Inc. (Edmonton, AB, Canada). Stannous octoate was purchased from MP Biomedicals Inc. (Tuttlingen, Germany). (S)-4, 11-Diethyl-4, 9-di-OH-1, 12-dihydro-4H-2-oxa-6,12a-diaza-dibenzo[b, h]fluorene-3,13-dione (SN-38) (purity > 97%) was purchased from abcr GmbH (Karlsruhe, Germany). All other chemicals and reagents used were of analytical grade.

5.2.2. Synthesis of block copolymers and A83B4C63

The block copolymers of methoxy poly(ethylene oxide)-*b*-poly(α-benzyl carboxylate-ε-caprolactone (mPEO-*b*-PBCL) with two different degrees of polymerization (DP = 16 and 26) for the PBCL block were synthesized by ring-opening polymerization of α-benzyl carboxylate-ε-caprolactone using methoxy-PEO (MW: 5000 $gmol^{-1}$) as an initiator and stannous octoate as catalyst according to a previously described method [354].

The polysubstituted imidopiperidine compound, 2-[hydroxy(2-methoxyphenyl)methyl]-6-(naphthalene-1-ylmethyl)-1-[(4-nitrophenyl)amino]-2H, 4aH, 7aH-pyrrolo[3,4-b]pyridine-5,7-dione or A83B4C63 was synthesized using a three-component aza[4+2]/allylboration reaction and purified to homogeneity via HPLC as previously described method [280]. The structure of the compound was confirmed by ^{1}H NMR, IR, and LC-MS as previously reported [267].

5.2.3. Synthesis of carboxyl-terminated mPEO$_{114}$-*b*-PBCL$_{16}$ block copolymers

The mPEO-*b*-PBCL block copolymer with DP of 16 (mPEO$_{114}$-*b*-PBCL$_{16}$) was chemically modified through reaction with succinic anhydride to generate mPEO-*b*-PBCL copolymer with the end-capped carboxylic acid functional group (mPEO$_{114}$-*b*-PBCL$_{16}$-COOH) as previously described with minor modifications [254]. In brief, 4 g of mPEO$_{114}$-*b*-PBCL$_{16}$ and succinic anhydride (1.5 times molar excess of polymer) were mixed and placed in a previously flame-dried ampoule. The ampoule was sealed and kept in an oven for 6 h reaction at 140ºC. Thereafter, COOH-terminated block copolymers were dissolved in dichloromethane and subsequently, precipitated in hexane and centrifuged at 3000 rpm [355]. The supernatant was discarded and the final product was washed twice with hexane, then dried in a vacuum oven overnight at room temperature.

5.2.4. Conjugation of SN-38 to mPEO$_{114}$-*b*-PBCL$_{16}$-COOH copolymers

Conjugation of SN-38 to mPEO$_{114}$-*b*-PBCL$_{16}$-COOH was performed by activation of carboxylic acid terminal group on PBCL block using oxalyl chloride and 4-dimethylaminopyridine (DMAP). At first, 1 g of mPEO$_{114}$-*b*-PBCL$_{16}$-COOH was added into 5 mL of refluxed dichloromethane (DCM) in a round bottom flask under continuous magnetic stirring and heat. Then, 200 µL of oxalyl chloride was added to the reaction mixture under the same reflux condition and left for 5 h. During the reaction, the acidity of the reaction mixture was checked every hour by pH paper. After 5 h of the reaction, the content was semi-dried by heat. When the reaction content reached to ¼ of the original volume, dry anhydrous hexane (~ 5 mL) was added into the semi-dried polymer in the flask. Immediately after discarding the hexane, residual dried polymer was collected inside the flask. Meanwhile, 50 mg of SN-38 and 30 mg of DMAP were added in 5 mL of dimethylformamide (DMF), subsequently vortexed, and water bath sonicated until SN-38 was

completely dissolved. Then, the solution of SN-38 and DMAP was transferred to round bottom flask which contained the polymer. This flask was then placed in ice-water bath while stirring under Ar gas. After 20 min, the ice was removed, and the reaction was left under continuous stirring at room temperature overnight. The next day, the reaction mixture was identified with reddish color and was diluted with 7 mL of dimethyl sulfoxide (DMSO), then dialyzed against DMSO for 48 h and deionized water for 24 h to remove unreacted SN-38 and other impurities. The solution inside the dialysis bag was freeze-dried to obtain a dry product.

5.2.5. Characterization of block copolymers and drug-copolymer conjugates

The synthesized mPEO-*b*-PBCL block copolymers and mPEO-*b*-PBCL-SN-38 conjugates were characterized for their number average molecular weights by ^{1}H NMR (600 MHz Avance III - Bruker, East Milton, ON, Canada) using deuterated chloroform ($CDCl_3$) as solvent. The DP of PBCL block was calculated from the ^{1}H NMR based on the ratio of the peak intensity of protons from the ethylene (-CH_2CH_2O-) moiety of PEO (δ = 3.65 ppm) to the peak intensity of the protons from the (-OCH_2-) methylene of caprolactone block (δ = 4.05 ppm), considering a molecular weight of 5000 $gmol^{-1}$ for the PEO block. The level of carboxylic acid termination of mPEO-*b*-PBCL block copolymer was also measured based on ^{1}H NMR. The level of SN-38 conjugation was expressed in loading percentage (% w/w) with respect to the carboxylic acid-terminated residue of mEPO-*b*-PBCL.

5.2.6. Preparation of polymer micellar formulations of A83B4C63 and/or SN-38 and their characterization

Table 5.1 shows the formulation details of different samples under this study, including the mixing ratio between the PM components, i.e., $mPEO_{114}$-*b*-$PBCL_{16}$-SN-38, $mPEO_{114}$-*b*-$PBCL_{26}$, and/or A83B4C63, in each formulation. Nano-formulations were prepared as described before

[267]. In brief, the weighted amounts of different PM components (with respective ratios according to **Table 5.1**) were dissolved in 1 mL of acetone. Then, this solution was added dropwise to 3 mL of aqueous phase (deionized water) and left overnight with continuous stirring with a magnetic bar under fume hood to completely evaporate the organic solvent. The un-encapsulated drug was removed by centrifugation at 11600 × g for 5 min to obtain drug-loaded PMs. The size (Z-average diameter), polydispersity index (PDI), zeta potential (ZP), and critical micellar concentration (CMC) of the formulations prepared from individual or mixed block copolymer components were measured by dynamic light scattering (DLS) using a Malvern Zetasizer 3000 (Malvern Instruments Ltd, Malvern, UK). SN-38 conjugation level was measured using Synergy-H1 BioTEK microplate reader (Winooski, VT, USA) at a wavelength of 383 nm. A83B4C63 loading was measured using a Varian Prostar 210 HPLC system. Reversed phase chromatography was carried out with a Microsorb-MV 5 µm C18-100 Å column (4.6 mm × 250 mm) with 20 µL of sample injected and eluted under isocratic conditions with a solution of 0.1% trifluroacetic acid: acetonitrile (1:1 v/v) at a flow rate of 0.7 mL/min at room temperature. Detection was performed at 280 nm wavelength for A83B4C63 using a Varian 335 Photodiode Array HPLC detector (Varian Inc., Palo Alto, CA, USA). In this study, A83B4C63 control was solubilized in DMSO for all *in vitro* experiments.

To investigate micellar stability, CMC of the block copolymers was also determined by DLS technique following a previously published method [294]. In brief, a series of micellar solutions of PM_{26}, PM_{26}/A83, PM_{16}-SN-38, PM_{16}-SN-38:PM_{26}, and PM_{16}-SN-38:PM_{26}/A83 with a polymeric concentration range of 1500 to 0.05 µg/mL were prepared in glass vials. The intensity of the scattered light for prepared samples was detected at an angle of 173º under single attenuator index. Measurements were carried out in polystyrene cells at 25ºC. The count rate (Kcps) as a

function of the intensity of the scattered light was plotted against the concentrations of block copolymers with or without payloads.

To determine the stability of micelles against dissociation, kinetic stability was also measured by DLS method as previously described [356]. In brief, micelles were prepared using individual copolymers or a combination of polymers with the compositions detailed in **Table 5.1**. The total polymer concentration was 3 mg/mL. Micelles were incubated with an aqueous solution of destabilizing agent, sodium dodecyl sulfate (SDS) (20 mg/mL) at a ratio of 2:1 (v/v). The intensity of scattered light and PDI were measured at different incubation time intervals (0, 1, 2, 4, 8, and 24 h).

Table 5.1: Formulation details for samples under study, including the mixing ratio between the micellar components. The number shown in the subscript of the formulation names indicates the degree of polymerization of each block in the copolymers as determined by ^{1}H NMR spectroscopy.

Formulation keys	**Formulations details**	**Mixing ratio (w/w)**
PM_{16}-SN-38	$mPEO_{114}$-*b*-$PBCL_{16}$-SN-38	-
PM_{16}-SN-38:PM_{26}	$mPEO_{114}$-*b*-$PBCL_{16}$-SN-38 + $mPEO_{114}$-*b*-$PBCL_{26}$	1:1
PM_{16}-SN-38:PM_{26}/A83	$mPEO_{114}$-*b*-$PBCL_{16}$-SN-38 + $mPEO_{114}$-*b*-$PBCL_{26}$ + A83B4C63	1:1:0.33
PM_{26}/A83	$mPEO_{114}$-*b*-$PBCL_{26}$ + A83B4C63	1:0.33
PM_{26}	$mPEO_{114}$-*b*-$PBCL_{26}$	-
A83	A83B4C63 + DMSO	-

5.2.7. Transmission electron microscopy (TEM)

The morphology of self-assembled structures under study was investigated by TEM using a Morgagni TEM (Field Emission Inc., Hillsboro, OR) with Gatan digital camera (Gatan, Pleasanton, CA). In brief, 20 μL of micellar solution with a polymer concentration of 0.5 mg/mL was placed on a copper-coated grid. The grid was held horizontally for 1 min to allow the colloidal particles to settle down. The excess fluid was removed by filter paper. The copper-coated grids holding the aqueous samples were then negatively stained by 2% phosphotungstic acid. After 2 min, the excess fluid was removed by filter paper and the grid was loaded into the TEM for image analysis.

5.2.8. *In Vitro* drug release

In vitro release of SN-38 and A83B4C63 from the self-assembled structures was investigated using dialysis-bag diffusion technique. Each dialysis bag (Spectra Por dialysis tubing, MWCO = 3.5 kDa, Spectrum Laboratories, Rancho Dominguez, CA, U.S.A.), containing 3 mL of the micellar formulation in water or free SN-38 and A83B4C63 dissolved in DMSO, was immersed into 300 mL release medium (4% albumin in ultrapure water) maintained at 37ºC in a shaking water bath with 65 rpm (Julabo SW 22, Seelbach, Germany). At selected time intervals (0, 1, 2, 4, 6, 8, and 24 h), 300 μL aliquots from inside of the dialysis bag were withdrawn and replaced with equal volume of fresh release media (water). The concentrations of SN-38 in collected samples were determined by UV-Vis spectrophotometer (BioTEK, Winooski, VT, USA). Detection was performed at a wavelength of 383 nm. The concentrations of A83B4C63 in collected samples were measured and analyzed using a Varian Prostar 210 HPLC system. All experiments were carried out in triplicate.

5.2.9. Cell lines

Two CRC cell lines, HCT116 and HT-29 originally purchased from ATCC were used. The cells were cultured at 37ºC in 5% CO_2 in a humidified incubator in a 1:1 mixture of Dulbecco's modified Eagle medium and F12 (DMEM/F12) supplemented with 10% FBS, 50 U/mL penicillin, 50 mg/mL streptomycin, 2 mmol/L L-glutamine, 0.1 mmol/L nonessential amino acids, and 1 mmol/L sodium pyruvate. All culture supplements were purchased from GIBCO, Life Technologies Inc. (Burlington, ON, CA). All cell lines were routinely tested for mycoplasma in the lab.

5.2.10. *In vitro* synergy and antagonism evaluation

The day before the treatment, 2×10^3 HCT116 and HT-29 cells were plated in each well of 96-well flat-bottomed plates. Then cells were treated with irinotecan, PM_{26}/A83, SN-38, PM_{16}-SN-38, irinotecan + PM_{26}/A83, SN-38 + PM_{26}/A83, PM_{16}-SN-38 + PM_{26}/A83 for 48 h. The cells were treated with the formulations at 0.001, 0.01, 0.1, 1, 10, and 100 μM concentrations for irinotecan and SN-38 formulations. The treating concentrations of A83B4C63 as part of formulations were 5, 10, 20, and 40 μM for the combination treatments and the control cells received only 0.1% DMSO. After the incubation time point, cells were treated with the MTS reagent (CellTiter 96® AQueous One Solution Cell Proliferation Assay, Promega, USA) to measure their viability. Each experiment was performed in quadruplicates. The cell viability percentages were calculated using the following formula:

$$\text{Cell viability (\%)} = \frac{\text{Absorbance of treated cells} - \text{Absorbance of blank well}}{\text{Absorbance of untreated cells} - \text{Absorbance of blank well}} \times 100$$

The cell viability data following a combination template was processed using Loewe classical synergy models in Combenefit® software program [377].

5.2.11. *In vitro* cytotoxicity assay

The CellTiter 96® AQueous One Solution Cell Proliferation Assay (MTS) kit from Promega, USA was used to assay the cytotoxicity of irinotecan, irinotecan + PM_{26}/A83, SN-38, SN-38 + PM_{26}/A83, PM_{16}-SN-38, PM_{16}-SN-38 + PM_{26}/A83, PM_{16}-SN-38:PM_{26}, and PM_{16}-SN-38:PM_{26}/A83 in HCT116 and HT-29 cells according to the provided company protocol. In brief, 2×10^3 cells were plated in each well of 96-well flat-bottomed plates 24 h prior to the treatments. Then, cells were treated with the formulations at the concentration range of 0.001 to 100 μM for irinotecan and SN-38 formulations. The PM_{26}/A83 with a fixed concentration as of 10 μM was used for the combination treatments and the control cells received only 0.1% DMSO. The choice of this concentration was based on the results of synergy evaluation, in which at a concentration of 10 μM for A83B4C63, a synergy with SN-38 at a concentration range of 0.01-1 μM has been observed. After different experimental incubation time points (24, 48, and 72 h), 20 μL of MTS reagent was added in each well and further incubated for 1 h at 37ºC before measuring the absorbance at 490 nm using BioTEK microplate reader. Each experiment was performed in quadruplicates. The cell viability percentages were calculated using the formula mentioned in previous method section.

5.2.12. Western blot analysis

Western blotting was performed to assess the *in vitro* levels of caspase-3, caspase-7, PARP, and γ-H2AX proteins after treating both HCT116 and HT-29 cell lines with A83, irinotecan, irinotecan + PM_{26}/A83, SN-38, SN-38 + PM_{26}/A83, PM_{16}-SN-38, PM_{16}-SN-38 + PM_{26}/A83, PM_{16}-SN-38:PM_{26}, PM_{16}-SN-38:PM_{26}/A8B4C63, and PM_{26}/A83. In brief, 1×10^6 cells were plated in each well of 6-well plates 24 h prior to the treatments. Then, the cells were treated with the media containing various treatments the final concentrations equivalent to the respective IC_{50}

concentrations of irinotecan, SN-38, PM_{16}-SN-38, and PM_{16}-SN-38:PM_{26} for 6 h in combination with or without 10 μM PM_{26}/A83. The cells of 3 controls received only 0.1% DMSO, 10 μM A83, and 10 μM PM_{26}/A83, respectively. Protein extracts for western blot analysis were prepared using commercial RIPA lysis buffer (ThermoFisher Scientific, Canada) supplemented with a cocktail of protease inhibitors (Millipore Sigma, Canada). Protein concentrations were measured using the BCA assay kit (Pierce/ThermoFisher Scientific, Canada) according to the manufacturer's protocol. Equal concentrations of protein were separated by SDS-PAGE and transferred to nitrocellulose membranes. After blocking with 5% skimmed milk in TBST (50 mM Tris-HCl, pH 7.4, 150 mM NaCl, and 0.1% Tween 20), the blots were incubated with the respective primary antibodies (cleaved caspase-3 cat# 9661S, cleaved caspase-7 cat# 9491S, PARP cat# 9542S, phospho-histone H2A.X (Ser139) cat# 9718S) and secondary antibody (HRP-linked anti-rabbit IgG cat# 7074S) purchased from Cell Signaling Technology (Whitby, ON, Canada). The protein bands were detected using an enhanced chemiluminescence (ECL) based system (Pierce/ThermoFisher Scientific, Canada). The band intensities for the PNKP protein were quantified by performing optical density analysis using ImageJ software. Each experiment was carried out in triplicate.

5.2.13. Statistical analysis

Data are shown as mean ± standard error of at least three experiments. GraphPad Prism9 software (La Jolla, CA, USA) was used for statistical analysis. The significance of difference between groups was assessed using one-way ANOVA followed by Tukey's post-hoc analysis. If a significant difference was found among the groups, median ranks between pairs of groups were compared using the Mann-Whitney U test. Differences in the physicochemical characterization of micellar formulations were also tested using the unpaired student's t-test. A value of $p \leq 0.05$ was considered as statistically significant in all experiments.

5.3. Results

5.3.1. Characterization of block copolymers and PM formulations

The ^{1}H NMR spectra of PM_{16}-SN-38 and peak assignments are shown in **Supplementary Fig. 5.1**. Using ^{1}H NMR data as reported before, the DP of PBCL block in mPEO-*b*-PBCL copolymers used for SN-38 conjugation or A83B4C63 loading was found to be 16 and 26, respectively [254, 267, 294, 321, 322]. The end-capped carboxylic acid functional group conversion of PBCL block of mPEO-*b*-PBCL copolymer was 65-67%. The conjugated content (% w/w) of SN-38 to mPEO-*b*-PBCL-COOH was 15.67 ± 0.34 as measured by UV spectroscopy.

The physicochemical characterizations of the self-assembled PM_{16}-SN-38, PM_{16}-SN-38:PM_{26}, PM_{16}-SN-38:PM_{26}/A83, PM_{26}/A83, and PM_{26} micelles were also performed by measuring their average diameter, surface charge, PDI, and CMC as summarized in **Table 5.2**. The average diameters of all the micellar formulations were below 100 nm with PDI range below 0.22. The average hydrodynamic diameter of PM_{16}-SN-38 was significantly lower ($p < 0.0001$) than that of it mixed micelle with PM_{26}, i.e., PM_{16}-SN-38:PM_{26} (without A83). Co-encapsulation of PM_{16}-SN-38 and A83B4C63 in PM_{16}-SN-38:PM_{26}/A83 resulted in larger size (58.41 ± 0.29 nm) among all the formulations under study.

The mean zeta potential for PM_{16}-SN-38 was on the negative side. The zeta potential of PM_{26}/A83 and PM_{26}, on the other hand was neutral. When PM_{16}-SN-38 formed mixed micelles with PM_{26} (without or with A83B4C63 encapsulation), i.e., in PM_{16}-SN-38:PM_{26}, PM_{16}-SN-38:PM_{26}/A83, the zeta potential shifted towards the neutral range (from 0.07 to 0.08 mV), which was significantly different from the zeta potential of PM_{16}-SN-38 micelles ($P < 0.003$) but not different from that of PM_{26} samples.

The measured CMCs of PM_{16}-SN-38, PM_{16}-SN-38:PM_{26}, PM_{16}-SN-38:PM_{26}/A83, PM_{26}/A83, and PM_{26} were 0.33 ± 0.09, 0.54 ± 0.12, 0.47 ± 0.22, 0.43 ± 0.11, and 0.48 ± 0.21 μg/mL, respectively (Table 2). No statistical significance was identified between the CMCs of the formulations under study.

The loading of SN-38 in the mixed micellar formulation, i.e., PM_{16}-SN-38:PM_{26}, PM_{16}-SN-38:PM_{26}/A83, of that in the PM_{16}-SN-38 owing to 1:1 molar mixing ratio of polymers. The A83B4C63 encapsulation, was found to significantly decrease in mixed micellar formulation of PM_{16}-SN-38:PM_{26}/A83 co-encapsulating both SN-38 and A83B4C63, compared to that of PM_{26}/A83 ($P< 0.05$) (**Table 5.2**).

Table 5.2. Physicochemical characteristics of all self-assembled micellar formulations (n = 4).

Micellar Formulations [a]	Size [b] ± SD (nm)	PDI [c] ± SD	Zeta Potential [d] ± SD (mV)	CMC [e] ± SD (μg/mL)	SN-38 Loading [f] (% w/w)	A83B4C63 Loading [g] (% w/w)
PM_{16}-SN-38	17.99 ± 0.04 [h]	0.21 ± 0.01	-1.69 ± 0.24 [h]	0.33 ± 0.09	15.67 ± 0.34 [h]	-
PM_{16}-SN-38:PM_{26}	46.69 ± 0.27 [h]	0.15 ± 0.01	0.08 ± 0.02	0.54 ± 0.12	7.64 ± 0.83	-
PM_{16}-SN-38:PM_{26}/A83	58.41 ± 0.29 [h]	0.18 ± 0.01	0.07 ± 0.01	0.47 ± 0.22	7.91 ± 0.66	16.13 ± 0.11
PM_{26}/A83	53.31 ± 0.21 [h]	0.19 ± 0.02	0.09 ± 0.01	0.43 ± 0.11	-	23.06 ± 0.63 [h]
PM_{26}	47.39 ± 0.17 [h]	0.17 ± 0.01	0.09 ± 0.03	0.48 ± 0.21	-	-

[a] The number shown in the subscript indicates the degree of polymerization of each block as determined by ^{1}H NMR spectroscopy.
[b] Hydrodynamic diameter (Z average) determined by DLS.
[c] Average PDI of micellar size distribution.
[d] Average surface charge (zeta potential) of the micelles.
[e] Average CMC measured by DLS.
[f] SN-38 loading (w/w %) $= \frac{\text{Amount of conjugated SN}-38}{\text{Total amount of polymer}} \times 100$; measured using UV-Vis spectrophotoscopy.
[g] A83B4C63 loading (w/w %) $= \frac{\text{Amount of conjugated SN}-38 \text{ or A83B4C63}}{\text{Total amount of polymer}} \times 100$; measured using HPLC.
[h] Differences were considered significant at $*p \leq 0.05$ (either one-way ANOVA multiple comparison test following Tukey's method or student's t-test)

5.3.2. Transmission electron microscopy (TEM)

The morphology of the self-assembled structures was investigated by TEM, confirming the formation of spherical-shaped micelles with uniform size in most cases (**Fig. 5.2A-5.2E)**. The exception was PM_{26}/A83 which showed deviations from spherical morphology and signs of aggregation under current experimental conditions. Moreover, a similar distribution pattern in the micellar population having a clear boundary was observed in TEM images of all micelles, indicating the lower aggregation tendency of micelles, except for PM26/A83. Dynamic light scattering profiles showed formulation of a single peak for micelles formed from one or a mixture of block copolymers understudy **(Fig 5.2F-5.2J).** The trend of change in the average diameter and size distribution between samples was similar in the two methods of analysis, i.e., TEM and DLS. For instance, PM_{16}-SN-38 showed the smallest average diameter and narrow polydispersity in both methods **(Fig 5.2A** and **5.2F)**. Whereas PM_{16}-SN-38:PM_{26}/A83 showed larger average diameter and high polydispersity **(Fig 5.2C** and **5.2H)**.

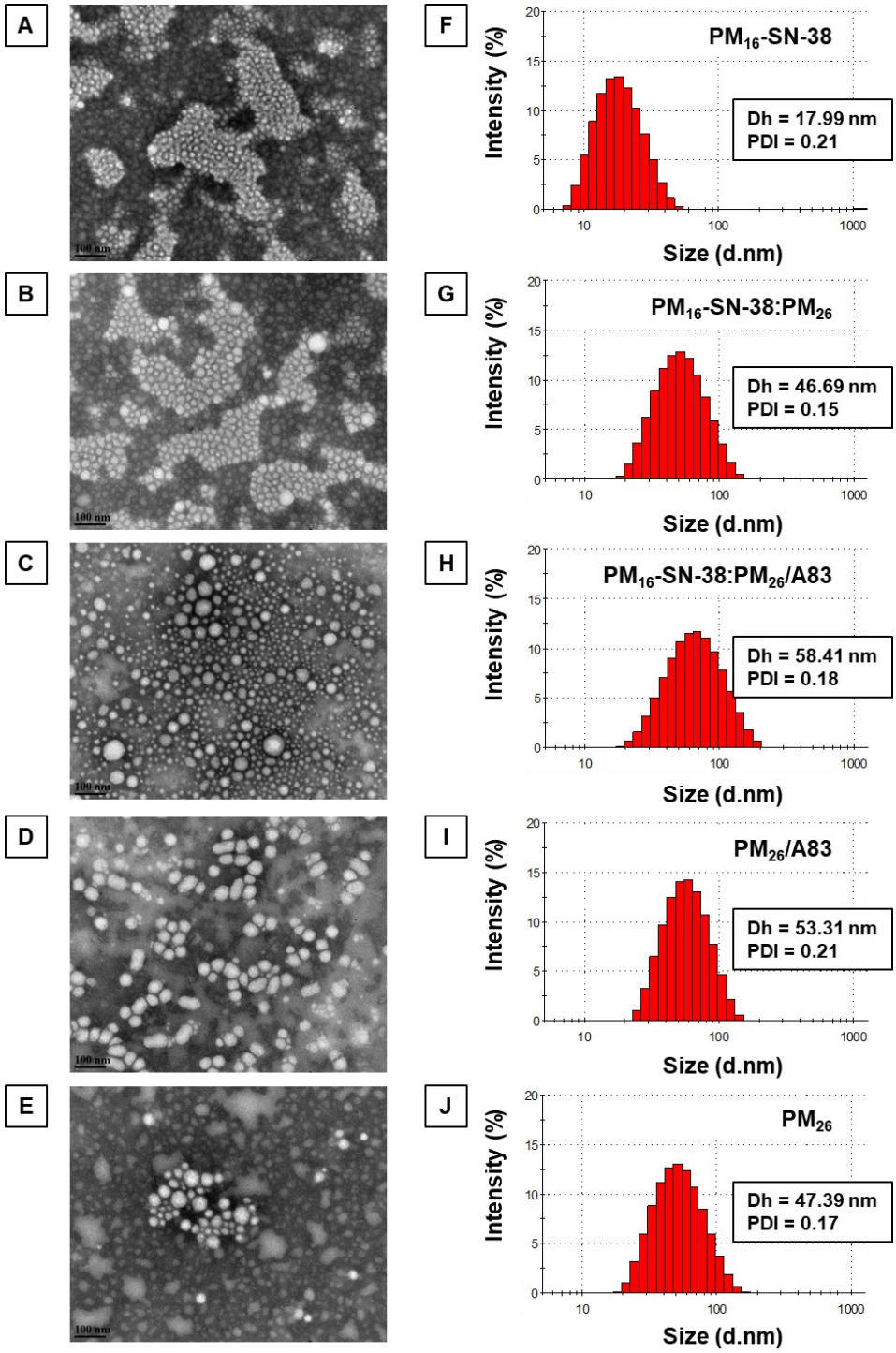

Figure 5.2: TEM images of the polymeric micelles formed from (A) PM_{16}-SN-38, (B) PM_{16}-SN-38:PM_{26}, (C) PM_{16}-SN-38:PM_{26}/A83, (D) PM_{26}/A83, and (E) PM_{26}. Images were obtained at a magnification of 110,000X at 75 kV. The bar in the bottom left corner of each image indicates a scale of 100 nm. Hydrodynamic diameter (D_h), PDI, and size distribution of (F) PM_{16}-SN-38, (G) PM_{16}-SN-38:PM_{26}, (H) PM_{16}-SN-38:PM_{26}/A83, (I) PM_{26}/A83, and (J) PM_{26} micelles in aqueous medium were obtained by dynamic light scattering (DLS) using Zetasizer Nano (Malvern).

5.3.3. Kinetic stability

The kinetic stability of block copolyme micelles was investigated by following the dissociation of micellar peak in the presence of a destabilizing surfactant, i.e., SDS, after 0, 1, 2, 4, 8, and 24 h incubation using DLS technique. **Fig. 5.3A** and **5.3B** represent the % intensity of micellar peak and PDI, respectively, for PM_{16}-SN-38, PM_{16}-SN-38:PM_{26}, PM_{16}-SN-38:PM_{26}/A83, and PM_{26}/A83 micelles over 24 h in the presence of SDS. All the micellar formulations exhibited complete resistance against the destabilizing agent and remained intact throughout the incubation period up to 24 h. As shown in **Fig. 5.3B**, no significant dissociation of the micellar structures was detected since the DLS-obtained PDI was in similar ranges (0.1 to 0.14) for the formulations in this study following incubation with SDS. Overall data suggest that all the micellar formulations are kinetically stable regardless of the payloads and their composition.

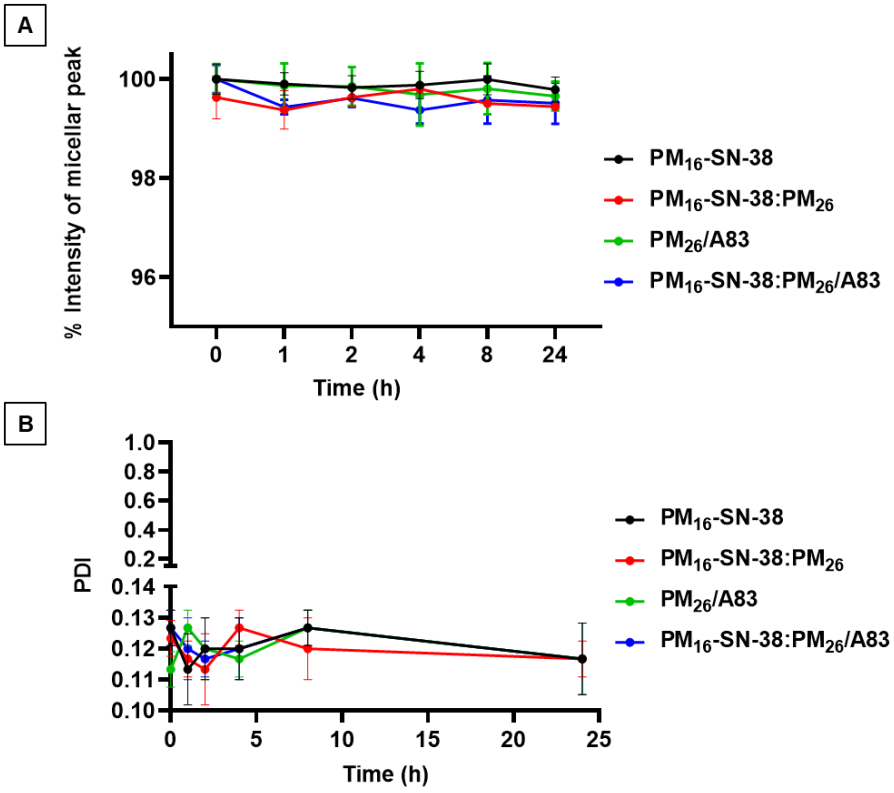

Figure 5.3: Average (A) percentage of intensity and (B) PDI of PM_{16}-SN-38, PM_{16}-SN-38:PM_{26}, PM_{26}/A83, and PM_{16}-SN-38:PM_{26}/A83 micellar formulations (3 mg/mL) in the presence of SDS (20 mg/mL) at a ratio of 2:1 (v/v) as a function of time up to 24 h.

5.3.4. *In vitro* drug release

Fig. 5.4 shows the comparative *in vitro* release profiles of A83B4C63 and SN-38 from their respective formulations compared to free A83B4C63 and SN-38, under experimental conditions. Within 6 h, 98.81 ± 2.09% of A83B4C63 and 96.46 ± 1.43% of SN-38 as free drugs solubilize with the aid of DMSO were released from the dialysis bag indicating the existence of near sink condition [357]. In contrast, only 27.46 ± 2.53% and 43.88 ± 4.18% of A83B4C63 were released over 6 h from PM_{26}/A83 and PM_{16}-SN-38:PM_{26}/A83 micelles, respectively. Similarly, only 34.49 ± 5.23%, 28.28 ± 2.62%, and 20.70 ± 4.52% of SN-38 were released over 6 h from PM_{16}-SN-38, PM_{16}-SN-38:PM_{26}, and PM_{16}-SN-38:PM_{26}/A83 micelles, respectively. In addition, the release of A83B4C63 from PM_{16}-SN-38:PM_{26}/A83 micelles over 24 h was 76.36 ± 1.41% (**Fig. 5.4A**), which was significantly higher than that of PM_{26}/A83 (42.70 ± 0.72) micelles and significantly lower that of free SN-38 (99.81 ± 0.01%). In contrast, the release of SN-38 from PM_{16}-SN-38:PM_{26}/A83 micelles over 24 h was 44.15 ± 2.61%, which was significantly lower than that of PM_{16}-SN-38 (74.16 ± 3.65) and PM_{16}-SN-38:PM_{26} micelles (57.94 ± 3.69%) (**Fig. 5.4B**). The overall *in vitro* release study supports the efficiency of micellar formulations for sustaining the release of both A83B4C63 and SN-38. It also showed release of SN-38 to slow down but release of A83B4C63 to increase upon formation of mixed micelles (PM_{16}-SN-38:PM_{26}/A83) compared to individual micelles encapsulating each drug alone (PM_{16}-SN-38 or PM_{26}/A83).

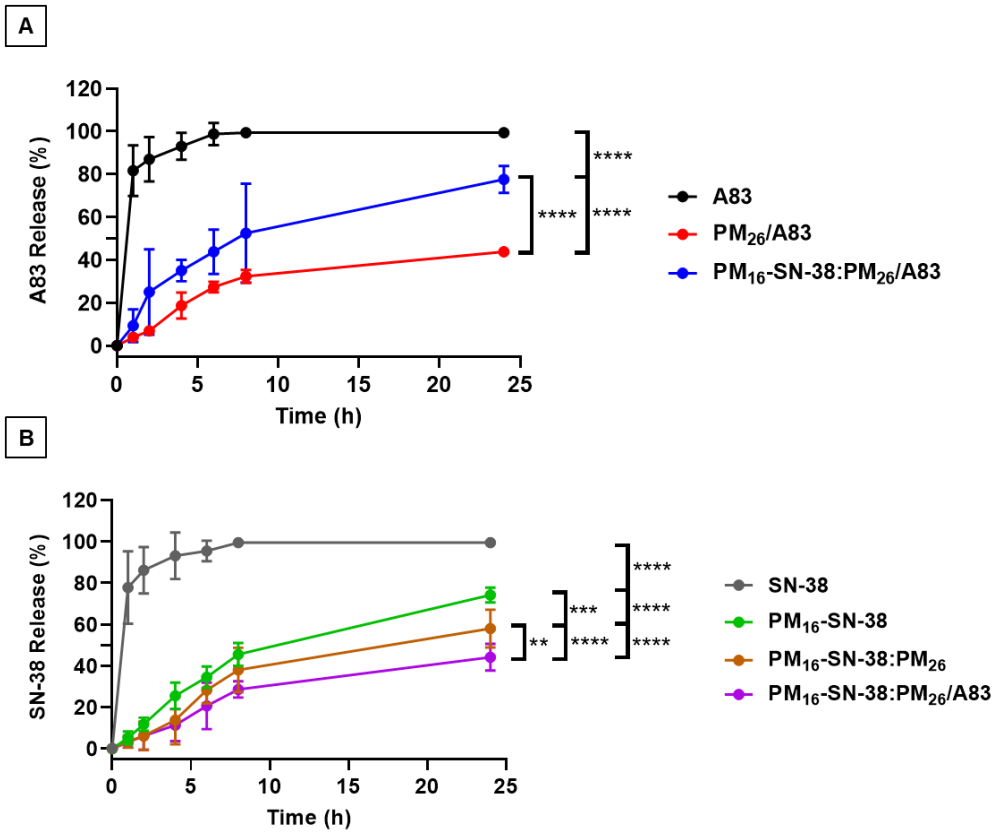

Figure 5.4: (A) The A83B4C63 release profile from PM_{26}/A83 and PM_{16}-SN-38:PM_{26}/A83 micelles compared to the free A83 from dialysis tubing (MWCO = 3.5 kDa) in aqueous solution (4% albumin in ultrapure water) at 37ºC. (B) The SN-38 release profile from PM_{16}-SN-38, PM_{16}-SN-38:PM_{26}, and PM_{16}-SN-38:PM_{26}/A83 micelles compared to the free SN-38 from dialysis tubing (MWCO = 3.5 kDa) in aqueous solution (4% albumin in ultrapure water) at 37ºC. Significances of the differences were considered if $*p \leq 0.05$, $**p \leq 0.01$, $***p \leq 0.001$, $****p \leq 0.0001$ following one-way ANOVA multiple comparison test following Tukey's method. Data are represented as mean ± SD (n = 3).

5.3.5. Evaluation of synergy between the combination treatments

To further assess the synergistic versus additive effects of combinations of PNKP inhibitor and TOP1 inhibitor, and to predict the effective synergistic doses of these two drugs as combination therapy against CRC cell lines, we conducted software program-based analysis of our cell viability data. **Fig. 5.5** shows the graphical outputs from the Combenefit® software that represent the combination dose response surface mapping the synergy as well as antagonism distribution. For interpreting the value of synergy scores, Combenefit® software has normalized input data as cell viability inhibition percentage to directly infer the proportion of cellular

responses attributing to the interactions of various concentrations of both drugs. Therefore, the combination scores near zero in the surface plot yields inadequate confidence on synergy or antagonism. However, the combination scores below -10, between -10 to 10, and above 10 for the combination of two drugs are likely to be considered antagonism, additivity, and synergy, respectively. Irinotecan in combination with PNKP inhibitor mostly showed additive scores, also confirming the inefficacy to kill CRC cell lines as revealed by the cell viability experiments at studied concentrations **(Fig 5.5A** and **5.5B).** Loewe models suggested the clear synergistic effects for combining encapsulated PNKP inhibitor and TOP1 inhibitor SN-38 (as free or encapsulated) at a concentration range between 0.01 to 10 μM for TOP1 inhibitor and between 10 to 40 μM for PNKP inhibitor. Since both SN-38 and PM_{16}-SN-38 are extremely toxic to cells, the combinatorial effects were not considered synergistic at higher concentrations of SN-38 by the software. When combining free SN-38 with PM_{26}/A83, the synergy scores reached to 50 in 10-40 μM range of A83B4C63 concentration (**Fig. 5.5C** and **5.5D**). Combining PM_{26}/A83 with PM_{16}-SN-38 produced a synergy score of 50 between 10 and 40 μM concentrations for A83B4C63 and 0.01 and 1 μM concentrations for SN-38 (**Fig. 5.5E** and **5.5F**).

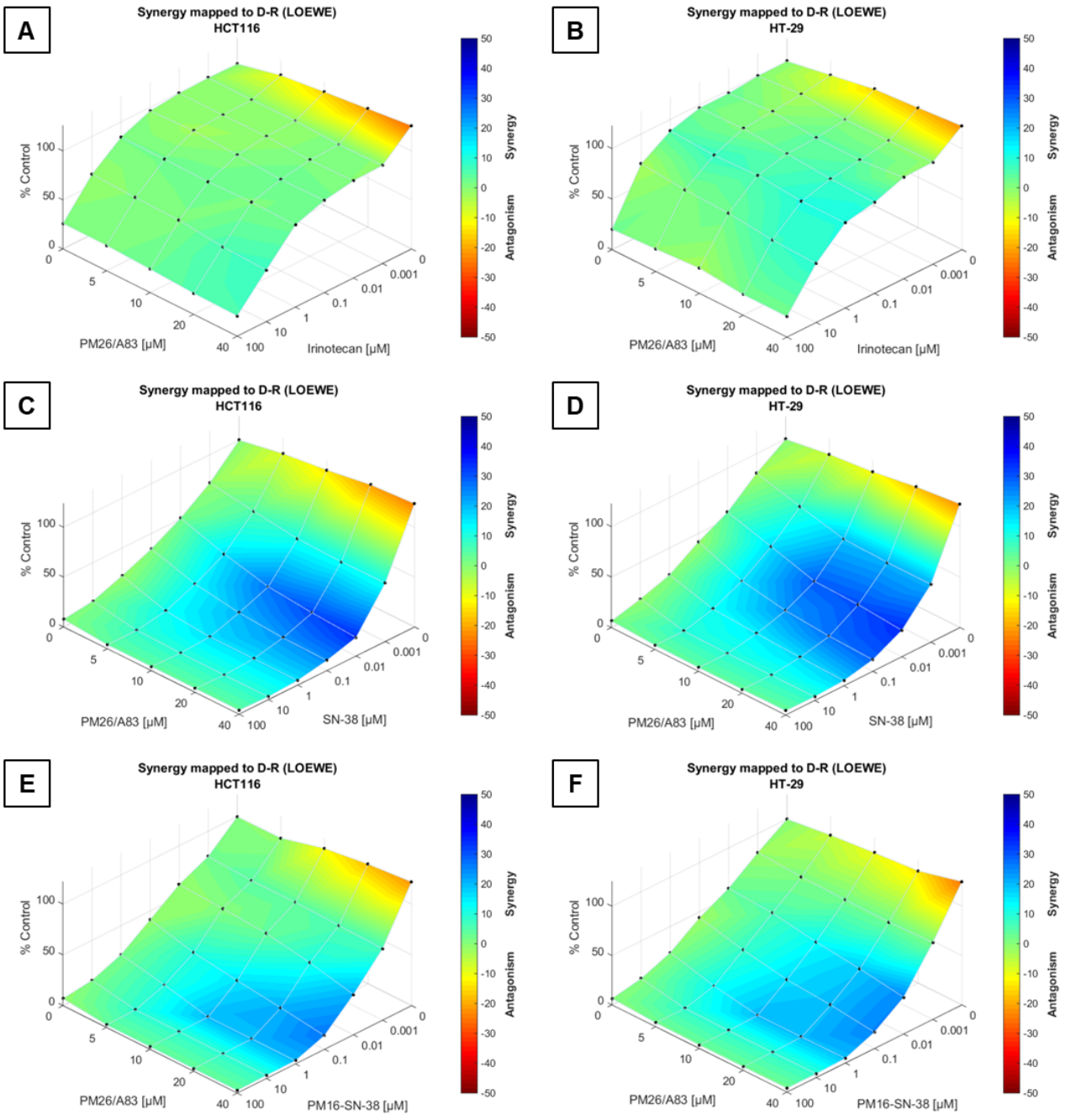

Figure 5.5: Analysis of additive versus synergistic effects for the combination of TOP1 and PNKP inhibitors as free or part of different formulations at indicated concentrations in (A, C, and E) HCT116 and (B, D, and F) HT-29 cells. Data is a representative model of three independent experiments.

5.3.6. *In vitro* cytotoxicity

The MTS assay was performed at 24-72 h to determine the anticancer activity for the combination of TOP1 and PNKP inhibitors with or without nano-delivery against CRC cell lines (HCT116 and HT-29) in comparison to empty polymeric micelles, TOP1 inhibitors SN-38 or irinotecan alone, and PNKP inhibitor alone (**Fig. 5.6).**

As summarized in **Table 5.3**, in HCT116 the IC_{50} of irinotecan was 7.3 ± 3.7, 3.9 ± 1.7 and 6.3 ± 1.6 μM following 24, 48, and 72 h incubation. Upon combination of irinotecan with PM_{26}/A83 the IC_{50} decreased to 5.7 ± 2.5, 4.2 ± 1.2, and 3.9 ± 1.0 μM at the same incubation times, respectively. The difference in mono versus combination therapy was significant for the 72 h incubation time. Similar trend was observed in HT-29 cell line, where the decrease in IC_{50} between mono and combination therapy was found to be significant after 48 h incubation time. As expected, at similar concentration range, treatment of both cell lines with SN-38 led to higher cytotoxicity compared to that for irinotecan (**Table 5.3**). In both cell lines, PM_{16}-SN-38 was shown to have similar IC_{50} to that of free SN-38, in all incubation times.

Adding PM_{26}/A83 to both cell lines while treating them with either free SN-38 or PM_{16}-SN-38 led to a decrease in the IC_{50} of SN-38 in all incubation times and in both cell lines. For instance, in HCT116 cells, the IC_{50} of free SN-38 was decreased from 0.14 ± 0.04, 0.05 ± 0.01, 0.02 ± 0.01 μM at 24, 48, and 72 h to 0.012 ± 0.001, 0.007 ± 0.001, and 0.002 ± 0.001 μM upon combination with PM_{26}/A83. For PM_{16}-SN-38, co-treatment of HCT116 cells led to a decrease to IC_{50} from 0.12 ± 0.05, 0.05 ± 0.01, and 0.01 ± 0.002 μM to 0.013 ± 0.001, 0.008 ± 0.001, and 0.003 ± 0.001 μM for 24, 48 and 72 h incubation times, respectively (*$p < 0.05$, student's t-test). The results showed similarly superior cytotoxicity of SN-38 + PM_{26}/A83 and that of PM_{16}-SN-38+PM_{26}/A83 samples over other treatments at all incubation time points against both cell lines.

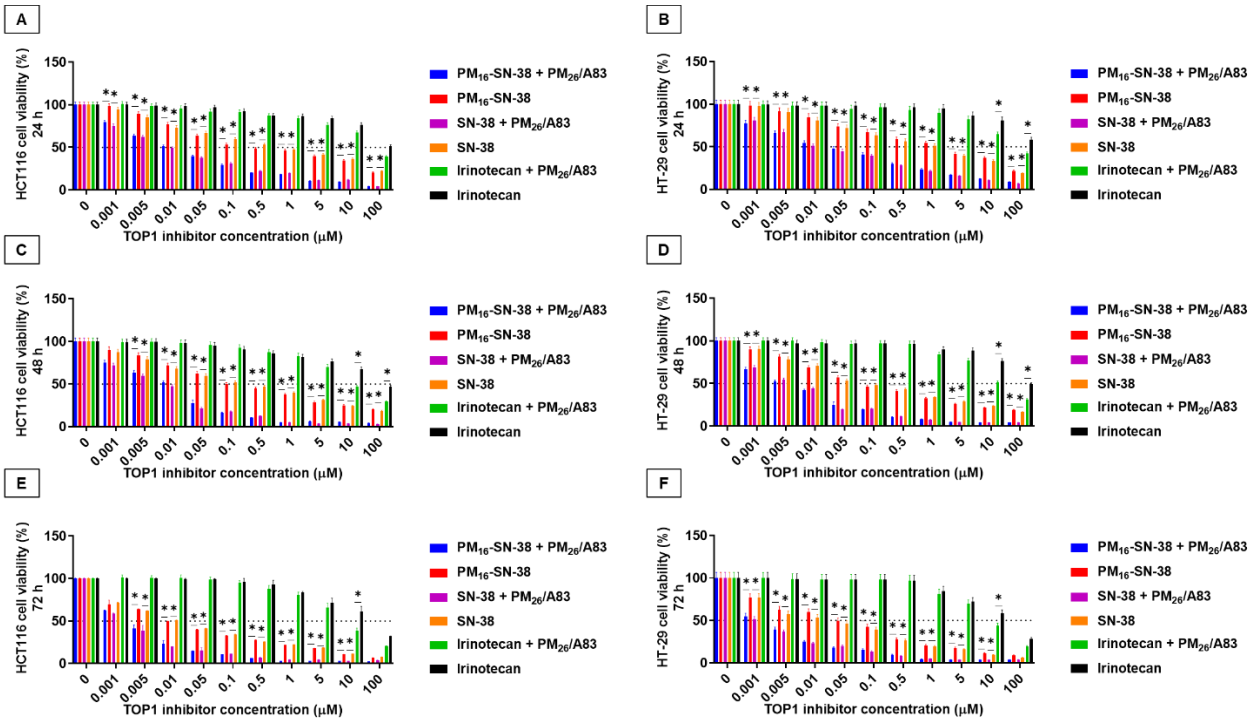

Figure 5.6: *In vitro* cytotoxicity of free irinotecan (black), irinotecan + PM_{26}/A83 (green), SN-38 (orange), SN-38 + PM_{26}/A83 (purple), PM_{16}-SN-38 (red), and PM_{16}-SN-38 + PM_{26}/A83 (blue) in (A, C, and E) HCT116 and (B, D, and F) HT-29 cell lines after 24 h, 48 h, and 72 h incubation at 37ºC in 5% CO_2. The cells were treated with the free TOP1 inhibitor or their polymeric micelles at a range of concentration from 0.001 to 100 μM. For the combination treatments, the concentration of A83B4C63-encapsulated micelles was 10 μM. SN-38 as free drug was solubilized with the aid of DMSO and the untreated cells received only 0.1% DMSO. The differences were considered significant if $*p \leq 0.05$; Student's t test. Each point represents mean ± SD (n = 4).

Table 5.3. IC_{50} range of irinotecan, irinotecan + PM_{26}/A83, SN-38, SN-38 + PM_{26}/A83, PM_{16}-SN-38, and PM_{16}-SN-38 + PM_{26}/A83 against HCT116 and HT-29 cell lines after 24, 48, and 72 h of incubation (n = 4). IC_{50} values were determined after plotting the cell viability percentages vs. various drug concentrations using GraphPad Prism 9 software. The graph was then fitted with a non-linear regression and sigmoid dose-response curve to obtain the IC_{50} values. The number shown in the subscript of the formulation names indicates the degree of polymerization of each block of the copolymers as determined by ^{1}H NMR spectroscopy.

Cells	**Time (h)**	**IC_{50} (μM)**					
		Irinotecan	**Irinotecan + PM_{26}/A83**	**SN-38**	**SN-38 + PM_{26}/A83**	**PM_{16}-SN-38**	**PM_{16}-SN-38 + PM_{26}/A83**
HCT116	24	7.3 ± 3.7	5.7 ± 2.5	0.14 ± 0.04	0.012 ± 0.001	0.12 ± 0.05	0.013 ± 0.001
	48	3.9 ± 1.7	4.2 ± 1.2	0.05 ± 0.01	0.007 ± 0.001	0.05 ± 0.01	0.008 ± 0.001
	72	6.3 ± 1.6	3.9 ± 1.0	0.02 ± 0.01	0.002 ± 0.001	0.01 ± 0.002	0.003 ± 0.001
HT-29	24	10.7 ± 4.5	7.6 ± 2.6	0.28 ± 0.08	0.018 ± 0.004	0.35 ± 0.10	0.018 ± 0.004
	48	11.6 ± 4.3	6.0 ± 1.7	0.05 ± 0.01	0.005 ± 0.001	0.04 ± 0.01	0.005 ± 0.001
	72	7.1 ± 2.2	5.8 ± 1.7	0.02 ± 0.01	0.002 ± 0.001	0.02 ± 0.01	0.002 ± 0.001

We then made a comparison between the cytotoxicity of PM_{16}-SN-38:PM_{26} and that of PM_{16}-SN-38:PM_{26}/A83 co-delivery system (**Fig. 5.7** and **Table 5.4**). Similar to combination treatment of PM_{16}-SN-38 + PM_{26}/A83 that showed higher cytotoxicity in HCT116 and HT-29 cell lines compared to PM_{16}-SN-38, alone; the co-delivery system of PM_{16}-SN-38:PM_{26}/A83 was more cytotoxic than PM_{16}-SN-38:PM_{26}. In the HCT116 cells, the average IC_{50} of co-delivery system was 0.02, 0.03 and 0.01 μM at 24, 48, and 72 h incubation, based on SN-38 concentration, while PM_{16}-SN-38:PM_{26} without A83, showed IC_{50}s of 0.19, 0.16, and 0.03 μM at the same incubation times. This represents a 9.5, 5.3, and 3 fold decrease in the IC_{50} of the co-delivery system over the same polymeric micellar structure without A83, which was similar to the level of reduction in IC_{50} for the combination treatment of PM_{16}-SN-38 + PM_{26}/A83 compared to PM_{16}-SN-38 alone. Similar trend was observed in HT-29 cells.

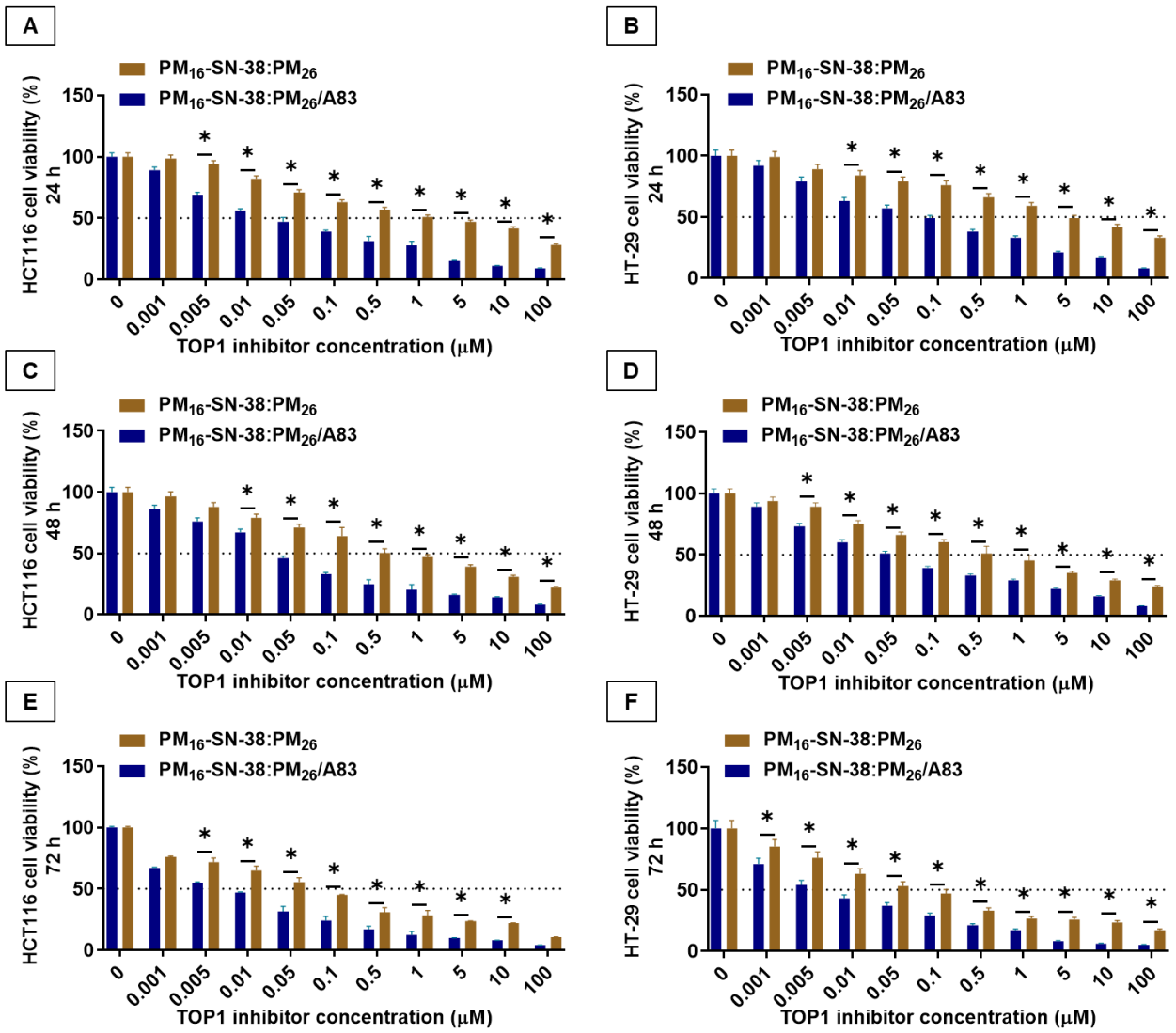

Figure 5.7: *In vitro* cytotoxicity of PM_{16}-SN-38:PM_{26} (brown) and PM_{16}-SN-38:PM_{26}/A83 (teal) in (A, C, and E) HCT116 and (B, D, and F) HT-29 cell lines after 24 h, 48 h, and 72 h incubation at 37ºC in 5% CO_2. The cells were treated at a range of concentration from 0.001 to 100 μM of SN-38. However, the concentrations of co-encapsulated PNKP inhibitor were varied. The differences were considered significant if $*p \leq 0.05$; Student's t test. Each point represents mean ± SD (n = 4).

Table 5.4. IC_{50} range of PM_{16}-SN-38:PM_{26} and PM_{16}-SN-38:PM_{26}/A83 against HCT116 and HT-29 cell lines after 24, 48, and 72 h of incubation (n = 4). IC_{50} values were determined after plotting the cell viability percentages vs. various drug concentrations using GraphPad Prism 9 software. The graph was then fitted with a non-linear regression and sigmoid dose-response curve to obtain the IC_{50} values. The number shown in the subscript of the formulation names indicates the degree of polymerization of each block of the copolymers as determined by ^{1}H NMR spectroscopy.

Cells	Time (h)	IC_{50} (μM)	
		PM_{16}-SN-38:PM_{26}	**PM_{16}-SN-38:PM_{26}/A83**
HCT116	24	0.19 ± 0.07	0.02 ± 0.007
	48	0.16 ± 0.05	0.03 ± 0.005
	72	0.03 ± 0.01	0.01 ± 0.001
HT-29	24	0.32 ± 0.11	0.07 ± 0.02
	48	0.10 ± 0.03	0.04 ± 0.01
	72	0.03 ± 0.01	0.01 ± 0.001

5.3.7. Expression of apoptosis mediators for the combination versus monotherapies

As shown in **Fig. 5.8**, PM_{26}, free A83 and PM_{26}/A83 showed no apoptotic signaling reflecting the inertness and nontoxic characteristics of the delivery system and lack of off target activity by the PNKP inhibitor A83B4C63 at 10 μM. Addition of PM_{26}/A83 as PNKP inhibitor to irinotecan significantly increased the expression of cleaved PARP, γ-H2AX, cleaved caspase 3 and 7 in both cell lines. Addition of PM_{26}/A83 to PM_{16}-SN-38, did not affect cleaved PARP, γ-H2AX expression significantly except in HT-29 cells where γ-H2AX expression was increased with the co-treatment. The cleaved caspase 3 expression, however showed a significant increase in expression in both cell lines upon co-treatment with these formulations compared to monotherapy with PM_{16}-SN-38, however ($*p < 0.05$).

In HCT116 cells, the formulation designed for co-delivery of TOP1 and PNKP inhibitor, i.e., PM_{16}-SN-38:PM_{26}/A83 at its IC_{50} concentration revealed significantly higher expression of cleaved PARP ($*p \leq 0.05$, student's t-test), when compared to the co-treatment with individual

formulations, i.e., PM_{26}/A83 + PM_{16}-SN-38. However, no significant difference was observed for the expression of cleaved PARP between these treatments in HT-29 cell line. Moreover, in HT-29 cells, the PM_{16}-SN-38:PM_{26}/A83 treatment showed significantly higher expression of γ-H2AX (*$p \leq 0.05$, student's t-test) compared to the co-treatment with the individual formulations, i.e., PM_{26}/A83 + PM_{16}-SN-38. In contrast, no significant difference was observed for the expression of γ-H2AX between these treatments in HCT116 cell line. Notably, no significant differences were obtained between co-delivery formulation (PM_{16}-SN-38:PM_{26}/A83) and combination (PM_{16}-SN-38 + PM_{26}/A83) treatments in both cell lines in the expression cleaved caspase 3 and 7. Based on these data, the similar expression levels of these apoptosis mediators in CRC cell lines upon co-delivery (PM_{16}-SN-38:PM_{26}/A83) and combination (PM_{16}-SN-38 + PM_{26}/A83) treatments demonstrated both structural integrity and anticancer efficacy of the payloads using polymeric micellar NPs.

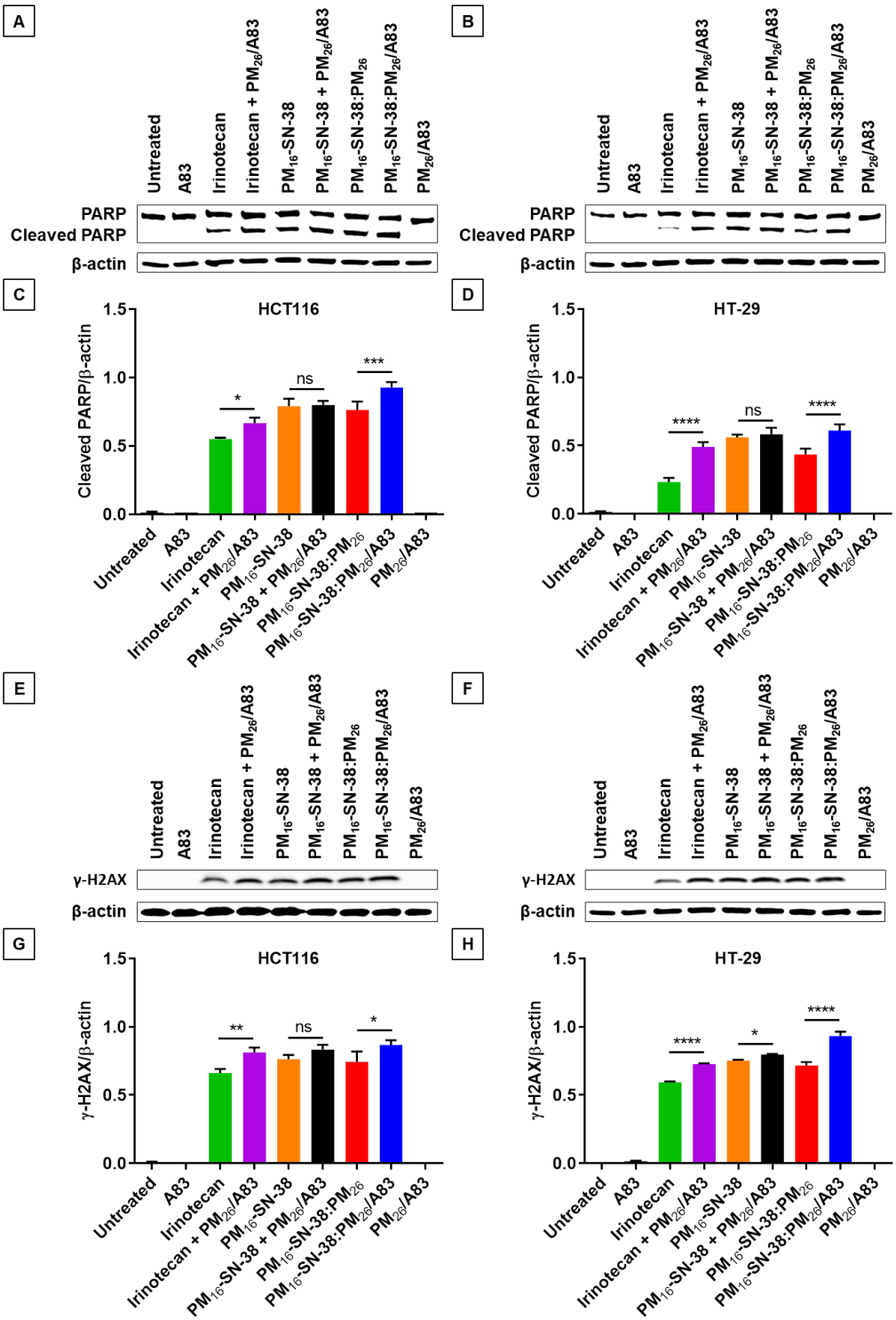
A
B
Untreated
A83
Irinotecan
Irinotecan + PM26/A83
PM16-SN-38
PM16-SN-38 + PM26/A83
PM16-SN-38:PM26
PM16-SN-38:PM26/A83
PM26/A83
PARP
Cleaved PARP
β-actin
C
D
HCT116
HT-29
Cleaved PARP/β-actin
1.5
1.0
0.5
0.0
*
ns
***
****
E
F
γ-H2AX
β-actin
G
H
γ-H2AX/β-actin
**

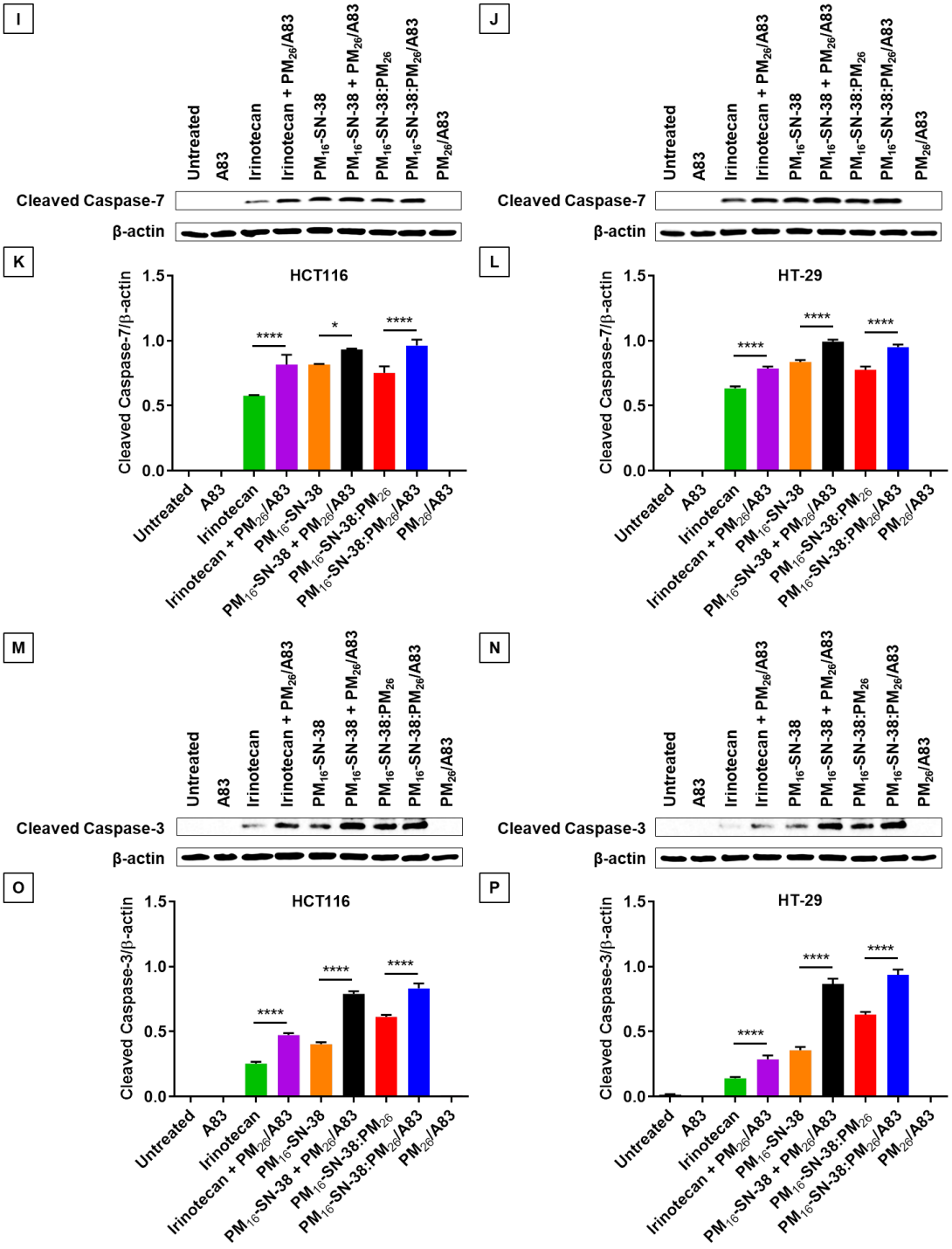

Figure 5.8: Western blot detection of (A and B) cleaved PARP, (E and F) γ-H2AX, (I and J) cleaved caspase-7, and (M and N) cleaved caspase-3 in both cell lines after 6 h exposure to the respective treatments at 37ºC in 5% CO_2 (n = 3). β-actin was used as a loading control. The conditions for all sample preparations and western blots were the same. Data are expressed as mean ± SD (n = 3). The statistical analysis of (C and D) cleaved PARP, (G and H) γ-H2AX, (K and L) cleaved caspase-7, and (O and P) cleaved caspase-3 was performed after normalized to β-actin. Differences were considered significant if * $P \leq 0.05$, ** $P \leq 0.01$, *** $P \leq 0.001$, and **** $P \leq 0.0001$ following two-way ANOVA followed by Tukey's method.

5.4. Discussion

The resistances to the conventional chemotherapies and the development of metastasis are the main causes of poor prognosis for advanced CRC. In last 2-3 decades, CRC patients have been exclusively treated with the chemotherapies based on fluoropyrimidines until the recognition of TOP1 enzyme as a valid therapeutic target in the cancer. As a result, a second generation semisynthetic camptothecin derivative, i.e., irinotecan as TOP1 inhibitor has been approved for clinical use in CRC patients. However, irinotecan is a prodrug which needs enzymatic conversion to produce its active metabolite, SN-38 in liver. Such conversion in liver needs higher frequent doses of irinotecan and eventually it results in suboptimal therapeutic responses, which requires combination treatment(s) in most advanced and some primary CRC patients [378].

Our research group has previously reported on the development of novel inhibitors of a DNA repair enzyme known as PNKP that can sensitize CRC to the cytotoxic effect of TOP1 inhibitors. We have also developed polymeric micellar formulations for SN-38 as well as a lead PNKP inhibitor known as A83B4C63 [254, 267, 331]. The primary objective of this study was to investigate the synergy between polymeric micellar formulations of SN-38 and A83B4C63 combination as individual micelles added together or mixed micelles co-delivering both drugs (**Table 5.1**) against CRC cell lines, *in vitro*.

First, SN-38 was chemically conjugated to the poly(ester) end of mPEO-*b*-PBCL with a lower DP of 16, using activation of the COOH group at the polymer end. This has led to > 600 folds increase in water solubilized levels of SN-38 (25 μg/mL to over 15 mg/mL). The level of SN-38 conjugation to the carboxyl group at the PBCL end increased by ~5% where activation of carboxyl group by oxalyl chloride was pursued, compared to our previously reported SN-38 conjugation [254]. For comparison, the conjugated level of SN-38 to PEO-poly(glutamic acid)

polymers in the NK012 formulation is reported at 20 % w/w, while SN-38 conjugation to the mPEO-*b*-PBCL end of this paper is at 16 % w/w [255].

With respect to A83B4C63 encapsulation, the use of mixed block copolymers of PM_{16}-SN-38:PM_{26} instead of PM_{26} alone led to a decrease in the encapsulated levels of A83B4C63 (**Table 5.2**). Although the achieved loading still increased the water-soluble levels of A83B4C63, from 1 μM to 10.67.

Micelles co-encapsulating SN-38 and A83, showed increased average diameter compared to polymeric micelles encapsulating each drug, although the average diameter of the co-delivery systems. was still < 60 nm (**Table 5.2** and **Fig. 5.2**). Like polymeric micelles delivering individual SN-38 or A83, the mixed micelles containing both drugs showed high thermodynamic and kinetic stability (**Table 5.2** and **Fig. 5.3**). The high stability of the polymeric micellar structure is mainly attributed to the presence of benzyl carboxylate group that may lead to π–π stacking and rigidity of the core structure [254]. Similar to micelles for individual drugs, the releases of SN-38 and A83B4C63 from the mixed micellar formulation co-encapsulating both drugs was sustained compared to free drugs [254]. However, the release of A83B4C63 was higher from the co-delivery systems compared to micelles encapsulating A83B4C63 alone, the release of SN-38 was lower from the co-delivery system compared to that of PM-SN-38 alone.

We then investigated the synergy between SN-38 as free and polymeric micellar formulation with that of PM_{26}/A83 formulation at different concentrations and ratios, first, using Combenefit® software. Our data revealed a synergy between free SN-38 and PM_{16}-SN-38 with PM_{26}/A83 at a concentration range of 0.01-1 μM for SN-38 and 10-40 μM for A83 **(Fig 5.5).**

Thereafter, we assessed the efficacy for this combination formulation in human CRC cell lines while keeping the concentration of A83 fixed at 10 μM. The cytotoxicity data revealed

significantly higher cell viability reduction for the combination treatments compared to their counterparts with SN-38 treatment only. Perhaps due to the efficient intracellular release of SN-38, all micellar SN-38 formulations showed significantly higher cell viability reduction than conventional irinotecan with or without PNKP inhibitor in human CRC cell lines. The effect of combination treatment with PNKP + TOP1 inhibitor was also observed in the increased DNA damage and mediators of apoptosis in CRC cells compared to their respective individual treatments with TOP1 inhibitor within 6 h.

In both HCT116 and HT-29 CRC cell lines, the co-delivery of TOP1 and PNKP inhibitors using mixed micelles induced significant cytotoxicity, DNA damage and increase of apoptosis biomarkers compared to its counterpart with TOP1 inhibitor encapsulation only [4], while the PNKP enzyme involved in repairing the single strand DNA breaks by SN-38 similar DNA damaging agents. Ideally, PNKP catalyzes the restoration of 5'-phosphate and 3'-hydroxyl termini and allow DNA ligase to allow the rejoin the breaks. PNKP also ensures that 5'-OH termini are phosphorylated although its phosphatase activity was predominant over the kinase activity in strand breaks with both 3'-phosphate and 5'-OH termini. When TOP1-DNA “dead-end” complex is generated by SN-38, TOP1 enzyme was found to be attached to the DNA 3'-phosphate covalently through a tyrosine residue and subsequently released from the DNA by Tyrosyl-DNA Phosphodiesterase 1 or TDP1 for processing prior to ligation steps. Therefore, PNKP was found to participate in the correction 3'-phosphate and 5'-OH termini of the DNA breaks [117]. In case of regular single stranded DNA breaks, PNKP is not considered to be the underlying DNA repair enzyme unless TOP1 is inhibited by TOP1 inhibitor. Similarly in this study, the non-toxicity of both free and micellar PNKP inhibitors were evidenced by no cell viability reduction up to 40 μM dose after 72 h treatment and also further verified by no expression levels of cleaved PARP and γ-

H2AX in CRC cell lines. Due to non-toxic behavior of our novel PNKP inhibitor, IC_{50} concentration was not measurable up to 40 μM treating dose which was 3 times higher treating dose than the required dose (10 μM) for desired chemo-sensitization in this study. This observation was also in agreement with our previous *in vivo* study where neither systemic nor tissue toxicity was identified in healthy CD-1 mice receiving A83B4C63 up to 50 mg/kg dose intravenously either solubilized with the aid of Cremophor EL: Ethanol formulation or similar micellar formulation (PM_{26}/A83) investigated in this study [331].

It appears that the co-delivery of A83B4C63 and SN-38 in one polymeric micellar formulation (PM_{16}-SN-38:PM_{26}/A83), potentiated the effect of A83B4C63. This was evident from similar cell viability at much lower ratios of A83 to that of SN-38 in co-delivery systems (PM_{16}-SN-38:PM_{26}/A83) in both cell lines compared to that of combination treatment (PM_{16}-SN-38 + PM_{26}/A83).

5.5. Conclusion

Most importantly, the chemical conjugation of SN-38 to the hydrophobic core of self-associating PEO-poly(ester) micelles was successful with a higher w/w loading in this study, leading to a suitable water-soluble SN-38 formulation for systemic administration. Co-delivery of both TOP1 and PNKP inhibitors in PEO-poly(ester) based polymeric micelles showed promising *in vitro* chemo-sensitizing synergy in human CRC cell lines. The overall findings demonstrate PM16-SN-38:PM26 as a potential co-delivery platform for a novel combination treatment option against CRC.

Supporting Information

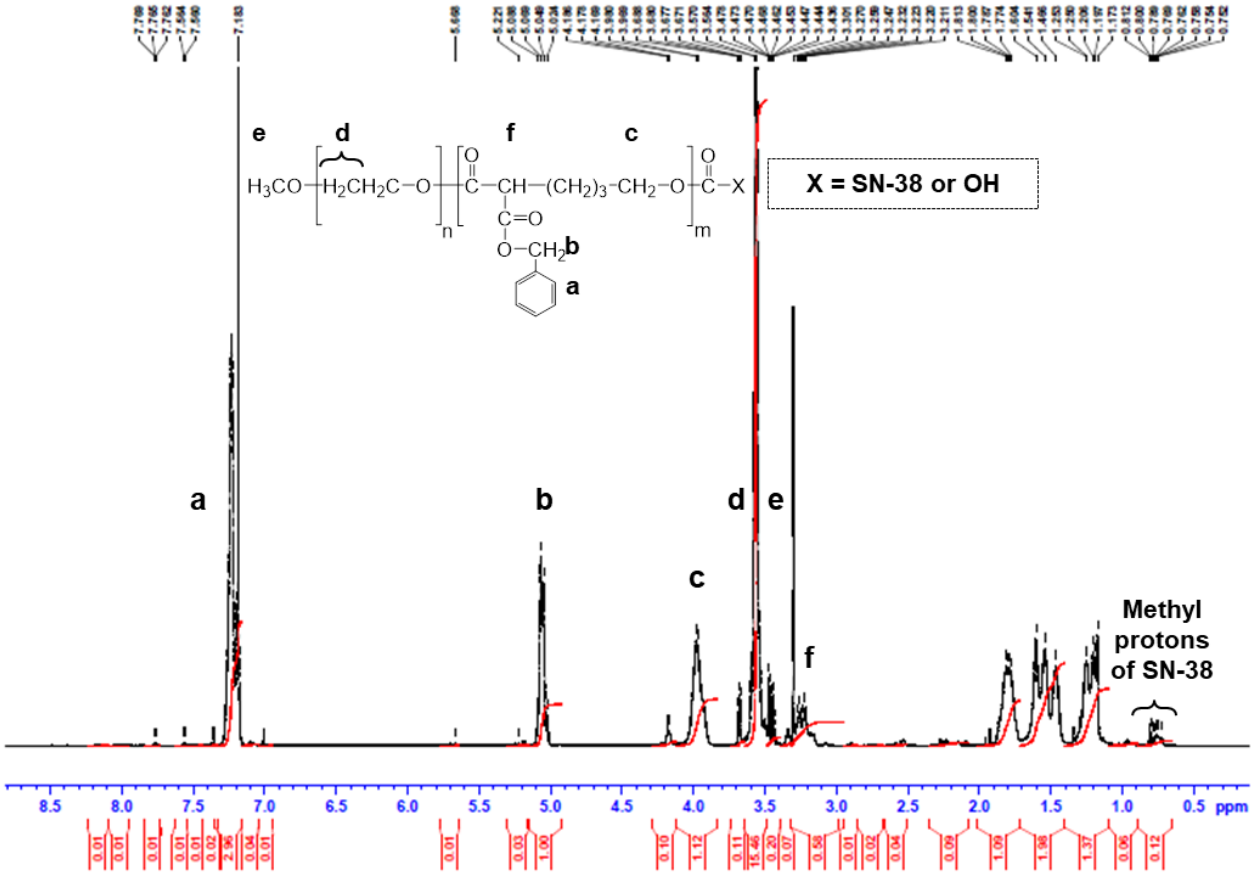

Supplementary Figure 5.1: ^{1}H NMR spectra and corresponding peak assignments for PM_{16}-SN-38.

Chapter 6: Pharmacokinetic and tissue distribution of poly(ethylene oxide)-poly(e-caprolatone) micellar formulations of an inhibitor of polynucleotide kinase 3′-phosphatase (PNKP) in head and neck cancer bearing xenografts in mice

6.1. Introduction

Under the class of squamous cell carcinoma, head and neck cancer (HNC) is one of most prevalent. It accounts for approximately 6% of all cancers worldwide, with > than 900,000 new cases diagnosed and an annual mortality rate of 350,000 per year [379, 380]. Recurrence and metastasis is common in HNC with a median survival of < 1 year for patients with reoccur ant or metastatic disease [381, 382]. The localized ionizing radiation after surgery is a primary treatment option for early staged-resectable HNC. Alongside, the DNA-damaging chemotherapeutics such as cisplatin, oxaliplatin are considered as adjunct or secondary treatment option [383]. In most cases, the complex anatomical localization of HNC limits the success of surgery as the therapy of choice for this type of cancer [382, 384]. Radiation therapy can enhance the duration of survival in patients but will reduce their quality of life by damaging the nearby tissues. On the top of this, tumor resistance to the DNA-damaging therapies, such as radiation, is an additional limiting factor for the success of clinical outcomes in head and neck cancer. Therefore, development of more effective treatments for head and neck cancer is required.

In function, ionizing radiation result in DNA damage that can lead to cell death. However, the inherent ability of cells to repair intracellular DNA damage, can jeopardize the expected clinical outcome to radiation therapy [385]. In the last decades, significant interests have been materialized to develop suitable DNA repair inhibitors as mono or combination therapeutics in cancer treatment [126, 202, 203]. In this regard, our research team has validated a novel DNA repair enzyme called polynucleotide kinase/phosphatase (PNKP), as a therapeutic target in different cancers. PNKP phosphorylates DNA 5′-hydroxyl termini and dephosphorylates DNA 3′-phosphate termini, allowing DNA ligase to rejoin the DNA strand breaks caused by DNA-damaging therapies [118, 119]. Subsequently, the validity of PNKP as a therapeutic target was

proven in sensitizing cancer cells to topoisomerase-1 inhibitor and ionizing radiation [118-120, 126, 238]. Our research team has also identified and successfully synthesized a lead PNKP inhibitor, named as A83B4C63 that effectively sensitized various cancer cells at micro molar concentration to low dose ionizing radiation and topoisomerase-1 inhibitor [202, 203, 267].

A83B4C63 is a polysubstituted imidopiperidine-based small molecule that was limited for *in vivo* investigation due to its hydrophobic property. In order to improve the water-soluble level of hydrophobic small molecules, their encapsulation into biocompatible NPs is now a common practice. To this purpose, various polymeric or lipid-based NPs of therapeutics have gained the most attention in aspect of passive targeting attribution due to leaky tumor vasculature and enhanced permeability and retention (EPR) effect [386, 387] [388]. In previous chapters we have reported on the success of a polymeric micellar formulation using α-benzyl carboxylated poly(ε-caprolatone) (PBCL) as the core forming block in the encapsulation and tumor targeted delivery of A83B4C63 to CRC xenografts in mice. In this chapter, the function of polymeric micelles based on methoxy-poly(ethylene oxide)-*b*-poly(ε-caprolactone) (mPEO-*b*-PCL) (without benzyl carboxylate substitution in the core) in the solubilization and targeted delivery of A83B4C63 to head and neck tumor was investigated (**Fig. 6.1**). Our main goal was to improve the aqueous-solubility of PNKP inhibitor suitable for intravenous administration using polymeric micelles based on FDA approved components. We chose to investigate the biodistribution of A83B4C63 as part of PEO-PCL nano-formulation in head and neck cancer as a more relevant solid tumor for the combination of radiation therapy with the PNKP inhibitor.

We aimed to determine the level of the PNKP inhibitor in various tissues including xenografted tumors to identify the suitable dose and interval schedule for combination treatment with ionizing radiation. The resulting biodistribution profiles of A83B4C63-encapsulated mPEO-

b-PCL-based polymeric micelles were also compared with the conventional solubilized formulations of A83B4C63 dissolved in PEG-400.

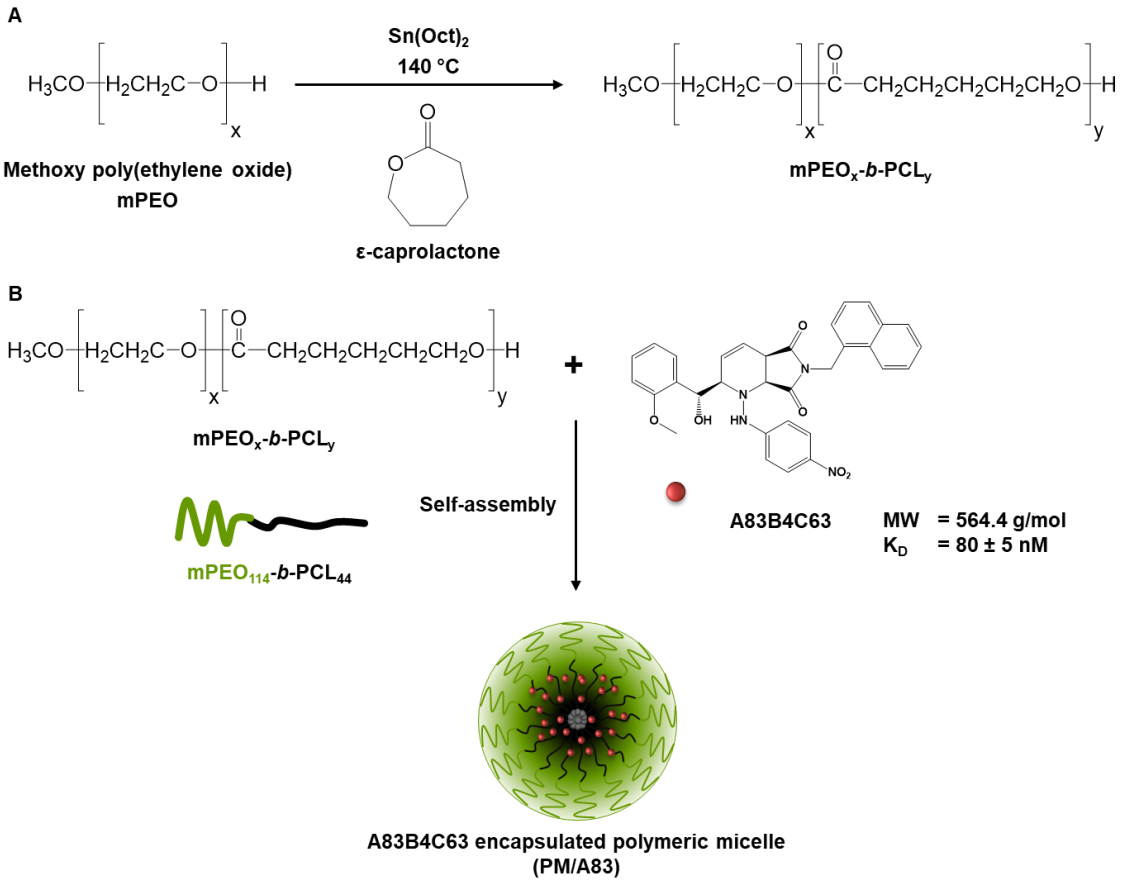

Figure 6.1: (A) Scheme to synthesize $mPEO_{114}$-*b*-PCL_{44}. (B) Self-assemble of block copolymers and encapsulation of A83B4C63 in micelles of $mPEO_{114}$-*b*-PCL_{44}.

6.2. Materials and methods

6.2.1. Materials

Methoxy-polyethylene oxide (PEO) (average molecular weight of 5000 g/mol) and polyethylene glycol (PEG) (average molecular weight of 400 g/mol with a density of 1.28 g/mL) all research grade organic solvents were purchased from Sigma (St. Louis, MO, USA). ε-Caprolactone was purchased from Lancaster Synthesis (UK). Stannous octoate was purchased

from MP Biomedicals Inc. (Tuttlingen, Germany). Heparin sodium for injection (1000 $IUmL^{-1}$, USP) was purchased from Fresenius Kabi (Toronto, Ontario, Canada).

6.2.2. Synthesis of A83B4C63 and PEO_{114}-*b*-PCL_{44} copolymer

The polysubstituted imidopiperidine compound, A83B4C63, was synthesized using a three-component aza[4+2]/allylboration reaction and purified to homogeneity via HPLC as previously described [280]. The structure of the compound was confirmed by NMR, IR, and LC-MS as previously reported [267]. The block copolymer, PEO_{114}-*b*-PCL_{44} with 44 degree of polymerization (DP) for the PCL block was synthesized by ring-opening polymerization of ε-caprolactone using methoxy-PEO (MW: 5000 $gmol^{-1}$) as an initiator and stannous octoate as catalyst. The synthesized copolymers were characterized for their average molecular weights by ^{1}H NMR (600 MHz Avance III - Bruker, East Milton, ON, Canada) using deuterated chloroform ($CDCl_3$) as solvent and tetramethylsilane as an internal reference standard.

6.2.3. Preparation of the conventional and PEO-PCL formulations of A83B4C63

A83B4C63-loaded PEO_{114}-*b*-PCL_{44} polymeric micelles (PM/A83) were prepared as previously described method. In brief, 10 mg A83B4C63 and 30 mg PEO-*b*-PCL polymer were completely dissolved in acetone. Then, the organic phase was transferred dropwise to 10 mL aqueous phase and left overnight with continuous stirring with a magnetic bar under vacuum to completely evaporate the organic solvent. The un-encapsulated A83B4C63 was removed by centrifugation at 11600 × g for 5 min to obtain PM/A83. The PM/A83 solution was then transferred into Amicon Ultra-15 centrifugal filter tubes (molecular weight cut-off, 100 kDa; Millipore, ON, Canada) and centrifuged at 11600 × g for 20 min at 4ºC.

PEG-400 was used to solubilize A83B4C63 to prepare the free drug (FD) formulation (FD/A83) as a control according to our in-house method. In brief, 4.61 g of PEG-400 and 10 mg

of A83B4C63 were weighted and mixed properly by 5 min vortex followed by 5 min water bath sonication. Thereafter, 0.4 mL of 50% dextrose solution was added to make the formulation isotonic at a concentration of 5% dextrose.

6.2.4. Physicochemical characterizations of polymeric micellar formulation

The average size, polydispersity index (PDI), and surface charge of the PMs were measured by dynamic light scattering (DLS) using a Malvern Zetasizer 3000 (Malvern Instruments Ltd, Malvern, Worcestershire, UK). The level of A83B4C63 loading into the polymeric micelles was measured using a Varian Prostar 210 high performance liquid chromatography (HPLC) system following previously described method [267]. In brief, 25 µL of the drug-loaded polymeric micellar nanoparticle (PM/A83) and solubilized formulation was added in 275 µL of the mobile phase. Alongside, the standard samples of free A83B4C63 were also diluted using the similar mobile phase. All samples were run on a Shimadzu LC-10AD HPLC system and the detection was performed at 280 nm wavelength for A83B4C63 using a Varian 335 Photodiode Array HPLC detector (Varian Inc., Palo Alto, CA, USA). The reversed phase chromatography was carried out with a Microsorb-MV 5 µm C18-100 Å column (4.6 mm × 250 mm) with 20 µL of sample injected and eluted under isocratic conditions with a solution of 0.1% trifluroacetic acid / acetonitrile (1:1 v/v) at a flow rate of 1 $mLmin^{-1}$ at room temperature. The retention time was 3.32 min. The assay was found linear over the examined range of 1-1000 μgmL^{-1} in mobile phase with a correlation co-efficient of 0.999. The lowest limit of quantification was set at 1 μgmL^{-1}. The inter- and intra-day variations were less than 10% for all the concentrations. The method was specified, and no interfering peak was observed.

6.2.5. Transmission electron microscopy (TEM)

The morphology of self-assembled structures under study was investigated by TEM using a Morgagni TEM (Field Emission Inc., Hillsboro, OR) with Gatan digital camera (Gatan, Pleasanton, CA). In brief, 20 μL of micellar solution with a polymer concentration of 0.5 $mgmL^{-1}$ was placed on a copper-coated grid. The grid was held horizontally for 2 min to allow the colloidal particles to settle down. The excess fluid was removed by filter paper. The copper-coated grids holding the aqueous samples were then negatively stained by 2% phosphotungstic acid. After 2 min, the excess fluid was removed by filter paper and the grid was loaded into the TEM for image analysis.

6.2.6. Cell lines

Human head and neck squamous cell carcinoma cell line, FaDu, was purchased directly from American Type Culture Collection (ATCC HTB-43, Manassas, VA, USA). Cells were expanded and frozen at early passage in liquid nitrogen until used. Cells were routinely cultured at 37˚C in 5% CO_2 in a humidified incubator in a 1:1 mixture of Dulbecco's modified Eagle medium and F12 (DMEM/F12) supplemented with 10% fetal bovine serum (FBS), 50 UmL^{-1} penicillin, 50 $mgmL^{-1}$ streptomycin, 2 $mmolL^{-1}$ L-glutamine, 0.1 $mmolL^{-1}$ nonessential amino acids, and 1 $mmolL^{-1}$ sodium pyruvate. All culture supplements were purchased from Invitrogen (Burlington, ON, CA). Prior to initiation of experiments, cells were tested for mycoplasma contamination by PlasmoTest™ - Mycoplasma Detection Kit (InvivoGen, San Diego, CA, USA). FaDu cell line was routinely tested for mycoplasma in the lab.

6.2.7. Cytotoxicity assay

The CellTiter 96® AQueous One Solution Cell Proliferation Assay (MTS) kit was purchased from Promega, USA and used to assay the cytotoxicity of FD/A83 and PM/A83 in FaDu

cell lines according to the company provided protocol. In brief, 5×10^3 cells were plated in each well of 96-well flat-bottomed plates 24 h prior to the treatments. Then, cells were treated with the both formulations at the concentration ranges of 1.25 to 80 µM. The control cells received only 5% dextrose. After different experimental incubation time points, 20 µL of MTS reagent was added in each well and further incubated for 1 h at 37ºC before measuring the absorbance at 490 nm using BioTEK microplate reader. Each experiment was performed in quadruplicates. The cell viability percentages were calculated using the following formula:

$$\text{Cell viability (\%)} = \frac{\text{Absorbance of treated cells} - \text{Absorbance of blank well}}{\text{Absorbance of untreated cells} - \text{Absorbance of blank well}} \times 100$$

6.2.8. *Ex vivo* blood binding assay

Freshly heparinized rat whole blood was obtained from the University of Alberta Health Sciences Lab Animal Services. Then, 1 mL of the freshly drawn heparinized rat blood was transferred to the clean glass tubes. For the concentration dependent assay, an appropriate volume (50 µL) of FD/A83 and PM/A83 formulations was added to each tube to give the final concentrations of 25, 50, 250, and 500 $ngmL^{-1}$ of A83B4C63. The whole blood samples were gently mixed and the test samples and were then incubated at 37°C for 1.5 h. After the incubation period, 200 µL aliquot of the incubated whole blood was withdrawn and transferred into new the glass tubes and the remainder was centrifuged at 1500 rpm for 15 min. 200 µL aliquot of generated plasma samples were pipetted into glass tubes. All whole blood samples were lysed through the addition of an equal volume of water followed by 10 min water bath sonication. After the cell lysis, the total content of each tube was directly used for A83B4C63 extraction. All the collected plasma and whole blood lysates were kept frozen at -20°C till sample extraction and drug analysis.

The collected plasma or whole blood lysate samples were extracted using a protein precipitation method. Calibration standards were prepared by addition of the acetonitrile drug

spiking solutions into control rat plasma and whole blood lysate samples, respectively. A seven-point calibration standard covering the concentration range 5, 10, 25, 50, 100, 250, and 500 $ngmL^{-1}$ was used. The standard samples were treated together with assay samples. The samples or calibration standards collected or prepared as described above was mixed with acetonitrile at a 1:1 ratio. The blood lysate mixture was sonicated for 5 min to ensure complete extraction of the compound and both blood and plasma samples were vortexed and centrifuged at 3000 rpm for 10 min. An appropriate aliquot of the resulting supernatant was transferred to a clean glass tube and the solution was then evaporated to dry using a centrifugal speed vacuum concentrator (SpeedVac). The residuals, with vigorous vortexing, were reconstituted in 100 µL mixture of acetonitrile: water (1:1) containing propranolol hydrochloride as the internal standard. A volume of 10 µL was injected for LC/MS analysis. The LC/MS system (Waters Quattro Micro ± ES MS Triple Quadrupole, Milford, MA, USA) coupled with an Agilent Technology: Poroshell 120 SB-C18 2.1×50 mm, 2.7-micron column. The mobile phase consisted of 50:50 v/v ratios of water with 0.1% formic acid and acetonitrile with 0.1% formic acid. The blood/plasma concentration ratio was calculated from the ratio of total drug concentration in the blood to its total concentration in plasma at equilibrium.

6.2.9. *In vivo* xenograft tumor-bearing animal experiments

Animal experiments were conducted using 6-week-old athymic female NIH-III nude mice. After one week acclimatization period in the biosafety containment level-2 facility of Health Sciences Laboratory Animal Services at University of Alberta, mice were subcutaneously inoculated with 3×10^6 FaDu cells in a 100 µl mixture (1:1 v/v) of culture media and matrigel matrix (Corning, MA, USA) on the right flanks. The FaDu cells implanted mice were routinely monitored every day for tumor growth.

When the average tumor volume reached to approximately 500 mm^3, mice were randomly assigned and grouped into 1 control and 5 test groups (3 mice per group) to identify the biodistribution profile of intravenously administered FD/A83 and PM/A83 with at different time points including 2, 6, 24, 48, and 72 h. The xenograft mice received FD/A83 and PM/A83 3 times intravenously with one day apart at a dose of 15 $mgkg^{-1}$. The control xenograft mice received 5% dextrose. After the last injections of each experimental time points, all mice were euthanized and sacrificed by cardiac puncture to collect the blood samples in heparinized tubes. Subsequently, all excised xenograft tumors and organs including brain, heart, lung, liver, kidney, and spleen were collected, snap-frozen using liquid nitrogen, and preserved in -80°C for later extraction and pharmacokinetic analysis.

6.2.10. Extraction method and quantification of A83B4C63 by LC/MS

To quantify the A83B4C63 levels in blood and tissue samples, a mass spectrometry (MS/MS) method was developed and validated in our laboratory. The collected whole blood samples of the mice were centrifuged at 2000 × g for 5 min at 4ºC to separate the plasma. 250 µL of plasma of each sample was mixed properly with a solution of acetonitrile: water (50:50 v/v) using a vortex for 5 min with 1:1 ratio. The precipitated proteins in plasma samples were centrifuged at 2000 × g for 5 min at 4ºC and then, 250 µL of blood plasma was transferred into an LC/MS glass vial and completely dried out by speed vacuum using liquid nitrogen. Similarly, all the tissue samples were also processed to extract the drug. In brief, a portion of tissue samples were weighted and homogenized completely with deionized water at a 1:1 w/v ratio. Then acetonitrile was added at a 50:50 v/v ratio and vortexed for 5 min to precipitate proteins in tissue samples. The precipitated proteins in tissue samples were centrifuged at 2000 × g for 5 min at 4ºC. The supernatant was collected and 100 µL of the supernatant was transferred into the LC/MS glass

vials to dry out completely using speed vacuum under the liquid nitrogen. Propranolol dissolved in the solution of acetonitrile: water with 50:50 ratios was used as an internal standard. Therefore, the dried residues of the test sample vials were reconstituted with 100 µL of internal standard solution with vigorous vortexing before placing into the auto-sampler of the LC/MS (Waters Quattro Micro ± ES MS Triple Quadrupole, Milford, MA, USA) fitted with an Agilent Technology: Poroshell 120 SB-C18 2.1x50 mm, 2.7 micron column. The mobile phase consisted of 50:50 v/v ratios of water with 0.1% formic acid and acetonitrile with 0.1% formic acid. Analyst software (version 1.6) was used for the quantitation step of corresponding A83B4C63 peak intensity.

6.2.11. Biodistribution and pharmacokinetic analysis

After the extraction procedure, mouse plasma and all the tissues were subjected for biodistribution studies to quantitate the concentration of A83B4C63 at different time points after systemic administration in mice. Thereafter, the quantitative correlation between the A83B4C63 concentrations and the experimental time points was investigated and analyzed according to non-compartmental model. Pharmacokinetic analysis was also investigated using the collected mouse serum at different time points. The area under the plasma concentration-time curve (AUC_{0-t}) was calculated using the linear trapezoidal rule from zero to last detectable sample time point. Due to destructive sampling procedure used for collecting blood and tissue samples from the mice at each time point, the AUC was not obtainable for individual animal. In addition, due to the nature of the experiments, the Bailer method, which incorporates partial AUC and variability associated with each of the mean concentrations at corresponding sampling time, was used to estimate the SD of the AUCs. The pairwise comparison of the AUCs was then carried out at a level of 0.05 (α =0.05). The critical value of Z (Z_{crit}) for the two- sided test after Bonferroni adjustment was 2.24.

The observed Z (Zobs) was also calculated based on Bailer's method. A Z_{obs} value greater than Z_{crit} was considered for a significant difference between the AUCs. The terminal elimination rate constant, β, was estimated using the linear least square regression of the log- linear phase of the concentration-time curves. The highest observed concentration and corresponding sampling time point were defined as the peak plasma concentration (C_{max}) and time-to-peak concentration (T_{max}), respectively. The above indices were reported in tissue samples.

6.2.12. Statistical analysis

GraphPad Prism6 software (La Jolla, CA, USA) was mostly used for statistical analysis. Significance test for the differences between groups were analyzed using two-way ANOVA following Tukey's model. If a significant difference was found among the groups, median ranks between pairs of groups were compared using the Mann-Whitney U test. A value of $p \leq 0.05$ was considered as statistically significant in all experiments, unless otherwise stated.

6.3. Results

6.3.1. Physicochemical characterizations

Table 6.1 exhibits the physicochemical characteristics of A83B4C63-encapsulated mPEO-*b*-PCL micelles (PM/A83). A83B4C63-encapsulated micelles had an average diameter below 60 nm. The polydispersity index (PDI) was below 0.2 and the surface of the micelles was neutral in charge. A83B4C63 loading and encapsulation efficiency (EE) reached to 19.71 ± 0.54 (% w/w) and 70.06 ± 1.88 %, respectively. Both PM/A83 and PEG-400-based (FD/A83) solubilizing resulted in water-solubility levels of A83B4C63 (≥ 10 mg/mL) that was considered to be suitable for IV administration for investigating their biodistribution profile *in vivo*. Moreover, critical micellar concentration was also measured using dynamic light scattering method and calculated to be 3.41 ± 0.08 µg/mL.

Table 6.1: Physicochemical characterizations (n = 4).

Formulations [a]	Size [b] ± SD (nm)	PDI [c] ± SD	Zeta Potential [d] ± SD (mV)	CMC [e] ± SD (μgmL-1)	A83B4C63 Loading [f] (% w/w)	A83B4C63 Encapsulation Efficiency [g] (%)
$mPEO_{114}$-b-PCL_{44}/A83B4C63 (PM/A83)	51.54 ± 0.18	0.19 ± 0.01	0.08 ± 0.05	3.41 ± 0.08	19.71 ± 0.54	70.06 ± 1.88

[a] The number shown in the subscript indicates the degree of polymerization of each block as determined by ^{1}H NMR spectroscopy.
[b] Hydrodynamic diameter (Z average) determined by DLS.
[c] Average PDI of micellar size distribution.
[d] Average surface charge (zeta potential) of the micelles.
[e] Average CMC measured by DLS.
[f] A83B4C63 loading (w/w %) $= \frac{\text{Amount of encapsulated A83B4C63}}{\text{Total amount of polymer}} \times 100$
[g] A83B4C63 encapsulation efficiency (%) $= \frac{\text{Amount of encapsulated A83B4C63}}{\text{Initial amount of A83B4C63 added}} \times 100$

6.3.2. Transmission electron microscopy (TEM)

The morphology of the self-assembled structures was investigated by TEM images, confirming the formation of spherical and oval shaped PM/A83 with uniform size (**Fig. 6.2B)**. Moreover, a similar distribution pattern in the micellar population having a clear boundary was observed in TEM images of all micelles, indicating the lower aggregation tendency of micelles.

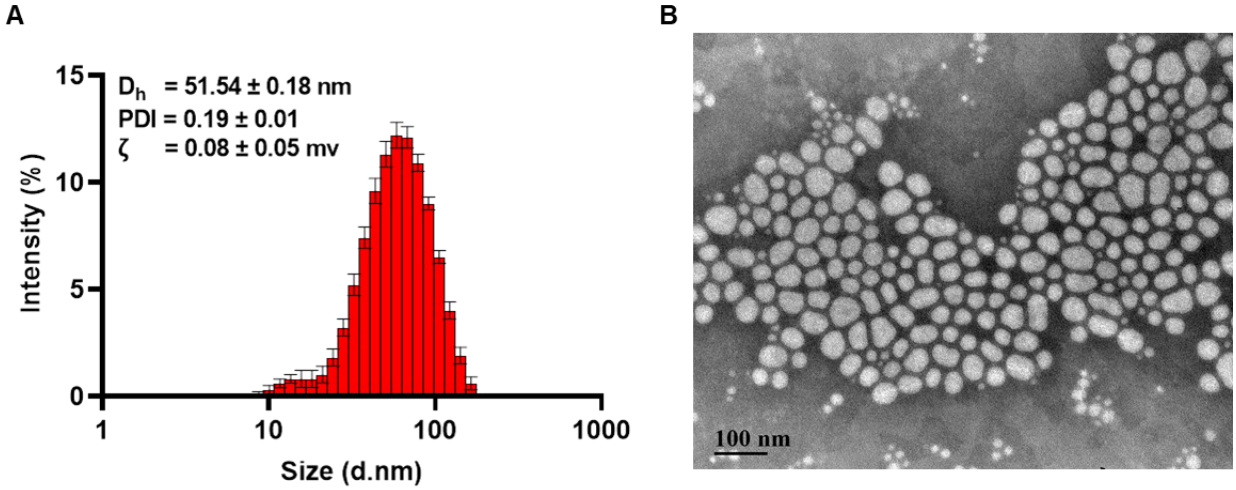

Figure 6.2: Hydrodynamic size distribution (A) and TEM image (B) of A83B4C63-encapsulated block copolymeric micellar formulation (PM/A83) in aqueous medium. Hydrodynamic diameter (D_h), PDI, zeta potential (ζ) and size distribution of PM/A83 micelles in aqueous medium were obtained using dynamic light scattering (DLS) technique. The TEM image was obtained at a magnification of 110,000X at 75 kV. The bar in the bottom left corner of each image indicates a scale of 100 nm.

6.3.3. *In vitro* cytotoxicity

The MTS assay was performed up to 72 h to determine the toxicity of the PNKP inhibition with the micellar delivery formulation (PM/A83) against FaDu cell lines in comparison to the conventional solubilizing free drug formulation (FD/A83). **Fig. 6.3** shows the average percentages of cell viability up to 72 h treatment with the formulations. Notably, no cell viability reduction was observed up to 80 µM concentration of A83B4C63 over 72 h treatments of both formulations. Overall data suggest that micellar delivery of PNKP inhibitor effectively preserved the safety of the drug without interfering the growth of FaDu cell line.

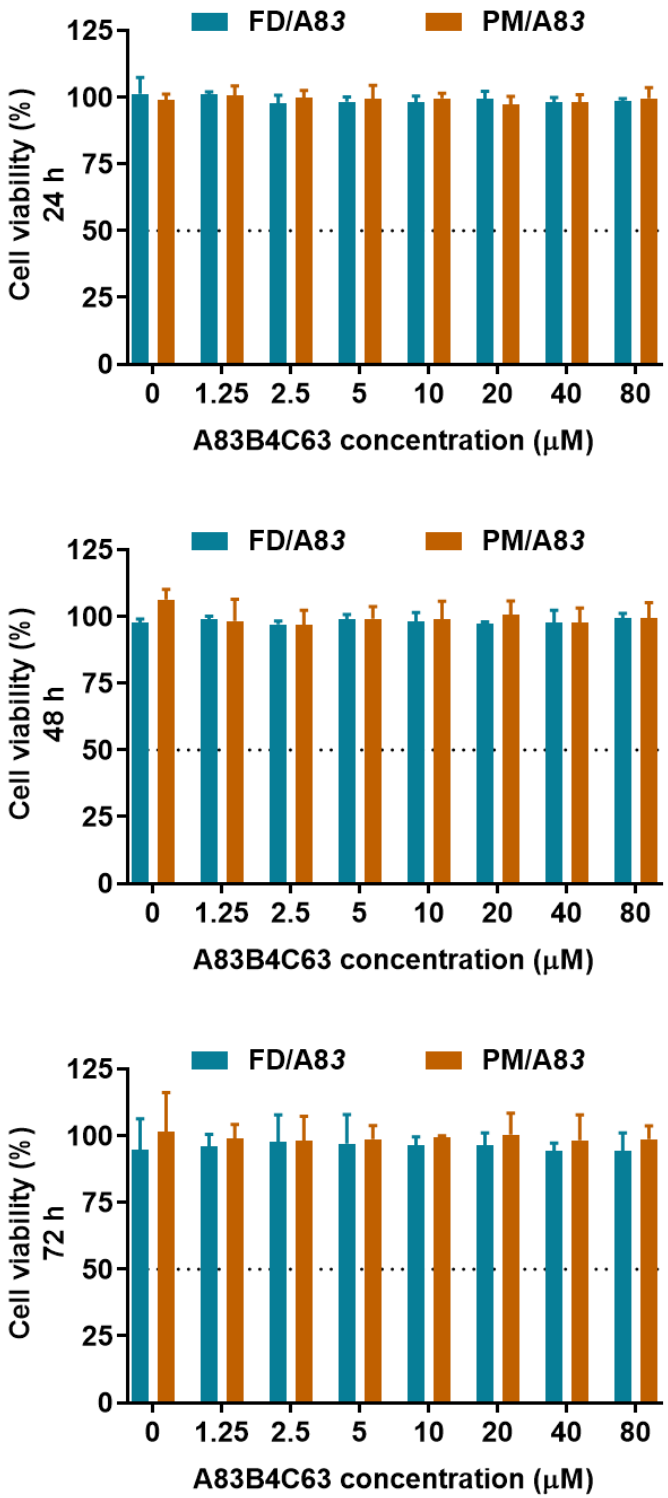

Figure 6.3: *In vitro* cytotoxicity of free versus micellar forms of A83B4C63 in FaDu cell lines after 24, 48, and 72 h incubation at 37ºC in 5% CO_2. The cells were treated with the free drugs and polymeric micelles with a range of concentrations from 0.001 μM to 80 μM. The untreated cells received only 5% dextrose. Each point represents mean ± SD (n = 4).

6.3.4. Blood binding evaluation

As represented in **Fig. 6.4**, the estimated values of blood to plasma concentration ratio at different concentrations of A83B4C63, which were added to the whole blood samples as PEG-400 (FD/A83) or micellar (PM/A83) formulations, were very close to unity exhibiting no noticeable binding of either free drug or micellar-loaded form to the rat red blood cells.

The blood binding study was conducted at the concentration up to 500 $ngmL^{-1}$ as in previous pharmacokinetic studies of this compound maximal concentrations of 500 $ngmL^{-1}$ were achieved in rat plasma following intravenous administration of 10 $mgkg^{-1}$ of the compound as the PEG solution or micellar formulation. The values of blood to plasma concentration ratios over different concentrations indicated negligible deviations from the unity at some concentrations. Red blood cell partitioning of the free compound seemed to be concentration-independent over the concentration range of 25 to 500 $ngmL^{-1}$, indicating that partitioning involves only passive diffusion and the distribution of the micellar A83B4C63 throughout the blood was uniform and homogeneous.

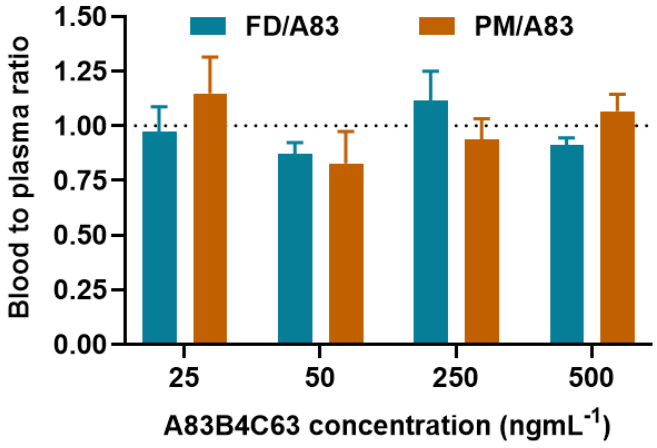

Figure 6.4: Blood to plasma ratio (mean ± SD, n = 3) after spiking blood with FD/A83 and PM/A83.

6.3.5. Biodistribution and pharmacokinetic profile of A83B4C63

6.3.5.1. A83B4C63 in mice serum

Fig. 6.5 shows the A83B4C63 plasma concentration versus time curve for FD/A83 and PM/A83 after IV administration to the mice. Over the experimental study periods, the A83B4C63 concentrations in both formulations followed a gradual declining trend after the last injection in the test mice. However, A83B4C63 concentration was significantly lower in the FD/A83-treated mice blood plasma than that of PM/A83-treated mice throughout the study period and was quantifiable in plasma only up to 24 h. On the contrary, PM/A83 maintained the plasma concentration of A83B4C63; being quantifiable, up to 72 h post systemic administration.

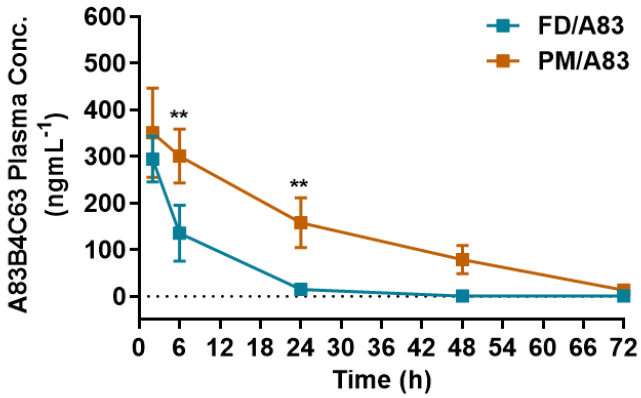

Figure 6.5: A83B4C63 Plasma concentration versus time curves of FD/A83 and PM/A83 formulations in FaDu xenograft tumor-bearing mice.

Table 6.2, **6.3**, and **6.4** demonstrated the key pharmacokinetic parameters of A83B4C63 obtained after analyzing the plasma samples from test mice. The obtained AUC value was significantly higher in plasma of PM/A83-treated mice than that of FD/A83-treated mice. Higher AUC value resulting from the PM/A83 treatment may indicate a decrease in elimination rate (Ke), which was reflected in its corresponding calculated $t_{1/2}$ = 13.32 h. However, $t_{1/2}$ was incalculable based on the obtained plasma concentration of A83B4C63 in FD/A83-treated mice due to absence

of plasma concentration of A83B4C63 after 24 h post injection. But this shows the elimination half-life should be shorter for the FD/A83, nevertheless. The mean residence times (MRT) of FD/A83 and PM/A83 were 7.31 ± 1.10 h and 21.43 ± 1.52 h, respectively (**Table 6.4**).

Table 6.2: Area under the curve of Micellar and Free A83B4C63 formulations. Significant differences between FD/A83 and PM/A83 were distinguished at *p value of 0.05.

Specimen	**AUC (2-72 h)**	
	FD/A83 (ng*h/mL)	**PM/A83** (ng*h/mL)
Plasma	2375.07 ± 411.75	9348.89 ± 875.09*
Tumor	169.93 ± 86.82	601.05 ± 170.04*
Kidney	780.17 ± 100.03	736.06 ± 100.17
Spleen	1954.30 ± 322.59*	195.82 ± 36.37
Liver	581.59 ± 90.17	6605.82 ± 810.33*
Lung	588.96 ± 93.31	1610.11 ± 141.52*
Heart	524.83 ± 80.28	793.85 ± 227.37

6.3.5.2. Biodistribution of A83B4C63 formulations in the specimens of FaDu bearing mice

A83B4C63 concentrations in excised FaDu xenograft tumors from mice at different experimental time points after the systemic administration with FD/A83 and PM/A83 were measured and reported in **Fig. 6.6A**. The tumoral concentration versus time profile of A83B4C63 indicated a sharp decline in FD/A83-treated group by 24 h post administration while the PM/A83 formulation demonstrated a prolonged accumulation in xenograft tumors up to 72 h. The PM/A83 formulation showed significantly higher A83B4C63 concentration than its counterpart at 24 and 48 h post injection ($P < 0.05$). The plasma and tumor $AUC_{(2\text{-}72\ h)}$ was significantly higher (by around 3.9 and 3.5 fold, respectively) for the PM/A83 compared to the one for the free drug ($p <$

0.05). The obtained MRTs of FD/A83 and PM/A83 were 12.82 ± 9.74 h and 27.52 ± 4.44 h, respectively (**Table 6.4**). **Fig. 6.6B** shows the tumor to plasma ratios of A83B4C63 at different time points from both formulations. The tumor to plasma ratios in all time points was below 1, in the tumor even for the PM/A83 formulation (**Table 6.2**).

Table 6.3: Tissue to plasma ratios of area under the curve of micellar and free A83B4C63 in mice (n = 3, *$p \leq 0.5$, student's t-test).

Tissue	**AUC ratio (tissue: plasma)**	
	FD/A83	**PM/A83**
Tumor	0.072	0.064
Kidney	0.328*	0.079
Spleen	0.565*	0.021
Liver	0.168	0.707*
Lung	0.171	0.172
Heart	0.152*	0.085

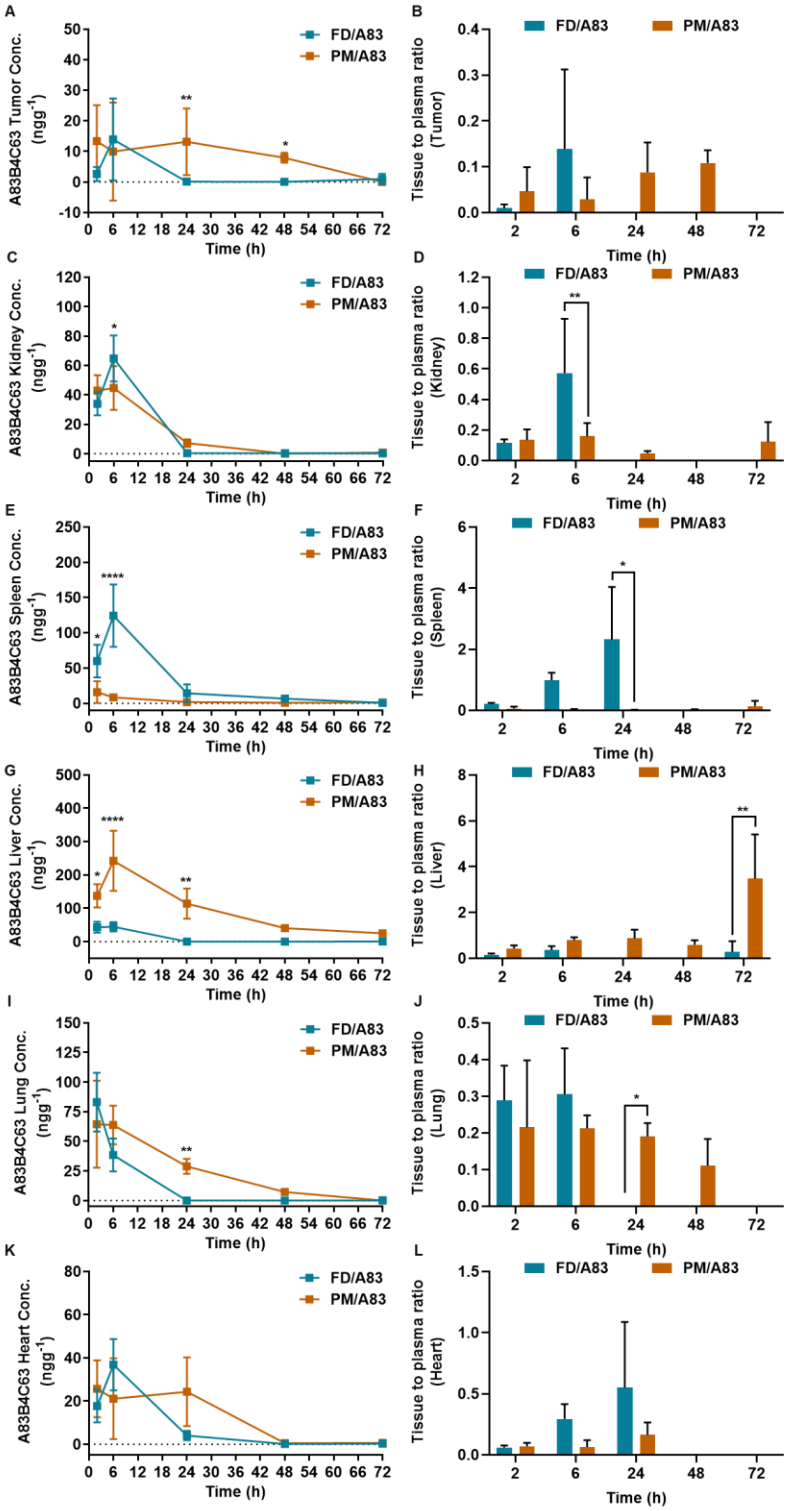

Figure 6.6: Biodistribution profile of FD/A83 and PM/A83 formulations in FaDu xenograft tumor-bearing mice (n = 3). Differences were considered significant if *$p \leq 0.05$, **$p \leq 0.01$, ***$p \leq 0.001$, and ****$p \leq 0.0001$ following two-way ANOVA followed by Tukey's method.

Among under tissues, significantly higher concentration of PM/A83 formulation was achieved in the liver and lungs as evidenced by significantly higher $AUC_{(2\text{-}72\ h)}$ in these organs when compared to free drug (**Table 6.2**). Analysis of the concentration versus time profile for the two formulations in the liver showed significantly higher concentration of drug delivered by PMs at 24 h and shorter time points compared to the free drug (**Fig. 6.6G** and **6.6H**). However, the Kp value was only significantly higher for the NP-delivered A83 at 72h time point compared to free drug (**Fig. 6.6G** and **6.6H**). In the lung, PM/A83 formulation led to significantly higher drug levels at 24h post dose compared to free drug and Kp values were also significantly higher for this formulation at the same time point and onwards (**Figure 6.6I** and **6.6J**). Analysis of the pharmacokinetic parameters also showed a significant increase in the MRT of PM/A83 formulation compared to free drug in liver and lung (**Table 6.3**). FD/A83 resulted in similar drug AUC level in kidney and heart compared to its PM/A83 formulation, but the AUC ratio of A83 in these organs compared to plasma was significantly higher for the free drug. This can be attributed to higher plasma concentrations of A83 delivered by PM/A83. The level of A83B4C63 in kidney at 6 h post dose was higher for free drug time point compared to that of PM/A83 ($*p < 0.05$). Similar trend was observed for the Kp value at 6 h time point. (**Fig. 6.6C-D** and **Table 6.3**).

Table 6.4: Tissue and plasma PK parameters of micellar and free A83B4C63 formulations.

Specimen	Formulations	Pharmacokinetic parameters			
		$T_{1/2}$ (h)	C_{max}[a]	T_{max} (h)	MRT (h)
Plasma	FD/A83	ND[b]	293.75 ± 49.01	2	7.31 ± 1.10
	PM/A83	13.32*	350.76 ± 95.66*	2	21.43 ± 1.52*
Tumor	FD/A83	-	13.91 ± 13.41	6	12.82 ± 9.74
	PM/A83	-	27.03 ± 1.37*	6	27.52 ± 4.44*
Kidney	FD/A83	-	64.76 ± 15.68	6	6.47 ± 0.99
	PM/A83	-	52.42 ± 7.56	2	9.83 ± 1.03
Spleen	FD/A83	-	124.29 ± 44.32*	6	17.77 ± 5.26*
	PM/A83	-	17.17 ± 13.69	2	12.50 ± 3.39
Liver	FD/A83	-	45.88 ± 15.53	6	6.67 ± 1.59
	PM/A83	-	242.32 ± 90.22*	6	21.54 ± 1.56*
Lung	FD/A83	-	83.08 ± 24.86	2	5.29 ± 0.64
	PM/A83	-	72.05 ± 30.12	6	17.17 ± 2.28*
Heart	FD/A83	-	36.85 ± 11.84	6	9.41 ± 1.65
	PM/A83	-	35.41 ± 4.76	6	19.17 ± 2.80*

According to the defined pharmacokinetic analysis in **Table 6.4**, no significant difference was determined for the C_{max} and MRTs of FD/A83 and PM/A83 in kidney (**Table 6.4**). Similar to the kidney, the $AUC_{(2\text{-}72h)}$ of A83 in the spleen was found to be similar in mice that received free or NP formulation of the drug. The tissue to plasma AUC ratio was, however, higher for the free drug. The analysis of the concentration versus time profile showed higher spleen concentrations for the free drug at 2 (*$p < 0.05$) and 6 h (**$p < 0.01$) post dose compared to PM/A83 formulation

(**Fig. 6.6E** and **6.6F**). Moreover, a significant higher Kp values were obtained for the free drug at 24 h post dose compared to PM/A83, $*p < 0.05$ (**Fig. 6.6E** and **6.6F**). The C_{max} and MRT were found to be higher for the free drug in spleen, as well (**Table 6.4**).

In the heart, similar to kidneys, while the AUC did not reveal any significant difference between the NP and free drug formulation, the AUC ratios was found to be significantly higher for the free drug. In the concentration versus time profile no significant difference in drug concentrations or K_P values was shown in all timepoints under study. The MRT of the PM/A83 was still longer for than that of the free drug in the lung.

6.4. Discussion

In this present study, A83B4C63; inhibitor of PNKP, was encapsulated in di-block mPEO-*b*-PCL micelles (PM/A83) and its biodistribution was compared to that for the A83B4C63 solubilized with the aid of PEG-400 as an inert solubilizing agent. For the micellar delivery of hydrophobic A83B4C63 in this study, FDA-approved di-block mPEO-*b*-PCL polymer with a degree of polymerization 44. This selection was based on our initial investigation of the physicochemical characteristics of PM/A83 formulation, that have shown appropriate diameter, polydispersity index and solubilization level of A83B4C63 for *in vivo* administration. micellar formulation of A83B4C63, i.e., PM/A83, showed promising unimodal size distribution below 100 nm, evaluated by DLS technique as well as by TEM image. Primarily, both of these formulation strategies were envisioned to improve the aqueous solubility level of this hydrophobic small molecule drug for further *in vivo* investigation.

It is well-known that polymeric micelles with average size between 10-100 nm firmly retain the required colloidal properties that are suitable in delivering hydrophobic drugs following

intravenous route of administration. Size of the PMs may have significant role in determining the *in vivo* bio-fate of systemically administered micellar payload [253, 389, 390]. Upon systemic administration, nanoparticles' size less than 10 nm are believed to be rapidly cleared from the biological system followed by renal filtration [253, 391, 392]. Similarly, the hydrodynamic size of the nanoparticles above 200 nm also exhibited rapid body clearance due to the recognition by reticuloendothelial system (RES) of the organs (e.g. liver, spleen) [389, 393].

Surface charge is also an important parameter to be considered prior to *in vivo* investigation [394]. Mostly, the presence of positive charge or cationic surface of the nanoparticle was attributed to the accelerated cell uptake and RES-mediated rapid clearance compared to neutral to low range negatively charged particles [395]. In our study, the neutral zeta potential value was obtained from the micellar PM/A83 that was safe and suitable for IV administration. Because, it is also reported that the complex aggregates, being formed between negatively charged plasma proteins and positively charged nanoparticles stimulate both RES recognition and downstream embolism in blood capillaries during systemic circulation [253, 393, 396-398]. The neutral surface charge of our micellar nanoparticles was obtained due to the hydrophilic methoxy PEG shell that possess the stealth effect in preventing complex aggregation and opsonization by blood compartmental proteins [253, 393, 399-401].

Since, most anticancer therapeutics required high efficacious dose, they often end up unwanted sever toxicity [402]. However, nanoparticulate delivery systems were introduced to spare the toxicity by improving bioavailability and accessibility into solid tumors [402-404]. We used head and neck cancer (FaDu) xenograft tumor-bearing athymic NIH-III nude female mice to determine the fate of A83 delivered by the $mPEO_{114}$-*b*-PCL_{44} self-associating micelles in comparison to its conventional formulation. The mice were injected with 3 IV injections of

A83B4C63 at a dose of 15 $mgkg^{-1}$ every other day. At defined time points, mice were euthanized, and drug concentrations were measured at tumor, plasma, and main organs.

First, to identify the suitability of plasma (versus whole blood) in our investigations, the % of partitioning of A83B4C63 to red blood cells, was assessed. to the results confirmed that A83B4C63 from either of the formulations did not reach to any notable binding % to rat's red blood cells up to 500 $ngmL^{-1}$ concentrations, validating the use of plasma samples in our biodistribution studies instead of whole blood.

As a novel lead PNKP inhibitor, A83B4C63 falls under new molecule category. No previous report on the pharmacokinetic parameters of this molecules including its half-life ($t_{1/2}$), area under the plasma concentration versus time curve (AUC), maximum plasma concentration (C_{max}), time to reach maximum plasma concentration (T_{max}), and mean residence time (MRT) of the drug following intravenous administration was available. We expected the PM/A83 formulation to improve its AUC, $t_{1/2}$, and MRT in plasma and tumor compared to the free drug In effect, we observed a significant but marginal increase in the AUC of A83B4C63 in plasma and tumor by its PM/A83 formulation (by 3.9 and 3.5 folds, respectively) compared to the PEG400 formulation of this compound. An increase in A83B4C63 AUC was also observed in the liver and lung of animals with the PM/A83 formulation, while drug levels in other normal tissues stayed similar for both formulations.

A parallel increase in the MRT of the PM/A83 formulation was observed in plasma, tumor and most of the normal tissues understudy compared to its PEG-400 formulation. The only exception was the spleen which showed a significantly higher MRT for the free drug compared to its PM formulation. A general evaluation of the Kp and tissue to plasma AUC rations reveal a trend in early time point distribution of free drug in kidneys and spleen and a late time point (>6 -

48 h) distribution of PM/A83 formulation of this compound in tumor, liver and lungs. It should be noted that the KP value only gets to values > 1, in the liver for the PM/A83 formulation and in the spleen for PEG-400 formulation, revealing the major sites of accumulation for these formulations in this tumor bearing mice.

6.5. Conclusion

Our results showed that mPEO-*b*-PCL micelles may be used as effective solubilizing agents for the delivery of A83B4C63. The *in vivo* data, a marginal increase in tumor drug levels by this formulation in comparison to the free drug but does not support great promise in drug targeting. The obtained data under this biodistribution and pharmacokinetic study provides valuable insight about the in vivo characteristics, residency time, and level of A83B4C63 concentration in tumors or other organs in immunocompromised NIH-III mice, which could be used to further determine the dose escalation strategy and the combination treatment plans with either chemotherapy or ionizing radiation.

6.6. Acknowledgments

This study was supported by the NanoMedicines Innovation Network (NMIN) grant to Afsaneh Lavasanifar (). Sams Sadat was supported by Alberta Innovates and CIHR Fellowship. The authors thank the Advanced Microscopy Facility (AMF), Department of Biological Sciences, University of Alberta for assistance with TEM analysis.

Chapter 7: Conclusion and future direction

Mutation or loss of tumor suppressor genes plays a key role in tumor development and therapeutic resistance in cancer patients. Such loss of tumor suppressor genes in only cancer cells have brought new scopes for developing targeted cancer therapeutics by means of synthetic lethality partnership with other non-essential genes or protein. While the expression or functionality of either one of these two non-essential genes in normal cells leads to cell survival. In this thesis, we have shown the potential of small molecule inhibitors of PNKP to induce a synthetic lethal response in PTEN-depleted cancer cells and their respective xenografted mice models when delivered by NPs. In respect to this purpose, we have used very stable NPs based on PEO-*b*-PBCL to encapsulate A83B4C63 since free PNKP inhibitors are poorly water-soluble compounds. The results of our study have shown the encapsulation of A83B4C63 into PEO-*b*-PBCL NPs overcame this limitation, improving the solubilized drug levels to > 6 mg/mL, which made this compound suitable for systemic administration in animals. The overall physicochemical characteristics including slow *in vitro* release of A83B4C63, low CMC and kinetic stability of PEO-*b*-PBCL also retained its higher biological stability compared to its CE or PEG formulation as NP formulations of A83B4C63 revealed higher plasma and tumor drug levels 48 h post dose in mice.

The encapsulated A83B4C63 was shown to be active as a monotherapeutic in PTEN-deficient HCT116 cells. *In vitro*, it caused higher levels of caspase 7 expression in $PTEN^{-/-}$ cell treated but no caspase 3 or PARP expression, which needs to be further explored in order to identify the underlying mechanism of such synthetic lethal partnership.

According to our preclinical evaluation, our MTD study, under systemic administration of A83B4C63 did not reveal any notable biochemical, and histopathological changes in healthy CD-1 mice. Our results showed A83B4C63 either as CE or NP formulation were well-tolerated up to

the tested dose of 50 mg/kg. Further *in vivo* studies with 25 mg/kg dose of A83B4C63 via polymeric micelles was able to retard the growth of $PTEN^{-/-}$ and $Luc^{+}/PTEN^{-/-}$ HCT116 xenografts significantly. However, free A83B4C63-solubilized formulations failed to show any substantial anticancer effect, which was also confirmed by Ki67 staining of tumor xenografts. The similar level of distributed A83B4C63 in $PTEN^{-/-}$ versus $PTEN^{+/+}$ tumors ruled out the further evidence for the synthetic lethality as the main reason behind effectiveness of this formulation in PTEN-negative tumors as monotherapy.

Human PNKP phosphorylates DNA 5′-termini and dephosphorylates DNA 3′-termini, therefore allowing DNA ligases to rejoin the strands and plays a key role in both single- and double-strand breaks repair. Moreover, the downregulation of PNKP by siRNA or its inhibition by small molecule inhibitors have shown to make cancer cells sensitive to IR and TOP1 inhibitors. Our *in vitro* studies on wild type HCT116 cells revealed the activity of A83B4C63 either as CE or NP formulation in enhancing DNA damage by IR. This was evidenced through the measurement of γ-H2AX foci formation, which showed an increase in foci numbers upon co-treatment of cells with IR plus both A83B4C63 formulations compared to the IR treatment alone. The NP formulation showed a significant increase in the level of induced γ-H2AX foci formation only at 40 min after the radiation and not at the longer time points, when compared to the CE formulation. The reason for this observation is not clear and needs to be further investigated. Similar to the microscopy results, A83B4C63 formulations + IR reflected higher mediator markers of apoptosis compared to the IR alone.

For the *in vivo* radio-sensitizing studies, a relatively low fractionated dose (3 x 5 Gy) of IR was used and well-tolerated by the animals. The wild type HCT116 xenografts showed significant retardation of tumor growth only when NP/A83 treatment was combined with the fractionated

dose of IR using SARRP facility. The activity of NP/A83 as radio-sensitizer was also confirmed by IVIS imaging and PET imaging using [^{18}F]FLT as the anti-proliferative marker in live animals. Collectively these data validated the intravenously administered NP/A83 as more effective radio-sensitizer in wild type CRC xenografts in mice. However, similar animal studies with various doses need to be further performed in future to identify the effective dose of PNKP inhibitors.

A83B4C63 is a new investigational drug and the effect of CE on its pharmacokinetic profile is not yet clearly known. Our data on the biodistribution of NP/A83 versus CE/A83 formulations at 4, 24, and 48 h post last injection warrants further investigation with more time points and dose-dependent experiments. In all studies, we only used the PEO-PBCL copolymer with DP = 26 based on *in vitro* studies. In future, similar formulations with different DPs could be considered to investigate the optimum formulation composition based on *in vivo* pharmacokinetics.

We also developed TOP1 inhibitor (SN-38)-conjugated micellar delivery system to its solubility in water and to co-deliver with PNKP inhibitor in respect to develop chemo-sensitizer for wild type cancer cells. To this end, SN-38 was chemically conjugated to the poly(ester) core of different micellar formulations, i.e., mPEO-*b*-PBCL and mPEO-*b*-PCCL. Our studies showed that, as a result of SN-38 chemical conjugation to mPEO-*b*-PBCL and mPEO-*b*-PCCL copolymers, the solubilized levels of SN-38 in water improved to > 10 mg/mL, which meets the criteria for systemic therapy. The conjugation level of SN-38 in micellar formulations study were about to 18% (w/w), which needs further optimization to increase the loading without interfering the potency of SN-38. In our study, the release of SN-38 from the micellar SN-38 was significantly slower and validated the slow cleavage of the linkage between SN-38 and the polymeric backbone and/or cleavage of SN-38-caprolactone derivatives from the micellar core.

Micellar SN-38 formulations resulted in similar viability reduction in human CRC cell lines as free SN-38 and significantly enhanced the mediators of apoptosis markers compared to irinotecan in all the CRC cell lines at their respective IC_{50}s. In our study, micellar SN-38 no hemolytic activity at IC_{50} concentration.

Therefore, we aimed to investigate the synergy between polymeric micellar formulations of SN-38 and A83B4C63 combination as individual micelles added together or mixed micelles co-delivering both drugs against CRC cell lines, *in vitro*. To this end, SN-38 was also chemically conjugated to the poly(ester) end of mPEO-*b*-PBCL with a lower DP of 16, using activation of the COOH group at the polymer end. This led to > 600 folds increase in water solubilized levels of SN-38 (25 μg/mL to over 15 mg/mL) and in respect to A83B4C63 co-encapsulation, the mixed micellar formulation (PM_{16}-SN-38:PM_{26}/A83) increased the water-soluble levels of A83B4C63 from 1 μM to 10.67. The synergy between A83B4C63 and mixed micellar SN-38 formulation was confirmed Combenefit® software based on the cell viability data. Our data revealed a synergy between free SN-38 and PM_{16}-SN-38 with PM_{26}/A83 at a concentration range of 0.01-1 μM for SN-38 and 10-40 μM for A83B4C63.

At a fixed A83B4C63 concentration (10 μM), the cytotoxicity data revealed significantly higher cell viability reduction for the combination treatments compared to their counterparts with SN-38 treatment only. The effect of combination treatment with PNKP + TOP1 inhibitor was also observed for increasing DNA damage and mediators of apoptosis in CRC cells compared to their respective individual treatments with TOP1 inhibitor within 6 h. Due to non-toxic behavior of our novel PNKP inhibitor, IC_{50} concentration was not measurable up to 40 μM treating dose which was 3 times higher treating dose than the required dose (10 μM) for desired chemo-sensitization in this study. Therefore, the co-delivery of A83B4C63 and SN-38 in one polymeric micellar

formulation (PM_{16}-SN-38:PM_{26}/A83) potentiated the effect of A83B4C63. This was evident from similar cell viability at much lower ratios of A83 to that of SN-38 in co-delivery systems (PM_{16}-SN-38:PM_{26}/A83) in both cell lines compared to that of combination treatment (PM_{16}-SN-38 + PM_{26}/A83). The most important limitation of this study was that it was not desirably possible to control the loading as well as the treatment concentration of both A83B4C63 and TOP1 inhibitor while formulating co-delivery platform i.e., mixed micelles. In future, a systematic study design needs to be performed to control the loading ratio between TOP1 inhibitor and PNKP inhibitor.

Moreover, conjugating PNKP inhibitor to copolymer has not been investigated yet for its similar efficacy to inhibit the activity of intracellular PNKP. In future, the conjugation of PNKP inhibitor to copolymer can be considered to investigate for its anticancer efficacy. Upon successful conjugation of PNKP inhibitor to copolymer might have benefit over physical encapsulation and further mixed micellar co-delivery system.

In summary, our preclinical data have demonstrated that NPs of a PNKP phosphatase inhibitor, i.e., A83B4C63 exhibit *in vivo* synthetic lethality in a PTEN-deficient CRC xenograft model. The preclinical tests also demonstrated the safety profile of the micellar NPs of A83B4C63 in healthy mice in respect to identify maximum tolerated dose under intravenous administration. Although, binding capacity of A83B4C63 was confirmed by CETSA experiments, the development of a third generation of the PNKP inhibitor with nano molar IC_{50} and K_D value could be considered in future. In addition, a targeted NP-based drug delivery could be a better option to access the solid tumors, *in vivo*. For example, programmed death-ligand 1 is over-expressed in CRC. The development of anti-PD-L1-targeted NP-based delivery system and encapsulation of PNKP inhibitor could be a future proposal to have more accessibility to the solid tumors, *in vivo*. According to the pharmacokinetic investigation with an IV dose of 25 mg/kg, we observed

significantly higher concentration of A83B4C63 in tumor tissues at 48 h time point which was below IC_{50} concentration that was observed *in vitro*. A dose increases up to 50 mg/kg could be tried and more sampling time points are suggested to obtain clearer pharmacokinetic and biodistribution profile of the NPs of PNKP inhibitor.

Combination therapy is currently a popular strategy for treating cancers with either chemo- or radio-sensitizers. The co-delivery of new chemotherapeutic drug and its novel chemo-sensitizing DNA repair enzyme inhibitor is an exciting area in the field of combination therapy against various cancers. Here, we successfully established poly(ethylene oxide)-poly(ester)-based mixed micellar NPs to co-encapsulate both PNKP inhibitor and TOP1 inhibitor, SN-38 which is an active metabolite of irinotecan. A successful conjugation between SN-38 and methoxy-poly(ethylene oxide)-block-poly(α-benzyl carboxylate-ε-caprolactone) (mPEO-*b*-PBCL) was performed to improve the water-solubility of SN-38 without debilitating its anticancer potency. All the physicochemical characterization and *in vitro* evaluation were also performed, and the overall data demonstrated a clear synergistic chemo-sensitization in CRC cell lines due to the co-delivered PNKP inhibitor. However, a complete preclinical *in vivo* investigation could be considered as a proof of new concept for a promising nanomedicine as a novel combination treatment option against not only advanced but also regular CRC patients.

Since the loss of expression or inhibition of PNKP makes cancer cells sensitive to DNA damage by IR and topoisomerase I inhibitors, we also investigated radio-sensitizing anticancer activity of our developed NP of A83B4C63 in wild-type CRC xenograft in mice. Systemic delivery of our NP of A83B4C63 at a systemic dose of 25 mg/kg (3 times a week) effectively sensitized the wild type CRC xenograft to the fractionated irradiation dose of 3 x 5 Gy using an image-guided SARRP facility. Since the PNKP inhibition showed synthetic lethality in PTEN-deficient CRC

xenograft in mice, such radio- and chemo-sensitizing preclinical studies could also be performed to observe the efficacy in PTEN-deficient CRC xenograft mice models. With such combination preclinical studies, it is expected to yield complete suppression of PTEN-deficient cancers.

References

1. Lewis, T. and M. Dimri, *Biochemistry, DNA Repair*, in *StatPearls*. 2020, © 2020, StatPearls Publishing LLC.: Treasure Island FL.
2. Ma, X., T.-S. Tang, and C. Guo, *Regulation of translesion DNA synthesis in mammalian cells.* Environmental and Molecular Mutagenesis, 2020. **61**(7): p. 680-692.
3. Vindigni, A. and S. Gonzalo, *The two faces of DNA repair: disease and therapy.* Mo Med, 2013. **110**(4): p. 314-9.
4. Andres, S.N., et al., *Recognition and repair of chemically heterogeneous structures at DNA ends.* Environ Mol Mutagen, 2015. **56**(1): p. 1-21.
5. Tiwari, V. and D.M. Wilson, 3rd, *DNA Damage and Associated DNA Repair Defects in Disease and Premature Aging.* American journal of human genetics, 2019. **105**(2): p. 237-257.
6. Lange, S.S., K.-i. Takata, and R.D. Wood, *DNA polymerases and cancer.* Nature reviews. Cancer, 2011. **11**(2): p. 96-110.
7. Helleday, T., et al., *DNA repair pathways as targets for cancer therapy.* Nature Reviews Cancer, 2008. **8**(3): p. 193-204.
8. Branzei, D. and M. Foiani, *Regulation of DNA repair throughout the cell cycle.* Nature Reviews Molecular Cell Biology, 2008. **9**(4): p. 297-308.
9. Hübscher, U. and G. Maga, *DNA replication and repair bypass machines.* Curr Opin Chem Biol, 2011. **15**(5): p. 627-35.
10. Wang, L.H., et al., *Loss of Tumor Suppressor Gene Function in Human Cancer: An Overview.* Cell Physiol Biochem, 2018. **51**(6): p. 2647-2693.
11. Torgovnick, A. and B. Schumacher, *DNA repair mechanisms in cancer development and therapy.* Frontiers in Genetics, 2015. **6**(157).
12. Lindahl, T., *Instability and decay of the primary structure of DNA.* Nature, 1993. **362**(6422): p. 709-15.
13. Wang, W., et al., *Structural basis of transcriptional stalling and bypass of abasic DNA lesion by RNA polymerase II.* Proc Natl Acad Sci U S A, 2018. **115**(11): p. E2538-E2545.
14. Loeb, L.A. and B.D. Preston, *Mutagenesis by apurinic/apyrimidinic sites.* Annu Rev Genet, 1986. **20**: p. 201-30.
15. Catalano, M.J., et al., *Chemical structure and properties of interstrand cross-links formed by reaction of guanine residues with abasic sites in duplex DNA.* J Am Chem Soc, 2015. **137**(11): p. 3933-45.
16. Rogozin, I.B., et al., *Mutational signatures and mutable motifs in cancer genomes.* Brief Bioinform, 2018. **19**(6): p. 1085-1101.
17. Liu, X. and F.L. Meng, *Generation of Genomic Alteration from Cytidine Deamination.* Adv Exp Med Biol, 2018. **1044**: p. 49-64.
18. Bębenek, A. and I. Ziuzia-Graczyk, *Fidelity of DNA replication-a matter of proofreading.* Curr Genet, 2018. **64**(5): p. 985-996.
19. Williams, J.S., S.A. Lujan, and T.A. Kunkel, *Processing ribonucleotides incorporated during eukaryotic DNA replication.* Nat Rev Mol Cell Biol, 2016. **17**(6): p. 350-63.
20. Madireddy, A. and J. Gerhardt, *Replication Through Repetitive DNA Elements and Their Role in Human Diseases.* Adv Exp Med Biol, 2017. **1042**: p. 549-581.
21. Neil, A.J., J.C. Kim, and S.M. Mirkin, *Precarious maintenance of simple DNA repeats in eukaryotes.* Bioessays, 2017. **39**(9).
22. Kaushal, S. and C.H. Freudenreich, *The role of fork stalling and DNA structures in causing chromosome fragility.* Genes Chromosomes Cancer, 2019. **58**(5): p. 270-283.

23. Patel, D.R. and R.S. Weiss, *A tough row to hoe: when replication forks encounter DNA damage.* Biochem Soc Trans, 2018. **46**(6): p. 1643-1651.
24. Richard, P. and J.L. Manley, *R Loops and Links to Human Disease.* J Mol Biol, 2017. **429**(21): p. 3168-3180.
25. Santos-Pereira, J.M. and A. Aguilera, *R loops: new modulators of genome dynamics and function.* Nat Rev Genet, 2015. **16**(10): p. 583-97.
26. Brooks, P.J., *The cyclopurine deoxynucleosides: DNA repair, biological effects, mechanistic insights, and unanswered questions.* Free Radic Biol Med, 2017. **107**: p. 90-100.
27. Wu, S., et al., *Evaluating intrinsic and non-intrinsic cancer risk factors.* Nature Communications, 2018. **9**(1): p. 3490.
28. Cadet, J. and T. Douki, *Formation of UV-induced DNA damage contributing to skin cancer development.* Photochem Photobiol Sci, 2018. **17**(12): p. 1816-1841.
29. Mullenders, L.H.F., *Solar UV damage to cellular DNA: from mechanisms to biological effects.* Photochem Photobiol Sci, 2018. **17**(12): p. 1842-1852.
30. Jackson, S.P. and J. Bartek, *The DNA-damage response in human biology and disease.* Nature, 2009. **461**(7267): p. 1071-8.
31. Dizdaroglu, M. and P. Jaruga, *Mechanisms of free radical-induced damage to DNA.* Free Radic Res, 2012. **46**(4): p. 382-419.
32. Cadet, J., et al., *Formation and repair of oxidatively generated damage in cellular DNA.* Free Radic Biol Med, 2017. **107**: p. 13-34.
33. Foray, N., M. Bourguignon, and N. Hamada, *Individual response to ionizing radiation.* Mutat Res, 2016. **770**(Pt B): p. 369-386.
34. Tiwari, V., et al., *Akt1/NFκB signaling pathway activation by a small molecule DMA confers radioprotection to intestinal epithelium in xenograft model.* Free Radic Biol Med, 2017. **108**: p. 564-574.
35. Reisz, J.A., et al., *Effects of ionizing radiation on biological molecules--mechanisms of damage and emerging methods of detection.* Antioxid Redox Signal, 2014. **21**(2): p. 260-92.
36. Bhatia, S. and C. Sklar, *Second cancers in survivors of childhood cancer.* Nat Rev Cancer, 2002. **2**(2): p. 124-32.
37. Cheung-Ong, K., G. Giaever, and C. Nislow, *DNA-damaging agents in cancer chemotherapy: serendipity and chemical biology.* Chem Biol, 2013. **20**(5): p. 648-59.
38. Maslov, A.Y., et al., *5-aza-2'-deoxycytidine-induced genome rearrangements are mediated by DNMT1.* Oncogene, 2012. **31**(50): p. 5172-9.
39. Chen, Q., et al., *The FA/BRCA pathway is involved in melphalan-induced DNA interstrand cross-link repair and accounts for melphalan resistance in multiple myeloma cells.* Blood, 2005. **106**(2): p. 698-705.
40. Lehmann, A.R., et al., *Translesion synthesis: Y-family polymerases and the polymerase switch.* DNA Repair (Amst), 2007. **6**(7): p. 891-9.
41. Salehan, M.R. and H.R. Morse, *DNA damage repair and tolerance: a role in chemotherapeutic drug resistance.* British Journal of Biomedical Science, 2013. **70**(1): p. 31-40.
42. Canitrot, Y., et al., *Overexpression of DNA polymerase beta in cell results in a mutator phenotype and a decreased sensitivity to anticancer drugs.* Proc Natl Acad Sci U S A, 1998. **95**(21): p. 12586-90.
43. Kyle, R.A., *Diagnosis and management of multiple myeloma and related disorders.* Prog Hematol, 1986. **14**: p. 257-82.
44. Durie, B.G. and S.E. Salmon, *The current status and future prospects of treatment for multiple myeloma.* Clin Haematol, 1982. **11**(1): p. 181-210.

45. Yang, H.H., et al., *Overcoming drug resistance in multiple myeloma: the emergence of therapeutic approaches to induce apoptosis.* J Clin Oncol, 2003. **21**(22): p. 4239-47.
46. Dalton, W.S., et al., *Characterization of a new drug-resistant human myeloma cell line that expresses P-glycoprotein.* Cancer Res, 1986. **46**(10): p. 5125-30.
47. Mulcahy, R.T., H.H. Bailey, and J.J. Gipp, *Up-regulation of γ-glutamylcysteine synthetase activity in melphalan-resistant human multiple myeloma cells expressing increased glutathione levels.* Cancer Chemotherapy and Pharmacology, 1994. **34**(1): p. 67-71.
48. Huschtscha, L.I., et al., *Characteristics of cancer cell death after exposure to cytotoxic drugs in vitro.* Br J Cancer, 1996. **73**(1): p. 54-60.
49. Walker, P.R., et al., *Topoisomerase II-reactive chemotherapeutic drugs induce apoptosis in thymocytes.* Cancer Res, 1991. **51**(4): p. 1078-85.
50. Takezawa, J., Y. Ishimi, and K. Yamada, *Proteasome inhibitors remarkably prevent translesion replication in cancer cells but not normal cells.* Cancer Sci, 2008. **99**(5): p. 863-71.
51. McElwain, T.J. and R.L. Powles, *High-dose intravenous melphalan for plasma-cell leukaemia and myeloma.* Lancet, 1983. **2**(8354): p. 822-4.
52. Alexanian, R., et al., *Treatment for multiple myeloma. Combination chemotherapy with different melphalan dose regimens.* JAMA, 1969. **208**(9): p. 1680-5.
53. Chanan-Khan, A.A., et al., *Lenalidomide in combination with dexamethasone improves survival and time-to-progression in patients ≥65 years old with relapsed or refractory multiple myeloma.* Int J Hematol, 2012. **96**(2): p. 254-62.
54. Albertella, M.R., A. Lau, and M.J. O'Connor, *The overexpression of specialized DNA polymerases in cancer.* DNA Repair (Amst), 2005. **4**(5): p. 583-93.
55. Dimopoulos, M.A., et al., *Melphalan-induced DNA damage in vitro as a predictor for clinical outcome in multiple myeloma.* Haematologica, 2007. **92**(11): p. 1505-12.
56. Kelland, L.R., et al., *Establishment and characterization of an in vitro model of acquired resistance to cisplatin in a human testicular nonseminomatous germ cell line.* Cancer Res, 1992. **52**(7): p. 1710-6.
57. Chao, C.C., et al., *Enhanced host cell reactivation of damaged plasmid DNA in HeLa cells resistant to cis-diamminedichloroplatinum(II).* Cancer Res, 1991. **51**(2): p. 601-5.
58. Sheibani, N., M.M. Jennerwein, and A. Eastman, *DNA repair in cells sensitive and resistant to cis-diamminedichloroplatinum(II): host cell reactivation of damaged plasmid DNA.* Biochemistry, 1989. **28**(7): p. 3120-4.
59. van Gent, D.C., J.H. Hoeijmakers, and R. Kanaar, *Chromosomal stability and the DNA double-stranded break connection.* Nat Rev Genet, 2001. **2**(3): p. 196-206.
60. Borek, C., et al., *Inhibition of malignant transformation in vitro by inhibitors of poly(ADP-ribose) synthesis.* Proc Natl Acad Sci U S A, 1984. **81**(1): p. 243-7.
61. Mitra, S., et al., *Complexities of DNA base excision repair in mammalian cells.* Mol Cells, 1997. **7**(3): p. 305-12.
62. Eisenbrand, G., et al., *DNA adducts and DNA damage by antineoplastic and carcinogenic N-nitrosocompounds.* J Cancer Res Clin Oncol, 1986. **112**(3): p. 196-204.
63. Brown, J.S., et al., *Targeting DNA Repair in Cancer: Beyond PARP Inhibitors.* Cancer Discov, 2017. **7**(1): p. 20-37.
64. Nemec, A.A., S.S. Wallace, and J.B. Sweasy, *Variant base excision repair proteins: contributors to genomic instability.* Seminars in cancer biology, 2010. **20**(5): p. 320-328.
65. Trivedi, R.N., et al., *Human methyl purine DNA glycosylase and DNA polymerase beta expression collectively predict sensitivity to temozolomide.* Molecular pharmacology, 2008. **74**(2): p. 505-516.

66. Chatterjee, N. and G.C. Walker, *Mechanisms of DNA damage, repair, and mutagenesis.* Environmental and molecular mutagenesis, 2017. **58**(5): p. 235-263.
67. Yoshizawa, K., et al., *Gastrointestinal hyperplasia with altered expression of DNA polymerase beta.* PloS one, 2009. **4**(8): p. e6493-e6493.
68. Friedberg, E.C., *How nucleotide excision repair protects against cancer.* Nat Rev Cancer, 2001. **1**(1): p. 22-33.
69. Shen, X. and L. Li, *Mutagenic repair of DNA interstrand crosslinks.* Environmental and molecular mutagenesis, 2010. **51**(6): p. 493-499.
70. Wood, R.D., *Mammalian nucleotide excision repair proteins and interstrand crosslink repair.* Environ Mol Mutagen, 2010. **51**(6): p. 520-6.
71. Spivak, G., *Nucleotide excision repair in humans.* DNA Repair (Amst), 2015. **36**: p. 13-18.
72. Schärer, O.D., *Nucleotide excision repair in eukaryotes.* Cold Spring Harbor perspectives in biology, 2013. **5**(10): p. a012609-a012609.
73. Lehmann, J., et al., *Xeroderma Pigmentosum - Facts and Perspectives.* Anticancer Res, 2018. **38**(2): p. 1159-1164.
74. Kraemer, K.H., et al., *Xeroderma pigmentosum, trichothiodystrophy and Cockayne syndrome: a complex genotype-phenotype relationship.* Neuroscience, 2007. **145**(4): p. 1388-96.
75. Kartalou, M. and J.M. Essigmann, *Mechanisms of resistance to cisplatin.* Mutat Res, 2001. **478**(1-2): p. 23-43.
76. Fukui, K., *DNA mismatch repair in eukaryotes and bacteria.* J Nucleic Acids, 2010. **2010**.
77. Lin, X., et al., *DNA polymerase zeta accounts for the reduced cytotoxicity and enhanced mutagenicity of cisplatin in human colon carcinoma cells that have lost DNA mismatch repair.* Clin Cancer Res, 2006. **12**(2): p. 563-8.
78. Masuda, K., et al., *Relationship between DNA Mismatch Repair Deficiency and Endometrial Cancer.* Molecular biology international, 2011. **2011**: p. 256063-256063.
79. Drummond, J.T., et al., *Isolation of an hMSH2-p160 heterodimer that restores DNA mismatch repair to tumor cells.* Science, 1995. **268**(5219): p. 1909-12.
80. Janysek, D.C., et al., *Clinical use and mechanisms of resistance for PARP inhibitors in homologous recombination-deficient cancers.* Translational Oncology, 2021. **14**(3): p. 101012.
81. Rothkamm, K., et al., *Pathways of DNA double-strand break repair during the mammalian cell cycle.* Mol Cell Biol, 2003. **23**(16): p. 5706-15.
82. Biehs, R., et al., *DNA Double-Strand Break Resection Occurs during Non-homologous End Joining in G1 but Is Distinct from Resection during Homologous Recombination.* Mol Cell, 2017. **65**(4): p. 671-684 e5.
83. Helleday, T., *Homologous recombination in cancer development, treatment and development of drug resistance.* Carcinogenesis, 2010. **31**(6): p. 955-960.
84. Al-Minawi, A.Z., et al., *The ERCC1/XPF endonuclease is required for completion of homologous recombination at DNA replication forks stalled by inter-strand cross-links.* Nucleic Acids Research, 2009. **37**(19): p. 6400-6413.
85. Helleday, T., et al., *DNA double-strand break repair: from mechanistic understanding to cancer treatment.* DNA Repair (Amst), 2007. **6**(7): p. 923-35.
86. Hoeijmakers, J.H., *Genome maintenance mechanisms for preventing cancer.* Nature, 2001. **411**(6835): p. 366-74.
87. Shammas, M.A., et al., *Dysfunctional homologous recombination mediates genomic instability and progression in myeloma.* Blood, 2009. **113**(10): p. 2290-2297.
88. Patel, K.J., et al., *Involvement of Brca2 in DNA repair.* Mol Cell, 1998. **1**(3): p. 347-57.

89. Savolainen, L. and T. Helleday, *Transcription-associated recombination is independent of XRCC2 and mechanistically separate from homology-directed DNA double-strand break repair.* Nucleic Acids Res, 2009. **37**(2): p. 405-12.
90. Wooster, R., et al., *Identification of the breast cancer susceptibility gene BRCA2.* Nature, 1995. **378**(6559): p. 789-92.
91. Moynahan, M.E., A.J. Pierce, and M. Jasin, *BRCA2 is required for homology-directed repair of chromosomal breaks.* Mol Cell, 2001. **7**(2): p. 263-72.
92. Teodoridis, J.M., et al., *CpG island methylation of DNA damage response genes in advanced ovarian cancer.* Cancer Res, 2005. **65**(19): p. 8961-7.
93. Taniguchi, T., et al., *Disruption of the Fanconi anemia-BRCA pathway in cisplatin-sensitive ovarian tumors.* Nat Med, 2003. **9**(5): p. 568-74.
94. Sakai, W., et al., *Secondary mutations as a mechanism of cisplatin resistance in BRCA2-mutated cancers.* Nature, 2008. **451**(7182): p. 1116-20.
95. Edwards, S.L., et al., *Resistance to therapy caused by intragenic deletion in BRCA2.* Nature, 2008. **451**(7182): p. 1111-5.
96. Swisher, E.M., et al., *Secondary BRCA1 mutations in BRCA1-mutated ovarian carcinomas with platinum resistance.* Cancer Res, 2008. **68**(8): p. 2581-6.
97. Hansen, L.T., et al., *The role of RAD51 in etoposide (VP16) resistance in small cell lung cancer.* Int J Cancer, 2003. **105**(4): p. 472-9.
98. Hansen, L.T., et al., *DNA repair rate and etoposide (VP16) resistance of tumor cell subpopulations derived from a single human small cell lung cancer.* Lung Cancer, 2003. **40**(2): p. 157-64.
99. Rothkamm, K., et al., *Radiation-induced genomic rearrangements formed by nonhomologous end-joining of DNA double-strand breaks.* Cancer Res, 2001. **61**(10): p. 3886-93.
100. Jeggo, P.A. and M. Löbrich, *How cancer cells hijack DNA double-strand break repair pathways to gain genomic instability.* Biochem J, 2015. **471**(1): p. 1-11.
101. Bétermier, M., P. Bertrand, and B.S. Lopez, *Is non-homologous end-joining really an inherently error-prone process?* PLoS Genet, 2014. **10**(1): p. e1004086.
102. Brady, N., et al., *Increased error-prone NHEJ activity in myeloid leukemias is associated with DNA damage at sites that recruit key nonhomologous end-joining proteins.* Cancer Res, 2003. **63**(8): p. 1798-805.
103. Gaymes, T.J., G.J. Mufti, and F.V. Rassool, *Myeloid leukemias have increased activity of the nonhomologous end-joining pathway and concomitant DNA misrepair that is dependent on the Ku70/86 heterodimer.* Cancer Res, 2002. **62**(10): p. 2791-7.
104. Bau, D.T., et al., *DNA double-strand break repair capacity and risk of breast cancer.* Carcinogenesis, 2007. **28**(8): p. 1726-30.
105. Vaidya, A., et al., *Knock-in reporter mice demonstrate that DNA repair by non-homologous end joining declines with age.* PLoS Genet, 2014. **10**(7): p. e1004511.
106. Lin, C., et al., *Nuclear receptor-induced chromosomal proximity and DNA breaks underlie specific translocations in cancer.* Cell, 2009. **139**(6): p. 1069-83.
107. Lieber, M.R., *Mechanisms of human lymphoid chromosomal translocations.* Nat Rev Cancer, 2016. **16**(6): p. 387-98.
108. Ali, H., et al., *Nonreciprocal chromosomal translocations in renal cancer involve multiple DSBs and NHEJ associated with breakpoint inversion but not necessarily with transcription.* Genes Chromosomes Cancer, 2013. **52**(4): p. 402-9.
109. Adamo, A., et al., *Preventing nonhomologous end joining suppresses DNA repair defects of Fanconi anemia.* Mol Cell, 2010. **39**(1): p. 25-35.
110. Pace, P., et al., *Ku70 corrupts DNA repair in the absence of the Fanconi anemia pathway.* Science, 2010. **329**(5988): p. 219-23.

111. Yang, S. and X.Q. Wang, *XLF-mediated NHEJ activity in hepatocellular carcinoma therapy resistance.* BMC Cancer, 2017. **17**(1): p. 344.
112. McCormick, A., et al., *Ovarian Cancers Harbor Defects in Nonhomologous End Joining Resulting in Resistance to Rucaparib.* Clinical cancer research : an official journal of the American Association for Cancer Research, 2017. **23**(8): p. 2050-2060.
113. Takagi, M., *DNA damage response and hematological malignancy.* Int J Hematol, 2017. **106**(3): p. 345-356.
114. Charames, G.S. and B. Bapat, *Genomic instability and cancer.* Curr Mol Med, 2003. **3**(7): p. 589-96.
115. Wilson, D.M., 3rd, T.M. Sofinowski, and D.R. McNeill, *Repair mechanisms for oxidative DNA damage.* Front Biosci, 2003. **8**: p. d963-81.
116. Kruman, II and E.I. Schwartz, *DNA damage response and neuroprotection.* Front Biosci, 2008. **13**: p. 2504-15.
117. Weinfeld, M., et al., *Tidying up loose ends: the role of polynucleotide kinase/phosphatase in DNA strand break repair.* Trends in biochemical sciences, 2011. **36**(5): p. 262-271.
118. Bernstein, N.K., et al., *The molecular architecture of the mammalian DNA repair enzyme, polynucleotide kinase.* Mol Cell, 2005. **17**(5): p. 657-70.
119. Weinfeld, M., et al., *Tidying up loose ends: the role of polynucleotide kinase/phosphatase in DNA strand break repair.* Trends Biochem Sci, 2011. **36**(5): p. 262-71.
120. Karimi-Busheri, F., et al., *Molecular characterization of a human DNA kinase.* J Biol Chem, 1999. **274**(34): p. 24187-94.
121. Loizou, J.I., et al., *The protein kinase CK2 facilitates repair of chromosomal DNA single-strand breaks.* Cell, 2004. **117**(1): p. 17-28.
122. Koch, C.A., et al., *Xrcc4 physically links DNA end processing by polynucleotide kinase to DNA ligation by DNA ligase IV.* EMBO J, 2004. **23**(19): p. 3874-85.
123. Mani, R.S., et al., *Dual modes of interaction between XRCC4 and polynucleotide kinase/phosphatase: implications for nonhomologous end joining.* J Biol Chem, 2010. **285**(48): p. 37619-29.
124. Allinson, S.L., *DNA end-processing enzyme polynucleotide kinase as a potential target in the treatment of cancer.* Future Oncol, 2010. **6**(6): p. 1031-42.
125. Coquelle, N., et al., *Structural basis for the phosphatase activity of polynucleotide kinase/phosphatase on single- and double-stranded DNA substrates.* Proc Natl Acad Sci U S A, 2011. **108**(52): p. 21022-7.
126. Rasouli-Nia, A., F. Karimi-Busheri, and M. Weinfeld, *Stable down-regulation of human polynucleotide kinase enhances spontaneous mutation frequency and sensitizes cells to genotoxic agents.* Proc Natl Acad Sci U S A, 2004. **101**(18): p. 6905-10.
127. Bernstein, N.K., et al., *Polynucleotide kinase as a potential target for enhancing cytotoxicity by ionizing radiation and topoisomerase I inhibitors.* Anticancer Agents Med Chem, 2008. **8**(4): p. 358-67.
128. Seifried, A., J. Schultz, and A. Gohla, *Human HAD phosphatases: structure, mechanism, and roles in health and disease.* FEBS J, 2013. **280**(2): p. 549-71.
129. Dobson, C.J. and S.L. Allinson, *The phosphatase activity of mammalian polynucleotide kinase takes precedence over its kinase activity in repair of single strand breaks.* Nucleic Acids Res, 2006. **34**(8): p. 2230-7.
130. Kaelin, W.G., Jr., *The concept of synthetic lethality in the context of anticancer therapy.* Nat Rev Cancer, 2005. **5**(9): p. 689-98.
131. Kaelin, W.G., Jr., *Synthetic lethality: a framework for the development of wiser cancer therapeutics.* Genome Med, 2009. **1**(10): p. 99.

132. Overington, J.P., B. Al-Lazikani, and A.L. Hopkins, *How many drug targets are there?* Nat Rev Drug Discov, 2006. **5**(12): p. 993-6.
133. Dobzhansky, T., *Genetics of natural populations; recombination and variability in populations of Drosophila pseudoobscura.* Genetics, 1946. **31**(3): p. 269-290.
134. Iglehart, J.D. and D.P. Silver, *Synthetic lethality--a new direction in cancer-drug development.* N Engl J Med, 2009. **361**(2): p. 189-91.
135. Nijman, S.M., *Synthetic lethality: general principles, utility and detection using genetic screens in human cells.* FEBS Lett, 2011. **585**(1): p. 1-6.
136. Cairney, C.J., et al., *A 'synthetic-sickness' screen for senescence re-engagement targets in mutant cancer backgrounds.* PLOS Genetics, 2017. **13**(8): p. e1006942.
137. Szczurek, E., N. Misra, and M. Vingron, *Synthetic sickness or lethality points at candidate combination therapy targets in glioblastoma.* Int J Cancer, 2013. **133**(9): p. 2123-32.
138. Brough, R., et al., *Searching for synthetic lethality in cancer.* Curr Opin Genet Dev, 2011. **21**(1): p. 34-41.
139. McLornan, D.P., A. List, and G.J. Mufti, *Applying synthetic lethality for the selective targeting of cancer.* N Engl J Med, 2014. **371**(18): p. 1725-35.
140. Farmer, H., et al., *Targeting the DNA repair defect in BRCA mutant cells as a therapeutic strategy.* Nature, 2005. **434**(7035): p. 917-21.
141. Golan, T., et al., *Maintenance Olaparib for Germline BRCA-Mutated Metastatic Pancreatic Cancer.* N Engl J Med, 2019.
142. Sonnenblick, A., et al., *An update on PARP inhibitors--moving to the adjuvant setting.* Nat Rev Clin Oncol, 2015. **12**(1): p. 27-41.
143. Helleday, T., *The underlying mechanism for the PARP and BRCA synthetic lethality: clearing up the misunderstandings.* Mol Oncol, 2011. **5**(4): p. 387-93.
144. Bolderson, E., et al., *Recent advances in cancer therapy targeting proteins involved in DNA double-strand break repair.* Clinical cancer research : an official journal of the American Association for Cancer Research, 2009. **15**(20): p. 6314-6320.
145. Curtin, N.J., *DNA repair dysregulation from cancer driver to therapeutic target.* Nat Rev Cancer, 2012. **12**(12): p. 801-17.
146. Vilenchik, M.M. and A.G. Knudson, *Endogenous DNA double-strand breaks: Production, fidelity of repair, and induction of cancer.* Proceedings of the National Academy of Sciences, 2003. **100**(22): p. 12871.
147. Kuzminov, A., *Single-strand interruptions in replicating chromosomes cause double-strand breaks.* Proceedings of the National Academy of Sciences, 2001. **98**(15): p. 8241.
148. Lindahl, T. and B. Nyberg, *Heat-induced deamination of cytosine residues in deoxyribonucleic acid.* Biochemistry, 1974. **13**(16): p. 3405-3410.
149. Annunziata, C.M. and S.E. Bates, *PARP inhibitors in BRCA1/BRCA2 germline mutation carriers with ovarian and breast cancer.* F1000 Biol Rep, 2010. **2**.
150. Milella, M., et al., *PTEN: Multiple Functions in Human Malignant Tumors.* Front Oncol, 2015. **5**: p. 24.
151. Frattini, M., et al., *Phosphatase protein homologue to tensin expression and phosphatidylinositol-3 phosphate kinase mutations in colorectal cancer.* Cancer Res, 2005. **65**(23): p. 11227.
152. Molinari, F. and M. Frattini, *Functions and Regulation of the PTEN Gene in Colorectal Cancer.* Front Oncol, 2013. **3**: p. 326.
153. Gupta, A., et al., *Cell cycle checkpoint defects contribute to genomic instability in PTEN deficient cells independent of DNA DSB repair.* Cell Cycle, 2009. **8**(14): p. 2198-210.

154. Naguib, A., et al., *Alterations in PTEN and PIK3CA in colorectal cancers in the EPIC Norfolk study: associations with clinicopathological and dietary factors.* BMC Cancer, 2011. **11**: p. 123.
155. Ghidini, M., et al., *KRAS mutation in lung metastases from colorectal cancer: prognostic implications.* Cancer Med, 2016. **5**(2): p. 256-64.
156. Álvarez-Garcia, V., et al., *Mechanisms of PTEN loss in cancer: It's all about diversity.* Seminars in Cancer Biology, 2019. **59**: p. 66-79.
157. Squarize, C.H., et al., *PTEN deficiency contributes to the development and progression of head and neck cancer.* Neoplasia (New York, N.Y.), 2013. **15**(5): p. 461-471.
158. Nassif, N.T., et al., *PTEN mutations are common in sporadic microsatellite stable colorectal cancer.* Oncogene, 2004. **23**(2): p. 617-28.
159. Salvatore, L., et al., *PTEN in Colorectal Cancer: Shedding Light on Its Role as Predictor and Target.* Cancers (Basel), 2019. **11**(11).
160. De Roock, W., et al., *KRAS, BRAF, PIK3CA, and PTEN mutations: implications for targeted therapies in metastatic colorectal cancer.* Lancet Oncol, 2011. **12**(6): p. 594-603.
161. Salmena, L., A. Carracedo, and P.P. Pandolfi, *Tenets of PTEN tumor suppression.* Cell, 2008. **133**(3): p. 403-14.
162. Mendes-Pereira, A.M., et al., *Synthetic lethal targeting of PTEN mutant cells with PARP inhibitors.* EMBO Mol Med, 2009. **1**(6-7): p. 315-22.
163. Forster, M.D., et al., *Treatment with olaparib in a patient with PTEN-deficient endometrioid endometrial cancer.* Nat Rev Clin Oncol, 2011. **8**(5): p. 302-6.
164. Minami, D., et al., *Synergistic effect of olaparib with combination of cisplatin on PTEN-deficient lung cancer cells.* Mol Cancer Res, 2013. **11**(2): p. 140-8.
165. Zhao, Q., et al., *Inhibition of Rad51 sensitizes breast cancer cells with wild-type PTEN to olaparib.* Biomed Pharmacother, 2017. **94**: p. 165-168.
166. McCabe, N., et al., *Mechanistic Rationale to Target PTEN-Deficient Tumor Cells with Inhibitors of the DNA Damage Response Kinase ATM.* Cancer Res, 2015. **75**(11): p. 2159-65.
167. Hollander, M.C., G.M. Blumenthal, and P.A. Dennis, *PTEN loss in the continuum of common cancers, rare syndromes and mouse models.* Nat Rev Cancer, 2011. **11**(4): p. 289-301.
168. Tan, M.H., et al., *Lifetime cancer risks in individuals with germline PTEN mutations.* Clin Cancer Res, 2012. **18**(2): p. 400-7.
169. Zhang, H.Y., et al., *PTEN mutation, methylation and expression in breast cancer patients.* Oncol Lett, 2013. **6**(1): p. 161-168.
170. Nagata, Y., et al., *PTEN activation contributes to tumor inhibition by trastuzumab, and loss of PTEN predicts trastuzumab resistance in patients.* Cancer Cell, 2004. **6**(2): p. 117-27.
171. Pandolfi, P.P., *Breast cancer--loss of PTEN predicts resistance to treatment.* N Engl J Med, 2004. **351**(22): p. 2337-8.
172. Berns, K., et al., *A functional genetic approach identifies the PI3K pathway as a major determinant of trastuzumab resistance in breast cancer.* Cancer Cell, 2007. **12**(4): p. 395-402.
173. Razis, E., et al., *EGFR gene gain and PTEN protein expression are favorable prognostic factors in patients with KRAS wild-type metastatic colorectal cancer treated with cetuximab.* J Cancer Res Clin Oncol, 2014. **140**(5): p. 737-48.
174. Soria, J.C., et al., *Lack of PTEN expression in non-small cell lung cancer could be related to promoter methylation.* Clin Cancer Res, 2002. **8**(5): p. 1178-84.
175. Dearden, S., et al., *Mutation incidence and coincidence in non small-cell lung cancer: meta-analyses by ethnicity and histology (mutMap).* Ann Oncol, 2013. **24**(9): p. 2371-6.
176. Yokomizo, A., et al., *PTEN/MMAC1 mutations identified in small cell, but not in non-small cell lung cancers.* Oncogene, 1998. **17**(4): p. 475-9.

177. Marsit, C.J., et al., *PTEN expression in non-small-cell lung cancer: evaluating its relation to tumor characteristics, allelic loss, and epigenetic alteration.* Hum Pathol, 2005. **36**(7): p. 768-76.
178. Jin, G., et al., *PTEN mutations and relationship to EGFR, ERBB2, KRAS, and TP53 mutations in non-small cell lung cancers.* Lung Cancer, 2010. **69**(3): p. 279-83.
179. Berger, M.F., et al., *The genomic complexity of primary human prostate cancer.* Nature, 2011. **470**(7333): p. 214-20.
180. Roychowdhury, S. and A.M. Chinnaiyan, *Advancing precision medicine for prostate cancer through genomics.* J Clin Oncol, 2013. **31**(15): p. 1866-73.
181. Grasso, C.S., et al., *The mutational landscape of lethal castration-resistant prostate cancer.* Nature, 2012. **487**(7406): p. 239-43.
182. Koul, D., *PTEN signaling pathways in glioblastoma.* Cancer Biol Ther, 2008. **7**(9): p. 1321-5.
183. Endersby, R. and S.J. Baker, *PTEN signaling in brain: neuropathology and tumorigenesis.* Oncogene, 2008. **27**(41): p. 5416-30.
184. Dellas, A., et al., *Combined PTEN and p27kip1 protein expression patterns are associated with obesity and prognosis in endometrial carcinomas.* Clin Cancer Res, 2009. **15**(7): p. 2456-62.
185. Matias-Guiu, X. and J. Prat, *Molecular pathology of endometrial carcinoma.* Histopathology, 2013. **62**(1): p. 111-23.
186. Kouniavsky, G. and M.A. Zeiger, *Thyroid tumorigenesis and molecular markers in thyroid cancer.* Curr Opin Oncol, 2010. **22**(1): p. 23-9.
187. Mirmohammadsadegh, A., et al., *Epigenetic silencing of the PTEN gene in melanoma.* Cancer Res, 2006. **66**(13): p. 6546-52.
188. Wang, Y., et al., *Evidence of ultraviolet type mutations in xeroderma pigmentosum melanomas.* Proc Natl Acad Sci U S A, 2009. **106**(15): p. 6279-84.
189. Dankort, D., et al., *Braf(V600E) cooperates with Pten loss to induce metastatic melanoma.* Nat Genet, 2009. **41**(5): p. 544-52.
190. Nathanson, K.L., et al., *Tumor genetic analyses of patients with metastatic melanoma treated with the BRAF inhibitor dabrafenib (GSK2118436).* Clin Cancer Res, 2013. **19**(17): p. 4868-78.
191. Saal, L.H., et al., *Poor prognosis in carcinoma is associated with a gene expression signature of aberrant PTEN tumor suppressor pathway activity.* Proc Natl Acad Sci U S A, 2007. **104**(18): p. 7564-9.
192. Cordes, I., et al., *PTEN deletions are related to disease progression and unfavourable prognosis in early bladder cancer.* Histopathology, 2013. **63**(5): p. 670-7.
193. Hu, T.H., et al., *Down-regulation of tumor suppressor gene PTEN, overexpression of p53, plus high proliferating cell nuclear antigen index predict poor patient outcome of hepatocellular carcinoma after resection.* Oncol Rep, 2007. **18**(6): p. 1417-26.
194. Zhong, Y., et al., *Impaired phosphate and tension homologue deleted on chromosome 10 expression and its prognostic role in radical surgery for hepatocellular carcinoma with family aggregation resulting from hepatitis B and liver cirrhosis.* Exp Biol Med (Maywood), 2013. **238**(8): p. 866-73.
195. Aguirre, A.J., et al., *High-resolution characterization of the pancreatic adenocarcinoma genome.* Proc Natl Acad Sci U S A, 2004. **101**(24): p. 9067-72.
196. Perren, A., et al., *Mutation and expression analyses reveal differential subcellular compartmentalization of PTEN in endocrine pancreatic tumors compared to normal islet cells.* Am J Pathol, 2000. **157**(4): p. 1097-103.
197. Ying, H., et al., *PTEN is a major tumor suppressor in pancreatic ductal adenocarcinoma and regulates an NF-κB-cytokine network.* Cancer Discov, 2011. **1**(2): p. 158-69.
198. Squarize, C.H., et al., *PTEN deficiency contributes to the development and progression of head and neck cancer.* Neoplasia, 2013. **15**(5): p. 461-71.

199. Lee, J.I., et al., *Loss of PTEN Expression as a Prognostic Marker for Tongue Cancer.* Archives of Otolaryngology–Head & Neck Surgery, 2001. **127**(12): p. 1441-1445.
200. Mereniuk, T.R., et al., *Genetic screening for synthetic lethal partners of polynucleotide kinase/phosphatase: potential for targeting SHP-1-depleted cancers.* Cancer Res, 2012. **72**(22): p. 5934-44.
201. Mereniuk, T.R., et al., *Synthetic lethal targeting of PTEN-deficient cancer cells using selective disruption of polynucleotide kinase/phosphatase.* Mol Cancer Ther, 2013. **12**(10): p. 2135-44.
202. Freschauf, G.K., et al., *Identification of a small molecule inhibitor of the human DNA repair enzyme polynucleotide kinase/phosphatase.* Cancer Res, 2009. **69**(19): p. 7739-46.
203. Freschauf, G.K., et al., *Mechanism of action of an imidopiperidine inhibitor of human polynucleotide kinase/phosphatase.* J Biol Chem, 2010. **285**(4): p. 2351-60.
204. Zhou, X.P., et al., *PTEN mutational spectra, expression levels, and subcellular localization in microsatellite stable and unstable colorectal cancers.* Am J Pathol, 2002. **161**(2): p. 439-47.
205. Goel, A., et al., *Frequent inactivation of PTEN by promoter hypermethylation in microsatellite instability-high sporadic colorectal cancers.* Cancer Res, 2004. **64**(9): p. 3014-21.
206. Langlois, M.-J., et al., *The PTEN Phosphatase Controls Intestinal Epithelial Cell Polarity and Barrier Function: Role in Colorectal Cancer Progression.* PLOS ONE, 2010. **5**(12): p. e15742.
207. Fan, D., et al., *MicroRNA 26b promotes colorectal cancer metastasis by downregulating phosphatase and tensin homolog and wingless-type MMTV integration site family member 5A.* Cancer science, 2018. **109**(2): p. 354-362.
208. Sun, Y., H. Tian, and L. Wang, *Effects of PTEN on the proliferation and apoptosis of colorectal cancer cells via the phosphoinositol-3-kinase/Akt pathway.* Oncol Rep, 2015. **33**(4): p. 1828-36.
209. Bowen, K.A., et al., *PTEN loss induces epithelial--mesenchymal transition in human colon cancer cells.* Anticancer research, 2009. **29**(11): p. 4439-4449.
210. Jhawer, M., et al., *PIK3CA mutation/PTEN expression status predicts response of colon cancer cells to the epidermal growth factor receptor inhibitor cetuximab.* Cancer Res, 2008. **68**(6): p. 1953-61.
211. Laurent-Puig, P., et al., *Analysis of PTEN, BRAF, and EGFR status in determining benefit from cetuximab therapy in wild-type KRAS metastatic colon cancer.* J Clin Oncol, 2009. **27**(35): p. 5924-30.
212. Kanwar, S.S., A. Poolla, and A.P. Majumdar, *Regulation of colon cancer recurrence and development of therapeutic strategies.* World J Gastrointest Pathophysiol, 2012. **3**(1): p. 1-9.
213. Kennedy, R.H., et al., *Multicenter randomized controlled trial of conventional versus laparoscopic surgery for colorectal cancer within an enhanced recovery programme: EnROL.* J Clin Oncol, 2014. **32**(17): p. 1804-11.
214. Koopman, M., et al., *Sequential versus combination chemotherapy with capecitabine, irinotecan, and oxaliplatin in advanced colorectal cancer (CAIRO): a phase III randomised controlled trial.* Lancet, 2007. **370**(9582): p. 135-142.
215. Seymour, M.T., et al., *Different strategies of sequential and combination chemotherapy for patients with poor prognosis advanced colorectal cancer (MRC FOCUS): a randomised controlled trial.* Lancet, 2007. **370**(9582): p. 143-152.
216. Siegel, R.L., et al., *Colorectal cancer statistics, 2020.* CA: A Cancer Journal for Clinicians, 2020. **70**(3): p. 145-164.
217. Overgaard, M., J. Overgaard, and A. Sell, *Dose-response relationship for radiation therapy of recurrent, residual, and primarily inoperable colorectal cancer.* Radiotherapy and Oncology, 1984. **1**(3): p. 217-225.
218. Higgins, G.A., Jr., et al., *Preoperative radiotherapy for colorectal cancer.* Annals of surgery, 1975. **181**(5): p. 624-631.

219. Wolpin, B.M., et al., *Adjuvant Treatment of Colorectal Cancer.* CA: A Cancer Journal for Clinicians, 2007. **57**(3): p. 168-185.
220. Glimelius, B., et al., *A Systematic Overview of Radiation Therapy Effects in Rectal Cancer.* Acta Oncologica, 2003. **42**(5-6): p. 476-492.
221. Klein, C., et al., *Overcoming hypoxia-induced tumor radioresistance in non-small cell lung cancer by targeting DNA-dependent protein kinase in combination with carbon ion irradiation.* Radiat Oncol, 2017. **12**(1): p. 208.
222. Falk, M., *Nanodiamonds and nanoparticles as tumor cell radiosensitizers-promising results but an obscure mechanism of action.* Annals of translational medicine, 2017. **5**(1): p. 18-18.
223. Ledermann, J., et al., *Olaparib maintenance therapy in patients with platinum-sensitive relapsed serous ovarian cancer: a preplanned retrospective analysis of outcomes by BRCA status in a randomised phase 2 trial.* Lancet Oncol, 2014. **15**(8): p. 852-61.
224. Lee, J.M., J.A. Ledermann, and E.C. Kohn, *PARP Inhibitors for BRCA1/2 mutation-associated and BRCA-like malignancies.* Ann Oncol, 2014. **25**(1): p. 32-40.
225. Calabrese, C.R., et al., *Anticancer Chemosensitization and Radiosensitization by the Novel Poly(ADP-ribose) Polymerase-1 Inhibitor AG14361.* JNCI: Journal of the National Cancer Institute, 2004. **96**(1): p. 56-67.
226. Shiloh, Y., *ATM and related protein kinases: safeguarding genome integrity.* Nat Rev Cancer, 2003. **3**(3): p. 155-68.
227. Izzard, R.A., S.P. Jackson, and G.C. Smith, *Competitive and noncompetitive inhibition of the DNA-dependent protein kinase.* Cancer Res, 1999. **59**(11): p. 2581-6.
228. Sarkaria, J.N., et al., *Inhibition of phosphoinositide 3-kinase related kinases by the radiosensitizing agent wortmannin.* Cancer Res, 1998. **58**(19): p. 4375-82.
229. Hickson, I., et al., *Identification and characterization of a novel and specific inhibitor of the ataxia-telangiectasia mutated kinase ATM.* Cancer Res, 2004. **64**(24): p. 9152-9.
230. Rainey, M.D., et al., *Transient inhibition of ATM kinase is sufficient to enhance cellular sensitivity to ionizing radiation.* Cancer Res, 2008. **68**(18): p. 7466-74.
231. Zhao, Y., et al., *Preclinical evaluation of a potent novel DNA-dependent protein kinase inhibitor NU7441.* Cancer Res, 2006. **66**(10): p. 5354-62.
232. Shinohara, E.T., et al., *DNA-dependent protein kinase is a molecular target for the development of noncytotoxic radiation-sensitizing drugs.* Cancer Res, 2005. **65**(12): p. 4987-92.
233. Ismail, I.H., et al., *SU11752 inhibits the DNA-dependent protein kinase and DNA double-strand break repair resulting in ionizing radiation sensitization.* Oncogene, 2004. **23**(4): p. 873-82.
234. Suganuma, M., et al., *Sensitization of cancer cells to DNA damage-induced cell death by specific cell cycle G2 checkpoint abrogation.* Cancer Res, 1999. **59**(23): p. 5887-91.
235. Cariveau, M.J., et al., *Characterization of an NBS1 C-terminal peptide that can inhibit ataxia telangiectasia mutated (ATM)-mediated DNA damage responses and enhance radiosensitivity.* Mol Pharmacol, 2007. **72**(2): p. 320-6.
236. Sun, X., et al., *Identification and characterization of a small inhibitory peptide that can target DNA-PKcs autophosphorylation and increase tumor radiosensitivity.* Int J Radiat Oncol Biol Phys, 2012. **84**(5): p. 1212-9.
237. Abbotts, R., N. Thompson, and S. Madhusudan, *DNA repair in cancer: emerging targets for personalized therapy.* Cancer Manag Res, 2014. **6**: p. 77-92.
238. Chappell, C., et al., *Involvement of human polynucleotide kinase in double-strand break repair by non-homologous end joining.* EMBO J, 2002. **21**(11): p. 2827-32.
239. Navya, P.N., et al., *Current trends and challenges in cancer management and therapy using designer nanomaterials.* Nano Convergence, 2019. **6**(1): p. 23.

240. Bentzen, S.M., *Preventing or reducing late side effects of radiation therapy: radiobiology meets molecular pathology.* Nature Reviews Cancer, 2006. **6**(9): p. 702-713.
241. Binder, D., et al., *[Brain metastases of lung cancer].* Dtsch Med Wochenschr, 2006. **131**(4): p. 165-71.
242. Sen, M. and R. Prestwich, *Chemotherapy and Targeted Therapy.* Adv Otorhinolaryngol, 2016. **78**: p. 148-56.
243. R.Rate, W., L.J. Solin, and A.T. Turrisi, *Palliative radiotherapy for metastatic malignant melanoma: Brain metastases, bone metastases, and spinal cord compression.* International Journal of Radiation Oncology*Biology*Physics, 1988. **15**(4): p. 859-864.
244. Lipinski, C.A., *Drug-like properties and the causes of poor solubility and poor permeability.* J Pharmacol Toxicol Methods, 2000. **44**(1): p. 235-49.
245. Merisko-Liversidge, E.M. and G.G. Liversidge, *Drug nanoparticles: formulating poorly water-soluble compounds.* Toxicol Pathol, 2008. **36**(1): p. 43-8.
246. Senapati, S., et al., *Controlled drug delivery vehicles for cancer treatment and their performance.* Signal Transduction and Targeted Therapy, 2018. **3**(1): p. 7.
247. Cho, K., et al., *Therapeutic nanoparticles for drug delivery in cancer.* Clin Cancer Res, 2008. **14**(5): p. 1310-6.
248. Petros, R.A. and J.M. DeSimone, *Strategies in the design of nanoparticles for therapeutic applications.* Nat Rev Drug Discov, 2010. **9**(8): p. 615-27.
249. Sun, T., et al., *Engineered nanoparticles for drug delivery in cancer therapy.* Angew Chem Int Ed Engl, 2014. **53**(46): p. 12320-64.
250. Danhier, F., O. Feron, and V. Préat, *To exploit the tumor microenvironment: Passive and active tumor targeting of nanocarriers for anti-cancer drug delivery.* J Control Release, 2010. **148**(2): p. 135-46.
251. Pérez-Herrero, E. and A. Fernández-Medarde, *Advanced targeted therapies in cancer: Drug nanocarriers, the future of chemotherapy.* Eur J Pharm Biopharm, 2015. **93**: p. 52-79.
252. Upreti, M., A. Jyoti, and P. Sethi, *Tumor microenvironment and nanotherapeutics.* Translational cancer research, 2013. **2**(4): p. 309-319.
253. Sadat, S., S. Jahan, and A. Haddadi, *Effects of Size and Surface Charge of Polymeric Nanoparticles on in Vitro and in Vivo Applications.* Journal of Biomaterials and Nanobiotechnology, 2016. **07**: p. 91-108.
254. Sadat, S.M.A., et al., *Development of Self-Associating SN-38-Conjugated Poly(ethylene oxide)-Poly(ester) Micelles for Colorectal Cancer Therapy.* Pharmaceutics, 2020. **12**(11): p. 1033.
255. Koizumi, F., et al., *Novel SN-38-incorporating polymeric micelles, NK012, eradicate vascular endothelial growth factor-secreting bulky tumors.* Cancer Res, 2006. **66**(20): p. 10048-56.
256. Matsumura, Y. and K. Kataoka, *Preclinical and clinical studies of anticancer agent-incorporating polymer micelles.* Cancer Sci, 2009. **100**(4): p. 572-9.
257. Dawidczyk, C.M., et al., *State-of-the-art in design rules for drug delivery platforms: lessons learned from FDA-approved nanomedicines.* J Control Release, 2014. **187**: p. 133-44.
258. Estanqueiro, M., et al., *Nanotechnological carriers for cancer chemotherapy: the state of the art.* Colloids Surf B Biointerfaces, 2015. **126**: p. 631-48.
259. Peer, D., et al., *Nanocarriers as an emerging platform for cancer therapy.* Nat Nanotechnol, 2007. **2**(12): p. 751-60.
260. Adams, M.L., A. Lavasanifar, and G.S. Kwon, *Amphiphilic block copolymers for drug delivery.* J Pharm Sci, 2003. **92**(7): p. 1343-55.
261. Torchilin, V.P., *Multifunctional, stimuli-sensitive nanoparticulate systems for drug delivery.* Nat Rev Drug Discov, 2014. **13**(11): p. 813-27.

262. Houdaihed, L., J.C. Evans, and C. Allen, *Overcoming the Road Blocks: Advancement of Block Copolymer Micelles for Cancer Therapy in the Clinic.* Mol Pharm, 2017. **14**(8): p. 2503-2517.
263. Brody, H., *Colorectal cancer.* Nature, 2015. **521**: p. S1.
264. Eklof, V., et al., *The prognostic role of KRAS, BRAF, PIK3CA and PTEN in colorectal cancer.* Br J Cancer, 2013. **108**(10): p. 2153-63.
265. Reinhardt, H.C., et al., *Exploiting synthetic lethal interactions for targeted cancer therapy.* Cell Cycle, 2009. **8**(19): p. 3112-9.
266. Chan, D.A. and A.J. Giaccia, *Harnessing synthetic lethal interactions in anticancer drug discovery.* Nat Rev Drug Discov, 2011. **10**(5): p. 351-64.
267. Shire, Z., et al., *Nanoencapsulation of Novel Inhibitors of PNKP for Selective Sensitization to Ionizing Radiation and Irinotecan and Induction of Synthetic Lethality.* Mol Pharm, 2018. **15**(6): p. 2316-2326.
268. Weiss, R.B., et al., *Hypersensitivity reactions from taxol.* J Clin Oncol, 1990. **8**(7): p. 1263-8.
269. Sparreboom, A., et al., *Nonlinear pharmacokinetics of paclitaxel in mice results from the pharmaceutical vehicle Cremophor EL.* Cancer Res, 1996. **56**(9): p. 2112-5.
270. de Jonge, M.E., et al., *Population pharmacokinetics of orally administered paclitaxel formulated in Cremophor EL.* Br J Clin Pharmacol, 2005. **59**(3): p. 325-34.
271. Sykes, E., et al., *Effects of Cremophor EL on distribution of Taxol to serum lipoproteins.* Br J Cancer, 1994. **70**(3): p. 401-4.
272. Ellis, A.G. and L.K. Webster, *Inhibition of paclitaxel elimination in the isolated perfused rat liver by Cremophor EL.* Cancer Chemother Pharmacol, 1999. **43**(1): p. 13-8.
273. Gianni, L., et al., *Human pharmacokinetic characterization and in vitro study of the interaction between doxorubicin and paclitaxel in patients with breast cancer.* J Clin Oncol, 1997. **15**(5): p. 1906-15.
274. Scripture, C.D., W.D. Figg, and A. Sparreboom, *Paclitaxel chemotherapy: from empiricism to a mechanism-based formulation strategy.* Ther Clin Risk Manag, 2005. **1**(2): p. 107-14.
275. Henningsson, A., et al., *Association of CYP2C8, CYP3A4, CYP3A5, and ABCB1 polymorphisms with the pharmacokinetics of paclitaxel.* Clin Cancer Res, 2005. **11**(22): p. 8097-104.
276. Fransson, M.N., et al., *Influence of Cremophor EL and genetic polymorphisms on the pharmacokinetics of paclitaxel and its metabolites using a mechanism-based model.* Drug Metab Dispos, 2011. **39**(2): p. 247-55.
277. Xiong, X.B., et al., *Multifunctional polymeric micelles for enhanced intracellular delivery of doxorubicin to metastatic cancer cells.* Pharm Res, 2008. **25**(11): p. 2555-66.
278. Garg, S.M., et al., *Traceable PEO-poly(ester) micelles for breast cancer targeting: The effect of core structure and targeting peptide on micellar tumor accumulation.* Biomaterials, 2017. **144**: p. 17-29.
279. Fanta, M., et al., *Production, characterization, and epitope mapping of monoclonal antibodies against human polydeoxyribonucleotide kinase.* Hybridoma, 2001. **20**(4): p. 237-42.
280. Toure, B.B., et al., *A three-component reaction for diversity-oriented synthesis of polysubstituted piperidines: solution and solid-phase optimization of the first tandem aza[4+2]/allylboration.* Chemistry, 2003. **9**(2): p. 466-74.
281. Lee, C., J.S. Kim, and T. Waldman, *PTEN gene targeting reveals a radiation-induced size checkpoint in human cancer cells.* Cancer Res, 2004. **64**(19): p. 6906-14.
282. Jafari, R., et al., *The cellular thermal shift assay for evaluating drug target interactions in cells.* Nat Protoc, 2014. **9**(9): p. 2100-22.
283. Molavi, O., et al., *Synergistic antitumor effects of CpG oligodeoxynucleotide and STAT3 inhibitory agent JSI-124 in a mouse melanoma tumor model.* Immunol Cell Biol, 2008. **86**(6): p. 506-14.

284. Shahin, M., et al., *Engineered breast tumor targeting peptide ligand modified liposomal doxorubicin and the effect of peptide density on anticancer activity.* Biomaterials, 2013. **34**(16): p. 4089-4097.
285. Zaman, M.S., et al., *Curcumin Nanoformulation for Cervical Cancer Treatment.* Scientific Reports, 2016. **6**: p. 20051.
286. Chen, L.Y., et al., *Bcl2 and Ki67 refine prognostication in luminal breast cancers.* Breast Cancer Res Treat, 2015. **149**(3): p. 631-43.
287. Zhou, Y., et al., *Expression of ki67 in papillary thyroid microcarcinoma and its clinical significance.* Asian Pac J Cancer Prev, 2015. **16**(4): p. 1605-8.
288. Pathmanathan, N. and R.L. Balleine, *Ki67 and proliferation in breast cancer.* J Clin Pathol, 2013. **66**(6): p. 512-6.
289. Smukste, I. and B.R. Stockwell, *Restoring functions of tumor suppressors with small molecules.* Cancer Cell, 2003. **4**(6): p. 419-20.
290. Zhang, J., P.L. Yang, and N.S. Gray, *Targeting cancer with small molecule kinase inhibitors.* Nat Rev Cancer, 2009. **9**(1): p. 28-39.
291. Guo, X.E., et al., *Targeting tumor suppressor networks for cancer therapeutics.* Curr Drug Targets, 2014. **15**(1): p. 2-16.
292. Kalepu, S. and V. Nekkanti, *Insoluble drug delivery strategies: review of recent advances and business prospects.* Acta Pharm Sin B, 2015. **5**(5): p. 442-53.
293. Owen, S.C., D.P.Y. Chan, and M.S. Shoichet, *Polymeric micelle stability.* Nano Today, 2012. **7**(1): p. 53-65.
294. Garg, S.M., M.R. Vakili, and A. Lavasanifar, *Polymeric micelles based on poly(ethylene oxide) and alpha-carbon substituted poly(varepsilon-caprolactone): An in vitro study on the effect of core forming block on polymeric micellar stability, biocompatibility, and immunogenicity.* Colloids Surf B Biointerfaces, 2015. **132**: p. 161-70.
295. Paiva, I., et al., *Synthesis and Analysis of (64)Cu-Labeled GE11-Modified Polymeric Micellar Nanoparticles for EGFR-Targeted Molecular Imaging in a Colorectal Cancer Model.* Mol Pharm, 2020. **17**(5): p. 1470-1481.
296. Festing, M.F.W., *Inbred Strains Should Replace Outbred Stocks in Toxicology, Safety Testing, and Drug Development.* Toxicologic Pathology, 2010. **38**(5): p. 681-690.
297. Lloyd, R.L., et al., *Combined PARP and ATR inhibition potentiates genome instability and cell death in ATM-deficient cancer cells.* Oncogene, 2020.
298. Nakajima, T.E., et al., *Antitumor effect of SN-38-releasing polymeric micelles, NK012, on spontaneous peritoneal metastases from orthotopic gastric cancer in mice compared with irinotecan.* Cancer Res, 2008. **68**(22): p. 9318-22.
299. McMahon, M., et al., *Olaparib, Monotherapy or with Ionizing Radiation, Exacerbates DNA Damage in Normal Tissues: Insights from a New p21 Reporter Mouse.* Mol Cancer Res, 2016. **14**(12): p. 1195-1203.
300. Soung, Y.H., et al., *Inactivating mutations of CASPASE-7 gene in human cancers.* Oncogene, 2003. **22**(39): p. 8048-52.
301. Germain, M., et al., *Cleavage of automodified poly(ADP-ribose) polymerase during apoptosis. Evidence for involvement of caspase-7.* J Biol Chem, 1999. **274**(40): p. 28379-84.
302. Lyakhovich, A. and J. Surrallés, *Constitutive Activation of Caspase-3 and Poly ADP Ribose Polymerase Cleavage in Fanconi Anemia Cells.* Molecular Cancer Research, 2010. **8**(1): p. 46-56.
303. Bray, F., et al., *Global cancer statistics 2018: GLOBOCAN estimates of incidence and mortality worldwide for 36 cancers in 185 countries.* CA: A Cancer Journal for Clinicians, 2018. **68**(6): p. 394-424.

304. Høydahl, Ø., et al., *Long-term trends in colorectal cancer: incidence, localization, and presentation.* BMC Cancer, 2020. **20**(1): p. 1077.
305. Murphy, C.C., et al., *Patterns of Colorectal Cancer Care in the United States: 1990-2010.* J Natl Cancer Inst, 2015. **107**(10).
306. Hunter, J.E., et al., *NF-κB mediates radio-sensitization by the PARP-1 inhibitor, AG-014699.* Oncogene, 2012. **31**(2): p. 251-64.
307. Lagunas-Rangel, F.A. and R.M. Bermúdez-Cruz, *Natural Compounds That Target DNA Repair Pathways and Their Therapeutic Potential to Counteract Cancer Cells.* Front Oncol, 2020. **10**: p. 598174.
308. Gupta, P., et al., *Pharmacological targeting of differential DNA repair, radio-sensitizes WRN-deficient cancer cells in vitro and in vivo.* Biochem Pharmacol, 2021. **186**: p. 114450.
309. Wilson, A., et al., *Nitric oxide-donor/PARP-inhibitor combination: A new approach for sensitization to ionizing radiation.* Redox Biol, 2019. **24**: p. 101169.
310. George, T.J., et al., *National Cancer Institute (NCI) state of the science: Targeted radiosensitizers in colorectal cancer.* Cancer, 2019. **125**(16): p. 2732-2746.
311. Matsumura, Y. and H. Maeda, *A new concept for macromolecular therapeutics in cancer chemotherapy: mechanism of tumoritropic accumulation of proteins and the antitumor agent smancs.* Cancer Res, 1986. **46**(12 Pt 1): p. 6387-92.
312. Noguchi, Y., et al., *Early phase tumor accumulation of macromolecules: a great difference in clearance rate between tumor and normal tissues.* Jpn J Cancer Res, 1998. **89**(3): p. 307-14.
313. Kobayashi, H. and P.L. Choyke, *Super enhanced permeability and retention (SUPR) effects in tumors following near infrared photoimmunotherapy.* Nanoscale, 2016. **8**(25): p. 12504-12509.
314. Chen, L., et al., *Using PEGylated magnetic nanoparticles to describe the EPR effect in tumor for predicting therapeutic efficacy of micelle drugs.* Nanoscale, 2018. **10**(4): p. 1788-1797.
315. Aliabadi, H.M., et al., *Disposition of drugs in block copolymer micelle delivery systems: from discovery to recovery.* Clin Pharmacokinet, 2008. **47**(10): p. 619-34.
316. Malam, Y., M. Loizidou, and A.M. Seifalian, *Liposomes and nanoparticles: nanosized vehicles for drug delivery in cancer.* Trends Pharmacol Sci, 2009. **30**(11): p. 592-9.
317. Sadat, S.M.A., et al., *A synthetically lethal nanomedicine delivering novel inhibitors of polynucleotide kinase 3'-phosphatase (PNKP) for targeted therapy of PTEN-deficient colorectal cancer.* Journal of Controlled Release, 2021. **334**: p. 335-352.
318. Garg, S.M., M.R. Vakili, and A. Lavasanifar, *Polymeric micelles based on poly(ethylene oxide) and α-carbon substituted poly(ε-caprolactone): An in vitro study on the effect of core forming block on polymeric micellar stability, biocompatibility, and immunogenicity.* Colloids and Surfaces B: Biointerfaces, 2015. **132**: p. 161-170.
319. Harlow, E. and D. Lane, *Using antibodies : a laboratory manual / Ed Harlow, David Lane*. 1999, Cold Spring Harbor, N.Y: Cold Spring Harbor Laboratory Press.
320. Machulla, H.J., et al., *Simplified Labeling Approach for Synthesizing 3'-Deoxy-3'-[18F]fluorothymidine ([18F]FLT).* Journal of Radioanalytical and Nuclear Chemistry, 2000. **243**(3): p. 843-846.
321. Yu, S., et al., *Total synthesis of camptothecin and SN-38.* J Org Chem, 2012. **77**(1): p. 713-7.
322. Liu, Y., et al., *Comparison of two self-assembled macromolecular prodrug micelles with different conjugate positions of SN38 for enhancing antitumor activity.* Int J Nanomedicine, 2015. **10**: p. 2295-311.
323. Zereshkian, A., et al., *The human polynucleotide kinase/phosphatase (hPNKP) inhibitor A12B4C3 radiosensitizes human myeloid leukemia cells to Auger electron-emitting anti-CD123 ^{111}In-NLS-7G3 radioimmunoconjugates.* Nucl Med Biol, 2014. **41**(5): p. 377-83.

324. Bazak, R., et al., *Passive targeting of nanoparticles to cancer: A comprehensive review of the literature.* Molecular and clinical oncology, 2014. **2**(6): p. 904-908.
325. Zhang, H., et al., *Glycyrrhetinic Acid-Modified Norcantharidin Nanoparticles for Active Targeted Therapy of Hepatocellular Carcinoma.* J Biomed Nanotechnol, 2018. **14**(1): p. 114-126.
326. Xia, Y., et al., *Three dimensional plasmonic assemblies of AuNPs with an overall size of sub-200 nm for chemo-photothermal synergistic therapy of breast cancer.* Nanoscale, 2016. **8**(44): p. 18682-18692.
327. Xu, Z., et al., *Glutathione- and pH-responsive nonporous silica prodrug nanoparticles for controlled release and cancer therapy.* Nanoscale, 2015. **7**(13): p. 5859-5868.
328. Green, M.R., et al., *Abraxane, a novel Cremophor-free, albumin-bound particle form of paclitaxel for the treatment of advanced non-small-cell lung cancer.* Ann Oncol, 2006. **17**(8): p. 1263-8.
329. Wu, D., et al., *Nanomedicine applications in the treatment of breast cancer: current state of the art.* International journal of nanomedicine, 2017. **12**: p. 5879-5892.
330. Siegel, R.L., et al., *Colorectal cancer statistics, 2017.* CA Cancer J Clin, 2017. **67**(3): p. 177-193.
331. Sadat, S.M.A., et al., *A synthetically lethal nanomedicine delivering novel inhibitors of polynucleotide kinase 3'-phosphatase (PNKP) for targeted therapy of PTEN-deficient colorectal cancer.* J Control Release, 2021. **334**: p. 335-352.
332. Ran, Y., et al., *Solubilization of cyclosporin A.* AAPS PharmSciTech, 2001. **2**(1): p. E2.
333. Gelderblom, H., et al., *Cremophor EL: the drawbacks and advantages of vehicle selection for drug formulation.* Eur J Cancer, 2001. **37**(13): p. 1590-8.
334. Gelderblom, H., et al., *Modulation of cisplatin pharmacodynamics by Cremophor EL: experimental and clinical studies.* Eur J Cancer, 2002. **38**(1): p. 205-13.
335. Wu, M., et al., *Olaparib nanoparticles potentiated radiosensitization effects on lung cancer.* Int J Nanomedicine, 2018. **13**: p. 8461-8472.
336. Li, Z., et al., *FLT-PET is superior to FDG-PET for very early response prediction in NPM-ALK-positive lymphoma treated with targeted therapy.* Cancer Res, 2012. **72**(19): p. 5014-24.
337. Kuipers, E.J., T. Rosch, and M. Bretthauer, *Colorectal cancer screening--optimizing current strategies and new directions.* Nat Rev Clin Oncol, 2013. **10**(3): p. 130-42.
338. Bray, F., et al., *Global cancer statistics 2018: GLOBOCAN estimates of incidence and mortality worldwide for 36 cancers in 185 countries.* CA Cancer J Clin, 2018. **68**(6): p. 394-424.
339. Kuipers, E.J., et al., *Colorectal cancer.* Nat Rev Dis Primers, 2015. **1**: p. 15065.
340. Li, X.X., et al., *RNA-seq reveals determinants for irinotecan sensitivity/resistance in colorectal cancer cell lines.* Int J Clin Exp Pathol, 2014. **7**(5): p. 2729-36.
341. Lee, P.C., et al., *Targeting colorectal cancer cells with single-walled carbon nanotubes conjugated to anticancer agent SN-38 and EGFR antibody.* Biomaterials, 2013. **34**(34): p. 8756-65.
342. Inagaki, Y., et al., *Protooncogene (C-Myc) expression in the infiltrating cells of lesional skin from patients with systemic lupus erythematosus.* J Invest Dermatol, 1991. **97**(1): p. 80-4.
343. Roger, E., F. Lagarce, and J.P. Benoit, *Development and characterization of a novel lipid nanocapsule formulation of Sn38 for oral administration.* Eur J Pharm Biopharm, 2011. **79**(1): p. 181-8.
344. Gupta, E., et al., *Metabolic fate of irinotecan in humans: correlation of glucuronidation with diarrhea.* Cancer Res, 1994. **54**(14): p. 3723-5.
345. Garcia-Carbonero, R. and J.G. Supko, *Current perspectives on the clinical experience, pharmacology, and continued development of the camptothecins.* Clin Cancer Res, 2002. **8**(3): p. 641-61.

346. Wang, W., et al., *Effective conversion of irinotecan to SN-38 after intratumoral drug delivery to an intracranial murine glioma model in vivo. Laboratory investigation.* J Neurosurg, 2011. **114**(3): p. 689-94.
347. Kataoka, K., A. Harada, and Y. Nagasaki, *Block copolymer micelles for drug delivery: design, characterization and biological significance.* Adv Drug Deliv Rev, 2001. **47**(1): p. 113-31.
348. Greenwald, R.B., et al., *Drug delivery systems. 2. Camptothecin 20-O-poly(ethylene glycol) ester transport forms.* J Med Chem, 1996. **39**(10): p. 1938-40.
349. Wani, M.C., et al., *Plant antitumor agents. 25. Total synthesis and antileukemic activity of ring A substituted camptothecin analogues. Structure-activity correlations.* J Med Chem, 1987. **30**(10): p. 1774-9.
350. Pan, X.D., et al., *[Synthesis and antitumor activity of 20-O-linked camptothecin ester derivatives].* Yao Xue Xue Bao, 2004. **39**(8): p. 591-7.
351. Wang, C.Y., et al., *Synthesis and antitumor activity of 20-O-linked nitrogen-based camptothecin ester derivatives.* Bioorg Med Chem, 2004. **12**(13): p. 3657-62.
352. Matsumura, Y., *Preclinical and clinical studies of NK012, an SN-38-incorporating polymeric micelles, which is designed based on EPR effect.* Adv Drug Deliv Rev, 2011. **63**(3): p. 184-92.
353. Kenmotsu, H., et al., *The antitumor activity of NK012, an SN-38-incorporating micelle, in combination with bevacizumab against lung cancer xenografts.* Cancer, 2010. **116**(19): p. 4597-604.
354. Mahmud, A., X.B. Xiong, and A. Lavasanifar, *Development of novel polymeric micellar drug conjugates and nano-containers with hydrolyzable core structure for doxorubicin delivery.* Eur J Pharm Biopharm, 2008. **69**(3): p. 923-34.
355. Hakala, R.A., et al., *Hydrophobicities of poly(ε-caprolactone) oligomers functionalized with different succinic anhydrides.* European Polymer Journal, 2009. **45**(2): p. 557-564.
356. Saqr, A., et al., *Development of Traceable Rituximab-Modified PEO-Polyester Micelles by Postinsertion of PEG-phospholipids for Targeting of B-cell Lymphoma.* ACS Omega, 2019. **4**(20): p. 18867-18879.
357. Aliabadi, H.M. and A. Lavasanifar, *Polymeric micelles for drug delivery.* Expert Opin Drug Deliv, 2006. **3**(1): p. 139-62.
358. de la Harpe, K.M., et al., *The Hemocompatibility of Nanoparticles: A Review of Cell–Nanoparticle Interactions and Hemostasis.* Cells, 2019. **8**(10): p. 1209.
359. Goldberg, D.S., et al., *G3.5 PAMAM dendrimers enhance transepithelial transport of SN38 while minimizing gastrointestinal toxicity.* J Control Release, 2011. **150**(3): p. 318-25.
360. Ebrahimnejad, P., et al., *Characterization, blood profile and biodistribution properties of surface modified PLGA nanoparticles of SN-38.* Int J Pharm, 2011. **406**(1-2): p. 122-7.
361. Ebrahimnejad, P., et al., *Preparation and characterization of poly lactide-co-glycolide nanoparticles of SN-38.* PDA J Pharm Sci Technol, 2009. **63**(6): p. 512-20.
362. Ebrahimnejad, P., et al., *Preparation and in vitro evaluation of actively targetable nanoparticles for SN-38 delivery against HT-29 cell lines.* Nanomedicine, 2010. **6**(3): p. 478-85.
363. Hamaguchi, T., et al., *A phase II study of NK012, a polymeric micelle formulation of SN-38, in unresectable, metastatic or recurrent colorectal cancer patients.* Cancer chemotherapy and pharmacology, 2018. **82**(6): p. 1021-1029.
364. Gaucher, G., et al., *Block copolymer micelles: preparation, characterization and application in drug delivery.* J Control Release, 2005. **109**(1-3): p. 169-88.
365. Shen, C., S. Guo, and C. Lu, *Degradation behaviors of monomethoxy poly(ethylene glycol)-b-poly(ε-caprolactone) nanoparticles in aqueous solution.* Polymers for Advanced Technologies, 2008. **19**(1): p. 66-72.

366. Hu, Y., et al., *Degradation behavior of poly(epsilon-caprolactone)-b-poly(ethylene glycol)-b-poly(epsilon-caprolactone) micelles in aqueous solution.* Biomacromolecules, 2004. **5**(5): p. 1756-62.
367. Boice, A. and L. Bouchier-Hayes, *Targeting apoptotic caspases in cancer.* Biochim Biophys Acta Mol Cell Res, 2020. **1867**(6): p. 118688.
368. Mahmud, A., X.-B. Xiong, and A. Lavasanifar, *Development of novel polymeric micellar drug conjugates and nano-containers with hydrolyzable core structure for doxorubicin delivery.* European Journal of Pharmaceutics and Biopharmaceutics, 2008. **69**(3): p. 923-934.
369. Rossi, L., et al., *Erythrocyte-based drug delivery.* Expert Opin Drug Deliv, 2005. **2**(2): p. 311-22.
370. Huang, H., et al., *An Evaluation of Blood Compatibility of Silver Nanoparticles.* Sci Rep, 2016. **6**: p. 25518.
371. Vo, N.N.Q., E.O. Fukushima, and T. Muranaka, *Structure and hemolytic activity relationships of triterpenoid saponins and sapogenins.* J Nat Med, 2017. **71**(1): p. 50-58.
372. Falamarzian, A. and A. Lavasanifar, *Chemical modification of hydrophobic block in poly(ethylene oxide) poly(caprolactone) based nanocarriers: effect on the solubilization and hemolytic activity of amphotericin B.* Macromol Biosci, 2010. **10**(6): p. 648-56.
373. Alfayez, M., et al., *CPX-351 (vyxeos) in AML.* Leuk Lymphoma, 2020. **61**(2): p. 288-297.
374. Palakurthi, S., *Challenges in SN38 drug delivery: current success and future directions.* Expert Opin Drug Deliv, 2015. **12**(12): p. 1911-21.
375. Goldwirt, L., et al., *A new UPLC-MS/MS method for the determination of irinotecan and 7-ethyl-10-hydroxycamptothecin (SN-38) in mice: application to plasma and brain pharmacokinetics.* J Pharm Biomed Anal, 2012. **66**: p. 325-33.
376. Doi, H., et al., *Solubility-Improved 10-O-Substituted SN-38 Derivatives with Antitumor Activity.* ChemMedChem, 2017.
377. Di Veroli, G.Y., et al., *Combenefit: an interactive platform for the analysis and visualization of drug combinations.* Bioinformatics, 2016. **32**(18): p. 2866-8.
378. Xie, Y.-H., Y.-X. Chen, and J.-Y. Fang, *Comprehensive review of targeted therapy for colorectal cancer.* Signal Transduction and Targeted Therapy, 2020. **5**(1): p. 22.
379. Parkin, D.M., et al., *Global cancer statistics, 2002.* CA Cancer J Clin, 2005. **55**(2): p. 74-108.
380. Ferlay, J., et al., *Estimates of worldwide burden of cancer in 2008: GLOBOCAN 2008.* Int J Cancer, 2010. **127**(12): p. 2893-917.
381. Forastiere, A., et al., *Head and neck cancer.* N Engl J Med, 2001. **345**(26): p. 1890-900.
382. Lango, M.N., *Multimodal treatment for head and neck cancer.* Surg Clin North Am, 2009. **89**(1): p. 43-52, viii.
383. Murphy, B.A., J. Gilbert, and S.H. Ridner, *Systemic and global toxicities of head and neck treatment.* Expert Rev Anticancer Ther, 2007. **7**(7): p. 1043-53.
384. Carvalho, A.L., et al., *Trends in incidence and prognosis for head and neck cancer in the United States: a site-specific analysis of the SEER database.* Int J Cancer, 2005. **114**(5): p. 806-16.
385. Sinicrope, F.A., et al., *DNA mismatch repair status and colon cancer recurrence and survival in clinical trials of 5-fluorouracil-based adjuvant therapy.* J Natl Cancer Inst, 2011. **103**(11): p. 863-75.
386. Dvorak, H.F., *Leaky tumor vessels: consequences for tumor stroma generation and for solid tumor therapy.* Prog Clin Biol Res, 1990. **354A**: p. 317-30.
387. Kobayashi, H., R. Watanabe, and P.L. Choyke, *Improving conventional enhanced permeability and retention (EPR) effects; what is the appropriate target?* Theranostics, 2013. **4**(1): p. 81-9.
388. Maeda, H., *Tumor-selective delivery of macromolecular drugs via the EPR effect: background and future prospects.* Bioconjug Chem, 2010. **21**(5): p. 797-802.

389. Moghimi, S.M., A.C. Hunter, and T.L. Andresen, *Factors controlling nanoparticle pharmacokinetics: an integrated analysis and perspective.* Annu Rev Pharmacol Toxicol, 2012. **52**: p. 481-503.
390. Toy, R., et al., *The effects of particle size, density and shape on margination of nanoparticles in microcirculation.* Nanotechnology, 2011. **22**(11): p. 115101-115101.
391. Rao, J., *Shedding light on tumors using nanoparticles.* ACS Nano, 2008. **2**(10): p. 1984-6.
392. Kircher, M.F., et al., *A multimodal nanoparticle for preoperative magnetic resonance imaging and intraoperative optical brain tumor delineation.* Cancer Res, 2003. **63**(23): p. 8122-5.
393. Owens, D.E., 3rd and N.A. Peppas, *Opsonization, biodistribution, and pharmacokinetics of polymeric nanoparticles.* Int J Pharm, 2006. **307**(1): p. 93-102.
394. Wang, J., M. Sui, and W. Fan, *Nanoparticles for tumor targeted therapies and their pharmacokinetics.* Curr Drug Metab, 2010. **11**(2): p. 129-41.
395. Zhang, J.S., F. Liu, and L. Huang, *Implications of pharmacokinetic behavior of lipoplex for its inflammatory toxicity.* Adv Drug Deliv Rev, 2005. **57**(5): p. 689-98.
396. Cedervall, T., et al., *Detailed identification of plasma proteins adsorbed on copolymer nanoparticles.* Angew Chem Int Ed Engl, 2007. **46**(30): p. 5754-6.
397. Gessner, A., et al., *Nanoparticles with decreasing surface hydrophobicities: influence on plasma protein adsorption.* Int J Pharm, 2000. **196**(2): p. 245-9.
398. Nagayama, S., et al., *Time-dependent changes in opsonin amount associated on nanoparticles alter their hepatic uptake characteristics.* Int J Pharm, 2007. **342**(1-2): p. 215-21.
399. Avgoustakis, K., et al., *Effect of copolymer composition on the physicochemical characteristics, in vitro stability, and biodistribution of PLGA-mPEG nanoparticles.* Int J Pharm, 2003. **259**(1-2): p. 115-27.
400. Mosqueira, V.C.F., et al., *Biodistribution of Long-Circulating PEG-Grafted Nanocapsules in Mice: Effects of PEG Chain Length and Density.* Pharmaceutical Research, 2001. **18**(10): p. 1411-1419.
401. Patel, B., N. Gupta, and F. Ahsan, *Particle engineering to enhance or lessen particle uptake by alveolar macrophages and to influence the therapeutic outcome.* Eur J Pharm Biopharm, 2015. **89**: p. 163-74.
402. Desai, P.P., A.A. Date, and V.B. Patravale, *Overcoming poor oral bioavailability using nanoparticle formulations – opportunities and limitations.* Drug Discovery Today: Technologies, 2012. **9**(2): p. e87-e95.
403. Bulbake, U., et al., *Liposomal Formulations in Clinical Use: An Updated Review.* Pharmaceutics, 2017. **9**(2).
404. Muntimadugu, E., N. Kommineni, and W. Khan, *Exploring the Potential of Nanotherapeutics in Targeting Tumor Microenvironment for Cancer Therapy.* Pharmacological Research, 2017. **126**: p. 109-122.